Title

Seismic Responses and Protection Of Building Systems Using PBEE Methodology

Author

Shu, Zhan

Publication Date

2014

UNIVERSITY OF CALIFORNIA

Los Angeles

Seismic Responses and Protection Of Building Systems Using PBEE Methodology

A dissertation submitted in partial satisfaction of the

requirements for the degree Doctor of Philosophy

in Civil Engineering

by

Zhan Shu

2014

ABSTRACT OF THE DISSERTATION

Seismic Responses and Protection
Of Building Systems Using PBEE Methodology

by

Zhan Shu
Doctor of Philosophy in Civil Engineering
University of California, Los Angeles, 2014
Professor Jian Zhang, Chair

Buildings are vulnerable to earthquake ground motions. To help reduce the loss from earthquake events, seismic protective devices emerged in recent decades to improve the performance of building structures against earthquake loads. The ultimate goal of this research is to explore new devices and/or optimally design existing devices to better protect buildings such that the total cost (both direct and indirect) due to earthquake damages can be reduced to a minimum level. This is accomplished through the following research tasks:

First, this study established accurate numerical nonlinear models for different building systems so that their seismic performances can be calculated realistically including nonlinear behavior. The numerical models are validated by comparing simulated building performances with that of the shaking table test data of a full-scale building. Using these validated numerical models, the peak inelastic drift ratio and permanent residual drift ratio are evaluated and correlated with building performances.

Second, this research assembles a collection of practical seismic protective devices for buildings and their numerical models. The emerging trend of seismic control devices with adaptive stiffness and damping properties under different loading scenarios yet still remain largely passive is explored. In particular, a novel negative stiffness device is investigated along with two other seismic protective devices, namely the base isolation and nonlinear damping device through dimensional analysis. In addition, numerical modeling schemes of the these devices as well as well as the self-centering device are implemented.

Third, the proposed research intends to enable performance-based implementation of seismic protective devices that can logically take into account of the complexities, uncertainties and variability involved with the seismic responses of buildings. A comprehensive performance index depicting the total loss of the system has been invented to evaluate the building performance. In addition, the optimal range of design parameters of base isolation system for building systems is provided under the performance-based earthquake engineering framework.

The dissertation of Zhan Shu is approved.

Ertugrul Taciroglu

John W. Wallace

Steve Gibson

Jian Zhang, Committee Chair

University of California, Los Angeles

2014

To my dear parents

Zhijun Shu & Fuli Han

for your endless love, support,
encouragement and patience
throughout the years.
I love you!

谨以此论文献给我的父亲，母亲

舒志军 & 韩伏莅

感谢你们无尽的爱、
这些年你们对我的支持、
热忱的鼓励和不变的期待。
我爱你们！

TABLE OF CONTENTS

LIST OF FIGURES

LIST OF TABLES

ACKNOWLEDGMENTS

I would like to express my deepest gratitude to my adviser Professor Jian Zhang for her invaluable guidance, gracious support, and technical advice. Working under her supervision has been a unique instructive experience for me and I am really honored to have her as my adviser. Throughout my years at UCLA, not only has she provided a great source of inspiration to my research, but also raised me up to a better human being.

I would also like to express my appreciation to Prof. Wallace, who served on my reading committee and provided constructive feedback during the preparation of this manuscript. Special thanks are also due to Prof. Taciroglu for his valuable comments during the preparation throughout this dissertation. I feel grateful for Prof. Gibson and his instructions about control theory. I am also indebted to professors and for all their generosity in sharing their time and knowledge with me in answering my questions.

A part of this study was financially supported by NSF - Network for Earthquake Engineering Simulation Research Program: Development of Next Generation Adaptive Seismic Protection (NEESR-SG, CMMI-0830391) This support is gratefully acknowledged.

As an EERI student researcher I had the privilege of interacting with other EERI student researchers and Professors from other Universities. I would like to thank all the researchers who were involved in the EERI for creating a unique environment for productive research. Specially, I would like to express my gratitude to Professor Jian Zhang, the faculty advisor of the UCLA EERI chapter.

Now I would like to thank all my research group members, fellow students and professionals, as well as department staff, especially Maida Bassili, who supported me with their constructive comments, pleasant teamwork, and heart-warming help regarding various aspects of my life at UCLA.

I also want to thank all my friends in UCLA ASCE chapter. Thank you to all of you for creating an enjoyable environment to work and to interact. In addition, I would like to thank my friends at the University Cooperative Housing Association, who made my experience at UCLA unforgettable.

Finally, I would like to thank my family especially my father Zhijun Shu, my mother Fuli Han, for all their generous love and support during these years. Thanks for always being there for me. This dissertation is dedicated to them.

VITA

EDUCATION

- M.S. in Structural Engineering, University of California, Los Angeles (2007-2008)
- B.S. in Manage of Information System, Donghua University, Shanghai, China (2003-2007)

TEACHING AND RESEARCH ACTIVITIES (SELECTED)

- Graduate Teaching Assistant, Department of Civil and Environmental Engineering, University of California, Los Angeles, U.S.A. (2008-2013)
- Graduate Research Assistant, Department of Civil and Environmental Engineering, University of California, Los Angeles, U.S.A. (2009-2014)

HONORS AND AWARDS (SELECTED)

- UCLA Graduate Division, Fellowship Award, CA, U.S.A. (2010-2011, 2011-2012, and 2012-2013)
- Third Place in the 2011 Blind Analysis Contest: Numerical Prediction of Shaking Table Test of 5-story Steel Frame with and without Base Isolation (2011)

PROFESSIONAL ACTIVITIES (SELECTED)

- Journal Paper Reviewer: Earthquake Engineering and Engineering Vibration.
- member, ASCE, 2008-present
- Treasurer, EERI/UCLA Student Chapter, 2009-2011
- Webmaster, EERI/UCLA Student Chapter, 2011-2013
- Fundraiser, Overseas Chinese Civil and Structural Engineering Association, 2013-present

JOURNAL PUBLICATIONS (SELECTED)

Zhang J. and Shu Z. (2013). "*Optimal Design of Isolation Devices for Buildings Using Performance Based Methodology*". (Under Preparation)

Shu Z., Zhang J., and Nagarajaiah, S., (2013). "*Dimensional Analysis of Inelastic Structures with Negative Stiffness Devices and Supplemental Damping Devices*". (Under Preparation)

Shu Z. and Zhang J. (2013). "*Dimensional Estimation of Residual Drift Demand for Bilinear System Under Near Fault Ground Motions*". (Under Preparation)

Shu Z. and Li S. (2014), "*Optimal Seismic Design for Buildings with Concentrated Mass, an Innovative Performance-based Approach*". ". (Under Preparation)

Li S., Shu Z., Zhai C., Tong Q., Xie L. (2014). "*Evaluating Seismic Resistant Capability of Nuclear Power Plant Using the Fragility Function Method*" (Under Preparation)

1. INTRODUCTION

1.1 General

Protection of civil structures against earthquakes constitutes a significant task for structural engineers. Current practice for designing structures against seismic actions allows and often relies on ductile behavior that develops significant inelastic deformations during strong earthquakes in order to reduce the inertia forces inside the structure. On the other hand, inelastic hysteretic behavior may result with stiffness and strength degradation, increased inter-story drifts, and damage with residual drift.

This chapter briefly introduces earthquake damages to buildings, various building seismic behavior, and approaches to improve building performance. The observed damage mechanisms, configuration effects and practical engineering techniques not only motivate this research but also direct the whole study throughout the following chapters. Meanwhile, typical types of existing buildings have been introduced as the reference for implementing various building control devices throughout this study.

1.2 Historical Earthquake Events and Building Seismic Damages

Buildings reflect the civilization and culture of human beings. The loss of function and failure of buildings will result in loss of lives and direct economical suffering, which delays the post-earthquake recovery and causes further indirect economy loss.

For example, the 1964 Alaska earthquake, also known as the Great Alaskan Earthquake, caused significant amount of damage. Across south-central Alaska, ground fissures, collapsing buildings, and tsunamis directly caused about 139 deaths. The powerful earthquake produced earthquake liquefaction in the region as well. Ground fissures and failures caused major structural damage in several communities, much damage to property and several landslides. Anchorage sustained great destruction and damage to many inadequately engineered houses, buildings, and infrastructure (paved streets, sidewalks, water and sewer mains, electrical systems, and other man-made equipment).

More recently, serious building damage continued being reported in various areas around the world. The Kobe region in Japan was once considered to be sufficiently safe in terms of its seismic performance. However, the 1995 Kobe earthquake, which lasted for only 20 seconds, took away more than 6000 lives. Many of the collapsed buildings in Kobe were built before the development of strict seismic codes released in 1981. (vibrationdata.com). The Northridge earthquake happened 20 years ago in 1994 centered in the north-central San Fernando Valley region of Los Angeles, California. The earthquake shook the ground for about 15 seconds with a peak moment magnitude (M_W) of 6.7 and an incredibly high ground acceleration of 1.8g measured in urban Los Angeles area. The death toll was 57, with more than 8,000 injured. In addition, earthquake-caused property damage was estimated to be more than $20 billion, making it one of the costliest natural disasters in U.S. history. Buildings were severely damaged or collapsed and building code changes have been made since the event to avoid loss from buildings for future events. The 1999 Jiji (chi-chi) earthquake in Taiwan is also worth mentioning. The peak moment magnitude (M_W) was about 7.7, 2,415 people died and 11,305 people injured during the event. The loss of buildings made 100,000 people homeless. The total estimation of loss is about $10 billion.

Fig. 1.1 shows some severely damaged buildings from the aforementioned historical earthquake ground motions. One could easily notice that the conventionally designed buildings are not strong enough to undergo powerful earthquakes. They develop significant inelastic deformations that lead to major damages to the buildings under strong earthquake shakes.

(a) Penney Building in Anchorage, 1964 Alaska

(b) Kobe earthquake damage. Failure of the first story caused partial collapse of upper stories.

(c) Mid-story collapse, Kobe earthquake.

(d) Apartment building seriously damaged by 1994 Northridge earthquake.

(e) A collapsed building located in Nantou County from 1999 Jiji earthquake.

Fig. 1.1 Building failure mechanisms observed in the historical earthquakes. (images from vibrationdata.com, eqecat.com, wordpress.com)

Building structures, due to the distinct earthquakes and variant building designs, show different damage mechanisms. In general, damages are more likely to occur in ground level than higher story levels due to the overturning moment and larger base shear applied to the ground level structural members. For the local structural elements, the damages are usually lumped at the ends. Meanwhile, building damages are often concentrated in their critical regions. For examples, for concrete building frame system, the expected critical zones are shown in Fig. 1.2 (Mahin 1975). The inelastic deformations lead to inelastic hysteretic behaviors, stiffness and strength degradations, increased inter-story drifts, and damages with residual drifts. Such disadvantages have raised great concerns in practice and improvements are desired to achieve better structural seismic performance. Therefore, in the recent decades, seismic protective methods have drawn increasing attention from researchers and scholars in the realm of civil engineering.

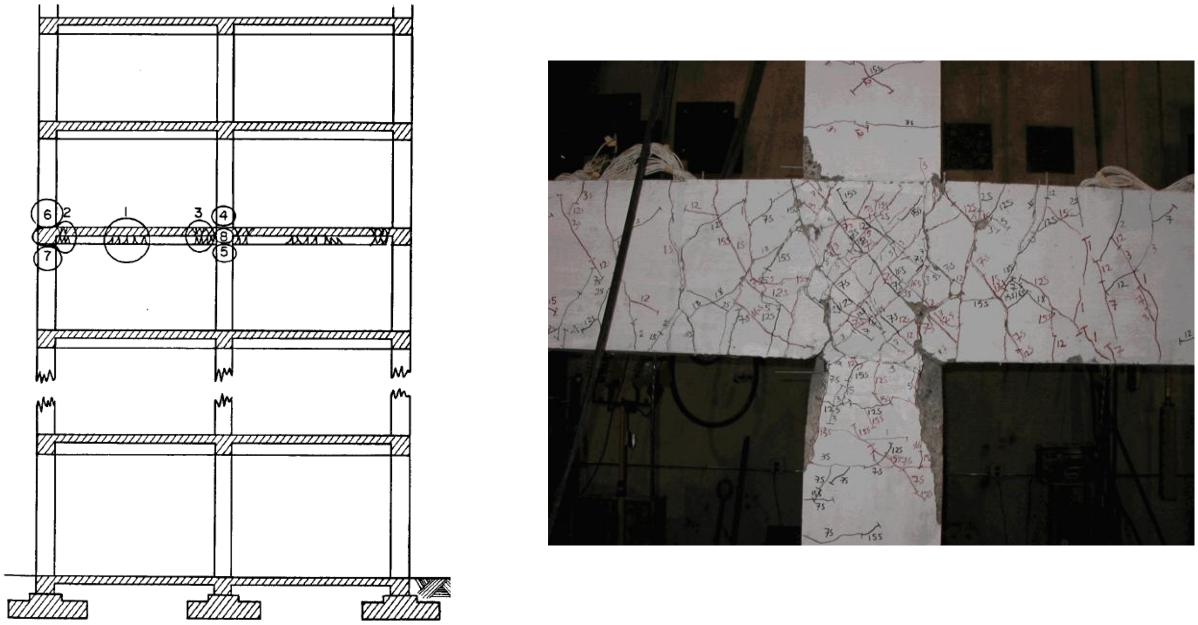

Fig. 1.2 Examples of critical regions in reinforced concrete frames

1.3 Understanding Building Performance for Structural Control

As buildings come in a wide range of shapes and functions. Much effort has been previously devoted to understand the building behaviors. Columns, walls, girders and beams are most common building structural elements. In addition, elements of reinforced concrete, steel and composite material are generally being used. Two typical types of building systems, the steel frame buildings and the reinforced concrete buildings, are introduced here. These two types are selected as most of existing building seismic protective technologies are implemented in such building systems.

1.3.1 Steel Frame Structures

When there is not enough room for the shear wall, an engineer or architect must design a special frame, called a moment frame to resist the horizontal forces. Most modern high-rise buildings and many mid- and low-rise buildings rely on steel moment frames to resist lateral loads arising from winds or earthquakes. Lateral loads from earthquakes result from internal inertial loads that develop as the ground, and therefore the building's foundation, accelerates. This is similar to the force that a passenger standing on a bus feels when the bus accelerates. In the case of a building, inertial forces are primarily at the floor levels, where the weights are concentrated.

According to HAZUS (2003), Steel Moment Frame (S1) is the type of buildings having a frame of steel columns and beams. In some cases, the beam-column connections have very small moment resisting capacity but, in other cases, some of the beams and columns are fully developed as moment frames to resist lateral forces. Usually the structure is concealed on the outside by exterior nonstructural walls, which can be of almost any material (curtain walls, brick masonry, or precast concrete panels), and on the inside by ceilings and column furring. Diaphragms transfer lateral loads to moment-resisting frames. The diaphragms can be almost any material as well. The frames develop their stiffness by full or partial moment connections. The frames can be located almost anywhere in the building. Usually the columns have their strong directions oriented so that some columns act primarily in one direction while the others act in the other orthogonal direction. Steel moment frame buildings are typically more flexible than shear wall buildings. This low stiffness can result in large inter-story drifts that may lead to relatively greater ductility of the system. Fig. 1.3 shows the in-side view of a real steel moment frame and one example modeling of a 4-story steel moment frame building by the software platform ETABS.

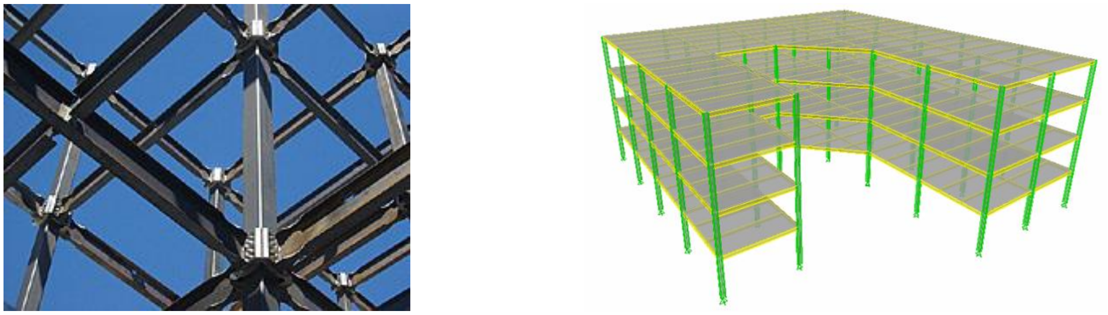

(a) steel moment frame inner-view **(b)** A moment frame building in ETABS

Fig. 1.3 Illustration of steel moment frames

During strong ground motion, the steel members are expected to behave in a ductile manner: stretching and absorbing energy. After the earthquake, permanent deformation of the steel-frame members is expected. Several special detailing provisions in the current code are intended to ensure ductile performance. In the 1994 Northridge Earthquake, the steel moment frames have not achieved such expected performance, which leads to many topics after the event to improve the steel design against severe ground motions.

Researchers in literature use different computational programs to model steel framing systems. The open source finite element framework, OpenSees (http://opensees.- berkeley.edu, documented by Mazzoni *et al.* 2006) is popular these years due to its capability to model fiber sections. The interaction of axial force and flexure is automatically incorporated in fiber sections such that a more accurate computation is expected. Zhang and Tang (2009) modeled a steel moment frame building to discuss the soil-structure interaction; a detailed case study of a realistic nine-story 2D steel moment-resisting frame is carried out in OpenSees. The elements are modeled using steel fiber section with force-based elements that considers the spread of plasticity. And the steel stress-strain curve was modeled with a bilinear model.

Although many of current OpenSees users are modeling the steel moment frames with fiber sections, the choice of inelastic steel sections (non-fiber sections) to model steel elements in OpenSees also works decently well. The inelastic sections define the steel section properties such as modulus, moment of inertia, and area. Then, the model feed these values into the calculation of the global stiffness matrix. Since the steel section is not composite, the result of fiber section model is very similar to that of inelastic sections.

In this study, nonlinear evaluations for steel moment frames were carried out using OpenSees. The 2D model of inelastic response of steel elements is using an inelastic steel section with steel01 material provided by OpenSees. This material behavior is similar to bilinear behavior. Reduced Beam Sections (RBS) can be considered by weakening specific areas of each local elements so that plastic deformation will be lumped in those plastic areas.

1.3.2 Reinforced Concrete Structures

Reinforced concrete (RC) structures designed according to present building codes as moment resisting space frames, shear-walls, coupled shear-walls or any combination thereof to withstand strong earthquake motions are expected to deform well into the inelastic range and dissipate the energy input by the base motion through stable hysteretic behavior of structural components. RC moment resisting frames are similar to steel moment frame buildings except that the frames are reinforced concrete. Fig. 1.4 shows a typical parking structure categorized as a concrete moment frame building. There are large varieties of RC frame systems. Some older concrete frames may be proportioned and detailed such that brittle failure of the frame members can occur in earthquakes leading to partial or full collapse of the buildings. Modern frames in zones of high seismicity are proportioned and detailed for ductile behavior and are likely to undergo large deformations during an earthquake without brittle failure of frame members and collapse.

When medium- to high-rise reinforced concrete moment resisting frames are subjected to severe seismic excitations, the behavior of members in the lower part of the building is controlled by lateral loads. Since it is not economically feasible to design RC structures to remain elastic during severe earthquake ground motions, the maximum girder moments are likely to exceed the yield moment of the cross-section in critical regions of the structure and lead to inelastic deformations.

(a) Outside view of parking building (b) Inside view of parking building

Fig. 1.4 Example of a concrete parking structure

Models of inelastic response of RC elements are more complicated based on their nature of combined material of concrete and steel. Concrete is assumed incapable of carrying tensile stress. Once cracking occurs, the concrete fiber cannot supply compressive strength until the crack is closed. Due to modern capacity design provisions for RC SMRF buildings (ACI 318R-02), the joints of RC frames are not expected to control the failure mechanism (Haselton *et al.* 2007), so generally RC buildings are modeled with a bilinear element, which accounts for cracking but not strength loss. Similarly, shear failure is not expected for the elements of RC SMRF buildings, so only flexural damage is modeled. (Goulet *et al.* 2007)

Numerical models of RC structures can be simple that no plastic hinges are included or can be complicated to capture the behavior that is better correlated with existing empirical relationships. Model complexity grows when accuracy is improved. There are two commonly observed imperfections of recent modeling approaches such as inelastic fiber models. First, they are more likely to fail to converge at some certain time steps. Second, longer computation time is consumed.

Haselton *et al.* (2007) created a relatively sophisticated model to better evaluate the seismic performance of a 4-story benchmark concrete frame building. Their work uses some of the current existing damage models to consider the strength loss, which is remarkable. Two models are adopted: a fiber model for low intensity levels (where cracking and initial yielding behavior governs) and a plastic hinge model to capture strength and stiffness deterioration and collapse. The fiber model consists of fiber beam-column elements with an additional elastic shear degree-of-freedom at each section, finite joint elements with panel shear and bond-slip springs, and column-base bond-slip springs. The plastic hinge model also includes the joint element, but the beam-column element lumps the bond slip and beam column yielding response into one concentrated hinge. Their element was modeled with in OpenSees (Fig. 1.5(a)). Bilinear material model was originally used and extended to a strength degrading model shown in Fig. 1.6(b). P-Delta effects are accounted for using a combination of gravity loads on the lateral-resisting frame and gravity loads on a leaning column element. The model includes 6.5% Rayleigh damping anchored to the first and third modal periods. Soil–structure interaction (SSI) was considered in some simulations, including foundation flexibility and damping as well as kinematic effects on ground motions at the foundation level of the building. SSI effects were found to be insignificant (Haselton *et al.* 2007) and are not discussed further. More details on all aspects of the structural modeling can be found in the report by Haselton *et al.* (2007).

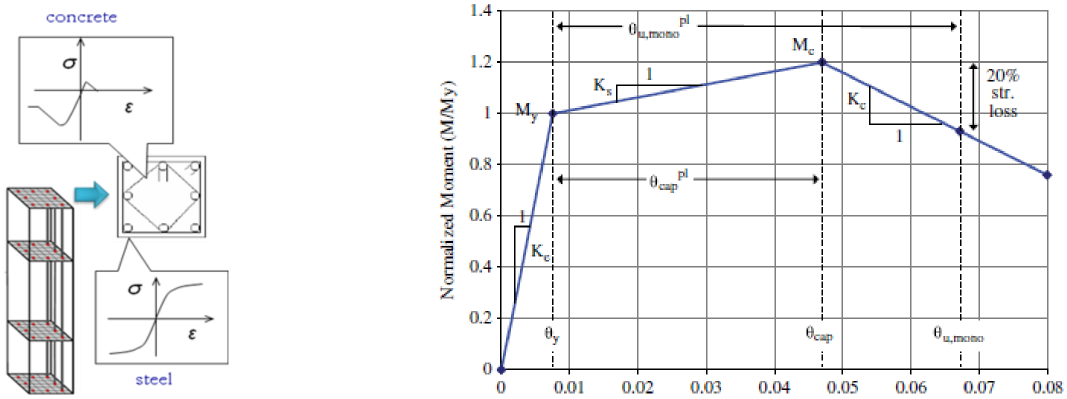

(a) RC fiber section model from OpenSees (b) Strength degrading model

Fig. 1.5 An example of OpenSees modeling scheme for concrete section and material

1.4 Structure Control and the Need for ASD devices

Structural control takes advantages of latest advanced computers, electronics, measurement techniques, instrumentation, controllers, materials, etc. These techniques make structures behave more like machines, aircrafts or human beings in the sense that they can be made adaptive or responsive to external forces. As a result, the building damage from earthquakes is reduced.

1.4.1 Passive Structural Control

One of the most intuitive approaches is commonly known as the passive seismic protection systems in the form of supplemental damping devices, base-isolation devices, and various energy dissipation systems such as the bracing-type visco-elastic and viscous fluid dampers. These passive systems have emerged as an effective approach for reducing response and limiting damage by shifting the inelastic energy dissipation from the building systems to the passive control systems. Passive seismic systems are activated by the structural motions and no external power or energy is needed. However, such passive systems are not sufficiently adaptive to ever-changing external excitation. They do not generally provide self-centering stiffness capability or counter stiffness degradation, offering limited help to reduce the residual displacement and system damage, etc. For example, design of passive base isolation devices became mature in recent decades and a detailed introduction of isolation device will be given in chapter four of this study.

1.4.2 Active Structural Control

Modern control theories were developed since 1960s, and it was almost immediately successfully applied to space vehicles as well as aeronautical systems. After a few years, ground vehicles started to be geared with control devices to reduce vibration. In early 1970s, the application of active control theory to control the vibration of civil engineering structures joins people's discussion. Active Control system has wide ranges of operation for vibration control of the structure. It makes the control system automatic in the manner that externally activated device supplies the control forces to change the response of the structure, depending on the measurement of external disturbance and structural responses. Sensors are employed for the measurement purposes, and with the help of computers, the required external forces are generated. The direction and magnitude of the control forces to be applied to the structure are estimated by designed algorithms (Soong and Reinhorn 1993). Active control systems are fully adaptive that are more efficient in reducing the structural response by means of control force generated from external power. Comparing to the passive systems, the active systems enhanced the effectiveness in motion control, which is only limited to the capacity of the control devices.

Since Yao proposed the concept of structural control for civil engineering structures in 1972 (Yao 1972), the reduction of structural response caused by dynamic loading has become a popular research subject for the last four decades. Many structural control concepts have been developed for this purpose. These research results show that active control has the ability to suppress vibration effectively due to its instantaneous response property. In 1989, the first full scale active control system was applied to a ten-storey building in Tokyo (Kobori *et al.* 1991). This application accelerated the development of structural control systems for actual buildings and widened the range of corresponding research.

Basic configuration of an active structural control system is shown in Fig. 1.6 (Kumar *et al.* 2007). It consists of: (i) Sensors located in the structure to measure either external excitations or structural responses, i.e., displacement, velocity and acceleration, (ii) Devices to process the measured information and compute necessary forces needed based on a given control algorithm and, (iii) Actuators, which are usually powered by external energy sources, to produce and apply the required forces in the desired direction.

The Active Mass Damper and Active Mass Driver system (AMD) system was the first active control system developed for the structural control purpose in late 1980s. Later on, Active Variable Stiffness System emerged aiming at the goal to adjust the structural stiffness so that resonant modes of the structure can be kept away from the seismic input at each time instant thus to suppress the structural responses. Active control using structural braces and tendons has been one of the most studied mechanisms. Systems of this type generally consist of a set of tendons or braces connected to a structure. Soong *et al.* (1991) studied Active Bracing System (ABS) analytically to show its effectiveness. Some of these active control systems have also been summarized in Chapter 4.

There are many constrains and limitations for the wide application of active control system to real civil buildings. Controlling of civil engineering structures has many difficulties due to their huge sizes, heavy weight and complicated settings. Active optimal control application is also limited for its demand of significant external power supply and huge force generation equipment, hence is vulnerable to power supply failure and may destabilize the structure.

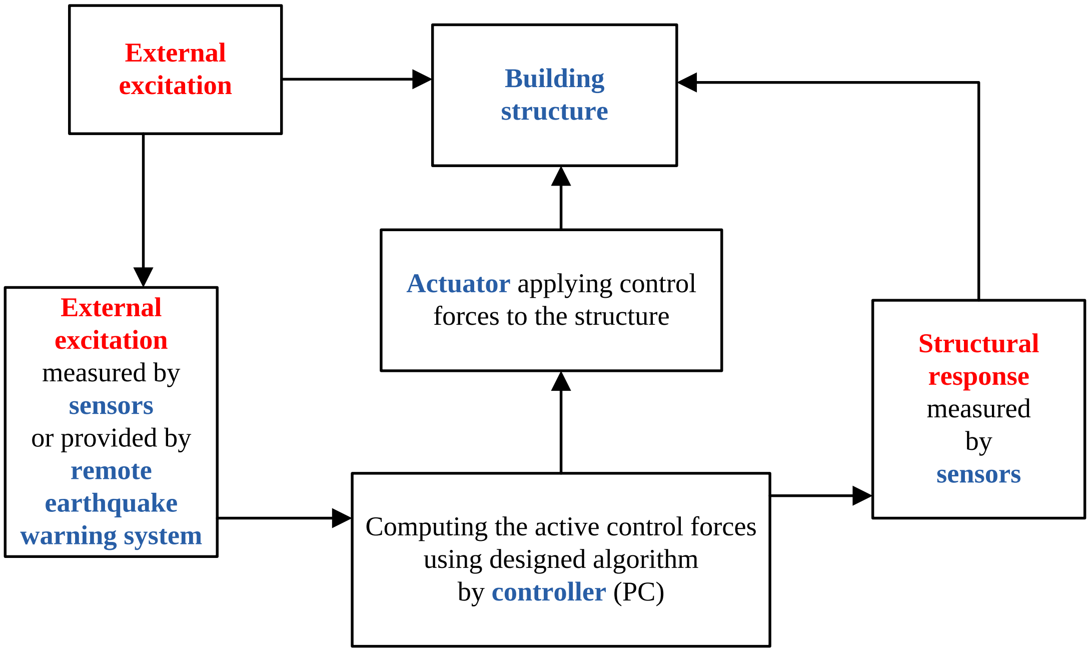

Fig. 1.6 Flow diagram of active control (adapted from Kumar *et al.* 2007)

1.4.3 Semi-active Structural Control

Semi-active control system is a natural evolution of passive control system as it incorporates adaptive factors to improve effectiveness of the passive system. It is often referred as controllable or intelligent passive system. Semi-active control system requires orders of magnitude smaller external power than a typical active control system, in which the control action is produced by the movement of the structure but is regulated by an external source of energy.

A typical semi-active control system consists of sensors, a control computer, an actuator and passive devices. The sensors measure the excitation and/or structural response, which are transmitted to the control computer for processing. The computer generates control signals based on the information from the sensors for the actuator. Then the actuator acts to adjust the behavior of the passive device. The actuator is only used to control the behavior of the passive device instead of applying control force directly onto the structure, thus it only requires a small power supply such as batteries. Semi-active control system also eliminates harmful potential such as destabilization. In addition, they are easy to manufacture and are reliable to operate at a cost of being a little more complex than passive system.

Recent investigations (introduced in following sections) have shown that a combination of adaptive stiffness and damping (ASD) devices can provide substantial response modification, particularly during near-fault pulse-type earthquakes. ASD devices offer structural response modification capability by optimally varying the restoring forces (stiffness) linked to the frequencies of vibration and dissipative forces (damping) that govern the behavior of a structural dynamic system. To date, adaptive stiffness systems have received relatively little attention in real practice as compared to supplemental damping systems and thus represent a significant gap in earthquake engineering.

Hence, development of new ASD devices is necessary to shift the energy dissipation and associated stiffness variations from the structural system to the ASD devices to reduce damage to building frames, eliminate residual inter-story drift, and provide self-centering capability.

1.5 Scope and Objectives

The objective of the research is to link the desired performance of the building structures with realistic practice and establish the criteria to select optimal stiffness and damping as well as the protection strategy for buildings to improve their performance against earthquakes. The passive and semi-active devices with adaptive stiffness and damping are referred as ASD system. The study aims at developing such ASD systems that can also adapt stiffness and damping automatically during a ground motion.

In real design practice, the building performance is earthquake dependent, structure dependent, and influenced by other variability. To improve the seismic response of buildings to specific performance level, performance-based earthquake engineering framework will be adopted with the consideration of all the uncertainties. With the application of structural control technology, it is expected that the performances of buildings achieve the design goal by optimally determining the mechanical properties and locations of the seismic protective devices. Chapter 3 of this work provides a logical and optimized way to optimally design the control devices for buildings and the method is applied to optimize the base isolation systems for building system in Chapter 5.

The major tasks of this comprehensive research program are summarized in the following:

1. Fully understand building response from earthquake ground motions. Optimized building performance with minimum damage is the design target for all the seismic protective devices. Accurate modeling of building system is desired. In addition, prediction of inelastic performance of buildings such as its peak transient drift and residual drift is desirable.

2. Develop a framework to evaluate the building performance under the Performance-based Earthquake Engineering (PBEE) framework. A performance index shall be specified to represent the performance of building against earth shaking and other uncertainties.

3. Develop the design scheme for the adaptive control devices and find their optimal design variables under PBEE framework. Given performance objective of the building structures, the design scheme is able to determine the mechanical properties and locations of the adaptive control devices.

4. Understand the performance of existing building protective devices, their advantages and disadvantages. Another objective of work is to present a method that accurately evaluates the effectiveness of a certain device. The mechanical properties of the device can be revealed without interfered by different excitation inputs.
5. Perform numerical simulation of the adaptive stiffness and damping devices at system level, i.e., apply the developed devices in realistic building model and identify the structural response modification, thus to determine the control strategy for real-world application.
6. Analytical and numerical study to discover the effects of stiffness and damping variation and identify strategies for varying stiffness and damping for the ASD devices during seismic excitation, i.e., to find out what are the best force-displacement loops the passive and semi-active control devices should have to provide the optimum performance.

1.6 Organization

This dissertation includes seven chapters in order to address the key issues and achieve the considered objectives of this research presented in the previous section.

A general description of existing building systems is presented and the need for seismic protective devices to improve building performances is addressed in Chapter 1. Chapter 2 includes a detailed highlight of current practice of PBEE framework and provides a general discussion of performance-based design framework for buildings, which includes the performance index, and error analysis, etc. In Chapter 3, estimations to the building nonlinear drifts (peak inelastic drift and residual drift) are provided under the dimensional analysis framework. Chapter 4 summarizes existing seismic protective devices for buildings and presented numerical modeling methods for a few typical protective devices. In addition, an adaptive stiffness device design - negative stiffness devices is introduced. Chapter 5 presents optimal isolation design for buildings under the PBEE framework. In Chapter 6, the seismic performance of negative stiffness devices is evaluated. The effectiveness of such device has been proved in a SDOF system. Ultimately, Chapter 7 provides the major findings and conclusions of this research along with the recommendations for the future work.

2. THE PERFORMANCE-BASED EARTHQUAKE ENGINEERING FOR BUILDING SYSTEMS

2.1 General

Structural engineers conventionally use allowable-stress design (ASD) and/or load-and-resistance-factor design (LRFD), which focus on individual structural elements and connections, and seek to ensure that none will experience loads or deformation greater than it is capable of withstanding. PBEE, a new emerging and promising approach, attempts to address performances primarily at the system level, i.e. a designed building as a whole will perform in some predictable way, in terms of risk of collapse, fatalities, repair costs, and post-earthquake loss of function. This chapter is a review of Performance-based earthquake engineering (PBEE). Details about current state of PBEE practice, structural control framework based on PBEE, fragility functions, ground motions, damage index and limit states and other considerations and challenges will be presented.

PBEE can be defined as the assessment of system level performance of a building, bridge, or other individual structural system subjected to seismic excitations, and the detailed design of its structural features to achieve prescribed performance goals (Haselton *et al.* 2007).

Modern building codes (e.g., ICC 2003; ASCE 2008) provide design guidelines intended to achieve a similar performance objective (life safety and some degree of damage control) under a specified ground motion hazard. New documents have been published in recent years that seek to provide for more-robust performance-based seismic design. Structural Engineers Association of California (SEAOC) (1995) proposed Vision 2000, which articulated the goal to "embrace a broader scope of design and construction quality assurance issues and … yield more predictable seismic performance over a range of earthquake demands." Vision 2000 describes various hazard levels: the frequent or 50%-in-30-years earthquake event, the occasional or 50%-in-50-years earthquake event, rare, or 10%-in-50-years earthquake event, and the very rare, or 10%-in-100-years earthquake event. Vision 2000 also defines various structural performance levels: fully operational, operational, life safety, and near collapse in terms of damage to structural and nonstructural components and in terms of consequences to the occupants and functions carried on within the facility. Vision 2000 offers relationships between these hazard and performance levels for various building categories (e.g., hospitals are considered to be critical facilities). This relationship is shown in Fig. 2.1, which indicates that the performance level that should be satisfied for the given hazard level and the type of structure.

Performance-based approaches were further codified with publication of the Seismic Evaluation and Retrofit of Concrete Buildings (ATC-40, 1996) and the National Earthquake Hazards Reduction Program (NEHRP) Guidelines for the Seismic Rehabilitation of Buildings and associated Commentary (FEMA 273 and 274, 1997). These documents addressed the rehabilitation of existing structures, and led to the most comprehensive guidelines for PBEE to date: the Pre-standard and Commentary for the Seismic Rehabilitation of Buildings (FEMA 356; ASCE 2000).

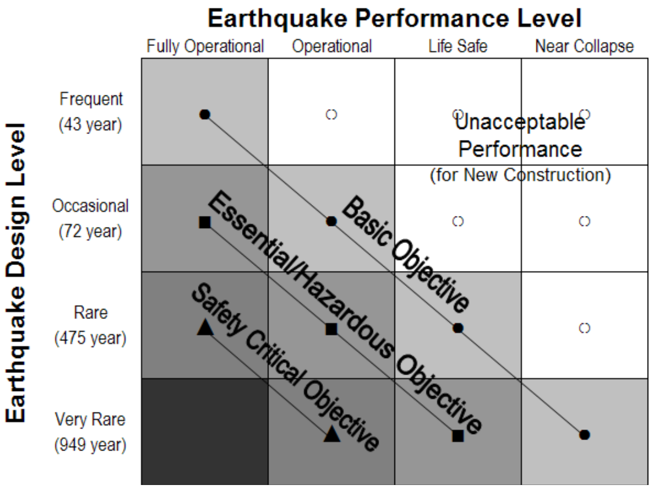

Fig. 2.1 Recommended seismic performance objectives for buildings. Mean recurrence intervals of 43 yrs, 72 yrs, 475 yrs, and 949 yrs correspond to Poisson arrival events with 50% probability of exceedance in 30 yrs, 50% in 50 yrs, 10% in 50 yrs, and 10% in 100 yrs, respectively (after SEAOC 1995). (figure from Vision 2000)

The FEMA 356 report was intended to encourage wider use of FEMA 273 by converting it into mandatory language, and to provide a basis for a future, nationally recognized, American National Standards Institute (ANSI) approved standard that incorporates its approaches and technologies into mainstream design and construction practice. It defines various target building performance levels and earthquake hazard levels similar to those presented in Vision 2000. A target building performance for a specific earthquake hazard is selected by the designer and the client together, and the building is designed according to the specifications of this standard. Performance levels are defined for structural and nonstructural systems, whose approximate damage is described in some detail.

Table 2.1 Target building performance levels, reproduced from Table C1-2 in FEMA 356 (ASCE 2000)

Damage Control and Building Performance Levels				
	Target Building Performance Levels			
	Collapse Prevention Level (5-E)	Life-safety Level (3-C)	Immediate Occupancy Level (1-B)	Operational Level (1-A)
Overall Damage	Severe	Moderate	Light	Very Light
General	Little residual stiffness and strength, but load bearing columns and walls function. Large permanent drifts. Some exits blocked. Infills and unbraced parapets failed or at incipient failure. Building is near collapse.	Some residual strength and stiffness left in all stories. Gravity load-bearing elements function. No out-of-plane failure of walls or tipping parapets. Some permanent drift. Damage to partitions. Building may be beyond economical repair.	No permanent drift. Structure substantially retains original strength and stiffness. Minor cracking of facades, partitions, and ceilings as well as structural elements. Elevators can be restarted. Fire protection operable.	No permanent drift. Structure substantially retains original strength and stiffness. Minor cracking of facades, partitions, and ceilings as well as structural elements. All systems important to normal operation are functional.
Nonstructural components	Extensive damage	Falling hazards mitigated but many architectural, mechanical, and electrical systems are damaged.	Equipment and contents are generally secure, but may not operate due to mechanical failure or lack of utilities.	Negligible damage occurs. Power and other utilities are available, possibly from standby sources.
Comparison with performance intended for buildings designed under the NEHRP provisions, for the Design Earthquake	Significantly more damage and greater risk.	Somewhat more damage and slightly higher risk.	Less damage and lower risk.	Much less damage and lower risk.

The performance levels and descriptions of corresponding physical damage are shown in Table 2.1. There are many tables in the standard for specific structural performance levels (e.g., for concrete frames, braced steel frames, metal deck diaphragms, etc.) and nonstructural performance levels (e.g., for glazing, piping, cladding, etc.). These tables also include some engineering limit states (e.g., drift values) believed to correspond to the various performance levels for a particular component. These limit states are not intended to be used as acceptance criteria or in the post-earthquake evaluation of damage, but are instead indicative of the range that exists for the limit states that typical structures undergo.

Rather recently, PEER is producing an analysis and design methodology that addresses seismic performance in terms of damage-repair cost and loss-of-use duration, as well as operability, life-safety, and collapse potential. The objective of the methodology is to estimate the frequency with which a particular performance metric will exceed various levels for a given design at a given location. Fig. 2.2 illustrates the PEER methodology. As it shows, PEER's PBEE approach involves four stages: hazard analysis, structural analysis, damage analysis, and loss analysis (Porter 2003).

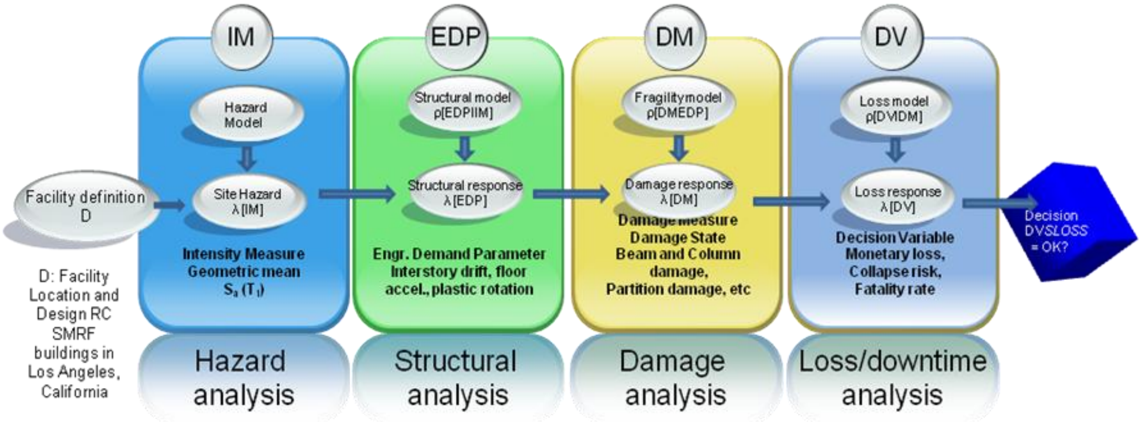

Fig. 2.2 PEER PBEE methodology framework. (adapted from Porter 2003)

The four stages are defined as follows:

(1) Hazard analysis: In the hazard analysis, one evaluates the seismic hazard ($\lambda[IM]$) at the building considering its location, structural, architectural, and other features (jointly denoted by design, D). The seismic hazard describes the annual frequency with which seismic excitation is estimated to exceed various levels. Seismic excitation is parameterized by an intensity measure IM such as $Sa(T_1)$, the damped elastic spectral acceleration at the fundamental period of the structure. The hazard analysis includes the selection of a number of ground-motion time histories whose IM values match different hazard levels of interest, such as 10%, 5%, and 2% exceedance probability in 50 years.

(2) Structural analysis: In the structural analysis, one creates a structural model of the building in order to estimate the uncertain structural response, measured in terms of a vector of engineering demand parameters (*EDP*), conditioned on seismic excitation ($p[EDP|IM]$). *EDP*s can include internal member forces and local or global deformations, including ground failure. The structural analysis might take the form of a series of nonlinear time-history structural analysis. The structural model need not be deterministic: some PEER analysis have included uncertainty in the mass, damping, and force-deformation characteristics of the model.

(3) Damage analysis: *EDP* is then input to a set of fragility functions that model the probability of various levels of physical damage (expressed by damage measures, or *DM*), conditioned on structural response, ($p[DM|EDP]$). Physical damage is described at a detailed level, defined relative to particular repair efforts required to restore the component to its undamaged state. Fragility functions currently in use give the probability of various levels of damage to individual beams, columns, nonstructural partitions, or pieces of laboratory equipment, as functions of various internal member forces, story drift, etc. They are compiled

from laboratory or field experience. For example, PEER has compiled a library of destructive tests of reinforced concrete columns for this purpose (Eberhard *et al.* 2001).

(4) Loss analysis. The last stage in the analysis is the probabilistic estimation of performance (parameterized by various decision variables, *DV*), conditioned on damage (*p[DV|DM]*). Decision variables measure the seismic performance of the building in terms of greatest interest to facility owners, whether in dollars, deaths, downtime, or other metrics. PEER's loss models for repair cost are upon well-established principles of construction cost estimation.

2.2 Structural Control Under PBEE Framework

The PBEE framework is simply summarized and illustrated in Fig. 2.3 (shaded blocks). Earthquake excitation is defined in terms of an intensity measure, *IM*. A structural model is used to predict the response, *EDP*, from the intensity measure. A damage model is then used to predict the physical damage, *DM*, associated with the response. Finally, a loss model allows prediction of loss, *DV*, from the physical damage.

Structural control (SC) technologies, including passive, active and semi-active control strategies, can get essentially involved in the PBEE process, by varying the characteristics of the structural model (structural stiffness and damping) and consequently changing the *EDP*, *DM*, and finally the *DV*. Thus, within the PBEE framework, both the intermediate outputs (*EDP* and *DM*) and the final gain (*DV*) can be adjusted to a specific level for the decision maker through implementation of structural control devices. The introduction of structural control methods has provided structural designers a powerful tool for performance-based design.

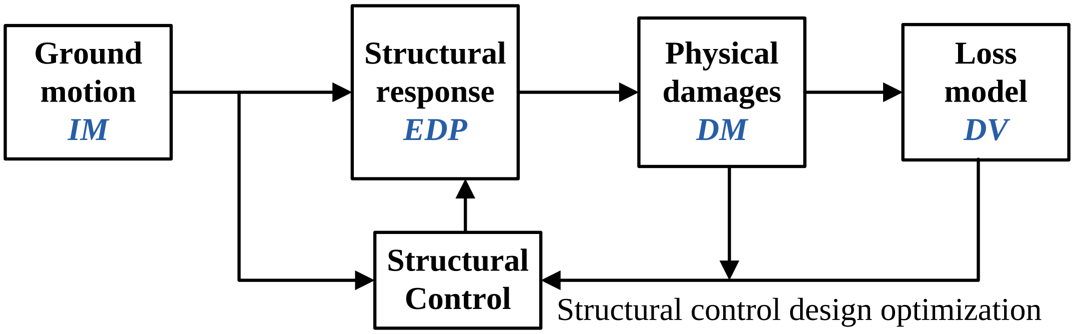

Fig. 2.3 Illustration of PBEE framework with structural control strategy

2.3 Fragility Function Methodology

Fragility functions are useful tools for assessing the seismic vulnerability of buildings in terms of prioritizing retrofit, pre-earthquake planning and post-earthquake loss estimation. Fragility functions define the conditional probability of attaining or exceeding a specified damage state for a given set of input intensity variables. Fig. 2.4 illustrates a typical fragility curve, in which damage probability, for several damage states are plotted as a function of earthquake intensity measures. In probabilistic term, a fragility curve starts at zero (at the lowest demand level that can cause failure) and increases to one (at the demand level causing certain failure).

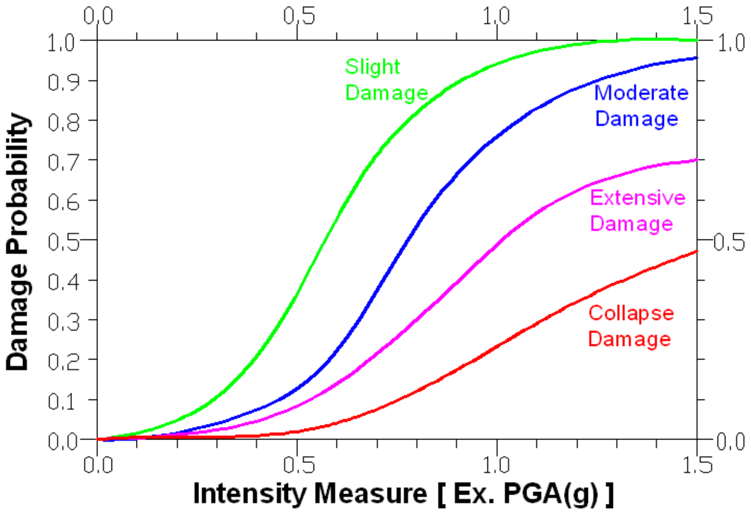

Fig. 2.4 A typical fragility curve

Depending on different data resources, fragility functions can be generated as empirical ones with observed damage data from past earthquakes (Basöz *et al.* 1999; Yamazaki and Hamada 2000) and analytical ones with numerical analysis results (Mander and Basöz 1999; Shinozuka *et al.* 2000; Mackie and Stojadinovic 2004; Choi and Nielson 2004). Due to the insufficiency of recorded damage data and the subjectivity in defining damage states, the application of empirical fragility functions is limited. In contrast, analytical fragility functions are increasingly used both in academic research and practical application. Analytical fragility functions are developed using seismic response data of buildings obtained from nonlinear time history analysis, elastic spectra analysis or nonlinear static analysis. Reasonably good agreement can be obtained between the analytical and empirical fragility functions (Shinozuka *et al.* 2000).

Porter (2007) presented six methods for creating fragility functions including three new ones: one for dealing with cases where no failure has been observed, another for situations where one must rely on expert opinion, and a third for updating an existing fragility function with new damage observations. The procedures are under consideration as a standard for ATC-58, a technology-transfer project by the Applied Technology Council to bring PEER’s performance-based earthquake engineering methodology to practice.

In a previous paper (Zhang and Huo 2009); a methodology was presented to estimate the seismic fragility for evaluating the effectiveness and optimum design of isolation devices for highway bridges. The paper employs the Probabilistic Seismic Demand Model (PSDM) to derive analytical fragility functions using nonlinear time history responses of bridges. The PSDM can be developed using a 'scaling' (like 'stripe') approach or 'cloud' approach (Baker 2006) to relate the engineering demand parameters (*EDP*s) to the ground motion intensity measures (*IM*s). With the 'scaling' approach, all motions are scaled to selective intensity levels corresponding to a prescribed seismic hazard level and incremental dynamic analysis (IDA) is performed at different hazard levels. On the other hand, the 'cloud' approach uses un-scaled earthquake ground motions. In this study, the 'cloud' approach, which is termed as PSDA (Probabilistic Seismic Demand Analysis) is mainly used. The PSDA method utilizes regression analysis to obtain the mean and standard deviation for each limit state by assuming the logarithmic correlation between median *EDP* and an appropriately selected *IM*:

$$EDP = a(IM)^b \tag{2.1}$$

where the parameters *a* and *b* are regression coefficients obtained from the response data of nonlinear time history analyses. By taking the logarithmic of above equation, one arrives at:

$$In(EDP) = Ina + bIn(IM) \tag{2.2}$$

The remaining variability in $In(EDP)$ at a given *IM* is assumed to have a constant variance for all *IM* range, and the standard deviation $\sigma_{EDP|IM}$ can be estimated as:

$$\sigma_{EDP|IM} = \sqrt{\frac{\sum_{i=1}^{n}[In(EDP_i) - (Ina + bIn(IM_i))]^2}{n-2}} \tag{2.3}$$

Subsequently, a capacity model uses the *EDP*s or functions of *EDP*s to derive the damage index (*DI*) that can be compared with the limit states (*LS*) correspondent to various damage states (*DS*) dictated. For simplicity, the *DI* is chosen the same as the *EDP* in this study. By further assuming a lognormal distribution of *EDP* at a given *IM*, the fragility functions (i.e. the conditional probability of reaching a certain damage state for a given *IM*) can be written as:

$$P[DI \geq LS \mid IM] = 1 - \phi\left(\frac{In(LS) - In(aIM^{b})}{\sigma_{EDP|IM}}\right) \tag{2.4}$$

where $\sigma_{EDP|IM}$ is the standard deviation of the logarithmic distribution computed from Eq. (2.3) and $\phi(\bullet)$ is the standard normal distribution function. Alternatively, the fragility function can be deployed as:

$$P[DI \geq LS \mid IM] = 1 - \int_{0}^{LS} \frac{1}{\sqrt{2\pi}\sigma_{EDP|IM}} \, e^{\frac{[In(EDP)-In(aIM^{b})]^{2}}{2\left(\sigma_{EDP|IM}\right)^{2}}} \, d(In(EDP)) \tag{2.5}$$

In contrast to the PSDA method, the IDA method requires more computational effort because of the scaling of earthquake motions to different *IM* levels, e.g. through increments. However, no a priori assumption needs to be made in terms of probabilistic distribution of seismic demand in order to derive the fragility curves. Nonlinear time history analyses are conducted at every *IM* level. The occurrence ratio of a specified damage state is computed and directly used as the damage probability at the given *IM* level, i.e. the damage probability is calculated as the ratio of the number of damage cases n_i for the damage state *i* over the number of total simulation cases N:

$$P[DI \geq LS \mid IM] = \frac{n_i}{N} \quad (i = 1 \text{ to } 4) \tag{2.6}$$

In most cases, IDA fragility curves can be fitted with either a normal cumulative distribution function:

$$P[DI \geq LS \mid IM] = \int_{-\infty}^{IM} \frac{1}{\sqrt{2\pi}\xi_{IM}} \, e^{-\frac{[IM-\mu_{IM}]^{2}}{2(\sigma_{IM})^{2}}} \, d(IM) \tag{2.7}$$

or a log-normal cumulative distribution function:

$$P[DI \geq LS \mid IM] = \int_0^{IM} \frac{1}{IM\sqrt{2\pi}\xi_{IM}} e^{-\frac{[In(IM)-\lambda_{IM}]^2}{2(\xi_{IM})^2}} d(IM) \qquad (2.8)$$

where σ_{IM} and μ_{IM} are the standard deviation and mean value of *IM* to reach the specified damage state based on the normal distribution while ξ_{IM} and λ_{IM} are standard deviation and mean value of *IM* to reach the specified damage state based on the lognormal distribution or a log-normal cumulative distribution function.

2.4 Earthquake Selection and Intensity Measure

2.4.1 Selected Ground Motions

The aforementioned PSDA method relies on a large number of nonlinear time history analyses to derive the fragility functions. Therefore, a significant number of earthquake records need to be selected so that a conceptually and statistically better prediction of building response can be obtained. In some of previous studies, researchers may either artificially generate ground motions or collect them from historical events that represent typical and sever earthquake events (Ryan and Chopra 2004). In this study, three ensembles were collected with more than one-hundred motions that represent pulse-type motions and non-pulse-like (far-field) motions. The first two ensembles are the acceleration and velocity pulse motions (Table 2.2 and 2.3) identified by Tang and Zhang (2011), representative of ground shaking relatively close to fault rupture during a large magnitude earthquake. These pulse-like motions dominate the maximum structural responses over a wide period range and they represent the large and sever earthquake motions. In addition to these large ground motions, another 50 earthquake records from several ensembles are selected as non-pulse-like (far-field) ground motions. These ground motion ensembles represent events with various probability of occurrence at different locations and occurring on firm soil conditions.

Table 2.2 Acceleration Pulse-type Motions

Number	Earthquake	#	Year	Magnitude M_w	Fault mechanism	Station Name	Pulse Direction	Distance to fault (km)	PGA (g)
1	COYOTELK/CYC	2	1979	5.7	Strike-slip	Coyote Lake Dam (SW Abut)	246	6.13	0.2795
2	LIVERMOR/B-LFA	6	1980	5.4	Strike-slip	Livermore—Fagundas Ranch	232	14.88	0.2586
3	COALINGA/A-ATC	8	1983	5.1	Reverse	Anticline Ridge Free-Field	45	12.47	0.8608
4	COALINGA/A-ATP	8	1983	5.1	Reverse	Anticline Ridge Pad	45	12.47	0.5578
5	COALINGA/E-CHP	10	1983	4.9	Reverse	Coalinga-14th & Elm (Old CHP)	252	12.18	0.2047
6	COALINGA/F-CHP	11	1983	5.2	Reverse	Coalinga-14th & Elm (Old CHP)	258	12.74	0.7349
7	MORGAN/G06	12	1984	6.2	Strike-slip	Gilroy Array #6	58	9.86	0.3365
8	PALMSPR/HCP	13	1986	6.1	Reverse–Oblique	Hurkey Creek Park	197	29.83	0.2425
9	WHITTIER/A-NOR	15	1987	6	Reverse–Oblique	Norwalk—Imp Hwy,SGrnd	190	20.42	0.2531
10	WHITTIER/B-ALH	16	1987	5.3	Reverse–Oblique	Alhambra—Fremont School	77	14.02	0.2485
11	WHITTIER/B-OBR	16	1987	5.3	Reverse–Oblique	LA—Obregon Park	77	15.19	0.3892
12	CAPEMEND/PET	21	1992	7	Reverse	Petrolia	260	8.18	0.7096
13	NORTHR/LOS	23	1994	6.7	Reverse	Canyon Country—W LostCany	32	12.44	0.5389
14	NORTHR/PAC	23	1994	6.7	Reverse	Pacoima Dam (downstr)	32	7.01	0.507
15	NORTHR/SCS	23	1994	6.7	Reverse	Sylmar—Converter Sta	32	5.35	0.908
16	NORTHR/SYL	23	1994	6.7	Reverse	Sylmar—Olive ViewMedFF	32	5.3	0.8439
17	KOBE/KJM	25	1995	6.9	Strike-slip	KJMA	140	0.96	0.8547
18	SMADRE/altde	19	1991	5.6	Reverse	Altadena—Eaton Canyon	152	13.17	0.4556
19	SMADRE/opark	19	1991	5.6	Reverse	LA—Obregon Park	152	27.4	0.2503
20	SMADRE/4734A	19	1991	5.6	Reverse	Pasadena—USGS/NSMP Office	152	17.13	0.3278
21	NORTH392/STC	24	1994	5.3	Reverse	Northridge—17645 SaticoySt	217	13.87	0.3278
22	NORTH392/GLB	24	1994	5.3	Reverse	Sun Valley—Sunland	217	16.49	0.3639
23	CHICHI03/CHY080	28	1999	6.2	Reverse	CHY080	270	22.37	0.4751
24	CHICHI06/TCU080	29	1999	6.3	Reverse	TCU080	275	10.2	0.646
25	LOMAP/LEX	18	1989	6.9	Reverse–Oblique	Los Gatos—Lexington Dam	38	5.02	0.5221

Table 2.3 Velocity Pulse-type Motions

Number	Earthquake	#	Year	Magnitude M_w	Fault mechanism	Station Name	Pulse Direction	Distance to fault (km)	PGA (g)
26	SFERN/PUL	1	1971	6.6	Reverse	Pacoima Dam (upper left abut)	195	1.81	1.5161
27	IMPVALL/H-AEP	3	1979	6.5	Strike-slip	Aeropuerto Mexicali	233	0.34	0.4071
28	IMPVALL/H-AGR	3	1979	6.5	Strike-slip	Agrarias	233	0.65	0.3782
29	IMPVALL/H-EMO	3	1979	6.5	Strike-slip	EC Meloland Overpass FF	233	0.07	0.3781
30	IMPVALL/H-E03	3	1979	6.5	Strike-slip	El Centro Array #3	233	12.85	0.2921
31	IMPVALL/H-E04	3	1979	6.5	Strike-slip	El Centro Array #4	233	7.05	0.524
32	IMPVALL/H-E05	3	1979	6.5	Strike-slip	El Centro Array #5	233	3.95	0.5457
33	IMPVALL/H-E06	3	1979	6.5	Strike-slip	El Centro Array #6	233	1.35	0.4506
34	IMPVALL/H-E07	3	1979	6.5	Strike-slip	El Centro Array #7	233	0.56	0.521
35	IMPVALL/H-HVP	3	1979	6.5	Strike-slip	Holtville Post Office	233	7.65	0.259
36	MAMMOTH/L-LUL	5	1980	5.9	Strike-slip	Long Valley Dam (Upr L Abut)	291	19.83	0.993
37	COALINGA/H-Z14	7	1983	6.4	Reverse	Parkfield—Fault Zone14	47	29.98	0.2941
38	COALINGA/D-TSM	9	1983	5.8	Reverse	Transmitter Hill	262	9.52	1.1231
39	COALINGA/F-CHP	11	1983	5.2	Reverse	Coalinga-14th & Elm (Old CHP)	258	12.74	0.7349
40	MORGAN/G06	12	1984	6.2	Strike-slip	Gilroy Array #6	58	9.86	0.3365
41	PALMSPR/NPS	13	1986	6.1	Reverse–Oblique	North Palm Springs	197	4.04	0.7827
42	SANSALV/GIC	14	1986	5.8	Strike-slip	Geotech Investig Center	302	6.3	0.8965
43	SANSALV/NGI	14	1986	5.8	Strike-slip	National Geografical Inst	302	6.99	0.6551
44	WHITTIER/A-DWN	15	1987	6	Reverse–Oblique	Downey—Co MaintBldg	190	20.82	0.2487
45	WHITTIER/A-OR2	15	1987	6	Reverse–Oblique	LB—Orange Ave	190	24.54	0.2557
46	SUPERST/B-PTS	17	1987	6.5	Strike-slip	Parachute Test Site	37	0.95	0.5103
47	LOMAP/G02	18	1989	6.9	Reverse–Oblique	Gilroy Array #2	38	11.07	0.4129
48	LOMAP/LEX	18	1989	6.9	Reverse–Oblique	Los Gatos—Lexington Dam	38	5.02	0.5221
49	ERZIKAN/ERZ	20	1992	6.7	Strike-slip	Erzincan	32	4.38	0.5285
50	CAPEMEND/PET	21	1992	7	Reverse	Petrolia	260	8.18	0.7096
51	LANDERS/YER_225	22	1992	7.3	Strike-slip	Yermo Fire Station	225	23.62	0.2218
52	NORTHR/LOS_032	23	1994	6.7	Reverse	Canyon Country-W Lost Cany	32	12.44	0.466
53	NORTHR/KAT_032	23	1994	6.7	Reverse	Simi Valley-Katherine Rd	32	13.42	1.0661
54	NORTHR/SCS_032	23	1994	6.7	Reverse	Sylmar-Converter Sta	32	5.35	0.5943
55	NORTHR/SCE_032	23	1994	6.7	Reverse	Sylmer-converer Sta East	32	5.19	0.8387
56	KOBE/KJM_140	25	1995	6.9	Strike-slip	KJMA	140	0.96	0.8543
57	KOBE/TAZ_140	25	1995	6.9	Strike-slip	Takarazuka	140	0.27	0.6452
58	KOBE/TAK_140	25	1995	6.9	Strike-slip	Takatori	140	1.47	0.682
59	KOCAELI/GBZ_184	26	1999	7.5	Strike-slip	Gebze	184	10.92	0.2383
60	CHICHI/CHY006_292	27	1999	7.6	Reverse–Oblique	CHY006	292	9.77	0.3115
61	CHICHI/CHY035_292	27	1999	7.6	Reverse–Oblique	CHY035	292	12.65	0.2612
62	CHICHI/CHY101_289	27	1999	7.6	Reverse–Oblique	CHY101	289	9.96	0.4513
63	CHICHI/TCU029_306	27	1999	7.6	Reverse–Oblique	TCU029	306	28.05	0.2207
64	CHICHI/TCU036_277	27	1999	7.6	Reverse–Oblique	TCU036	277	19.84	0.1346
65	CHICHI/TCU040_277	27	1999	7.6	Reverse–Oblique	TCU040	277	22.08	0.1452
66	CHICHI/TCU065_272	27	1999	7.6	Reverse–Oblique	TCU065	272	0.59	0.8218
67	CHICHI/TCU075_271	27	1999	7.6	Reverse–Oblique	TCU075	271	0.91	0.3331
68	CHICHI/TCU103_277	27	1999	7.6	Reverse–Oblique	TCU103	277	6.1	0.1323
69	CHICHI/TCU128_306	27	1999	7.6	Reverse–Oblique	TCU128	306	13.15	0.1874
70	CHICHI/TCU136_278	27	1999	7.6	Reverse–Oblique	TCU136	278	8.29	0.1694
71	CHICHI/TCU141_275	27	1999	7.6	Reverse–Oblique	TCU141	275	24.21	0.1043
72	STELIAS/059v2_160	4	1979	7.5	Reverse	Icy Bay	160	26.46	0.158
73	YOUNTVL/2016a_061	30	2000	5	Strike-slip	Napa Fire Station # 3	61	14.15	0.6006
74	CHICHI03/CHY024_270	28	1999	6.2	Reverse	CHY024	270	19.65	0.1868
75	CHICHI03/CHY080_270	28	1999	6.2	Reverse	CHY080	270	22.37	0.0593

Fig. 2.5(a) to Fig. 2.5(f) shows the fault normal (major) direction and fault parallel (secondary) direction acceleration spectra with 5% damping for pulse-type, far-field and all the

combined motions. Fig. 2.5(g) is the PGA distribution for the combined motions. The three ensembles have average PGA of 0.4796 (g), 0.571 (g) and 0.1466 (g), respectively. In addition, the average PGA for all the motions is 0.3359 (g).

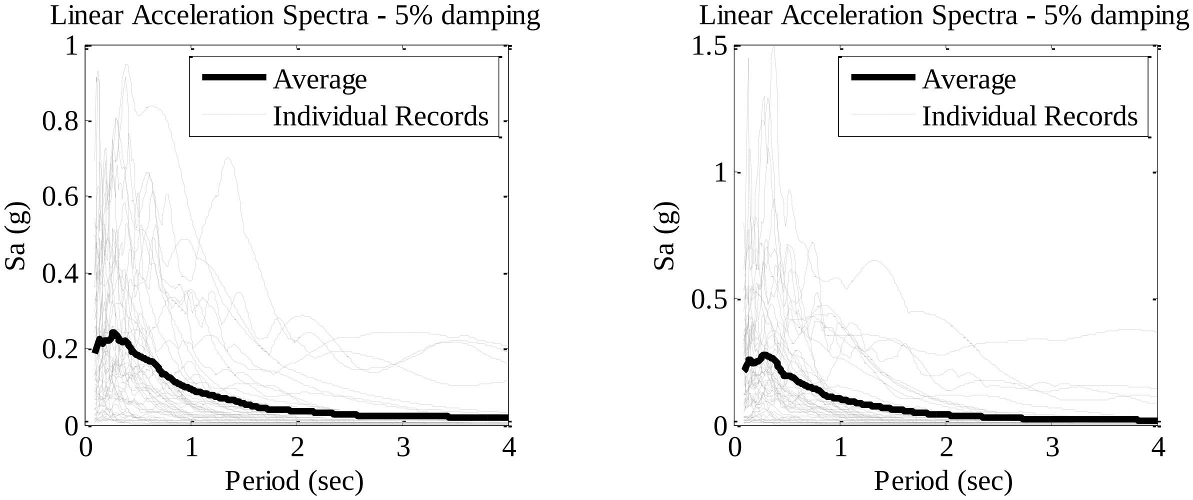

(a) Pulse-type motions FN direction

(b) Pulse-type motions FP direction

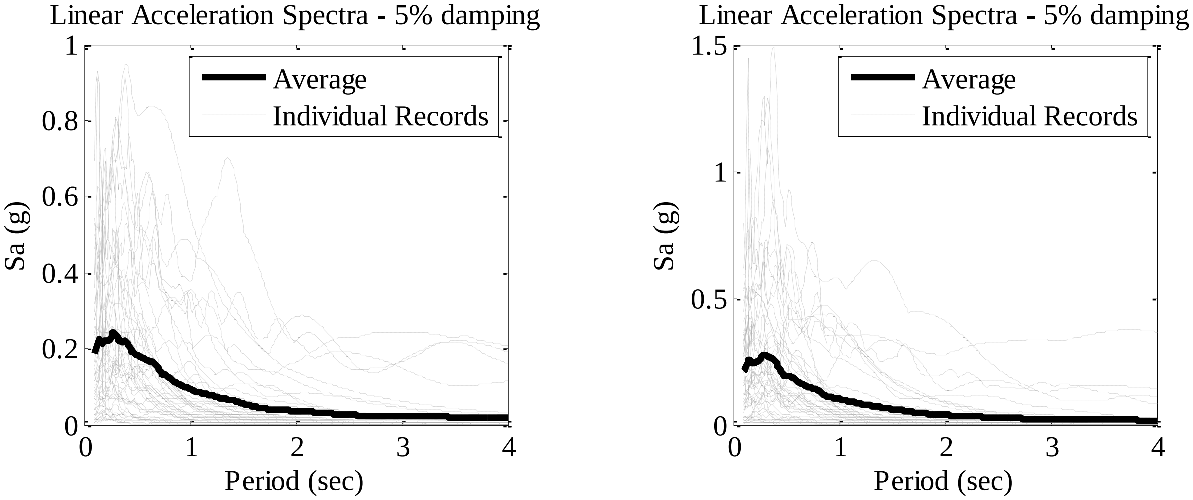

(c) Far-field motions FN direction

(d) Far-field motions FP direction

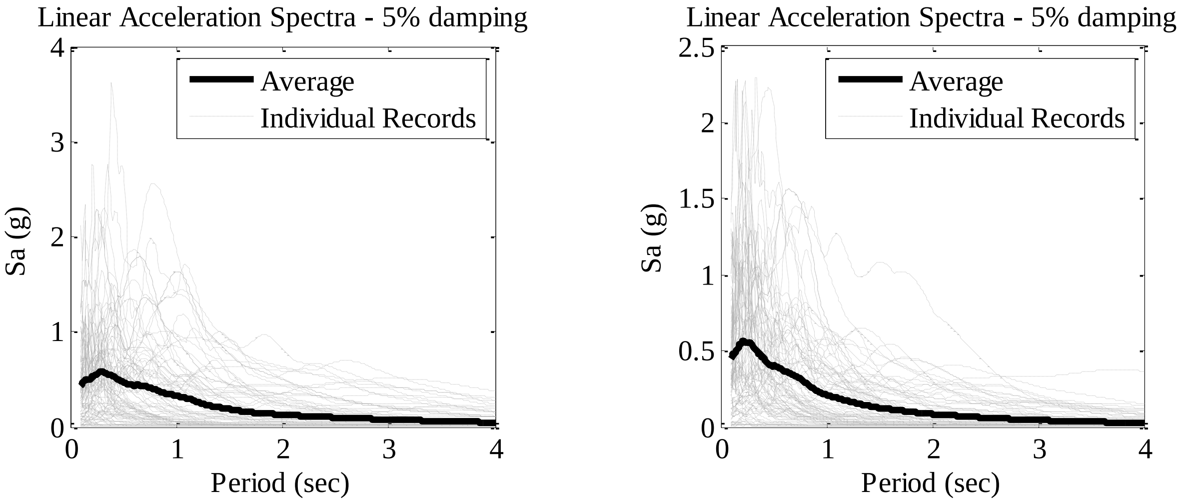

(e) All 100 motions FN direction **(f)** All 100 motions FP direction

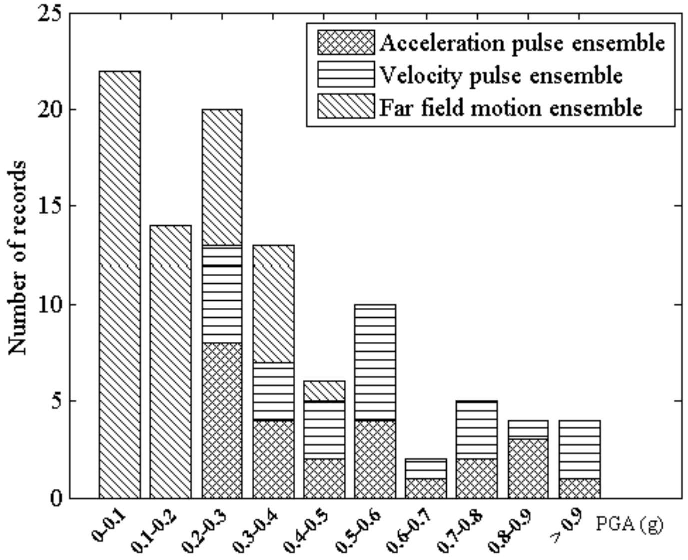

(g) PGA distribution

Fig. 2.5 Information of selected ground motion ensembles and the spectra

2.4.2 Definition of Intensity Measure

Intensity measure (*IM*) is defined as a variable to quantify the ground motion hazard at a site due to seismic events. Tothong and Luco (2007) assessed the performance of an *IM* with three indexes ‘efficiency’, ‘sufficiency’ and ‘scaling robustness’. An efficient *IM* is defined as the one that results in relatively small conditional deviation of *EDP* on *IM* and a sufficient *IM* makes the distribution of *EDP* given *IM* is independent of other intensity parameters. Scaling robustness ensures no change for the *IM* when the record is scaled. Another judging criterion for *IM* performance given by Padgett *et al.* (2008) evaluates *IM* with five indexes: efficiency, practicality, proficiency, sufficiency and hazard computability.

As pointed by Mackie and Stojadinović (2007), the intensity measures can be classified as two groups: structure-independent and structure-dependent *IM*s. In the study of Mackie and Stojadinović (2003, 2005), a comprehensive summary with about totally 90 kinds of *IM*s is done. The structure-independent *IM*s are also divided into two subcategories. The *IM*s of first sub-category are defined as the structure-independent *IM*s acting on earthquake time histories that have been filtered with SDOF, and the other subcategory *IM*s are filtered with other kinds of processes. Mackie and Stojadinović (2003, 2005) investigated the efficiencies of the *IM*. They summarized by comparing the dispersion of *EDP-IM* results of PSDM. Finally, Mackie and Stojadinović (2007) concluded that among structure-independent IMs PGA is not sufficient for structures with longer periods and PGV is probably the most reasonably efficient *IM*.

Based on the aforementioned five item criterion and also with dispersion analysis, Padgett *et al.* (2008) compared the performance of several *IM*, including PGA, PGV, PGD, Sa, IA, IV, CAV and CAD. Their conclusion states that PGA is the optimal one given its synthetic advantages. Therefore, in this study, PGA is used as the intensity measure of ground motions.

2.5 Damage Index and Limit States

In numerical fragility analysis, the structural responses under earthquakes are depicted and monitored by various *EDP*s. A capacity model is needed to measure the damage of structural component or system, described in terms of a damage index (i.e. *DI*) as a function of *EDP*s. The damage models are often formulated from the experimental data where observed damage and measured capacity of the specimens are correlated to the level of applied demand. The damage states (*DS*) are usually discrete and are marked by the associated limiting values (i.e. limit states *LS*) of the adopted *DI* to observe the onset of various damage stages. It is noted that uncertainties can also be introduced in the capacity model and contribute to the overall fragility.

2.5.1 Previous Studies and HAZUS Definition

A number of studies have developed the criteria for *DI* and corresponding *LS* based on damage status or loss of load-carrying capacity. Often used *DI* measures are curvature ductility, displacement ductility and residual displacement etc, and four damage states defined by HAZUS (FEMA 2003) are commonly adopted, namely slight, moderate, extensive and collapse damages.

For example, when buildings are base-isolated, the isolation devices will experience large displacements resulting in damage of isolation devices and neighboring structural members in addition to the possible damage in columns. Both the structural elements (i.e. beams, columns, and walls) and isolation system (i.e. bearings) can experience different damage states, leading to a comprehensive damage state which is difficult to be described by the damage state of only one component. Previous studies suggest that system fragility can be derived based on the functionality or repair cost after earthquakes (Mackie and Stojadinovic 2005) or be generated as a union of the component level fragility using a joint probabilistic seismic demand model (Nielson and Desroches 2007).

2.5.2 *Example: Damage Index and Limit States of MF Buildings*

This section provides example according to HAZUS definition about *DI* and *LS* for moment frame (MF) buildings. Steel moment frame (SMF) is one of the design schemes favored by structural engineers. Table 2.4 shows the definition of the four damage states from HAZUS about steel moment frame structures S1.

Table 2.4 Definition of damage states for Steel Moment Frame (S1) by HAZUS 2003

Slight Structural Damage:
Minor deformations in connections or hairline cracks in few welds.
Moderate Structural Damage:
Some steel members have yielded exhibiting observable permanent rotations at connections; few welded connections may exhibit major cracks through welds or few bolted connections may exhibit broken bolts or enlarged bolt holes.
Extensive Structural Damage:
Most steel members have exceeded their yield capacity, resulting in significant permanent lateral deformation of the structure. Some of the structural members or connections may have exceeded their ultimate capacity exhibited by major permanent member rotations at connections, buckled flanges and failed connections. Partial collapse of portions of structure is possible due to failed critical elements and/or connections.
Complete Structural Damage:
Significant portion of the structural elements have exceeded their ultimate capacities or some critical structural elements or connections have failed resulting in dangerous permanent lateral displacement, partial collapse or collapse of the building. Approximately 8% (low-rise), 5% (mid-rise) or 3% (high-rise) of the total area of S1 buildings with Complete damage is expected to be collapsed.

Building seismic resistance is highly dependent on the structural properties and configuration characteristics. For example, because the seismic code and building technology are changed with time, buildings with different vintages and design levels show distinctive seismic load carrying properties. The 1994 Northridge earthquake did a great impact to US building code. Buildings built before or after Northridge earthquake definitely behaviors differently. HAZUS takes this into consideration and proposed four different earthquake design levels. HAZUS (2003) describes methods for determining the probability of Slight, Moderate, Extensive and Complete damage to general building stock. General building stock represents typical buildings of a given model building type designed to either High-Code, Moderate-Code, or Low-Code seismic standards, or not seismically designed (referred to as Pre-Code buildings).

Capacity curves and fragility curves for High-Code, Moderate-Code, Low-Code and Pre-Code buildings are based on modern code (e.g., 1976 Uniform Building Code, 1985 NEHRP Provisions, or later editions of these model codes). Design criteria for various seismic design zones has also been specified. Also, HAZUS categorizes special moment frames by height. For example, the inter-story drift of a mid-rise steel moment frame at threshold of damage state is given by Table 2.5. One could easily see that for high code seismic design level, 0.4% of inter-story drift corresponds to slight damage of the structure while 5.33% of peak drift corresponds to the collapse. Compared with other levels of seismic designs, the high code design level has a larger tolerable *DS*.

Table 2.5 Damage states of different design level for S1 in terms of inter-story drift (from HAZUS 2003)

	Slight	Moderate	Extensive	Complete
High code seismic design level	*0.0040*	*0.0080*	*0.0200*	*0.0533*
Moderate code seismic design level	*0.0040*	*0.0069*	*0.0157*	*0.0400*
Low code seismic design level	*0.0040*	*0.0064*	*0.0135*	*0.0333*
Pre code seismic design level	*0.0032*	*0.0051*	*0.0108*	*0.0267*

Table 2.6 shows the definition of the four damage states from HAZUS about and RC moment frames. Similar to the S1 type building, four states of structural damage is specified in the table.

Table 2.6 Definition of damage states for Reinforced Concrete Moment Resisting Frames (C1) by HAZUS 2003

Slight Structural Damage:
Flexural or shear type hairline cracks in some beams and columns near joints or within joints.
Moderate Structural Damage:
Most beams and columns exhibit hairline cracks. In ductile frames some of the frame elements have reached yield capacity indicated by larger flexural cracks and some concrete spalling. Nonductile frames may exhibit larger shear cracks and spalling.
Extensive Structural Damage:
Some of the frame elements have reached their ultimate capacity indicated in ductile frames by large flexural cracks, spalled concrete and buckled main reinforcement; nonductile frame elements may have suffered shear failures or bond failures at reinforcement splices, or broken ties or buckled main reinforcement in columns which may result in partial collapse.
Complete Structural Damage:
Structure is collapsed or in imminent danger of collapse due to brittle failure of nonductile frame elements or loss of frame stability. Approximately 13%(low-rise), 10%(mid-rise) or 5%(high-rise) of the total area of C1 buildings with Complete damage is expected to be collapsed.

Correspondingly, the inter-story drift of a mid-rise concrete frame at threshold of damage state is given by Table 2.7:

Table 2.7 Damage states of different design level for C1 in terms of inter-story drift (from HAZUS 2003)

	Slight	Moderate	Extensive	Complete
High code seismic design level	*0.0027*	*0.0067*	*0.0200*	*0.5333*
Moderate code seismic design level	*0.0033*	*0.0058*	*0.0156*	*0.0400*
Low code seismic design level	*0.0033*	*0.0053*	*0.0133*	*0.0333*
Pre code seismic design level	*0.0021*	*0.0041*	*0.0105*	*0.0267*

2.6 Background in Earthquake Loss Estimation

A relatively large number of studies have been published dealing with earthquake loss estimation. Previous earthquake loss estimation studies can be categorized as regional loss estimation studies and building-specific loss estimation studies.

2.6.1 Regional Loss Estimation Studies

Regional loss estimation studies are aimed at the estimation of economic losses for a large number of buildings within a geographical region such as a city, a part of a city, county, state or at a country level. Freeman (1932) performed one of the earliest studies in loss estimation that provided rough estimates of probable average earthquake loss ratios for various localities and various types of buildings in order to develop a rational basis for estimating earthquake losses for the insurance industry. Later on, in 1970s, most regional earthquake loss estimation studies were confined within the insurance industry. At the same time, a series of regional loss estimation studies were conducted for the United States federal government to estimate economic losses and casualties, to evaluate functionality of essential facilities, and to study impacts on lifelines.

The study was pushed forward by Steinbrugge *et al.* (1969) and Whitman *et al.* (1973) in the form of damage probability matrices. Later on, the Applied Technology Council (ATC) launched a study that was published as ATC-13 (1985) and was entitled as "earthquake damage evaluation data for California". In addition to developing damage probability matrices for a vast majority of classes of construction, the study provided a well-documented and systematic way to use expert opinion for loss estimation. ATC-13 provided a way to estimate earthquake losses in different types of facilities in California, such as industrial, commercial, residential, utility and transportation facilities. Later on, the study presented in FEMA-177 (1989) was conducted to provide some guidelines for a consistent and standardized loss estimation methodology. The idea of developing a nationally applicable standardized methodology for estimating potential earthquake losses on regional basis was also one of the main objectives in preparation of the FEMA-249 (1994) report. Both these Federal Emergency Management Agency (FEMA) reports emphasized on a realistic evaluation of various sources of uncertainty in developing a loss estimation methodology. In particular, both FEMA studies emphasized that available loss estimation methodologies at that time, did not properly incorporate the uncertainty associated with the seismic hazard. Therefore, in 1997, the National Institute of Building Sciences (NIBS), Whitman *et al.*, and Kircher *et al.* introduced a standardized regional loss estimation methodology under the name HAZUS®. Instead of using qualitative measures of ground motion intensity, HAZUS® uses quantitative measures such as elastic spectral ordinates that intends to decrease the reliance on engineering judgment and expert opinion which were extensively used before in ATC-13. HAZUS® is implemented through PC-based Geographic Information System (GIS) software developed under agreements with NIBS.

In 2011, Chen and Wills performed a study to estimate the annual earthquake loss using HAZUS-MH, a geographic information system-based multi-hazard (MH) loss estimation tool developed by FEMA. They estimated the statewide average earthquake loss due to building damage to be approximately $2.8 billion per year, nearly 82% of this loss occurring in the top four Metropolitan Statistical Areas (MSAs) with the highest estimated annual losses. The distribution of estimated annual building losses on census tract level shows relatively higher values along the coast and in highly urbanized areas (Fig. 2.6). On the other hand, higher annualized percent earthquake losses (APELs) are estimated along the San Andreas Fault System, generally reflecting higher ground motion hazards (Fig. 2.7). More recent regional loss estimation studies were conducted on developing empirical fragility functions for different classes of building construction by investigating the correlation of building performance with recorded ground motions. (Sarabandi *et al*. 2004; King *et al.* 2004).

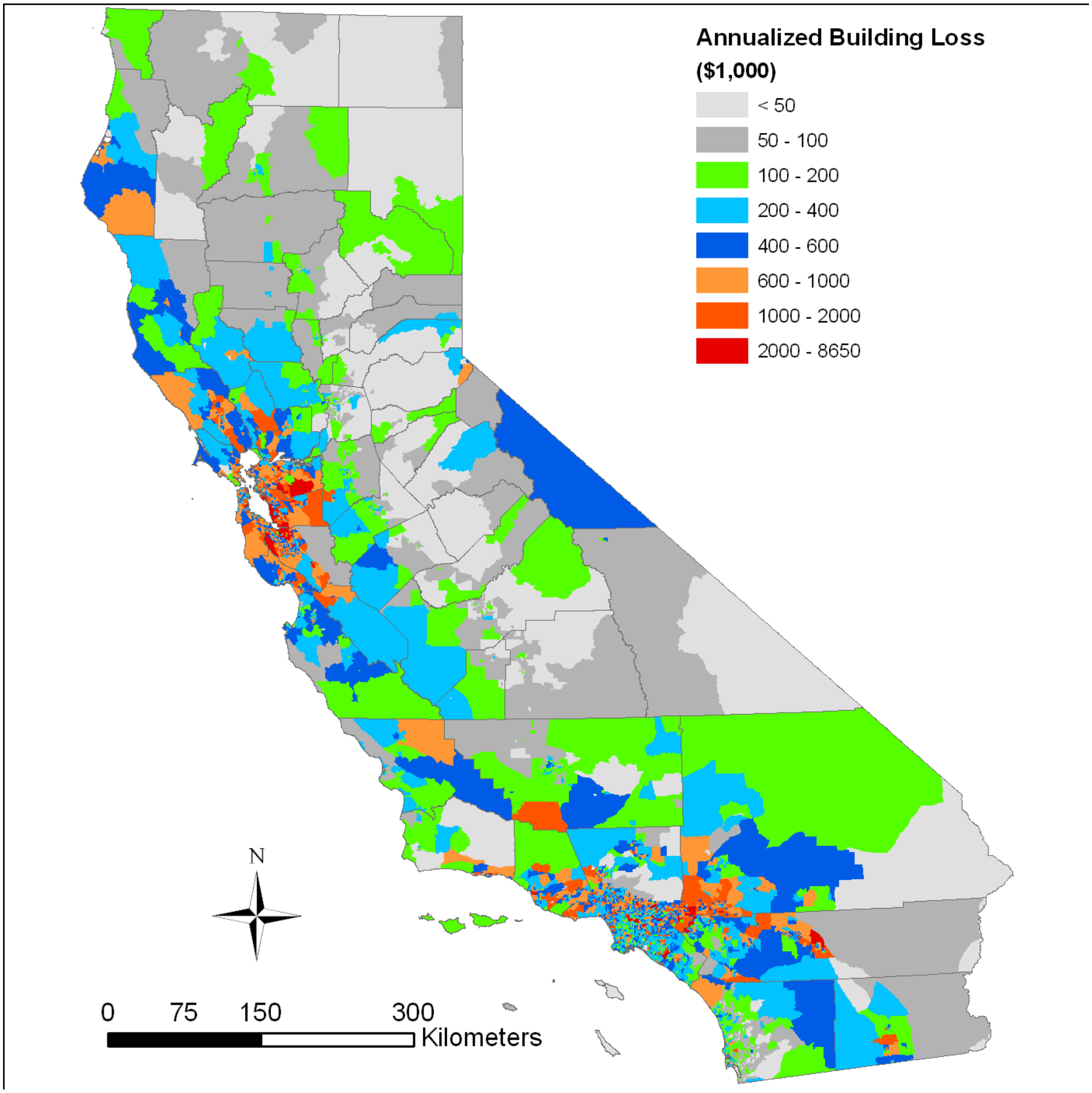

Fig. 2.6 Distribution of seismic risk in California by estimated annualized building loss on census tract level based on ground motions calculated using the 2008 USGS PSHA models and incorporating site-specific V_{S30} values

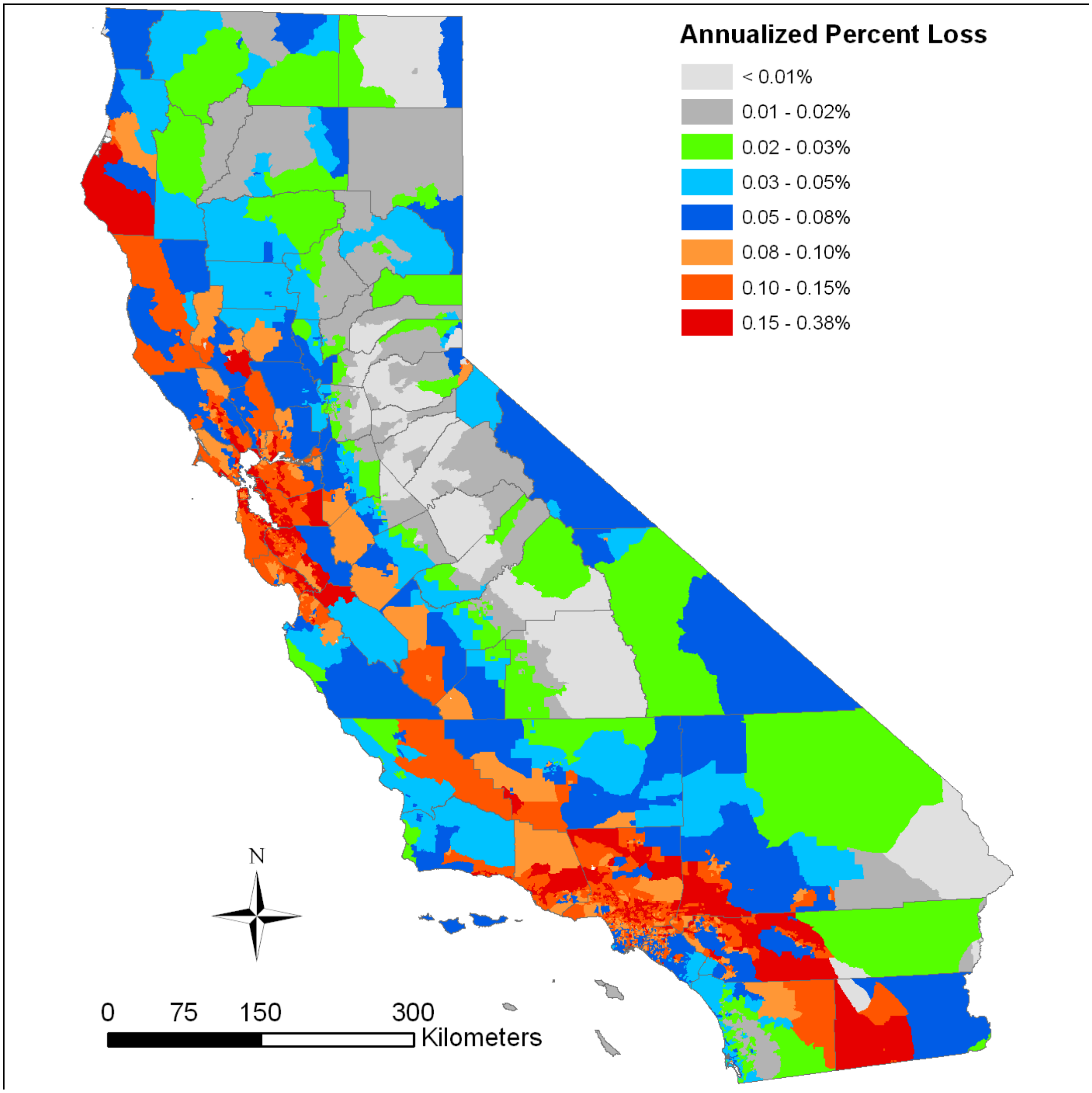

Fig. 2.7 Distribution of estimated annualized building percent loss by census tract based on ground motions calculated using the 2008 USGS PSHA models and incorporating site-specific V_{S30} values

Although regional loss estimation studies are proved to be useful in the insurance industry, they has certain disadvantages that limit their usability for the performance based earthquake engineering framework. For example, simple structural models are used based on SDOF systems neglecting higher modes and nonlinear effects. The basis of vulnerability functions used for damage assessment are typically not well documented and in many cases do not have a rational basis. Moreover, cost variability associated with repair or replacement of the structures is often not taken into account.

2.6.2 Building Specific Loss Estimation Studies

It is obvious that the regional loss estimation does not provide reliable estimation toward an individual structure. Less studies to estimate seismic loss for a specified building compared with the regional loss estimation studies.

In order to measure the performance of buildings, various types of performance indices have been invented. For example, for drift sensitive buildings such as parking lots, one could set the inter-story drift as the performance index; on the other hand, if a building contains valuable non-structural facilities, one need to develop a comprehensive performance index that incorporates the absolute roof acceleration or base shear.

Scholl (1979) proposed a deterministic component-based loss estimation methodology to identify, evaluate and correlate ground motion and structural parameters to improve predicting dollar losses in high-rise buildings. A structural model was created for the building and maximum floor responses were recorded. Damage to different structural and non-structural component categories in the building was defined as a percentage of the replacement cost of the component and was estimated using a library of motion-damage functions. The total damage in the building was computed as the sum of the damage estimated at different components. Gunturi (1993) evaluates the building damage in structural components, non-structural components, and contents of a certain story. They performed a nonlinear response history analysis on the structural model of the building and developed the damage indices for all three different damage components. The probabilistic nature of earthquake losses in a specific building has been taken into account in methodologies developed in late 1990s. Buildings will be excited with ensemble of simulated or selected ground motions rather than an individual motion. Monte Carlo simulation was used to develop motion-damage relationships for structural damage in low, mid and high reinforced concrete moment resisting frames in order to obtain fragility curves and damage probabilistic matrices. Porter and Kiremdjian (2001) proposed an assembly-based probabilistic loss estimation methodology that accounts for more sources of uncertainty than previous studies. The study incorporated the uncertainty in estimating the damage corresponding to each component and the uncertainty associated with estimating repair costs as a function of damage estimated in the component.

There are also limitations of existing building-specific loss estimation studies. For example, it is usually hard to incorporate collapse of the buildings. Consequently, the effects of collapse when estimating losses have typically not been taken into account. In addition, the effects of modeling uncertainty in estimating building losses have not been evaluated or propagated when estimating building losses. The existing studies also ignore the component level damage. Therefore, estimations of the dispersion of the building loss are either significantly over estimated or under estimated. Moreover, the component level fragility function for building does not provide realistic estimations of the probability of experiencing damage in the component as a function of increasing levels of deformation demands.

In chapter 5 of this study, in order to select the optimal design variables for base isolation systems for a building, a comprehensive performance index called total loss ratio has been proposed. The comprehensive total loss ratio is based on fragility curves for structural components, non-structural components, and the isolation system. The total loss ratio is trying to overcome the limitations of existing building-specific loss estimation, which has been proved an effective way of measuring the performance of a specific building against earthquakes.

2.7 Data Sampling for Performance-based Design

In order to achieve a performance-based design, it would be ideal if all the possible design features of the system were considered. For each design, a performance index (i.g. total loss ratio) is computed based on the presented performance model and compared with that of the other designs.

For example, Fig. 2.8 illustrates to the performance index as a function of two different design variables. The surface contains 169 nodes, corresponding to all the possible designs adopting different values of the two design variables over the user specified range. The performance of each design is generated from a fragility analysis undergoing multiple ground motions. For this case, variable one ranges from 1000 to approximately 10000; and variable two starts from zero and has an upper bond of 3000. The performance index for this case is reflected from the displacement fragility curves. All the 169 indices create the 3D surface of the plot. If the performance index corresponds to loss, the bottom points on the contour represents the smallest loss of a system leading to the repairing cost of a given hazard intensity, which also corresponds to a lowest fragility that incurs the best structural performance. The couple of these two variables at the bottom (optimizing) points on the surface therefore represent the optimal design.

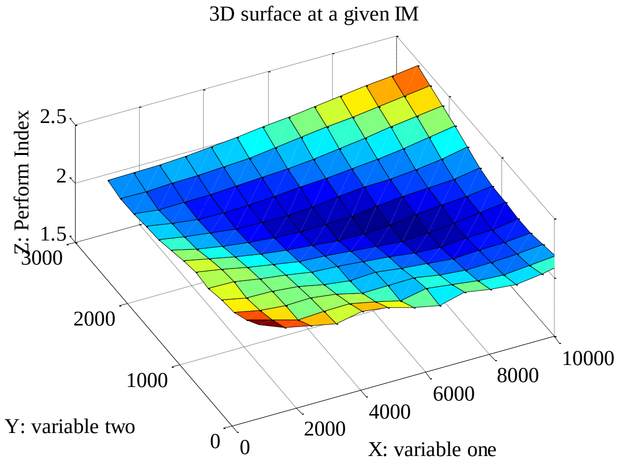

Fig. 2.8 Systematic sampling with generated performance surface

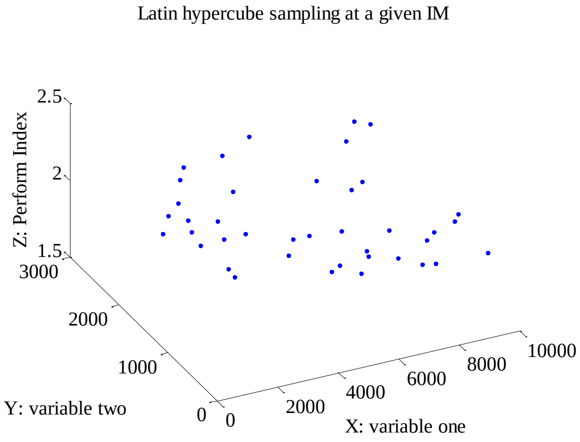

Fig. 2.9 Latin hypercube sampling with generated performance values

Systematically plotting the 3D surface of the performance index against the design variables makes it easier to indentify the optimal design range. Although this kind of performance evaluation has been applied to many previous works (Aslani and Miranda 2005, Zhang and Huo 2009), it still has some short comings. First, this method only evaluates two dimensions of design variables. In some optimal design cases, more design variables are coupled such that only plotting the performance index against two variables makes less sense. Second, the sampling of such method creates a mesh of the two design variables, which is a brutal approach that takes long time to run all the fragility analyses. This study applies another sampling method called Latin hypercube sampling (LHS) to choose the variables in a smarter way. LHS is a well-known statistical method for generating a sample of plausible collections of parameter values from a multidimensional distribution. A comparison of sampled variable in the case of optimizing two variables has been illustrated in Fig. 2.9. By comparing Fig. 2.8 and Fig 2.9, one could notice that the LHS method evaluates less designs compared with the approach generating 3D surface. Although the plot of LHS is not easy to read, it approaches the similar value of the optimal design. For example, in this case, the 3D surface corresponds to the optimal performance index of 1.8275 and the LHS approach corresponds to an optimal performance index of 1.8294. In addition, the LHS method would be able to choose design variables in more than two dimensions, which would also be useful for future purpose of optimal performance based design.

2.8 Error Analysis

In statistics and optimization, the error of a sample is the deviation of the sample from the (unobservable) true function value (Faraway 2004). From Eq. (2.2), lna and b can be estimated through linear regression between ln(*EDP*) and ln(*IM*). Suppose n pairs of (ln(*IM*), ln(*EDP*)) observations are available, i.e.,

$$\begin{gathered} In(EDP_1) = Ina + bIn(IM_1) + \varepsilon_1, \\ \cdots, \\ In(EDP_n) = Ina + bIn(IM_n) + \varepsilon_n . \end{gathered} \tag{2.9}$$

where ε_i is the error of the i^{th} measurement often assumed to be normally distributed with zero expectation and constant variance, i.e., $\varepsilon_i \sim N(0,\sigma^2)$. For notational simplicity, a matrix equation would replace the set of linear equations by:

$$y = \mathbf{X}\beta + \varepsilon . \tag{2.10}$$

where $y = (In(EDP_1),\cdots,In(EDP_n))^T$, $\beta = (Ina,b)^T$, $\varepsilon = (\varepsilon_1,\cdots,\varepsilon_n)^T$, and $\mathbf{X} = [\mathbf{1}, \boldsymbol{x}_1]$, with $\mathbf{1}=(1, \cdots,1)^{\mathrm{T}}$ and $\boldsymbol{x}_1=(\ln(\mathrm{IM}_1), \cdots, \ln(\mathrm{IM}_n))$. Following the least-square criterion, $\boldsymbol{\beta}$ is estimated from:

$$\boldsymbol{\beta}_{\mathrm{ls}} = (\mathbf{X}^{\mathrm{T}}\mathbf{X})^{-1}\mathbf{X}^{\mathrm{T}}\boldsymbol{y}. \tag{2.11}$$

and σ is defined by Eq. (2.3) and σ^2 is also written as:

$$\sigma 2 \approx \frac{RSS}{n-2} . \tag{2.12}$$

In Eq. (2.12), *RSS*, the residual sum of squares, is computed from the sum of squared difference between observations ($\boldsymbol{y}$) and model predictions ($\hat{\boldsymbol{y}}$), i.e.,

$$RSS = \| \boldsymbol{y} - \hat{\boldsymbol{y}} \|^2. \tag{2.13}$$

It can be shown that $\boldsymbol{\beta}_{\mathrm{ls}}$ follows normal distribution, i.e.,

$$\boldsymbol{\beta}_{\mathrm{ls}} \sim \mathrm{N}(\boldsymbol{\beta}\,,\, (\mathbf{X}^{\mathrm{T}}\mathbf{X})^{-1}\sigma^2). \tag{2.14}$$

Thus, with $\ln \hat{a}$, $\hat{b}$ and their variances σ_{11} and σ_{22} estimated from least-square regression, 95% confidence intervals could be constructed through:

$$\begin{gathered}[\, In\hat{a} - 1.96\sqrt{\sigma_{11}}\,, In\hat{a} + 1.96\sqrt{\sigma_{11}}\,], \\ [\, \hat{b} - 1.96\sqrt{\sigma_{22}}\,, \hat{b} + 1.96\sqrt{\sigma_{22}}\,]\end{gathered} \tag{2.15}$$

Consequently, a 95% confidence interval for *a* and *b* is:

$$\begin{gathered}[\, \hat{a} - e^{1.96\sqrt{\sigma_{11}}}\,, \hat{a} + \mathrm{e}^{1.96\sqrt{\sigma_{11}}}\,], \\ [\, \hat{b} - 1.96\sqrt{\sigma_{22}}\,, \hat{b} + 1.96\sqrt{\sigma_{22}}\,]\end{gathered} \tag{2.16}$$

Fig. 2.10 shows the fragility curve within 95% confidence interval for inter-story drift and absolute acceleration. Inter-story drift regressions usually correspond to larger errors than floor acceleration and this is also revealed in Fig. 2.10. In this study, 95% confidence interval corresponds to errors around 18% for inter-story drift fragility curves and 4% for the floor acceleration fragility curves. Considering sufficient amount of ground motion that provided enough sampling points, the general trend concluded from this study is fully reliable and serves as an enlightening PBD approach.

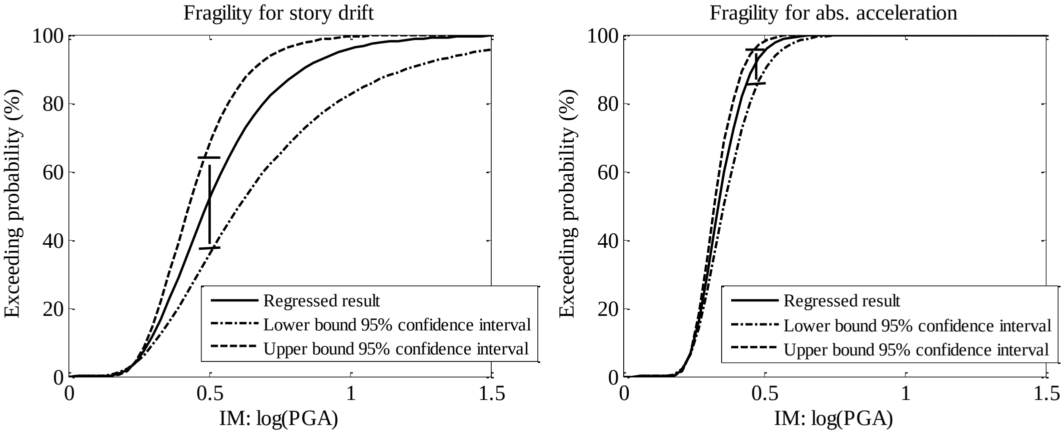

Fig. 2.10 Fragility curve within 95% confidence interval for inter-story drift and absolute acceleration

2.9 Other Considerations and Challenges

2.9.1 Uncertainties

Uncertainties exist at all stages of the PBEE framework. They are basically classified into aleatory uncertainty (i.e., randomness) and epistemic uncertainty. In the hazard analysis, it is uncertain what levels of seismic intensity (*IM*) the building will experience during its lifetime. The detailed ground motions that yield those *IM*s are also uncertain. In the structural analysis, the structural mass, damping, and force-deformation behavior are also with some random features. Furthermore, the other modeling assumptions during the structural analysis add uncertainties to the performance estimation as well. In the damage analysis, it is uncertain that to which structural response parameters the structural components are sensible. The characterization of damage states is also uncertain. There are uncertainties introduced when developing fragility functions, too. In the loss analysis, the economic modeling about cost of loss has several assumptions, hence results in uncertainties. All these sources of uncertainty should be taken into account in the PBEE framework.

The treatment of uncertainties can be performed using a deterministic sensitivity study, called tornado-diagram analysis, which measures the change in output performance resulting from varying one uncertain input from a lower-bound to upper-bound value, while holding all others at their best-estimated values.

2.9.2 Soil Structure Interaction

For bridge structure, when considering the structure alone, the actual behavior of the bridge under seismic load may significantly differ from that from the analysis since the response of a bridge during an earthquake depends not only on the bridge itself, but also on the characteristics of the ground motion and the subsoil conditions. Particularly for soft soils, the foundation input motion during the earthquake differs from the so-called free-field ground motion that may exist in the absence of the bridge. Soil structure interaction (SSI) is proved to be important while modeling a bridge structure.

For buildings, however, SSI effect is found to be insignificant from the aforementioned PEER report (Haselton *et al.*, 2007). The report studied in detail about the overview of Soil-Foundation-Structure Interaction (SFSI) mechanisms. Kinematic and inertial SSI Modeling is implemented to the benchmark building using the platform of OpenSees. From the report, it is observed that for the benchmark structure, the effects of SFSI on *EDP*s are minimal. The observation is based on the IDA plots comparing *EDP* response for fixed-base and flexible models. Based on the conclusion from the report, SSI effects are not intended to be included in this study either.

3. ESTIMATION OF STRUCTURAL DEMAND FOR GENERALIZED NONLINEAR CIVIL STRUCTURES

This chapter offers an innovative way to realistically predict the residual drift of bilinear SDOF systems directly from structural and ground motion characteristics. Along with total drift, residual drift provides key information on structural damages. This work proposes a simple yet reliable demand model to estimate the residual drift based on the nonlinear time history analyses of with different bilinear configurations that subject to a suite of near-fault ground motions. The model also incorporates a dimensionless nonlinearity index that takes into account of the pre-yielding strength, ground motion amplitude, and softening or hardening post-yield behavior. Guided by the rigorous dimensional analysis, both the maximum displacement responses and the residual drift of bilinear SDOF systems are presented in dimensionless form showing remarkable order. Strong correlation is revealed between the normalized nonlinear drift demands, the dimensionless structure-to-pulse frequency, and the dimensionless nonlinearity. Regressive equations for maximum displacement and residual drift demands are proposed and validated with the simulation results. The corresponding error of this approach is shown to be significantly lower than any of previous studies.

3.1 Introduction

Conventional seismic design approaches rely on the post-yielding behavior to dissipate the energy from earthquake motions. However, despite most of these structures are still standing after large motions, they end up unusable or irreparable. Larger inelastic behaviors may also introduce huge and permanent residual drifts throughout a structure. These residual drifts have become an important consideration in judging a structure's post-earthquake safety and the economic feasibility of repair. Modest amounts of residual drift may require costly and difficult adjustments to nonstructural components (e.g., re-plumbing of elevator rails, adjustments to building facades) and can lead to judgments that a building is unsafe during post-earthquake inspections. Larger residual drifts may require straightening of the structural frame or alternative measures to strengthen the frame for stability. At some stage, residual drifts may be large enough to seriously jeopardize structural stability to earthquake aftershocks and uneconomical to repair, in which case the cost of repair is on par with complete building replacement. (Mackie *et al.* 2011).

It is desirable to evaluate the likely magnitude of residual drifts for both retrofitting existing structures and designing new civil structures. In order to accurately measure a residual drift, two techniques are usually used: lab tests and nonlinear simulation. Existing shaking table tests reveal that the magnitude of residual drift is influenced by the material type and structure configuration. Kawashima *et al.* (1992) showed some individual tested specimen in Public Works Research Institute (Tsukuba, Japan). For some ground motions, the tested specimen yielded predominantly in one direction. In other words, on the other hand, the residual drifts for this case were close to the peak maximum drift. For some other cases, shaking table tests of reinforced concrete structures showed significant yielding occurring in both directions of loading and residual drifts were much lower than peak maximum drifts (MacRae *et al.* 1994). In addition, tests of some base-isolated structures indicated almost no residual drifts at all (Kawashima *et al.* 1991). These lab tests are usually time consuming and the test specimen are relatively expensive to construct compared with simulations that requires no lab resources or construction of specimen. However, accurate statistical simulation of displacements/drifts requires advanced nonlinear response-history analyses, with a large number of ground motions and with careful attention paid to cyclic hysteretic response of the models and numerical accuracy of the solutions.

Since the requirements for lab tests and direct simulations are complicated to implement, direct equations trying to estimate residual drifts would be desirable. In fact, researches in the past decades have presented equations both estimating maximum inelastic displacement and the residual drift.

Various efforts have been made to estimate the maximum inelastic displacement demand of structures under earthquakes. The first widely used approach is the displacement coefficient method assuming the inelastic displacement of a yielding structure can be obtained from multiplying displacement modification factor(s) and the spectral displacement of a linear elastic single degree-of-freedom (SDOF) system having the same initial stiffness and damping coefficient as the original nonlinear structure. In additional to the displacement coefficient method, the capacity spectrum method adopted by ATC-40 is also commonly used, which superposes capacity diagram plots on demand diagram plots to estimate the maximum displacement demand through an iterative procedure using a series of equivalent linear systems. However, replacing the inelastic spectra with highly damped elastic spectra is questionable, and the procedure may not converge to the correct response or it may significantly underestimate the deformation for a wide range of periods (Chopra and Goel 2000). Zhang *et al.* 2011 further elaborated the estimation of the maximum displacement for bridge columns by introducing a dimensionless nonlinearity index that better captures the bilinear mechanism.

Similar to estimating maximum displacements, the idea of estimating residual displacements/drift has been investigated for decades and various improved procedures on the same subject keep appearing. Riddell and Newmark (1979) and Mahin and Bertero (1981) first identified some of the key behavioral aspects associated with calculating residual drifts. MacRae and Kawashima (1997) investigated residual displacements in SDOF bilinear oscillators with a focus on bridge design. In 2003, Christopoulos *et al.* and Pampanin *et al.* conducted analyses of SDOF models with the primary emphasis on characterizing the effect of post-yield hardening stiffness and hysteretic unloading behavior on response. All the above studies reported residual drifts equal to a certain percentage of the total transient drift, depending on the hardening and hysteretic model.

Ruiz-Garcia and Miranda (2005, 2006a-c) had a slightly different approach that expressed their results in terms of a parameter, C_r, which related residual drift to elastic spectral displacement. They provided different ranges for this ratio within different periods of oscillators. After this study, in 2010, they developed a probabilistic estimation of residual drift demands of existing multi-story buildings. The proposed method selects an intensity measure of ground motions that are scaled to reach the same maximum inelastic displacement demand of an equivalent elasto-plastic SDOF system having the same initial lateral stiffness. Advantages of this approach are based on the fast computation of SDOF problems and great results from regression analysis were presented. Later on, ATC-58 completed the 75% draft in 2011, where a set of equations are proposed to relate residual story drift to peak transient story drift. The ATC summarized many factors that might influence the residual drift and the document finally proposed an estimation of residual drift that incorporates the yielding displacement of a building system.

Previous researches led to the conclusion that predicted residual drifts are sensitive to many features from two categories. First, the residual drift is related with the nonlinear system configurations. For example, for a bilinear system, parameters that would influence the magnitude of residual drift are the lateral strength of the structure (Q_d) relative to the earthquake demand, the inelastic post-yield stiffness (ε), and the cyclic unloading configuration of the system. The second category is related with earthquake input and response, which includes the magnitude of peak transient inelastic drifts, identification of pulses in the ground motions, and the duration of ground shaking. Hence, it seems hard but desirable to develop a method to evaluate residual drifts without doing much lab tests or running nonlinear analyses. Now that research have shown the significance for all these parameters on the residual drift, an ideal prediction would incorporate these features. However, because the difficulty to logically put many parameters together into an equation, not many studies has achieved this goal so far.

A mathematically sound approach based on physics method, the dimensional analysis, was developed recently to estimate the inelastic response by Makris and co-workers (Makris and Psychogios 2006, Makris and Black 2004a-c). The normalized displacement shows remarkable similarity, i.e. independent of the earthquake amplitude, for given normalized yielding displacement and strength. This work adopts the same concept and provides the estimation of maximum inelastic drift as well as the residual drift for a SDOF bilinear system with a focus on residual drift. The provided equation relates the drift demands with structure-to-pulse frequency ratio, normalized yielding displacement, and normalized strength. The method is efficient in reducing the scatter in the engineering demands and can directly estimate the inelastic displacement/drift and the residual drift without resorting to the linear response or the maximum inelastic displacement.

The objective for this study is to offer a new way to realistically predict the residual drift directly from structural and ground motion characteristics. This part of work is organized as follows. The first section is an introduction of the dimensional analysis framework for a bilinear system. The second section include numerical case studies of two famous ground motions shaking a sample nonlinear civil structure with observed permanent residual drifts. After that, this work proposed equations to estimate peak inelastic drift and residual drift under the dimensional analysis framework. Then, the authors proposed a validation of the proposed demand model by performing a detailed error analysis.

3.2 Dimensional Analysis and Simulation Framework for Nonlinear Structures

In order to evaluate the post earthquake residual drift, this study applies a set of dimensionless parameters to describe the normalized structural responses of a SDOF bilinear systems with remarkable order. The near-fault ground motions are selected because of their devastating effects on structures and kinematic characteristics of exhibiting distinguishable pulses that are compatible with the dimensional analysis.

3.2.1 Dimensional Analysis Framework for Nonlinear Structures

This study adopts a comprehensive study of nonlinear response under the framework of dimensional analysis. The proposed approach emerges from formal dimensional analysis first used by Makris and co-workers (Makris and Black 2004a-c) on elastic fixed-base structures and later extended to inelastic soil-structure systems (Zhang and Tang 2009), bridge columns (Zhang *et al.* 2011), and the nonlinear damping systems (Zhang and Xi 2012). The powerful framework provides an effective way of interpreting the otherwise largely scattered inelastic structural responses from time history analysis using recorded ground motions. By normalizing the inelastic drift demand with respect to the energetic length scale of ground motions, the similar response (i.e. independent of the intensity of ground motions) can be obtained. Here the dimensional analysis of a bilinear SDOF system is briefly discussed to provide the logical and mathematic background behind the proposed residual drift demand model for civil structures.

The dimensional analysis framework is based on the existence of a distinct time scale and length scale that characterize the most energetic component of the ground shaking. Such time and length scales emerge naturally from the distinguishable pulses and pulse-like near-fault ground motions (e.g. the acceleration amplitude a_p and duration T_p of the pulses), which dominate a wide class of strong earthquake record. For a bilinear SDOF system subject to a general pulse-type ground motion that can be characterized by its amplitude a_p and frequency ω_p (or equivalently $T_p = 2\pi / \omega_p$), its equation of motion can be expressed as:

$$\ddot{u} + 2\xi_s\omega_s\dot{u} + \omega_s u_y \tilde{f}_s(u,\dot{u}) = -a_p g(\omega_p t) \tag{3.1}$$

where u_y is the yield displacement, $\omega_s = \sqrt{k_s / m_s}$ is the circular frequency computed using the initial stiffness k_s and structural mass m_s, and the function $\tilde{f}_s(u,\dot{u})$ describes the nonlinear resisting force-displacement relationship that depends on the yield displacement u_y and post-yield stiffness hardening ratio ε. Given a specific waveform $g(t)$ of input ground acceleration, the peak displacement and the residual displacement of a bilinear SDOF system becomes a function of six variables (seven terms in the expression):

$$u_{\max} \equiv \max_t(|u(t)|) = f(\omega_s, \xi_s, u_y, \varepsilon, a_p, \omega_p) \tag{3.2}$$

$$u_R \equiv \operatorname*{end}_t(|u(t)|) = f(\omega_s, \xi_s, u_y, \varepsilon, a_p, \omega_p) \tag{3.3}$$

The seven terms appearing in Eq. (3.2) involves only two reference dimensions that are length [L] and time [T]. According to Buckingham's Π-theorem (Barenblatt 1996), the number of independent dimensionless Π-parameters is determined as: (7 variables) – (2 reference dimensions) = 5 Π-parameters. By normalizing the response to the characteristic length scale of ground motion, the normalized peak displacement ($\Pi_u \equiv u_{\max}\omega_p{}^2 / a_p$) and the normalized residual displacement ($\Pi_R \equiv u_{end}\omega_p{}^2 / a_p$) become functions of the normalized frequency ($\Pi_\omega \equiv \omega_s / \omega_p$), structural damping ratio ($\Pi_\xi \equiv \xi_s$), normalized structural yielding displacement ($\Pi_{uy} \equiv u_y\omega_p{}^2 / a_p$) or equivalently the normalized strength ($\Pi_Q \equiv Q_y / m_s a_p$), and post-yield stiffness ratio ($\Pi_\varepsilon \equiv \varepsilon$), which is formulated as follows.

$$\Pi_u \equiv \frac{u_{\max}\omega_p{}^2}{a_p} = \phi_u(\Pi_\omega, \Pi_\xi, \Pi_{uy}, \Pi_\varepsilon) = \widehat{\phi}_u(\Pi_\omega, \Pi_\xi, \Pi_Q, \Pi_\varepsilon) \tag{3.4}$$

$$\Pi_R \equiv \frac{u_{end}\omega_p{}^2}{a_p} = \phi_R(\Pi_\omega, \Pi_\xi, \Pi_{uy}, \Pi_\varepsilon) = \widehat{\phi}_R(\Pi_\omega, \Pi_\xi, \Pi_Q, \Pi_\varepsilon) \tag{3.5}$$

For a bilinear SDOF system, by normalizing the inelastic displacement demand with respect to the energetic length scale of ground motions, the similar response (i.e. independent of the intensity of ground motions) can be obtained. Under this powerful framework, one could conjecture that meaningful physical quantities involved in the nonlinear drift demand model for the SDOF bilinear system will include ground motion intensity measure (i.e. pulse acceleration, a_p or peak ground acceleration, a_g), ground motion frequency content (i.e. pulse frequency, ω_p), and structural characteristics (i.e. yield strength Q_y, yield displacement u_y, post-yield stiffness k_p, and natural frequency, ω_s), etc.

In order to estimate the residual drift accurately, appropriate dimensionless quantities need to be derived and then evaluated in terms of their influence on the dimensionless drift demand. In additional to the above-defined Π terms, Zhang *et al.* (2011) introduced another dimensionless measure Π_{NL} to capture the complex hysteretic nonlinear behavior of a bilinear oscillating system with the understanding of the direct impact of the energy dissipation mechanism. This term is expressed as follows:

$$\Pi_{NL} \equiv \frac{m_s a_g}{Q_y}\left(\frac{1}{1+k_p/k_e}\right)=\frac{m_s a_g}{Q_y}\left(\frac{1}{1+\varepsilon}\right) \tag{3.6}$$

where m_s is the deck mass; a_g is the input peak ground acceleration; Q_y and u_y are yield strength and yield displacement of the bilinear system; and (Q_y/u_y) and k_p are pre-yield and post-yield stiffness, respectively. The first term $m_s a_g/Q_y$ in Eq. (3.6) is similar to the inverse of the normalized strength Π_Q identified before in dimensional analysis except the pulse amplitude a_p is replaced by the peak ground acceleration a_g. This term indicates that the smaller the strength relative to the structural mass or the larger the input ground motion will result in larger nonlinearity in the structure. The second term $1/(1+\varepsilon)$ represents either reduced or increased energy dissipation capability due to softening (k_p<0) or hardening (k_p>0) behavior with reference to the elasto-plastic system.

3.2.2 Pulse Type Ground Motions

In this study, seventy-five near-fault ground motions are selected to study the nonlinear responses. Various studies have demonstrated that near-fault motions can impose extreme demands on structures, much more than the far-field records (Bertero *et al.* 1978, Hall *et al.* 1995, Malhotra 1999, Alavi and Krawinkler 2004). Near-fault ground motions often show impulsive characteristics exhibiting distinguishable pulses in their velocity and displacement time histories, occasionally also in acceleration time histories. The relatively long period pulses in near-fault ground motions are closely related to the seismological aspects of earthquakes, such as source mechanism, fault slip, and rupture directivity (Somerville 2003).

The pulses are directly related with the rise time and slip velocity of faulting, and can be formally extracted with various established methods. The peak inelastic drift and the residual drift is found to correlate well with the structure-to-pulse period ratio, T_s / T_p (Cuesta and Aschheim 2001, Alavi B, Krawinkler 2001, Mavroeidis *et al.* 2004, Akkar *et al.* 2004, Gillie *et al.* 2010). In 2010, Tang and Zhang proposed an improved method to derive the pulse representations using different pulse models. Their work also identified seventy-five pulse-like ground motions (twenty-five acceleration pulse motions and fifty velocity pulse motions) and their respective pulse representations. This ensemble of pulse-type motions are inherently used for this study and the detailed information has been provided in Chapter 2.

3.3 Inelastic Drifts for Bilinear SDOF Systems

Although estimating the inelastic drift is an uneasy goal, the aforementioned study to estimate peak inelastic displacement by Zhang *et al.* (2011) have been proved an innovative and accurate approach. On the other hand, that study was focused on the performance of a series of shear flexural interacted concrete columns. Therefore, in additional to the defined term that captures the general nonlinearity of a bilinear system, aspect ratio of the column is involved in their prediction as well as the regression was made considering the shear flexural interaction (SFI) effects. Actually, real structures may include other complicated behaviors based on different structure configurations. For example, in a recent paper by Dupuis *et al.* (2013), six shaking table tests show that by increasing the axial load helps to reduce the horizontal inelastic drift. However, this study tends not to incorporate such specified features into the estimation of residual drift for two reasons: first, these configurations are sometimes structure-specific and none of them can represent most of the other structures; second, incorporating various structure-specific features significantly complicates the model.

Another purpose of this study is to propose a general methodology of predicting the residual drift demand based on which extensive studies could be followed for specific structures. The bilinear model, on the other hand, has been generally recognized as a fundamental model to capture the nonlinear behavior. As an example, a bilinear system (Period 0.8 sec) is created with properties given in Table 3.1. The bilinear model was sampled to match the behavior of a real bridge column system, which is introduced in the validation part of this study. The system has a linear damping ratio of 1.5%, 0% nonlinear damping, and a 5% post-yielding stiffness. Such system is excited with two presented motions (Record #17, #26 from table 2.2 and 2.3) and the nonlinear time history responses are illustrated in Fig. 3.1(a). It can be clearly observed that residual drifts occurred after both ground motions hit the structure.

Table 3.1 Sample bilinear system configuration modeled according to a bridge column

Mass	w_o	ξ	D_y	ε	$\Pi_{\xi n}$
N-sec^2*/m*	*rad/sec*	-	*m*	-	-
926360	7.85	1.50%	0.0295	5%	0

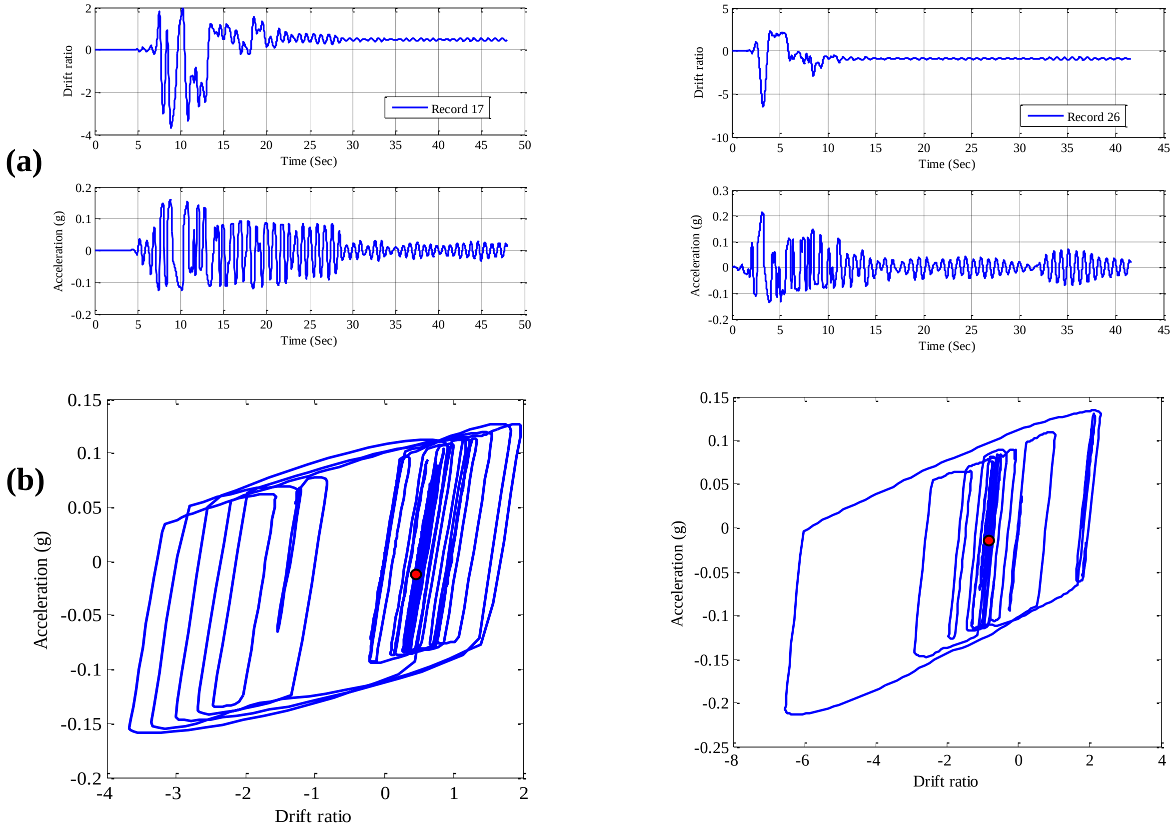

- Max Drift: 3.66%; Estimated: 2.61%; Error: 28%
- Max Residual Drift: 0.45%; Estimated: 0.46%; Error: 1.8%

- Max Drift: 5.46%; Estimated: 5.85%; Error: 7.3%
- Max Residual Drift: 0.95%; Estimated: 0.73%; Error: 23%

Fig. 3.1 Nonlinear response from two presented motions (#17 KJMA and #26 Pacoima Dam), (a) Time history, (b) System acceleration-drift behavior with 5% damping ratio

The hysteretic behavior of the bilinear system is illustrated by Fig. 3.1(b). The red circles locate the positions where the system motion stopped. Record #17 pushes the system to a peak transient drift of 3.66%. The motion of the SDOF system stopped at 0.45% residual drift. The next section of this study proposes a detailed method of estimating these inelastic drift demands. According to the proposed equations, the estimated peak transient drift is about 2.61%, corresponding to a 28% error. However, the estimated residual drift is 0.46%, which is very close to the computed residual. For record #26, the estimation has a 7.3% error for peak transient drift and a 23% error for residual drift.

3.4 Estimation of Inelastic Drift Ratios for Nonlinear Systems

3.4.1 Estimation of Peak Inelastic Drift Ratio

Before estimating the residual drift, an estimation of peak transient inelastic drift ratio is presented. For a generalized civil structure, this study recommends an estimated inelastic drift in the following format:

$$\Pi_U = \left|\Pi_\omega - c_1\right|^{-c_2} \Pi_{NL}{}^{c_3} < c_4 \Pi_{NL}{}^{c_3} \tag{3.7}$$

where c_1 to c_3 are constants to be determined from regression analysis aiming at minimizing error compared with numerical analyses. One could also notice that the normalized peak inelastic drift ratio is related with the structure-to-pulse frequency ratio $\Pi_\omega = \omega_s / \omega_p$ and the nonlinear index Π_{NL} shown in Eq. (3.6). c_4 in Eq. (3.7) is the upper bound for the first term $\left|\Pi_\omega - c_1\right|^{-c_2}$ in case Π_ω and c_1 are close values. For a simplified bilinear system, the estimation formula for the inelastic drift ratio under the dimensional framework is expressed in Eq. (3.8):

$$\Pi_U = \Pi_\omega{}^{-1.4} \Pi_{NL}{}^{0.15} < 2.0 \Pi_{NL}{}^{0.15} \tag{3.8}$$

Fig. 3.2 plots the normalized drift demand Π_U of a bilinear SDOF system against the structure-to-pulse frequency ratio Π_ω for the same sample bilinear case listed in Table 3.1. The dotted curve corresponds to the simulated values and the squares are the predictions from Eq. (3.8). For this specific case, the overall error between these curves is less than 25%. The validation section of this study will further evaluate the presented formulas and their accuracy compared with other approaches provided previously.

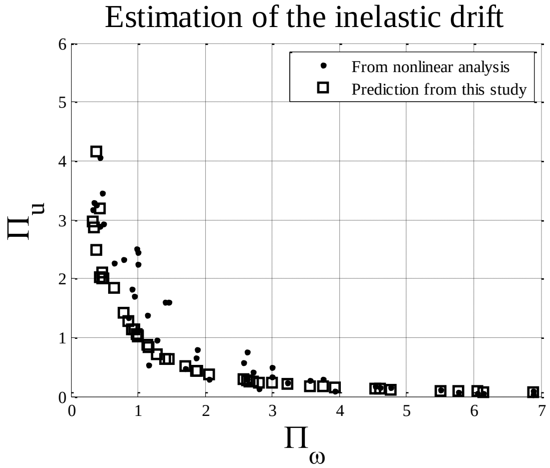

Fig. 3.2 Π_U - Π_ω relation for a bilinear system (T = 0.8 sec, 5% post yield hardening, 1.5% linear damping ratio)

In the later part of this chapter, this proposed approach will be compared with the ATC-40 approach, which superposes capacity diagram plots on demand diagram plots to estimate the maximum displacement demand through an iterative procedure using a series of equivalent linear systems. Better accuracy of Eq. (3.8) has been proved over the ATC-40 approach from error analysis.

3.4.2 Estimation of Residual Drift Ratio

The residual drift is not only sensitive to Π_U and Π_ω, but also highly sensitive to the post-yielding stiffness ratio ε. Based on this understanding, a set of regressive models are proposed to predict the inelastic drift ratio and the residual drift.

For prediction of residual drift Π_R, the regression procedure first adopts Weibull function to identify the relation between Π_R and Π_ω. Weibull function is chosen here because it comprehends different variations for nonlinear curve fitting. Fig. 3.3 shows four variations of

Weibull function. Mathematically, the Weibull function between variable *y* and *x* is presented in Eq. (3.9):

$$y = c\left(\frac{x}{a}\right)^{b-1} e^{\left(-\left(\frac{x}{a}\right)^{b}\right)} \tag{3.9}$$

where *a, b, c* are constants, *x* is non-zero and not infinitely large or small. Taking log for both side of Eq. (3.9), one could get:

$$\log y = -\frac{x^b}{a^b} + \log x^{b-1} + (\log ac - \log a^b) \tag{3.10}$$

Eq. (3.10) shows that a Weibull function provides the option to fit $\log(\Pi_R)$ with functions of Π_ω and/or $\log(\Pi_\omega)$. This study performed a nonlinear fitting to study the correlation between Π_R and Π_ω. In order to minimize the error, the fitting procedure suggests constant zero value for *b*, which indicates that a linear relationship between Π_R and Π_ω in log space.

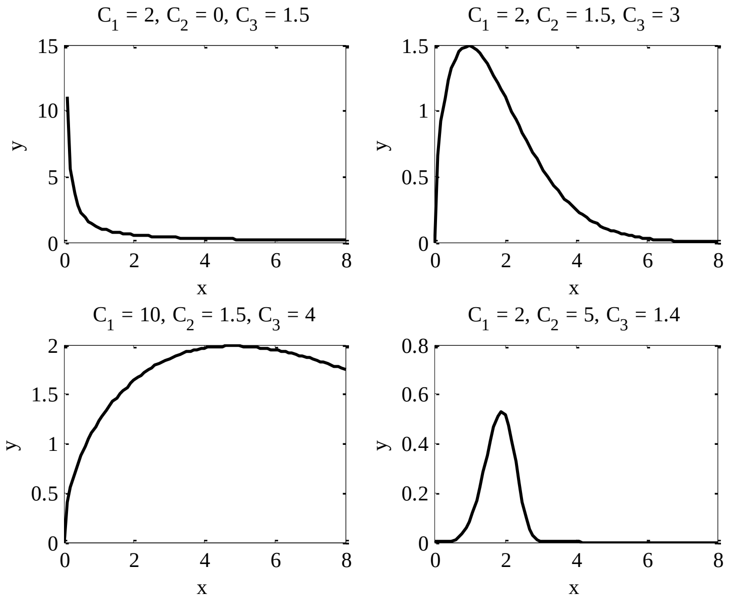

Fig. 3.3 Demonstrations for different variations for Weibull function

Although the Weibull function suggests a correlation between $\log(\Pi_R)$ and $\log(\Pi_\omega)$, it is still hard to provide the estimation formula for residual drift. Different formats of functions are systematically chosen with values of ε , Π_{NL} , Π_R and Π_ω that makes physical sense and minimizes overall error at the same time.

Similar to estimating the peak inelastic drift, an initial guess of the residual drift would be in the format of:

$$\Pi_R = c_5 \Pi_\omega{}^{c_6} \times \Pi_{NL}{}^{c_7} \tag{3.11}$$

where c_5, c_6, and c_7 are constants to be determined. However, this format could not incorporate the post-yielding stiffness ratio ε . In addition, by setting c_5, c_6, and c_7 constants, the influence of the nonlinearity is not significant enough to capture the change of residual drift.

With these remarks, huge effort of trial and error lead to the finalized formula of estimating the residual drift

$$\Pi_R = \begin{cases} (\frac{1}{4} - \varepsilon)\Pi_\omega{}^{\frac{1}{20}\Pi_{NL} - 2.4} \times \Pi_{NL}{}^{0.15} \quad (\varepsilon \le 25\%) \\ 0 \quad (\varepsilon > 25\%) \end{cases} \tag{3.12}$$

Eq. (3.12) is generally applicable for most of civil structures as they have smaller post-yielding stiffness than 25%. Compared with Eq. (3.11), c_5 and c_6 are not fixed as constants in the proposed formula and the updated coefficients involve the post-yielding stiffness ratio ε and the nonlinearity term Π_{NL} . One could notice that Π_R increases with Π_{NL} , which means when a system has larger nonlinearity, the estimated magnitude of residual drift gets larger. In addition,

Π_R decreases when the system's post yield stiffness ε gets larger. Notice that when ε is approaching 25%, estimation from Eq. (3.12) would be zero. This would not be the fact since the system is still nonlinear where residual drift could occur. However, when ε gets larger, most of the post-earthquake residual drifts can be minimized that estimation of zero residual would still be reasonable with small errors.

Fig. 3.4 plots the normalized residual drift Π_R of two different bilinear SDOF systems versus Π_ω. One could easily see that the system with 1% post-yielding stiffness and earlier yielding (smaller Q_D / W values) corresponds to larger residual drifts than the other system that yields later with 5% post-yielding stiffness. The estimated values for the two bilinear cases are expressed with solid red line and dotted black line in Fig. 3.4, which are reasonably close to the simulated data.

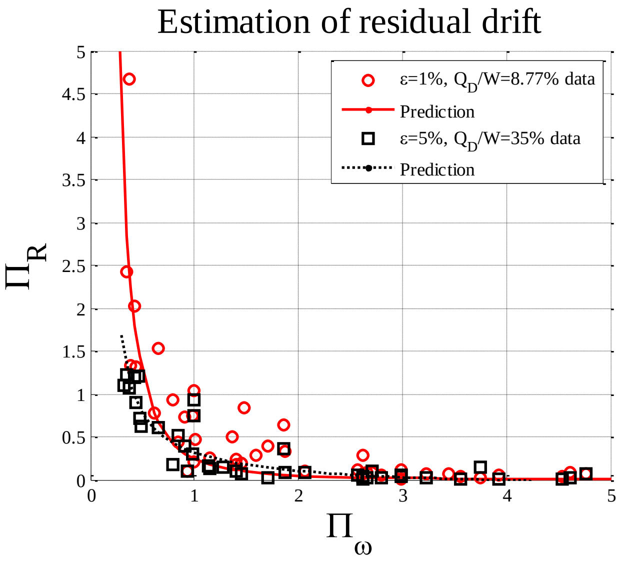

Fig. 3.4 Two different systems and their estimation of residual drifts

Notice that all the residual drifts less than 0.1% have been removed in this study as they are negligible. This filtering procedure will be further discussed as it also helps the error analysis in the later part of this chapter.

3.4.3 Correlation between Peak Inelastic Drift Ratio and Residual Drift Ratio

Existing studies tend to estimate residual drift by modifying the peak inelastic drift of the yielding structure. For example, In 2000 JSCE code, the residual drift after a system exceeds the yielding strength is provided as Eq. (3.13):

$$\begin{aligned}\delta_R &= \begin{cases} C_R(\mu_R-1)(1-\varepsilon)\delta_y & (\mu_R>1) \\ 0 \quad (\mu_R\le 1) \end{cases} \\ &= \begin{cases} C_R(\delta_{U\max}-\delta_y)(1-\varepsilon) & (\delta_{U\max}>\delta_y) \\ 0 \quad (\delta_{U\max}\le\delta_y) \end{cases}\end{aligned} \tag{3.13}$$

where, $\delta_{U\max}$, δ_y and δ_R are the maximum inelastic displacement, yield displacement and residual displacement, respectively; μ_R is response ductility factor of a bilinear system (i.g. columns) ($\mu_R=\delta_{U\max}/\delta_y$); ε is the post-yield stiffness ratio; C_R is a displacement factor depending on ε, and C_R is set as 0.5 for RC piers based on the residual displacement response spectrum (Kawashima *et al.* 1998).

However, setting C_R at a constant value turns out to be inaccurate, which is illustrated in Fig. 3.5. In fact, for an inelastic response ($\delta_{U\max}>\delta_y$), C_R can be back-computed from Eq. (3.13) when its residual drift and maximum drift are provided:

$$C_R=\frac{\delta_R}{(\delta_{U\max}-\delta_y)(1-\varepsilon)}=\frac{\Pi_R}{(\Pi_U-\Pi_{Dy})(1-\varepsilon)} \tag{3.14}$$

Fig. 3.5(a) shows the calculated C_R from Eq. (3.13) compare with the normalized results obtained from numerical analyses. It is obvious that the JSCE code is generally under estimating C_R. In addition, a significant over estimation happens near 2.5 of normalized displacement Π_U.

This indicates a big error of JSCE estimation. Fig. 3.5b shows the relationship between C_R and Π_ω, which is highly scattered. Fig. 3.5c shows the relationship between $\log(C_R)$ and $\log(\Pi_\omega)$, which is also scattered. Nevertheless, the relation between $\log(C_R)$ and $\log(\Pi_\omega)$ is relative closer to a linear fit, which corresponds to the following relation:

$$C_R = C_1 \Pi_\omega^{\;C_2} \tag{3.15}$$

where C_1 and C_2 are coefficients that are related to the bilinear system configuration yet to be determined. However, this approach becomes pointless because the large scattering of the data from the proposed equations.

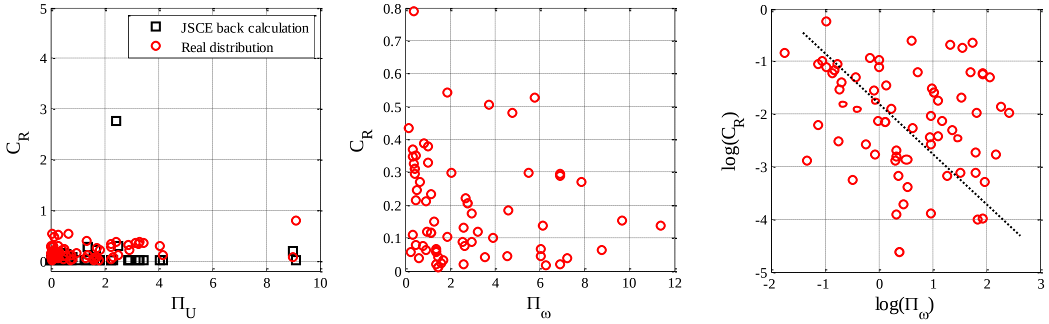

(a) **(b)** **(c)**

Fig. 3.5 JSCE formula. (a) Comparison of JSCE code and analytical data, (b) Relation between C_R and Π_ω, (c) Relation between C_R and Π_ω in log space

Different from the above approach, this study establishes a better correlation between Π_U and Π_R using the dimensional analysis. The variable C_R is redefined by dividing Π_R by Π_U. For a system with ε smaller than 25%, the new expression is presented in Eq. (3.16):

$$C_R = \frac{\Pi_R}{\Pi_U} = \frac{\delta_{U\max}}{\delta_R} = \frac{(\frac{1}{4}-\varepsilon)\Pi_{NL}^{\;0.15} \times \Pi_\omega^{\;\frac{1}{20}\Pi_{NL}-2.4}}{\Pi_\omega^{\;-1.4}\Pi_{NL}^{\;0.15}} = (\frac{1}{4}-\varepsilon)\Pi_\omega^{\;\frac{1}{20}\Pi_{NL}-1} \tag{3.16}$$

Eq. (3.16) indicates that C_R and Π_ω are correlated in such format closer to Eq. (3.15). The coefficients $C_1 = 25\% - \varepsilon$ and $C_2 = \Pi_{NL} / 20 - 1$ are now dependent on the system configuration. Instead of a constant value, this newer C_R establishes a dynamic relation between the maximum absolute drift and the residual drift that considers the system nonlinearity and the ground motion characteristics.

The proposed predictions for Π_R and C_R represent significant improvements over the existing residual drift demand models. The estimation of residual drift does not simply apply a coefficient to peak inelastic displacement. Instead, residual drifts are directly evaluated by the normalized drift demands without running nonlinear time history analyses. There are four benefits of such approach: 1) the prediction does not rely on a provided peak inelastic drift. An accurate peak inelastic drift can only be obtained from lab tests or numerical approaches. On the other hand, existing estimation of maximum inelastic drift creates an error that will be propagated if the result is further used to estimate residual drift. 2) The result of the prediction is in an ordered form under the framework of dimensional analysis. The prediction is more reliable and meaningful than any other existing approaches as it not only incorporates the features of different bilinear systems but also considers the ground motion characteristics. 3) A better relationship between the inelastic drift Π_U and the residual drift Π_R has been established.

3.5 Validations of the Proposed Method

This section tests the accuracy of the proposed residual drift demand model provided in Eq. (3.12) above. Different bilinear configurations and different near-fault pulse-type ground motions are used to compute the nonlinear responses. Errors of the proposed method and other existing approaches are presented. Different configurations of bilinear systems have been used for the validation and the results are presented in tables. In order to keep these tables short, ten out of seventy-five near-fault pulse type motions are randomly selected for this study. Table 3.2 lists the ten ground motions selected for the validation section.

Table 3.2 Ten pulse-type motions for validation of dimensionless residual drift

Number	Earthquake	Year	Magnitude	Fault mechanism	Station	Pulse	Distance to fault	PGA
			M_w		Name	Direction	(km)	(g)
8	PALMSPR/HCP	1986	6.1	Reverse–Oblique	Hurkey Creek Park	197	29.83	0.2425
9	WHITTIER/A-NOR	1987	6	Reverse–Oblique	Norwalk-Imp Hwy, SGrnd	190	20.42	0.2531
10	WHITTIER/B-ALH	1987	5.3	Reverse–Oblique	Alhambra-Fremont School	77	14.02	0.2485
25	LOMAP/LEX	1989	6.9	Reverse–Oblique	Los Gatos-Lexington Dam	38	5.02	0.5221
26	SFERN/PUL	1971	6.6	Reverse	Pacoima Dam (upper left	195	1.81	1.5161
27	IMPVALL/H-AEP	1979	6.5	Strike-slip	Aeropuerto Mexicali	233	0.34	0.4071
34	IMPVALL/H-E07	1979	6.5	Strike-slip	El Centro Array #7	233	0.56	0.521
50	CAPEMEND/PET	1992	7	Reverse	Petrolia	260	8.18	0.7096
54	NORTHR/SCS	1994	6.7	Reverse	Sylmar-Converter station	32	5.35	0.5943
69	Chichi/TCU	1999	7.6	Reverse–Oblique	TCU136	136	8.29	0.1874

3.5.1 Six Bilinear Configurations to Represent Generalized Civil Structures

In addition to different ground motions, the proposed method has been evaluated by investigating the inelastic response of a real bridge column model whose primary curve shows close enough behavior to a bilinear SDOF system. The sample system has a total deck mass of $926\,Mg$ and the initial elastic stiffness k_e equals $57MN/m$, corresponding to a structural period around 0.75 sec. The post-yielding stiffness k_p=5%k_e=2.85MN/m and yield strength $Q_y = 0.8MN$. In additional to the given column model, five other SDOF systems with same elastic stiffness k_e but different post-yielding stiffness k_p and yield strength Q_y are simulated:

- Small post-yielding stiffness k_p=1%k_e with yield strength Q_y;
- Larger post-yielding stiffness k_p=10%k_e with yield strength Q_y;
- Intermediate post-yielding stiffness k_p=5%k_e with yield strength $2Q_y$;

- Intermediate post-yielding stiffness k_p=5%k_e with yield strength $4Q_y$;
- Intermediate post-yielding stiffness k_p=5%k_e with yield strength $8Q_y$;

3.5.2 Comparison of the Proposed Formula with Existing Methods

Two existing methods to predict the residual drift ratio, the ATC-58 equation and the aforementioned JSCE formula, have also been evaluated and their estimations have been compared with the proposed method. These two models were selected because they were also developed using the non-degrading bilinear SDOF models subject to ground motions.

The method presented by ATC-58 is a piece-wise estimation of residual drift, which categories the residual drift to three expressions at different peak inelastic drift levels, which are shown in Eq. (3.17).

$$\begin{cases} \Delta_r = 0 \quad \Delta \le \Delta_y \\ \Delta_r = 0.3(\Delta - \Delta_y) \quad \Delta_y < \Delta < 4\Delta_y \\ \Delta_r = (\Delta - 3\Delta_y) \quad \Delta \ge 4\Delta_y \end{cases} \tag{3.17}$$

where Δ_r is the notation for residual drift, Δ stands for the peak transient drift, and Δ_y is the yielding drift. Residual drift is considered zero for the first phase when the system moves within its elastic range. The second phase and the third phase are calibrated such that when the ductility ratio is around four, the ratio of residual to peak transient drift is 0.23. Moreover, for ductility ratios near two and six, the ratios of residual to peak transient drift are 0.15 and 0.5, respectively. Ultimately, as the collapse point is reached, the residual drift will approach the peak transient drift.

The advantage of this approach is the dynamic calibrated coefficient that links the residual drift with the peak transient response. For example, at 3% total peak drift, the predicted residual drift would be 0.2 times the peak drift ratio. At 5% total drift, the predicted residual would be 0.38 times the peak transient drift. Then, the coefficient goes up to 0.56 times the peak transient when 7% total peak drift is reached. This Drift - intensity relation is illustrated in Fig. 3.6.

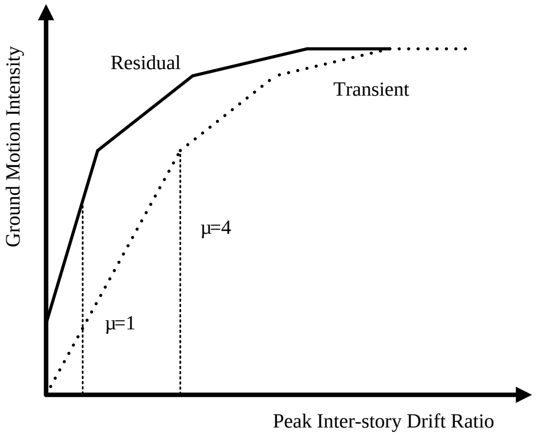

Fig. 3.6 ATC-58 Idealized model to estimate residual story drift from peak transient drift as a function of ground motion (GM) intensity

However, the ATC-58 formula comes with short comings. First, ATC equations won't be functional without estimated peak inelastic drift. Before estimating residual drift, one should provide methods to obtain the peak inelastic response and the accuracy of the peak inelastic drift can be questionable. In addition, the ATC equations only predict residual drifts for a narrow range of building systems. The equations do not consider nonlinearity effects for more generalized structures or distinguish between many of the behavioral effects that affect residual drifts. One could notice that the ATC equations contain no post-yielding stiffness. Therefore, the influence from post-yielding stiffness to the residual drift is not reflected in the equations except insofar as the post-yielding stiffness affects the peak transient drift ratio. The equations are presented in this simple format owing to the lack of physical data to validate modeling of residual displacements and due to the complexity of obtaining significant improvements in the residual drift estimates. These deficiencies are eliminated by Eq. (3.12) of this study, which fully captures the bilinear behavior for estimating residual drifts under the dimensional analysis framework.

Another approach that has been compared with Eq. (3.12) is the prediction of residual drift from the 2000 JSCE code. As shown in Eq. (3.13), the estimation of residual drift δ_R is also based on the peak inelastic drift $\delta_{U\max}$, which is hard to obtain without running simulations. Estimation of the inelastic displacement may introduce an error that will propagate to a larger error. In addition, the variable C_R has been proved far from being accurate. The estimated residual drift would be inaccurate due to the lack of connections between residual drift and the bilinear configurations.

Fig. 3.7 shows the normalized residual drifts Π_R solved from the nonlinear time history analyses and those predicted by the proposed demand model as well as the two published methods mentioned above. In this case, a system with 5% post-yielding stiffness and 17.5% strength to weight ratio is simulated and plotted with black squares. In addition, the proposed prediction in this study, the ATC prediction, and the JSCE prediction are plotted with red pluses, blue circles, and greed dots, respectively. The proposed model yields acceptable predictions on residual drift (64% error) whereas the ATC and JSCE formula produce larger dispersion, generating huge errors. In addition, when structure frequency is very close to the pulse frequency ($\Pi_\omega \approx 1$), the dispersion of the simulated data becomes relatively large such that the errors increase near this range of normalized frequency.

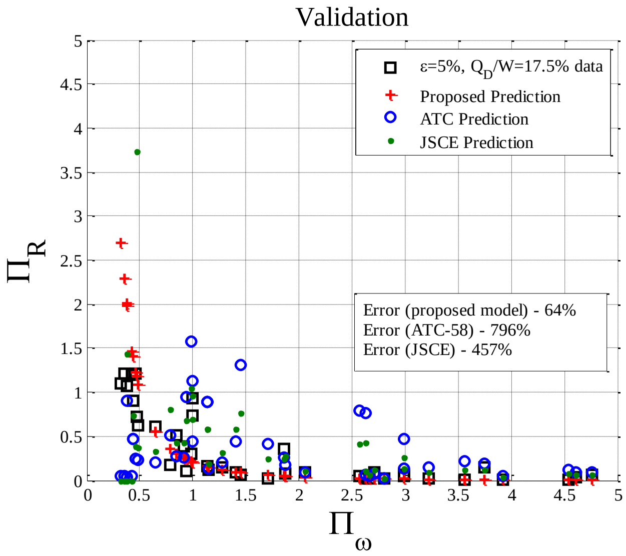

Fig. 3.7 Validation of proposed method by comparing with analytical data and the existing methods

3.5.3 *Error Estimation for the Proposed Method*

The accuracy of the proposed method is further proved by an error analysis. Traditionally, the overall normalized error is computed by the Eq. (3.18):

$$e = \frac{1}{N}\sum_{i=1}^{N}\left|\frac{R^i_{predict} - R^i}{R^i}\right| \tag{3.18}$$

where N is the number of cases computed, R^i stands for the simulated residual drift for the i^{th} ground motion, and $R^i_{predict}$ is the predicted residual drift. However, Eq. (3.18) is not the best formula to compute the error for residual drifts. One observation from the simulated results is that some ground motions may cause large peak inelastic displacements while those bilinear systems rest at their original locations. In other words, for some situations, the residual drifts might be extremely small and negligible. On the other side, these tiny residual drifts tends to create huge errors from Eq. (3.18). Therefore, an updated equation to estimate error for residual drift ratio is given as:

$$\tilde{e} = \frac{1}{\tilde{N}} \sum_{i=1}^{\tilde{N}} \left| \frac{R^i_{predict} - R^i}{R^i} \right| \tag{3.19}$$

where $\tilde{N}$ excluded all the cases with residual drifts smaller than 0.1%. For example, this approach eliminates about 10%-15% cases for bilinear systems with post-yielding stiffness k_p around 1%-5% of the elastic stiffness k_e. Increasing the post-yielding stiffness and/or increasing the yielding displacement will tend to reduce the residual drift. Consequently, the eliminated cases will also increase.

In order to cover a wider range of civil structures, estimations of residual drifts for all the six aforementioned cases of bilinear systems have been performed. Each table from Table 3.3(a) to Table 3.3(e) corresponds to one configuration of bilinear system. The second and the third column in each of the tables are the numerically simulated peak inelastic drifts and residual drifts for the bilinear system. The fourth to seventh column is the ATC predictions of peak inelastic drifts and residual drifts and their corresponding error. The eighth column is the JSCE prediction of residual drifts and the errors are given in the ninth column. The last four columns are the estimations and errors of peak inelastic drifts and residual drifts from this study.

Table 3.3 Validation data from ten motions for six different systems

Qd/Weight = 8.77% ε = 0.01

	Computed		ATC prediction				JSCE prediction		Our prediction			
Eq #	D_{max} (%)	D_R (%)	D_{max} est (%)	error (%)	D_R est (%)	error (%)	D_R est (%)	error (%)	D_{max} est (%)	error (%)	D_R est (%)	error (%)
8	0.343	0.177	0.442	28.744	0.033	81.157	0.055	68.909	0.330	3.910	0.207	17.004
9	0.762	0.375	0.578	24.199	0.159	57.529	0.263	29.922	0.588	22.815	0.154	58.890
10	0.343	0.202	0.523	52.280	0.033	83.467	0.055	72.721	0.330	3.937	0.180	10.781
25	5.239	2.500	1.097	79.067	5.099	104.005	2.754	10.171	1.800	65.637	0.301	87.967
26	5.614	4.344	3.158	43.743	6.349	46.168	3.373	22.359	5.483	2.319	0.800	81.589
27	2.161	0.343	0.780	63.905	1.465	327.297	0.955	178.493	1.763	18.433	0.160	53.279
34	6.366	1.117	0.606	90.482	8.856	692.872	4.613	313.037	3.177	50.094	0.188	83.151
50	5.541	1.166	1.351	75.616	6.107	423.637	3.253	178.894	3.412	38.422	0.276	76.348
54	6.430	0.637	0.865	86.543	9.072	1323.882	4.720	640.873	3.565	44.554	0.266	58.272
69	2.379	1.553	0.270	88.662	1.683	8.388	1.063	31.557	1.717	27.845	0.059	96.216
average				63.324		314.840		154.694		27.796		62.350

(a)

Qd/Weight = 8.77% ε = 0.05

	Computed		ATC prediction				JSCE prediction		Our prediction			
Eq #	D_{max} (%)	D_R (%)	D_{max} est (%)	error (%)	D_R est (%)	error (%)	D_R est (%)	error (%)	D_{max} est (%)	error (%)	D_R est (%)	error (%)
8	0.338	0.150	0.382	12.979	0.029	80.694	0.046	69.433	0.330	2.487	0.172	15.083
9	0.793	0.315	0.343	56.742	0.165	47.443	0.262	16.785	0.593	25.240	0.129	58.913
10	0.340	0.164	0.477	40.295	0.029	82.065	0.047	71.604	0.330	2.974	0.150	8.631
25	5.265	0.242	1.005	80.912	5.158	2031.982	2.680	1007.628	1.930	63.345	0.273	12.814
26	5.460	0.948	3.586	34.327	5.809	512.955	2.989	215.390	5.861	7.330	0.728	23.151
27	2.022	0.441	0.483	76.110	1.296	194.162	0.846	91.846	1.814	10.256	0.139	68.433
34	5.397	0.394	1.082	79.950	5.597	1321.352	2.888	633.477	3.369	37.581	0.176	55.416
50	5.110	0.335	1.249	75.557	4.641	1285.683	2.434	626.787	3.615	29.249	0.253	24.377
54	5.958	0.237	0.801	86.557	7.470	3048.820	3.778	1492.520	3.841	35.529	0.255	7.427
69	1.954	0.529	0.418	78.611	1.229	132.340	0.813	53.787	1.764	9.717	0.052	90.262
average				62.204		873.750		427.926		22.371		36.451

(b)

Qd/Weight = 8.77% ε = 0.1

	Computed		ATC prediction				JSCE prediction		Our prediction			
Eq #	D_{max} (%)	D_R (%)	D_{max} est (%)	error (%)	D_R est (%)	error (%)	D_R est (%)	error (%)	D_{max} est (%)	error (%)	D_R est (%)	error (%)
8	0.335	0.119	0.452	35.148	0.024	79.957	0.036	69.936	0.330	1.341	0.129	8.579
9	0.824	0.233	0.458	44.450	0.171	26.823	0.256	9.765	0.600	27.138	0.098	57.903
10	0.337	0.140	0.510	51.424	0.024	82.468	0.037	73.702	0.330	1.885	0.113	19.259
25	5.379	0.250	0.873	83.763	5.499	2097.315	2.704	980.571	2.046	61.963	0.221	11.515
26	5.310	0.302	2.088	60.679	5.268	1643.848	2.600	760.767	6.133	15.492	0.584	93.418
27	1.783	0.315	0.803	54.974	1.018	223.101	0.688	118.311	1.850	3.748	0.107	65.886
34	4.729	0.410	0.978	79.312	3.963	867.265	2.013	391.335	3.457	26.897	0.139	65.966
50	4.798	0.196	1.399	70.833	4.032	1957.313	2.044	942.993	3.755	21.732	0.204	4.261
54	6.081	0.161	0.938	84.580	7.838	4767.269	3.757	2232.906	4.097	32.620	0.223	38.472
69	1.536	0.107	0.355	76.881	0.771	620.518	0.577	438.961	1.788	16.400	0.040	62.914
average				64.204		1236.588		601.924		20.922		42.817

(c)

		Qd/Weight	=	17.54%				ε	=	0.05		
	Computed		ATC prediction				JSCE prediction		Our prediction			
Eq #	D_{max} (%)	D_R (%)	D_{max} est (%)	error (%)	D_R est (%)	error (%)	D_R est (%)	error (%)	D_{max} est (%)	error (%)	D_R est (%)	error (%)
8	0.351	0.007	0.542	54.717	0.005	*	0.000		0.313	10.759	0.166	
9	0.937	0.197	0.404	56.850	0.136	30.978	0.215	9.284	0.587	37.315	0.128	34.979
10	0.406	0.119	0.296	27.180	0.005	95.806	0.000	100.000	0.320	21.221	0.147	23.055
25	5.332	0.052	0.681	87.222	4.656		2.671		1.841	65.469	0.257	
26	5.301	0.178	2.100	60.381	4.553	2452.117	2.622	1369.772	5.535	4.420	0.675	278.101
27	0.889	0.181	0.738	16.991	0.122	32.901	0.193	6.241	1.744	96.153	0.132	27.452
34	4.473	0.200	0.689	84.607	3.022	1414.567	1.895	849.630	3.148	29.615	0.154	22.622
50	3.923	0.466	1.382	64.772	2.472	431.007	1.634	250.895	3.395	13.467	0.228	51.012
54	5.212	0.218	1.141	78.109	4.255	1849.079	2.481	1036.244	3.547	31.941	0.220	0.615
69	0.737	0.200	0.288	60.925	0.076	61.904	0.121	39.681	1.696	130.028	0.048	76.014
average				59.175		796.045		457.718		44.039		64.231

* The error for residual drift smaller than 0.1% is considered meaningless

(d)

		Qd/Weight	=	35.10%				ε	=	0.05		
	Computed		ATC prediction				JSCE prediction		Our prediction			
Eq #	D_{max} (%)	D_R (%)	D_{max} est (%)	error (%)	D_R est (%)	error (%)	D_R est (%)	error (%)	D_{max} est (%)	error (%)	D_R est (%)	error (%)
8	0.351	0.007	0.458	30.516	0.005	*	0.000		0.282	19.571	0.153	
9	1.068	0.017	0.505	52.702	0.030		0.048		0.584	45.367	0.127	
10	0.406	0.119	0.325	19.936	0.005	95.806	0.000	100.000	0.288	29.001	0.135	12.919
25	5.279	0.188	0.953	81.949	3.029	1514.592	2.358	1156.646	1.779	66.301	0.247	31.760
26	4.164	1.424	3.527	15.297	1.262	11.323	1.518	6.661	5.293	27.105	0.638	55.194
27	1.187	0.306	0.692	41.665	0.066	78.495	0.104	65.950	1.735	46.216	0.131	57.351
34	3.527	0.212	0.792	77.550	0.768	262.859	1.216	474.526	3.050	13.534	0.147	30.758
50	2.526	0.373	1.321	47.721	0.468	25.371	0.740	98.504	3.281	29.890	0.217	41.856
54	4.656	1.746	1.264	72.844	1.755	0.471	1.752	0.335	3.414	26.680	0.207	88.159
69	1.125	0.051	0.241	78.536	0.047		0.075		1.692	50.391	0.048	
average				51.872		284.131		271.803		35.406		45.428

* The error for residual drift smaller than 0.1% is considered meaningless

(e)

First, the estimation of peak inelastic drift this study proposed directly from structural and ground motion characteristics has been proved an accurate one. Errors of the presented method range from 20% to 50%. Compared with the proposed approach, the ATC-40 approach of estimating peak inelastic drifts is less accurate with approximately more than 50% error. ATC-40 replaces the inelastic spectra with highly damped elastic spectra, and the procedure may not converge to the correct response. Table 3.3 shows its significantly underestimated deformation for a wide range of periods, which matches the conclusion made by Chopra and Goel (2000).

Table 3.3 also proves that the proposed estimation of residual drift is more accurate than the two summarized existing approaches. For a structure with post-yielding stiffness ratio ε smaller than 10%, which is the case for generalized civil structures, the proposed estimation of residual drift receives error over the range of 40%-65%. On the other side, the ATC-58 and 2000 JSCE formulas produce huge error ranging from 150% to more than 1000%, which makes the estimations meaningless for real applications. Table 3.3(d) and Table 3.3(e) correspond the last two cases when the strength to weight ratio Q_D / W is large, which leads to smaller residual drifts. The shaded areas in the tables indicate that the errors are not estimated when simulated residual drifts are less than 0.1%.

3.6 Concluding Remarks

Estimating the residual drift has always been a challenging task. This study aims to develop a simple yet reliable demand model for estimating the residual drift for generalized non-degrading bilinear SDOF system under near-fault earthquake motions. Nonlinear time history analyses on six different configurations of SDOF bilinear systems are conducted under seventy-five selected near-fault ground motions. In additional to estimating the residual drift, a prediction of the peak inelastic displacement has also been presented and compared with previous approaches.

The study was presented under the framework of the rigorous dimensional analysis that represents responses with better order than common approaches. First, the residual drift is expressed in dimensionless form, which is normalized to the energetic length scale of ground motions. A dimensionless nonlinearity index is inherited from a previous paper to take into account of the structure strength, ground motion amplitude, and softening or hardening post-yield behavior. The normalized residual drift demand ($\Pi_R \equiv u_{end} \omega_p^{\ 2} / a_p$) is revealed to be strongly correlated to the post-yielding stiffness ratio ε, the structure-to-pulse frequency ratio $\Pi_\omega \equiv \omega_s / \omega_p$, and the dimensionless nonlinear index Π_{NL}. The dimensionless residual drift will increase if Π_{NL} increases and/or ε and Π_{ω} decreases. Two regressive equations are proposed to directly estimate the inelastic displacement and residual drift demand imposed by earthquake motions, respectively.

Compared with the simulated results from nonlinear time history analyses, the proposed model is able to give dependable predictions with a normalized error range from 40%-65%. The error is larger for the cases when structure frequency is smaller or near the neighborhood of the pulse frequency (i.e. $\Pi_{\omega} \approx 1$). Existing estimations of residual drift has also been studied and compared with the proposed methods in this study. Validations show that previous studies predicting the demand of residual drift produce errors that are too large such that these formulas are not desirable for the design of civil structures. In summary, the study offers a comparably reliable method to estimate the residual drift without relying on a provided maximum transient drift and a certain regressed coefficient. Such estimation is consistent with the underlying physics of the problem, which hinges upon the realistic features for the nonlinear systems.

4. SEISMIC PROTECTIVE DEVICES FOR BUILDINGS AND NUMERICAL MODELING SCHEME FOR SELECTED DEVICES

4.1 Introduction

To achieve the best structural responses during earthquakes, the optimal control theory of the civil structures had been proposed decades ago (Yang 1975). Structural control takes advantages of latest advanced computers, electronics, measurement techniques, instrumentation, controllers, materials, etc. These techniques make structures behave more like machines, aircrafts or human beings in the sense that they can be made adaptive or responsive to external forces. Over the past three decades, numerous control devices and strategies have been proposed to improve the safety and performance of civil engineering structures.

Through extensive research in the United States and throughout the world over the last several decades, innovative earthquake-resistant systems have been developed that have the potential to improve seismic performance levels significantly at reasonable cost. Chapter 1 briefly introduced three categories of the seismic protective systems: passive, semi-active, and active systems. This chapter provides examples and numerical models for some of the well-known building protective devices. In addition, a relative new passive ASD called the negative stiffness device has been introduced with a detailed explanation of its mechanical properties and numerical modeling scheme.

The presented seismic protective devices possess different mechanical behaviors, which manifests the supreme intelligence of civil engineers. Meanwhile, all these different devices serve the same goal, which is to provide safer civil structures that mitigate the seismic hazards to the minimum possible level.

4.2 Damping Systems

4.2.1 Passive Fluid Dampers

Passive fluid viscous dampers have been implemented in a number of structures for the primary purpose of dissipating energy from earthquake ground motion or sustained wind loading (Symans *et al.* 2008a, b). In the case of earthquake ground motion, the dampers prevent or limit structural damage whereas, for wind loading, the dampers reduce vibration levels to relieve occupant discomfort. The seminal testing of passive fluid dampers for seismic applications was performed by Constantinou and Symans (1993) and clearly demonstrated the ability of such dampers to improve the performance of building structures. Fluid viscous dampers consist of a metallic cylinder, filled with a low-viscosity fluid, and containing a piston head, which separates the two sides of the cylinder. As the damper is stroked, fluid passes around and/or through the piston head due to a pressure differential across the piston head. The orificing of the fluid results in the development of heat, which is dissipated through the metallic cylinder. For the range of frequencies typical of the fundamental mode of most structures, fluid dampers can be designed to exhibit insignificant restoring forces, resulting in behavior that is primarily rate-dependent (linear or nonlinear viscous) (Symans and Constantinou 1998). Fluid dampers also offer the advantage that they provide high-energy dissipation density (i.e., due to high internal fluid pressure, they are able to dissipate large amounts of energy for their size). The high-energy dissipation density results in physically compact dampers.

4.2.2 Variable Damping Systems

Symans *et al.* have developed variable damping systems that utilize variable orifice fluid dampers for structural systems and experimentally tested them at both the component level (Symans and Constantinou 1997a) and within multi-story building frames (Symans and Constantinou 1997b) and base-isolated structures (Madden *et al.* 2002; Symans and Reigles 2004). The variable damper consists of a metallic cylinder containing a piston rod/head assembly, a piston rod make-up accumulator (to minimize restoring forces) and is filled with silicone oil, as shown in Fig. 4.1(a) An external bypass loop containing a control valve is attached to the damper for modulating fluid flow. The pressure differential across the piston head, and thus the output force, was therefore modulated by the external control valve. Depending on the type of valve used, either two-stage (on-off) or continuously variable damping was generated. More complex models for describing the damper behavior over a wide frequency range were presented by Symans and Constantinou (1997a), which include a Maxwell model of linear visco-elasticity and a fundamental model based on fluid mechanics principles. Shaking table tests were performed by Symans and Constantinou (1997b) on a reduced-scale model of a three-story steel structure. The structure was subjected to historical earthquake records and was controlled by variable fluid dampers located in the diagonal bracing of the structure. The shaking table tests demonstrated that the peak response of the uncontrolled structure could be significantly reduced with the use of the variable damper control system.

The significant development in semi-active control is that Magnetorheological (MR) fluids have been developed and used in controllable fluid dampers (Carlson *et al.* 1996a, b). MR fluids typically consist of micron-sized, magnetically polarizable particles dispersed in a carrier medium such as mineral or silicone oil. Spencer *et al.* (1997) and Dyke *et al.* (1996) have conducted a number of studies to assess the usefulness of MR dampers (see Fig. 4.1(b)) for seismic response reduction. Spencer *et al.* (1998) and Yang *et al.* (2002) have developed and tested a large-scale MR damper suitable for full-scale applications. The first full-scale implementation of MR dampers - built by Sanwa Tekki using Lord Corporation MR fluid - have been implemented in the Tokyo National Museum of Emerging Science and Innovation. Since then MR dampers have been implemented in several cable stayed bridges and a smart base isolated building and a bridge. Gavin (1994) developed controllable fluid based variable damping systems using electrorheological (ER) fluids.

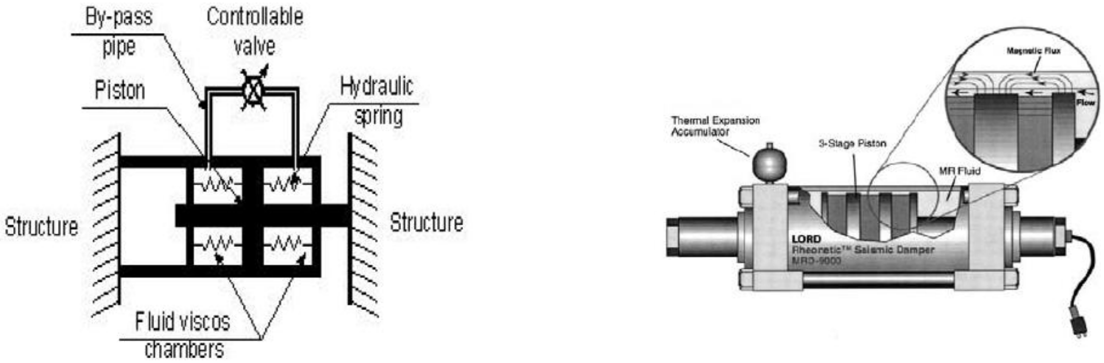

(a) Variable orifice fluid damper **(b)** MR damper

Fig. 4.1 Variable damping devices. (from Symans and Constantinou 1997a, Spencer *et al.* 1997, and Dyke *et al.* 1996)

Kajima Corp. of Japan has recently developed a significant and unique passive damper, HiDAXe, that has a performance equivalent to that of the semi-active switching oil damper, HiDAX (Tagami *et al.* 2004). Fig. 4.2 shows the HiDAXe damper and its force-displacement relationship. HiDAXe damper can maximize or minimize its damping coefficient by regulating the opening of an internal flow control valve housed within the device. It is fully adjustable, passive and has been implemented in several multistory high rise buildings in Japan by Kajima as reported in its Annual report for 2006, which also describes 20+ buildings in Japan with iDAX dampers. However, HiDAXe cannot adjust stiffness.

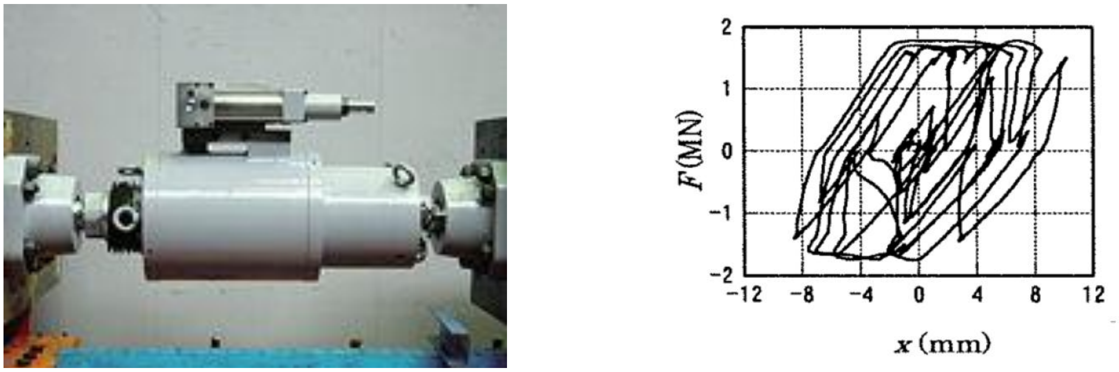

(a) HiDAXe Adjustable Passive Damper by Kajima

(b) Force-displacement relationship of HiDAX

Fig. 4.2 Variable damping systems by Kajima Company, Japan. (figure from Tagami *et al.* 2004)

4.3 Base Isolation Systems

4.3.1 General

Base isolation, also known as seismic base isolation or base isolation system, is one of the most popular means of protecting a structure against earthquake forces. It is meant to enable a building or non-building structure to survive a potentially devastating seismic impact through a proper initial design or subsequent modifications. Base isolation system can shift most of the structural motion to the base level and dissipates energy inside them (Kelly 1986).

The first use of rubber for earthquake protection was in an elementary school in Skopje, Yugoslavia (Seigenthaler 1970). In later on approaches to seismic isolation, the natural rubber sheets are laminated to steel plates. Considerable research effects were going on from 1970-1985 about the base isolation devices.

Isolation devices are relatively easy to manufacture. Many isolation mechanisms have been invented over the past decades for designing or retrofitting the buildings. Until now, three types of isolators are commonly used: elastomeric bearings (ERB), lead-rubber bearings (LRB), and friction pendulum systems (FPS) (Kelly 1986). Fig. 4.3(a-c) shows the sketches and the correspondent cyclic behaviors of these isolators. Table 4.1 summarizes the seismic performance of these isolation systems compared with un-isolated building. The general bilinear behaviors of the three types of bearings are different. For elastomeric bearings, the post-yielding stiffness K_2 is proportional to their area (A) multiplied by shear modulus (G) and is inversely proportional to their total thickness ($\sum t_r$) of the rubber layers, i.e. $K_2 = GA/\sum t_r$. The yielding displacement U_y is usually five to ten percent of the rubber layers' thickness $\sum t_r$ and the pre-yielding stiffness K_1 is usually as 5-15 times of post-yielding stiffness K_2. For lead rubber bearings, the Q_d is influenced by the yielding strength of the lead core F_y. The post-yielding stiffness will be usually a little stronger that of the elastomeric bearings due to the additional stiffness contribution from the lead core. The elastic stiffness K_1 of LRB is about 15-30 times of the post-yielding stiffness K_2. For the friction pendulum systems, Q_d is determined by the friction coefficient (μ_s) and sliding surface radius (R) and post-yielding stiffness $K_2 = W/R$, where W is the vertical load or structure weight. Due to the friction effect, this system usually has rigid pre-yielding stiffness (50-100 times the post-yielding stiffness K_2). The ratio between the pre-yielding stiffness K_1 and post-yielding stiffness K_2 is measured by a parameter $N = K_1/K_2$. In the subsequent parametric study, different parameters are selected to represent various isolation devices and the bearing pre- to post- stiffness ratio N will be set to 10, 20 and 50 to represent these types of isolation systems.

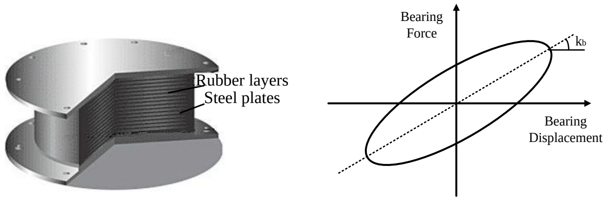

(a) Elastomeric bearing

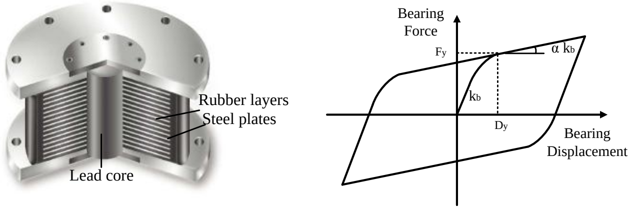

(b) Lead rubber bearing

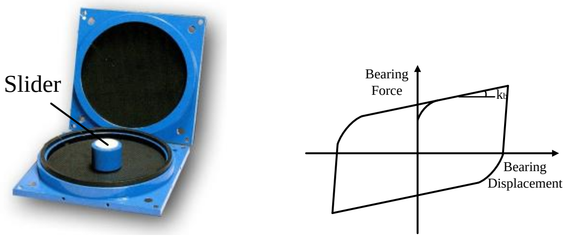

(c) Friction Pendulum

Fig. 4.3 Sketch and bilinear modeling of three most common seismic isolation devices

Table 4.1 Formulas of bilinear modeling for the three kinds of isolation devices (from Zhang and Huo 2009)

	Elastic stiffness K_1	Characteristic strength Q	Post-yielding stiffness K_2
ERB	$K_1 = NK_2\ (N = 5\text{-}15)$	From hysteresis loop	$K_2 = GA / \Sigma t_r$
LRB	$K_1 = NK_2\ (N = 15\text{-}30)$	$Fy = f_y A_{Lead}$	$K_2 = (1.15 - 1.20)\ GA / \Sigma t_r$
FPS	$K_1 = NK_2\ (N = 50\text{-}100)$	$Q = \mu W$	$K_2 = W / R$

Table 4.2 Properties for the three types of commonly used bearings

	Un-isolated	ERB	LRB	FPS
Structural deformation	high	low	low	low
Isolator displacement	-	moderate/high	low/moderate	low/moderate
Acceleration of structure	high	low	low/moderate	moderate
Advantages	-	■ low short-period attack on contents ■ simple uniform acceleration responses controlled by isolator properties, intensive to structural irregularities	■ low seismic forces ■ low base shears ■ low/moderate attack on contents ■ isolator 'locks' during wind	■ low isolator displacements ■ isolator 'locks' during wind
Disadvantages	-	■ susceptible to wind ■ large isolator displacement	■ moderate isolator damage	■ high attack on contents

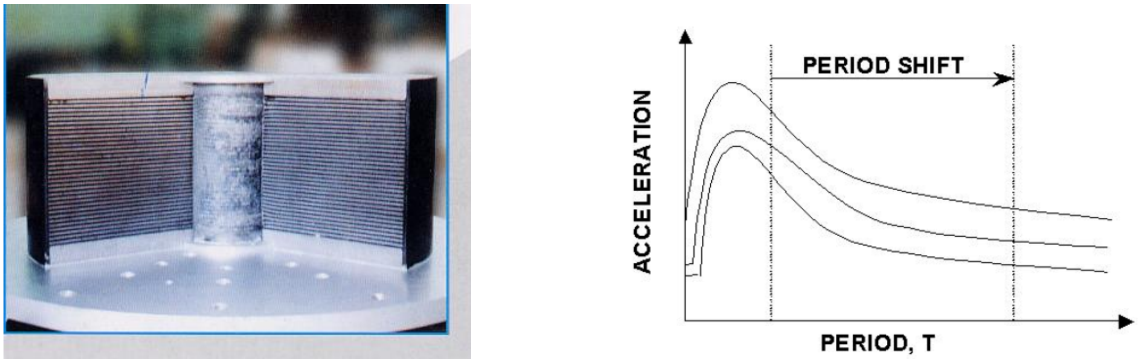

(a) Standard lead rubber bearing **(b)** Mechanism of rubber bearing isolation

Fig. 4.4 LRB base isolation systems

In 1986, the first base-isolated building in the United States was dedicated, which is the Foothill Communities Law and Justice Center located in the municipality of Rancho Cucamonga in San Bernardino County. The building is a 30 million dollar legal service centre for the county. The building sits on 98 isolators, which are multilayer natural rubber bearings reinforced with steel plates. And the energy of the high frequency component of the ground motion is isolated and cannot be transmitted to the superstructure (Kunde and Jangid 2003)

Fig. 4.5 Communities Law and Justice Center, San Bernardino, CA

By the year of 2000, the concept of Friction Pendulum Seismic Isolation Bearings were implemented worldwide: By placing these concave spherical bearings at each support point, the structure sways with a gentle pendulum motion during earthquake ground shaking. This allows the ground to shake without damaging the structure. Friction Pendulum seismic isolation provides structures with a higher level of seismic protection than conventional structural strength and ductility design. Compared to elastomeric bearings, friction pendulum bearings can be used for a wider range of applications, have simpler and more predictable properties, and are less expensive to install.

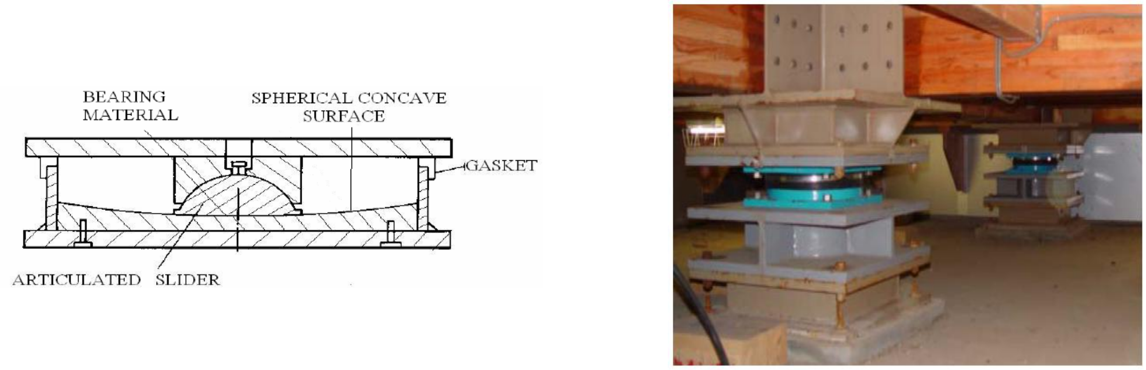

(a) FPS bearing configuration **(b)** FPS system construction

Fig. 4.6 Friction Pendulum systems

Base isolation is also used on a smaller scale - sometimes down to a single room in a building. Isolated raised-floor systems are used to safeguard essential equipment against earthquakes. The technique has been incorporated to protect statues and other works of art such as Rodin's Gates of Hell at the National Museum of Western Art in Tokyo's Ueno Park (Reitherman 2012).

4.3.2 Researches on Base Isolation Systems

Through the George E. Brown, Jr. Network for Earthquake Engineering Simulation (NEES), researchers are studying the performance of base isolation systems in 2012. The project, a collaboration among researchers at University of Nevada, Reno; University of California, Berkeley; University of Wisconsin, Green Bay; and the University at Buffalo, SUNY is conducting a strategic assessment of the economic, technical, and procedural barriers to the widespread adoption of seismic isolation in the United States. NEES resources have been used for experimental and numerical simulation, data mining, networking and collaboration to understand the complex interrelationship among the factors controlling the overall performance of an isolated structural system. This project involves shaking table and hybrid tests at the NEES experimental facilities at the University of California, Berkeley, and the University at Buffalo, aimed at understanding ultimate performance limits to examine the propagation of local isolation failures (e.g., bumping against stops, bearing failures, uplift) to the system level response. These tests, including a full-scale, three-dimensional test of an isolated 5-story steel building on the E-Defense shake table in Miki, Hyogo, Japan, will help fill critical knowledge gaps, validate assumptions regarding behavior and modeling, and provide essential proof-of-concept evidence regarding the importance of isolation technology.

4.3.3 1D and 2D Coupled Bilinear Modeling of Isolation Devices

A bilinear model shown in Fig. 4.7 generally represents the hysteretic behavior of isolation system (Naeim 1999).

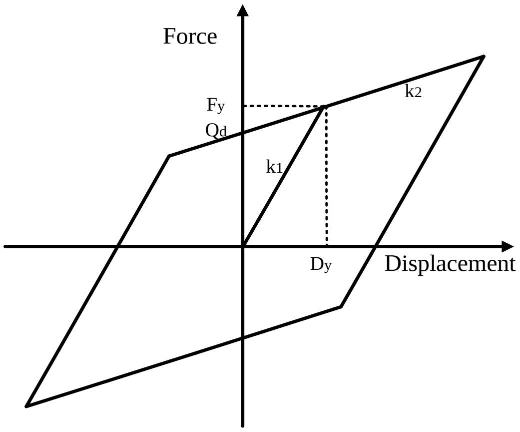

Fig. 4.7 Bilinear force to displacement relation

Kinematic hardening behavior gives a standard stress-strain relationship with a fixed yielding surface. In many metals subjected to cyclic loading, it is experimentally observed that the center of the yield surface experiences a motion in the direction of the plastic flow. This is called the isotropic hardening. A simple phenomenological model that captures the aforementioned effect is constructed by introducing an additional internal variable, denoted by q and called back stress, which defines the location of the center of the yield surface.

The 1D Rate-Independent Plasticity with combined kinematic and isotropic hardening is provided by Simo and Hughes (Simo and Hughes 1997). The elastic stress-strain relation is expressed as $\sigma = E(\varepsilon - \varepsilon^p)$, where ε is the total strain and ε^p is referred to as the *plastic strain;* The flow rule which is the change rate of the plastic strain is defined as: $\dot{\varepsilon}^p = \gamma \, sgn(\sigma - q)$, where $\gamma > 0$ is the absolute value of the slip rate and σ is the applied stress. The isotropic and kinematic hardening laws are expressed by the following equations:

$$\begin{aligned} \dot{q} &= | H \dot{\varepsilon}^p | = \gamma H_{kin} \, sgn(\sigma - q) \\ \dot{\alpha} &= | \dot{\varepsilon}^p | = \gamma \end{aligned} \tag{4.1}$$

where $sgn(\bullet)$ is the sign function. The yield condition is:

$$f(\sigma,q,\alpha) = |\sigma - q| - (\sigma_y + H_{iso}\alpha) \le 0 \tag{4.2}$$

The Kuhn-Tucker condition is:

$$\gamma \ge 0, \quad f(\sigma,q,\alpha) \le 0, \quad \gamma f(\sigma,q,\alpha) = 0 \tag{4.3}$$

The consistency condition is:

$$\gamma \dot{f}(\sigma,q,\alpha) = 0 \quad if \quad f(\sigma,q,\alpha) = 0 \tag{4.4}$$

The tangent elasto-plastic modulus is:

$$\gamma = \frac{E \, sgn(\sigma - q)\dot{\varepsilon}}{E + H_{iso} + H_{kin}} \tag{4.5}$$

The procedure of return mapping algorithm is summarized in the following table:

Table 4.3 Return mapping for combined kinematic and isotropic hardening (from Simo and Hughes book 1998)

```
1. Database at $x \in B$: $\{\varepsilon_n^p, \alpha_n, q_n\}$
2. Given strain field at $x \in B$: $\varepsilon_{n+1} = \varepsilon_n + \Delta\varepsilon_n$
3. Compute elastic trial stress and test for plastic loading
$\sigma_{n+1}^{trial} = E\ (\ \varepsilon_{n+1}\ -\ \varepsilon_n^p\ )\ =\ \sigma_n + E\ \Delta\varepsilon_n$; $\xi_{n+1}^{trial} = \sigma_{n+1}^{trial} - q_n$; $\varepsilon_{n+1}^{p\ trial} = \varepsilon_n^p$; $\alpha_{n+1}^{trial} = \alpha_n$;
$q_{n+1}^{trial} = q_n$; $f_{n+1}^{trial} = |\ \xi_{n+1}^{trial}\ | - (\ \sigma_y + H_{iso}\ \alpha_n\ )$
IF $f_{n+1}^{trial} \leq 0$ THEN
Elastic step: set $(\ )_{n+1} = (\ )_{n+1}^{trial}$ & EXIT
ELSE
Plastic step: Proceed to step 4.
ENDIF
4. Return mapping:
$\Delta\gamma = \dfrac{f_{n+1}^{trial}}{E + H_{iso} + H_{kin}} > 0$
$\sigma_{n+1} = \sigma_{n+1}^{trial} - \Delta\gamma\ E\ sgn\ (\ \xi_{n+1}^{trial}\ )$
$\varepsilon_{n+1}^p = \varepsilon_n^p + \Delta\gamma\ sgn\ (\ \xi_{n+1}^{trial}\ )$
$q_{n+1} = q_n + \Delta\gamma\ H_{kin}\ sgn\ (\ \xi_{n+1}^{trial}\ )$
$\alpha_{n+1} = \alpha_n + \Delta\gamma$
```

The above method is the classical approach to the problem given the yielding strength and the stiffness, and this approach is a stress-strain relationship. To fully define a bilinear behavior, only three out of following five values are required: the zero P-u intercept, Q_D; the pre-yielding stiffness, K_1; the yield displacement, u_y; the yield force, F_y ; and the post-yielding stiffness K_2.

In real structural control practice, a force-displacement relationship is preferred. The following is a brief summary about 1D Rate-Independent Plasticity with Kinematic Hardening (Makris and Zhang 2002).

The elastic force-displacement relation, flow rule, kinematic hardening laws, yielding condition, Kuhn-Tucker condition and consistency condition is summarized as follows:

$$F \ = \ K_1 \ U \ + \ F_p \tag{4.6}$$

$$\dot{U}^{p} \ = \ \gamma \ sgn \ (\ F_p^{n+1} \ ) \tag{4.7}$$

$$\dot{q} \ = \ \gamma \ H_{kin} \ sgn \ (\ \sigma \ - \ q \ ) \tag{4.8}$$

$$\phi(F_p) \ = \ \| F_p \| \ - \ Q_D \leq \ 0 \tag{4.9}$$

$$\gamma \ \geq 0, \quad \phi(F_p) \ \leq 0, \quad \gamma \ \phi(F_p) \ = \ 0 \tag{4.10}$$

$$\gamma \ \dot{\phi}(F_p) \ = \ \gamma \ \frac{F_p^T \cdot \dot{F}_p}{\| F_p \|} = 0 \quad if \quad \phi(F_p) \ = \ 0; \tag{4.11}$$

The return-mapping scheme of bilinear behavior is given in Table 4.4. The physical meaning of variables have been illustrated in Fig. 4.8. F_p stands for the plastic force, *K₁*, *K₂* are the pre- and post- yielding stiffness, and *U* is used for displacement.

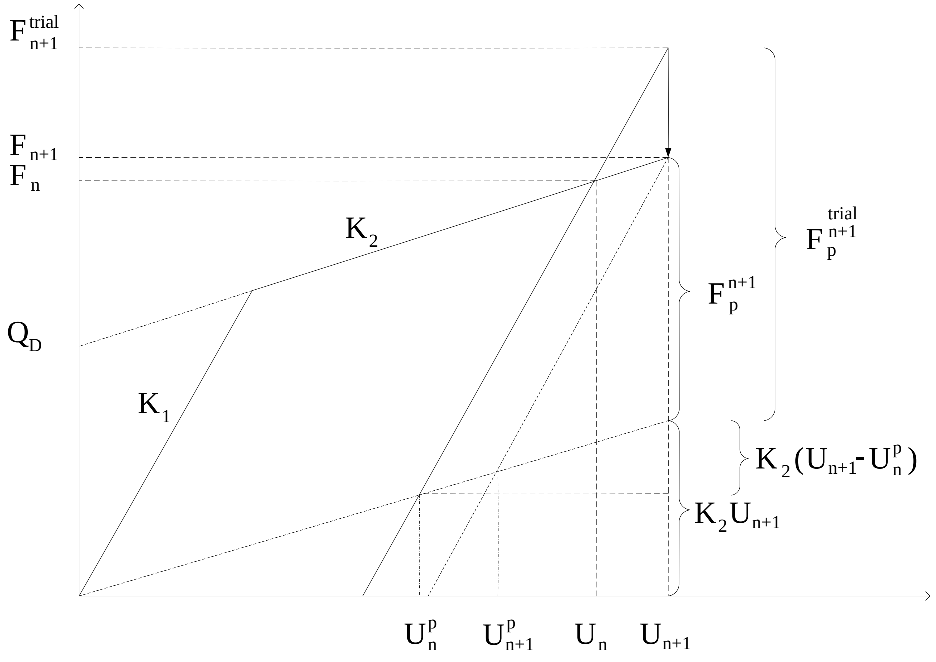

Fig. 4.8 Illustration of bilinear model

Table 4.4 Return mapping procedure for kinematic hardening

```
1. Database at $x \in B:\ \{U_n^p\}$
2. Given displacement field at $x \in B:\ U_{n+1} = U_n + \Delta U_n$
3. Compute elastic trial force and test for plastic loading
$U_{p\ n+1}^{trial} = U_n^p$ ; $F_{p\ n+1}^{trial} = (K_1 - K_2)(U_{n+1} - U_{p\ n+1}^{trial})$ ; $\phi^{trial} = \| F_{p\ n+1}^{trial} \| - Q_D \leq 0$
IF $\phi^{trial} \leq 0$ THEN
    Elastic step: set $(\ )_{n+1} = (\ )_{n+1}^{trial}$ & EXIT
ELSE
    Plastic step: Proceed to step 4.
ENDIF
4. Return mapping:
$\Delta\gamma = \dfrac{\Phi^{trial}}{K_1 - K_2} > 0$
$F_{p\ n+1} = Q_D\ sgn\ (F_{p\ n+1}^{trial})$
$U_{n+1}^p = U_{p\ n+1}^{trial} + \Delta\gamma\ sgn\ (F_{p\ n+1}^{trial})$
5. Calculate force for next step
$F_{n+1} = F_{p\ n+1} + K_2 U_{n+1}$
```

After introduction about 1D bilinear behavior, 2D bilinear behavior with combined hardening law is presented as follows. For a system shown in Fig. 4.9(a), assuming two directional excitation (i.e. x direction and y direction) happens. The x-y directions are orthogonal and the plastic stress/force is coupled in a circular yielding surface, which is $F_p = \sqrt{F_{p\,x}^2 + F_{p\,y}^2}$. This is shown in Fig. 4.9(b).

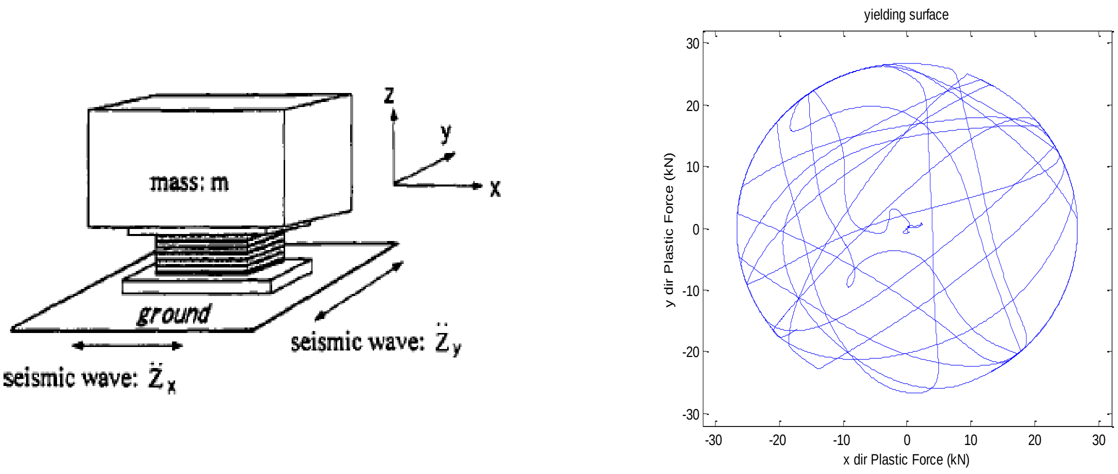

(a) Two directional excitation **(b)** a typical yielding surface of plastic force

Fig. 4.9 Two directional coupled bilinear model

For 2D coupled case, the plasticity rules and conditions are same as 1D case and the return-mapping scheme is summarized as follows:

Table 4.5 Return mapping procedure for 2D kinematic hardening

1. Database at $x \in B: \{U^{p}_{x\,n}, U^{p}_{y\,n}\}$

2. Given displacement field at

$$x \in B: U_{x\,n+1} = U_{x\,n} + \Delta U_{x\,n} \qquad y \in B: U_{y\,n+1} = U_{y\,n} + \Delta U_{y\,n}$$

3. Compute elastic trial force and test for plastic loading

$$U^{trial}_{x\,p\,n+1} = U^{p}_{x\,n} \qquad U^{trial}_{y\,p\,n+1} = U^{p}_{y\,n}$$

$$F^{trial}_{x\,p\,n+1} = (K_1 - K_2)(U_{x\,n+1} - U^{trial}_{x\,p\,n+1}) \qquad F^{trial}_{y\,p\,n+1} = (K_1 - K_2)(U_{y\,n+1} - U^{trial}_{y\,p\,n+1})$$

$$\phi^{trial}_{norm} = \sqrt{F^{trial\;2}_{x\,p\,n+1} + F^{trial\;2}_{y\,p\,n+1}}\;; \qquad \phi^{trial} = \phi^{trial}_{norm} - Q_D$$

IF $\phi^{trial} \leq 0$ THEN

Elastic step: set $(\;)_{n+1} = (\;)^{trial}_{n+1}$

Tangent Matrix = $\begin{bmatrix} K_1 & 0 \\ 0 & K_1 \end{bmatrix}$ & EXIT

ELSE

Plastic step: Proceed to step 4.

ENDIF

4. Return mapping:

$$\Delta\gamma = \frac{\phi^{trial}}{K_1 - K_2} > 0$$

$$F_{x\,p\,n+1} = F^{trial}_{x\,p\,n+1} - \Delta\gamma\ (K_1 - K_2)\ sgn\,(F^{trial}_{x\,p\,n+1})\,;$$

$$F_{y\,p\,n+1} = F^{trial}_{y\,p\,n+1} - \Delta\gamma\ (K_1 - K_2)\ sgn\,(F^{trial}_{y\,p\,n+1})\,;$$

$$U^{p}_{x\,n+1} = U^{trial}_{x\,p\,n+1} + \Delta\gamma\ sgn\,(F^{trial}_{x\,p\,n+1})\,;$$

$$U^{p}_{y\,n+1} = U^{trial}_{y\,p\,n+1} + \Delta\gamma\ sgn\,(F^{trial}_{y\,p\,n+1})$$

$$F_{p\,norm} = \sqrt{F^2_{x\,p\,n+1} + F^2_{y\,p\,n+1}}$$

$$\text{Tangent Matrix} = \begin{bmatrix} K_1 & 0 \\ 0 & K_1 \end{bmatrix} - \frac{K_1 - K_2}{F^2_{p\,norm}} \begin{bmatrix} F^2_{x\,p\,n+1} & F_{x\,p\,n+1} \cdot F_{y\,p\,n+1} \\ F_{x\,p\,n+1} \cdot F_{y\,p\,n+1} & F^2_{y\,p\,n+1} \end{bmatrix}$$

5. Calculate force for next step

$$F_{x\,n+1} = F_{x\,p\,n+1} + K_2 U_{x\,n+1} \qquad F_{y\,n+1} = F_{y\,p\,n+1} + K_2 U_{y\,n+1}$$

Along with this study, the 2D coupled section behavior has been developed as an OpenSees section called Bisec2. The Bisec2 command is used to construct a bidirectional object, which is two-dimensional generalization of one-dimensional elasto-plastic model with linear hardening. The material modeling method and its variables is demonstrated in Table 4.6.

Table 4.6 OpenSees modeling of bidirectional bilinear coupled section model

section Bisec2 $secTag $K1 $QD $K2

$secTag	Unique section object integer tag
$K1	the elastic stiffness for both directions
$QD	the yielding strength illustrated in Fig. 4.8
$K2	the post yielding stiffness

This model is well tuned up and can be useful for 3D models such as studying torsional behavior of an unsymmetrical building.

4.3.4 1D and 2D Coupled Bouc-Wen Model for Isolation Devices

The uni-axial Bouc-Wen model, originally proposed by Bouc (1971) and subsequently extended by Wen (1975, 1976), is used extensively in random vibration studies of inelastic systems. During this work, 1D Bouc-Wen model called BoucWenS1D has also been developed for OpenSees platform. Casciati (1989) considered the Bouc-Wen model as a smoothed form of the rate independent plasticity model and generalized it to a bidirectional case. The Bouc-Wen model is very versatile for modeling various seismic protection devices, such as sliding, elastomeric, or lead-rubber bearings. As the numerical computation becoming popular these days, the Bouc-Wen model has received large application in the structure-modeling field. The material modeling method and its variables is demonstrated in Table 4.7. Compared with the existing Bouc-Wen model in OpenSees, the developed model allows the user to specify the yielding displacement whereas the existing model always assume the value to be 1.

Table 4.7 OpenSees modeling of 1D Bouc-Wen material model

uniaxialMaterial BoucWenS1D $matTag $alpha $ko $n $Ao $gamma $beta $Ep

$matTag	Unique material object integer tag
$alpha	the ratio of the post-yielding to elastic stiffness
$ko	elastic stiffness
$n	defines how smooth the curve will turn when it yields
$Ao	Ao, beta and gamma effects the shape and define BoucWen nonlinear function: $\dot{z} = \frac{A_o\dot{\varepsilon} - \{\beta \mid \dot{\varepsilon} \mid z \mid z \mid^{n-1} + \gamma\dot{\varepsilon} \mid z \mid^{n}\}}{E_p}$
$gamma	
$beta	
$Ep	Is the strain value when the first yielding happens

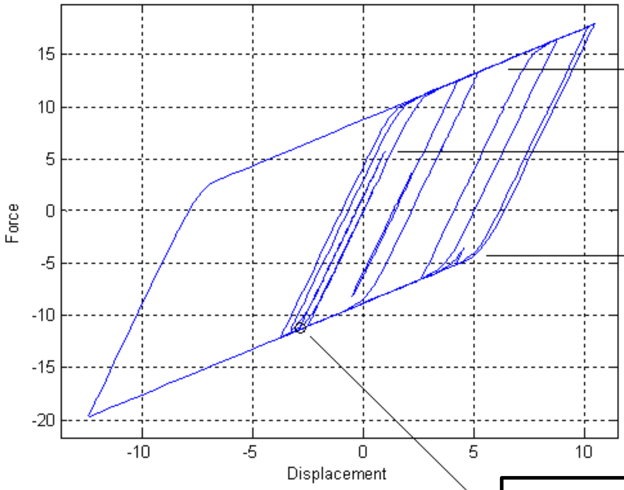

Post-yielding stiffness *αko*

Pre-yielding stiffness *ko*

n defines how smooth the curve turns when it yields

System yields at **displacement** *Ep or -Ep*

Fig. 4.10 A typical hysteretic behavior for 1D Bouc-Wen model

The stress is defined as the sum of a linear part and a hysteretic part:

$$\sigma = \alpha k_o \varepsilon + (1-\alpha) k_o E_p z \tag{4.12}$$

In the above, ε is the strain, *z* represents the hysteretic deformation, k_o is the elastic stiffness and α is the ratio of the post-yielding to elastic stiffness. To accommodate degradation, Baber and Noori (1985) formulated the rate of hysteretic deformation in the form:

$$\dot{z} = \frac{A_o \dot{\varepsilon} - \{\beta |\dot{\varepsilon}| z |z|^{n-1} + \gamma \dot{\varepsilon} |z|^n\}}{E_p} \tag{4.13}$$

where β, γ, and *n* are parameters that control the shape of the hysteretic loop, while *Ao* is given. E_p defines the strain where it starts to yield. The model may be rewritten as

$$\dot{z} = \frac{A_o - |z|^n [\beta \,\mathrm{sgn}(\dot{\varepsilon} z) + \gamma]}{E_p} * \dot{\varepsilon} = \frac{\partial z}{\partial \varepsilon} \frac{\partial \varepsilon}{\partial t} \tag{4.14}$$

This leads to the following expression for the continuum tangent (not the algorithmically consistent tangent):

$$k = \frac{\partial \sigma}{\partial \varepsilon} = \alpha k_o + (1-\alpha) k_o \frac{A_o - |z|^n \, [\beta \, \mathrm{sgn}(\dot{\varepsilon} z) + \gamma]}{E_p} \tag{4.15}$$

It is seen that the stiffness is composed of a linear term and a hysteretic contribution.

One must first derive incremental response equations to make the governing equations computational implementable. From the above equations the stress at time $t_{(n+1)}$ is obtained as:

$$\sigma_{(n+1)} = \alpha k_o \varepsilon_{(n+1)} + (1-\alpha) k_o E_p z_{(n+1)} \tag{4.16}$$

The rate equation for z is next discretized by a Backward Euler solution scheme. For a first-order ordinary differential equation of the form $\dot{y} = f(y(t))$, the scheme reads $y_{(n+1)} = y_n + \Delta t \, f(y(n+1))$. Applied to Eq. (4.13) the following is obtained:

$$z_{(n+1)} = z_{(n)} + \Delta t \, \frac{A_o - |z_{(n+1)}|^n \, [\gamma + \beta \, \mathrm{sgn}(\frac{(\varepsilon_{(n+1)} - \varepsilon_{(n)})}{\Delta t} z_{(n+1)})]}{E_p} \frac{(\varepsilon_{(n+1)} - \varepsilon_{(n)})}{\Delta t} \tag{4.17}$$

It is seen that Δt cancels from the equation, yielding a nonlinear equation in $z_{(n+1)}$. A Newton scheme of the form $x_{m+1} = x - f(x_m) / f'(x_m)$ to solve a general nonlinear equation $f(x) = 0$ may be used to solve for $z_{(n+1)}$ in Eq. (4.17). The procedure implemented in OpenSees to compute the stress for a given strain (given $\varepsilon_{(n+1)}$ to get $\sigma_{(n+1)}$) can now be summarized as follows:

Table 4.8 Computing the stress for a given strain

1. While ($|z_{(n+1)}^{old} - z_{(n+1)}^{new}| > tol$)

(a) Evaluate function *f*(*z*(*n*+1)):

$$\psi = \gamma + \beta \,\mathrm{sgn}((\varepsilon_{(n+1)} - \varepsilon_{(n)}) z_{(n+1)}) \tag{4.18}$$

$$\phi = A_o - |\, z_{(n+1)} \,|^n \,\psi$$

$$\mathrm{f}(\mathrm{z}_{(\mathrm{n+1})}) = \mathrm{z}_{(\mathrm{n+1})} - \mathrm{z}_{(\mathrm{n})} - \frac{\phi}{E_p}(\varepsilon_{(n+1)} - \varepsilon_{(n)}) \tag{4.19}$$

(b) Evaluate function derivatives (prime denotes derivative with respect to *z*(*n*+1)):

$$\phi' = -n \,|\, z_{(n+1)} \,|^{n-1} \,\mathrm{sgn}(z_{(n+1)})\psi \tag{4.20}$$

$$\mathrm{f}\,'(\mathrm{z}_{(\mathrm{n+1})}) = 1 - \frac{\phi'}{E_p}(\varepsilon_{(n+1)} - \varepsilon_{(n)}) \tag{4.21}$$

(c) Obtain trial value in the Newton scheme:

$$z^{new}_{(n+1)} = z_{(n+1)} - \frac{f(z_{(n+1)})}{f\,'(z_{(n+1)})} \tag{4.22}$$

(d) Update *z*(*n*+1) (and store the old value for the convergence check):

$$z^{old}_{(n+1)} = z_{(n+1)} \text{ and } z_{(n+1)} = z^{new}_{(n+1)} \tag{4.23}$$

2. Compute stress:

$$\sigma_{(n+1)} = \alpha k_o \varepsilon_{(n+1)} + (1-\alpha) k_o E_p z_{(n+1)} \tag{4.24}$$

In addition to the stress, the material algorithm must return the current algorithmically consistent tangent. This tangent is used in the global scheme to compute the nonlinear structural response. One needs to derive the tangent $\partial\sigma_{(n+1)} / \partial\varepsilon_{(n+1)}$ by utilizing the formulation by which the stress $\sigma_{(n+1)}$ is actually computed. Hence, the equations used in the Newton scheme must be differentiated with respect to $\varepsilon_{(n+1)}$. It turns out that the equation for $\partial \mathrm{z}_{(n+1)} / \partial\varepsilon_{(n+1)}$ is linear. The resulting implementable equations for the algorithmically consistent tangent read as follows:

Table 4.9 Implementable equations for the algorithmically consistent tangent for Bouc-Wen model

1. Compute auxiliary parameters:

$$\psi = \gamma + \beta \operatorname{sgn}((\varepsilon_{(n+1)} - \varepsilon_{(n)}) z_{(n+1)}) \tag{4.25}$$

$$\phi = A_o - | z_{(n+1)} |^n \, \psi \tag{4.26}$$

2. Compute $\frac{\partial z_{(n+1)}}{\partial \varepsilon_{(n+1)}}$ and tangent ((a) is more stable than (b)):

$$\frac{\partial z_{(n+1)}}{\partial \varepsilon_{(n+1)}} = \frac{E_p | z_{(n+1)} | \{A_o | z_{(n+1)} | - | z_{(n+1)} |^n [| z_{(n+1)} | + n(z_{(n)} - z_{(n+1)}) \operatorname{sgn}(z_{(n+1)}) \psi}{\{E_p | z_{(n+1)} | + (\varepsilon_{(n+1)} - \varepsilon_{(n)}) n | z_{(n+1)} |^n \operatorname{sgn}(z_{(n+1)}) \psi\}^2}$$

(4.27) from (4.22)

$$\frac{\partial z_{(n+1)}}{\partial \varepsilon_{(n+1)}} = \frac{\phi}{E_p}$$ (4.28) from (4.17)

$$k = \frac{\partial \sigma_{(n+1)}}{\partial \varepsilon_{(n+1)}} = \alpha k_o + (1-\alpha) k_o E_p \frac{\partial z_{(n+1)}}{\partial \varepsilon_{(n+1)}} \tag{4.29}$$

For the two-direction motion input of our building model, a coupled Bouc-Wen model is developed by Casati (1989). The F_p rate equation can be written as:

$$\dot{\mathbf{F}}_p = (K_1 - K_2)\dot{\mathbf{u}} - \left((K_1 - K_2) \frac{\mathbf{F}_p^T}{\| \mathbf{F}_p \|^2} \right) \mathbf{F}_p \mathbf{H}(\phi) \mathbf{H}(\dot{\phi}) \tag{4.30}$$

where $H(\phi)$ is the Heaviside function. $H(\phi)$ can be approximated with a smoothed function:

$$\mathbf{H}(\phi) = H(\| \mathbf{F}_p \| - Q_D) \approx \frac{\| \mathbf{F}_p \|^\eta}{Q_D^\eta} \tag{4.31}$$

where $\eta > 0$ describes the smoothness of the transition and $H(\dot{\phi})$ is defined as:

$$\mathbf{H}(\dot{\phi}) = \mathbf{H}(\mathbf{F}_p^T \mathbf{F}_p) = \frac{1 + \operatorname{sgn}(\mathbf{F}_p^T \dot{\mathbf{u}})}{2} \tag{4.32}$$

Therefore, the rate of plastic force is approximated with:

$$\dot{\mathbf{F}}_p = (K_1 - K_2)\dot{\mathbf{u}} - \frac{\| \mathbf{F}_p \|^{\eta-2}}{Q_D}(K_1 - K_2)(\mathbf{F}_p^T\dot{\mathbf{u}})\frac{1+\operatorname{sgn}(\mathbf{F}_p^T\dot{\mathbf{u}})}{2}\mathbf{F}_p \tag{4.33}$$

Defining a dimensionless plastic variable Z such that $F_p = Q_D Z$ and uni-axial "yield" displacement, $U^Y = Q_D / (K_1 - K_2)$, Eq. (4.33) becomes:

$$\dot{\mathbf{Z}}\mathbf{u}^Y = \dot{\mathbf{u}} - \| \mathbf{Z} \|^{\eta-2} *(\mathbf{Z}^T\dot{\mathbf{u}})\left(\frac{1}{2}+\frac{1}{2}\operatorname{sgn}(\mathbf{Z}^T\dot{\mathbf{u}})\right)\mathbf{Z} \tag{4.34}$$

Eq. (4.34) can be written in a more general form:

$$\dot{\mathbf{Z}}\mathbf{u}^Y = A\dot{\mathbf{u}} - \| \mathbf{Z} \|^{\eta-2} *(\mathbf{Z}^T\dot{\mathbf{u}})[\gamma + \beta\operatorname{sgn}(\mathbf{Z}^T\dot{\mathbf{u}})]\mathbf{Z} \tag{4.35}$$

where γ and β are dimensionless quantities that control the shape of the hysteretic loop. In this study, A = 1 and $\gamma = \beta = 0.5$. This results in the bound of variable Z as $\| Z \| \le 1$. By using Eq. (4.31) and $Q_D / U^Y = (K_1 - K_2)$, the rate of restoring force can be written as:

$$\dot{\mathbf{P}} = K_2\dot{\mathbf{u}} + \mathbf{F}_p = \{K_2 + A(K_1 - K_2) - (K_1 - K_2)\| \mathbf{Z} \|^{\eta-2}[\gamma + \beta\operatorname{sgn}(\mathbf{Z}^T\dot{\mathbf{u}})]\left(\mathbf{Z}\mathbf{Z}^T\right)\}\dot{\mathbf{u}} \tag{4.36}$$

$$\text{i.e. } \frac{\partial \mathbf{P}}{\partial \mathbf{u}} = K_2 + A(K_1 - K_2) - (K_1 - K_2)\| \mathbf{Z} \|^{\eta-2}[(\gamma + \beta\operatorname{sgn}(\mathbf{Z}^T\dot{\mathbf{u}})]\left(\mathbf{Z}\mathbf{Z}^T\right) \tag{4.37}$$

Therefore, the tangent stiffness matrix is:

$$K = \begin{bmatrix} \frac{\partial \mathbf{P}}{\partial \mathbf{u}} & -\frac{\partial \mathbf{P}}{\partial \mathbf{u}} \\ -\frac{\partial \mathbf{P}}{\partial \mathbf{u}} & \frac{\partial \mathbf{P}}{\partial \mathbf{u}} \end{bmatrix} \tag{4.38}$$

Different isolation devices possess different Bouc-Wen behaviors in terms of transition smoothness parameter η. The transition smoothness parameter is set to be two for elastomeric bearings, four for lead rubber bearings and eight for friction pendulum bearings. Fig. 4.11 illustrates the dynamic response for the three types of isolations under Kobe/KGM motion.

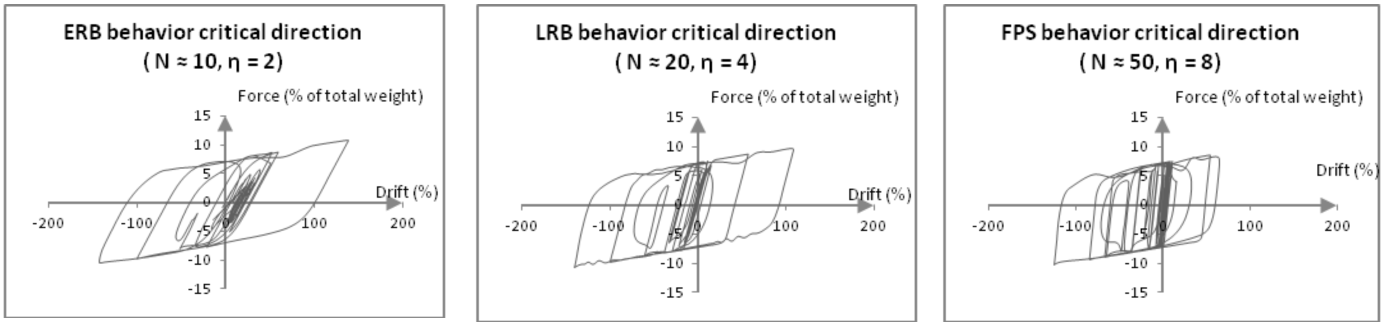

Fig. 4.11 Dynamic behaviors for different isolation system in major direction

4.4 Negative Stiffness Device

4.4.1 Introduction

Recent studies show that the Negative Stiffness Device (NSD) may serve as an innovative generation of adaptive stiffness and damping devices (ASD) that inherently benefits civil structures.

More than 50 years ago, the pioneering concept of negative stiffness was proposed and realized in vibration isolation systems (Molyneux 1957). Since then the application of NSD has been used but limited to vibration isolation of small, highly sensitive equipment and of seats in automobiles (Lee *et al.* 2007). For larger structures such as buildings and bridges, Reinhorn *et al.* (2005) proposed the concept of retrofitting them by weakening their stiffness and by simultaneously adding supplementary viscous damping to reduce the structural acceleration and horizontal drifts. To better improve the performance by reducing inelastic action, Nagarajaiah *et al.* (2010) and Pasala *et al.* (2011) proposed the novel design of negative stiffness device (NSD) that will provide a negative force onto the structure that is in the same direction as the ground motion over a specified displacement range. This study investigates the behavior of the negative stiffness system, which shifts the yielding away from the main structural system. The proposed NSD system eventually leads to the idea of apparent weakening that ensures structural stability at different displacement amplitudes.

4.4.2 The Proposed Negative Stiffness System

The proposed NSD system model this study investigates is based on the improved "true" NSD system Sarlis *et al.* (2012) introduced, in which a highly compressed machined spring develops the force in the direction of motion. Besides the pre-compressed spring, the proposed design includes a double chevron self-containing system that can resist the preload in the compressed spring and prevent the transfer of the vertical component of the preload to the structure. In addition, a gap spring assembly system is placed at the bottom that provides a predefined initial displacement after which the negative force is triggered. The NSD is implemented within an Adaptive Negative Stiffness System (ANSS), e.g. a combination of NSD and a viscous damper. The supplementary viscous damping devices parallel to the NSD serves to limit the displacement within the demand.

Sarlis *et al.* (2012) described the details in design and proposed an analytical model of NSD according to the design. The detailed description of the device and its mathematical expressions for is presented in the original paper; however, a brief summary of the system is included here for completeness. Fig. 4.12 shows the photo of designed NSD when it is at rest and being tested. To further explain the mechanism of the device, Fig. 4.13 shows schematically the un-deformed and deformed shape of the system. The two parts of the chevron bracer, the top "V" shape and the bottom "Λ" shape, are crossed with each other. Both point A and point E are pin connected to the top part of the bracer. When a motion happens, the lever AB imposes a displacement to point B, which causes the pivot plate BCD to rotate about the point C. The lever is axially rigid and its rigid body rotation can be neglected such that the horizontal displacement at point A is equal to the displacement at point B. Hence, due to the kinematics of points D and E, the pre-compressed spring rotates and its force facilitates the ground motion rather than opposing it. The motion of point D relative to point E is magnified by comparison to the motion of point A by the ratio of the lever of the pivot plate (DC to CB) and by additional factor due to combination of movement of point E (same as the displacement at A). The spring exhibits its minimum length when the device is un-deformed. As the device deforms horizontally, the spring extends, its pre-compression force reduces and its angle of inclination increases. The Gap Spring Assembly (GSA) system constraining the bottom side of the top part of the bracer eliminates the NSD effect within a small drift range.

(a) Tested NSD frame at rest

(b) Tested NSD frame undergoing a displacement input

Fig. 4.12 Tested NSD specimen

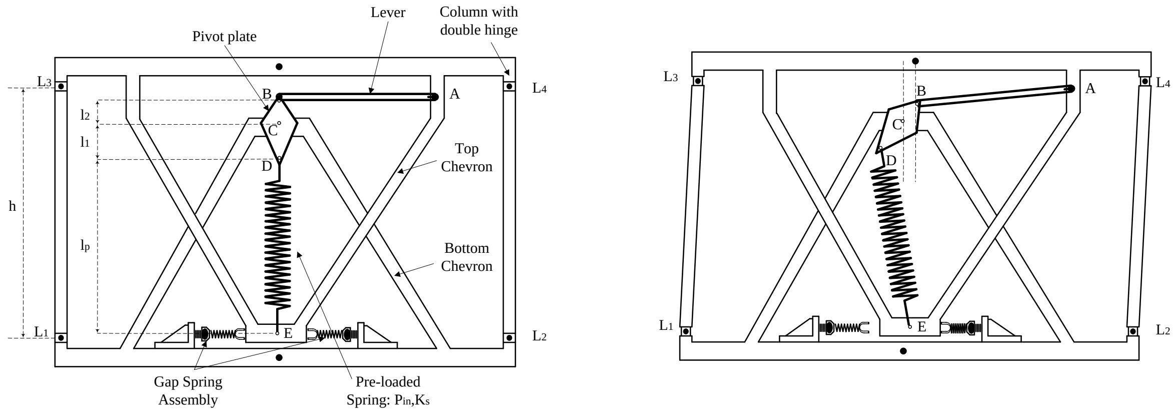

(a) Tested NSD frame at rest

(b) Tested NSD frame undergoing a displacement input

Fig. 4.13 Details and the mechanism of the NSD design

To provide the numerical expression for the NSD force, a detailed NSD center mechanism with its deformed shape is illustrated in Fig. 4.14. Define l_2 as the length of the pivot plate between point C and point B, l_1 is the length between point C and point D. Then, the relation of the displacement is: $u_B = u_E = -u_D l_2 / l_1 = u$. Define θ_s as the inclination angle of the spring and define θ_p as the angle of the pivot plate with respect to vertical. Expressions for angles θ_s and θ_p are given by: $\theta_s = \sin^{-1}[u(1 + l_2 / l_1) / l_s]$ and $\theta_p = \sin^{-1}(u / l_2)$.

The pre-compressed spring force F_s is given by: $F_s = P_{in} - K_s(l_s - l_p)$, where P_{in} is the pre-compression force of the vertical spring and should have a positive value and K_s is the stiffness of the pre-compressed vertical spring, l_s is the spring length at the deformed configuration, and l_p is the length of the spring when the NSD is un-deformed.

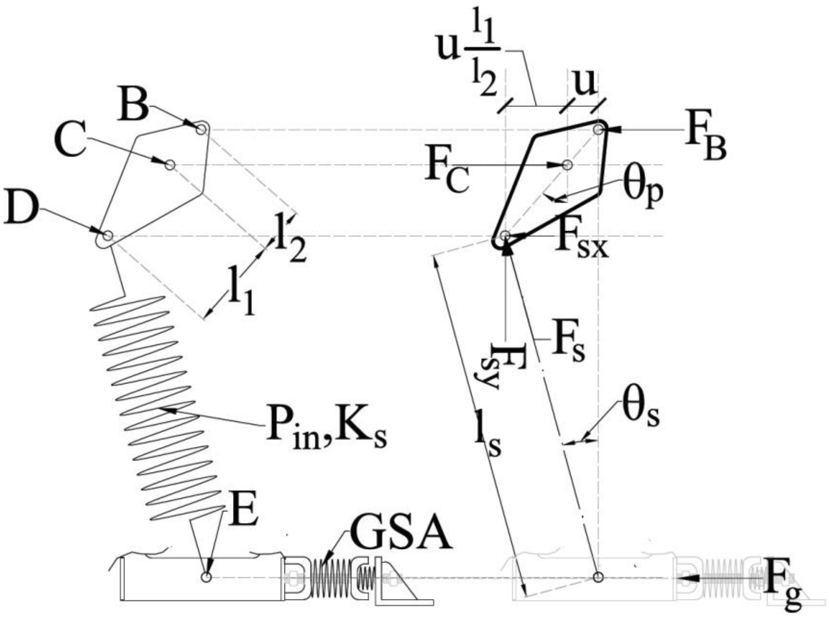

Fig. 4.14 Illustration of the NSD center mechanism

The spring force-displacement relation is shown in Fig. 4.15(a) and the formula for the NSD force is derived and expressed in Eq. (4.39):

$$F_{NSD} = -F_C + F_g - F_s \cos\theta_s (u/h) \tag{4.39}$$

$$= -\left(\frac{P_{in} + K_s l_p}{l_s} - K_s\right)\left(\frac{l_1}{l_2}\right)\left(2 + \frac{l_p + l_1}{\sqrt{l_p{}^2 - u^2}} + \frac{l_2}{l_1}\frac{h + l_p + l_1 - (l_1/l_2)\sqrt{l_2{}^2 - u^2}}{h}\right)u + F_g$$

where *h* is the height of the double-hinged column. l_s is given as:

$$l_s = \sqrt{\left(l_p + l_1 - l_1\sqrt{1-(\frac{u}{l_2})^2}\right)^2 + u^2\left(1 + \frac{l_2}{l_1}\right)^2} \tag{4.40}$$

where F_g is the GSA force. Fig. 4.15(b) shows the GSA force-displacement relationship. One could notice that the GSA behaves in a linear elastic manner within a designed range of displacement u'_y and stays at a constant magnitude after the displacement. The GSA is designed such as to cancel the negative force generated by the compression spring within the small displacement range $|u| \le u_y'$, which serves to control the onset of the NSD system.

For most practical implementations, one could assume that $h \approx l_p + l_1 + l_2$. Therefore, Eq. (4.39) can be reduced to:

$$F_{NSD} = -\left(\frac{P_{in} + K_s l_p}{l_s} - K_s\right)\left(\frac{l_1}{l_2}\right)\left(2 + \frac{l_2}{l_1} + \frac{l_p + l_1}{\sqrt{l_p^{\,2} - u^2}}\right)u + F_g \tag{4.41}$$

The negative stiffness generated by the NSD in the absence of the gap spring assembly can then be calculated as that force divided by displacement *u*. The NSD stiffness is expressed as:

$$K_{NSD}^{eff} = -\left(\frac{P_{in} + K_s l_p}{l_s} - K_s\right)\left(\frac{l_1}{l_2}\right)\left(2 + \frac{l_2}{l_1} + \frac{l_p + l_1}{\sqrt{l_p^{\,2} - u^2}}\right) \tag{4.42}$$

The component force-displacement relation is shown in Fig. 4.15(d).

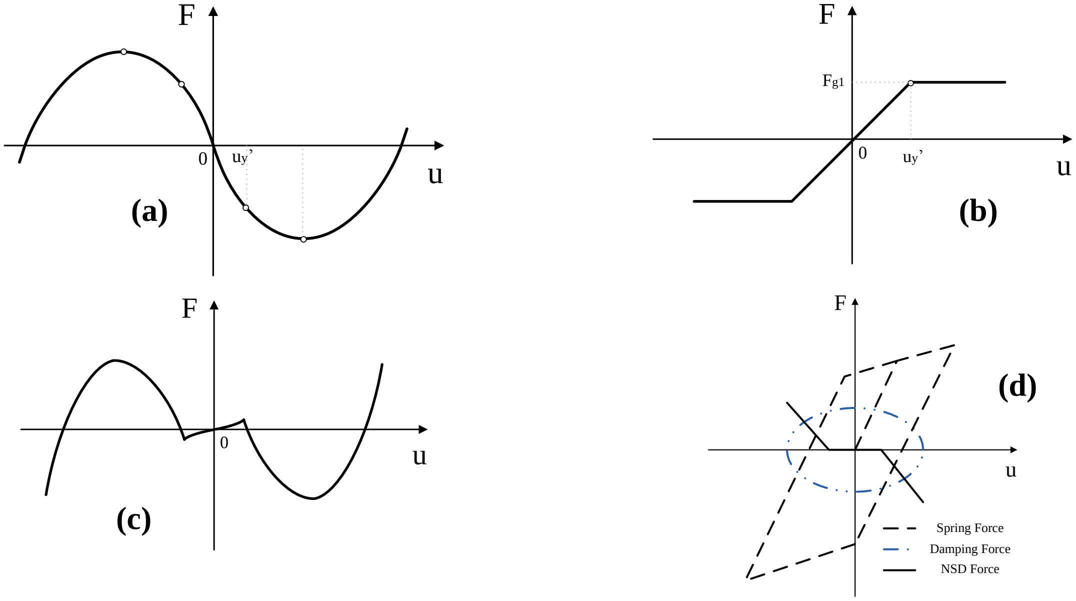

Fig. 4.15 Force displacement characteristics of (a) pre-compressed spring; (b) nonlinear elastic spring (GSA); (c) NSD system; (d) System force-displacement relationship at component level

The above expressions produce a force displacement illustrated in Fig. 4.15(c). The NSD behaves elastically that is fully defined by a series of physically meaningful variables such as $P_{in}, K_s, l_p, l_1, l_2, k_{s1}, k_{s2}$. In the next section, an equivalent model with less parameter to characterize the NSD behavior is proposed such that one could characterize the NSD behavior in a simpler manner. In addition, the presented reduction of parameters has negligible error. The systematic parametric analyses in this study provide a clear understanding of the NSD behavior based on the presented NSD model.

4.4.3 Four Different Stages for NSD System

The equations presented in the previous section were summarized from the mechanical properties of the NSD system. The expression of the negative stiffness force includes many parameters that are physically obtained from the geometry of the design such as $P_{in}, K_s, l_p, l_1, l_2, k_{s1}, k_{s2}$, etc. All of these parameters as a whole define a negative stiffness system. The NSD force-displacement relationship modeled by the aforementioned comprehensive model is plotted as follows in Fig. 4.16:

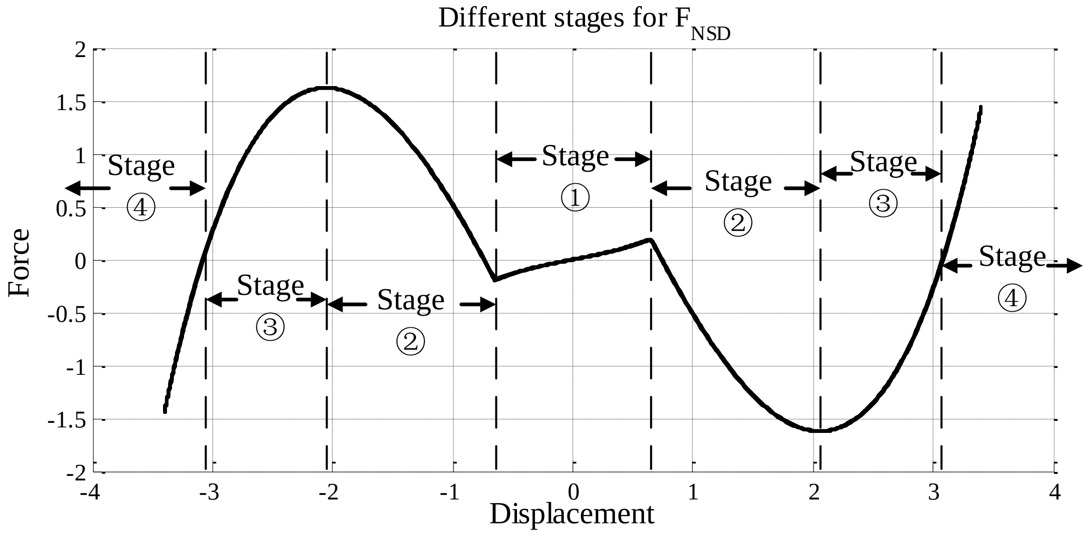

Fig. 4.16 Different stages for NSD system

This study categorizes the NSD response into four different stages (shown in Fig. 4.16): Stage one starts when system is at rest and covers the displacement range smaller than the gap width. The device moves together with the structure with minimum force applied onto the system. For this stage, the NSD could be considered inactive while only a very small positive stiffness is provided by the system. Stage two happens when the system displacement exceeds the gap length and engages the pre-compressed spring. Negative force is introduced to the system since this stage, which pushes the structure in the direction of its displacement. The gap assembly system extends the activation of the negative stiffness force to this stage so that forces transferred on the superstructure are reduced. Stage three happens when the negative stiffness gradually starts fading until the compressed spring is relaxed to its natural length. This characteristic helps to eliminate tensional effects and prevents further negative force at an excessive displacement level. Stage four corresponds to the case when the spring eventually becomes positive when huge horizontal displacement occurs. The stage that the spring reaches positive stiffness is defined as stiffening effect of NSD that happens for earthquakes beyond the maximum considered earthquake where NSD can act as displacement restrainer. However, the cost to reduce the displacement is to increase the system internal force rapidly. The system internal force / absolute acceleration will be easily doubled or tripled within short displacement range after this stage is reached, which might lead to the damage of NSD incorporated system. Further study about this stage will be discussed later in chapter 6.

4.4.4 Numerical Model for NSD System with Reduced Parameters

From the above introduction, one could find the aforementioned numerical model from Eq. (4.39) to Eq. (4.42) physically depicts the designed mechanism with a serious of variable such as $P_{in}, K_s, l_p, l_1, l_2, k_{s1}, k_{s2}$. This study names such model as the physical model where each of these parameters has physical meanings related with NSD behavior. However, the fact that too many parameters are coupled in the equation impedes the parametric study of the NSD system. Based on the demand, this study proposes a "cleaner" model with fewer variables that are connected with the characteristics of the tested NSD force-displacement response. The model would have less parameters and its behavior should match that of the given model. With a trial and error process, a cubic function model was developed and its equations are given as:

$$F_{NSD} = \begin{cases} a\ (x - x_0)^3 + c\ (x - x_0) & x > x_{neg} \\ a\ (x + x_0)^3 + c\ (x + x_0) & x < -x_{neg} \\ a\ x^3 - \dfrac{c}{8}\ x & -x_{neg} < x < x_{neg} \end{cases}; \tag{4.43}$$

In Eq. (4.43), four parameters are needed: a, c, x_0, and x_{neg}. x_0 defines the transition of stage one and two when negative stiffness starts as shown in Fig. 4.19. The displacement x_0 is the threshold when NSD produces zero force and it is slightly different from x_{neg}, which remarks the horizontal displacement where the maximum gap length is reached (NSD engaged). Hence, x_{neg} can be computed by solving the equation: $a\ (x - x_0)^3 + c\ (x - x_0) = a\ x^3 - c\ x / 8$. Therefore, there are only three parameters, i.e. a, c, x_0, which are coefficients and variables for the cubic function that helps fully characterize the behavior of the NSD system. This study names such model as the cubic model.

Assuming the original structural system is a bilinear system, one could define D_y as the system yielding displacement, and Q_D is the characteristic strength of the system, which is given as D_y (K_1-K_2), where K_1 and K_2 are the pre- and post- yielding stiffness. To compute a, c, x_0, the following expressions are given:

$$a = \sqrt{\frac{27}{4}} \frac{\beta^- Q_D}{\left[(\gamma^- - \delta^-) D_y\right]^3},$$

$$c = -\sqrt{\frac{27}{4}} \frac{\beta^- Q_D}{(\gamma^- - \delta^-) D_y},$$

$$x_0 = \delta^- D_y \tag{4.44}$$

Eq. (4.44) establishes a link from the variables a, c, and x_0 to δ^-, β^-, and γ^- that are directly related with design criteria of the NSD system. To make NSD best effective, one should design x_0 such that it is proportional (δ^- times) to the system yielding displacement D_y. β^- is the ratio of the peak amplitude for the NSD to the Q_D of the bilinear system, which is related to the capacity of the pre-compressed spring. x_r defines the relaxation length, where the NSD system goes from stage three to stage four. After the displacement x_r, the spring will be in tension and is not a negative stiffness spring anymore. When designing NSD, one could assume that x_r is usually proportional (γ^- times) to the system yielding displacement, i.e.

$$x_r = \gamma^- D_y = \sqrt{-c / a} \tag{4.45}$$

Fig. 4.17 gives a clear picture of different displacement levels x_{neg}, x_0, x_{cr}, x_r. The variable x_{cr} is the critical displacement when the maximum NSD force is reached and it is expressed as: $x_{cr} = x_0 + \sqrt{-c/(3a)}$. To sum up, this study defines three terms that fully characterizes the NSD system, i.e. $x_o^- = \delta^- D_y$, $Q^- = \beta^- Q_D$, and $x_r = \gamma^- D_y$. This means providing the set [δ^- , β^- , γ^-] or the set [x_o^-, Q^-, x_r] can fully define a given NSD system for a bilinear system.

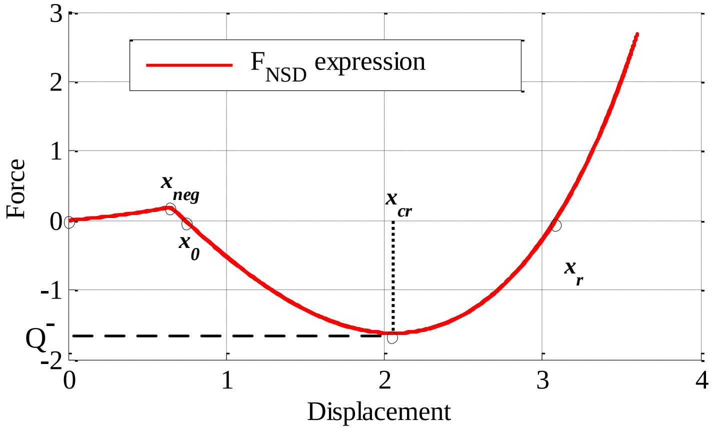

Fig. 4.17 Definitions for x_{neg}, x_0, x_{cr}, x_r. x_{cr} for the cubic NSD model

A further study of the system has been performed in chapter 6, where a comprehensive dimensional study shows the effectiveness of the proposed system. Also, recommendations for the design of NSD system are also provided.

4.5 Self-centering Device

For moderately strong or strong earthquakes, the building structures may behave inelastically resulting in cracks or residual deformations of the structural members. To address such drawback of traditional yielding systems, research efforts have developed new earthquake-resistant systems called self-centering (SC) systems with the potential to eliminate residual drifts and inelastic deformations under strong earthquakes. SC systems exhibit a softening flag-shaped force-drift behavior due to: (1) separations developed in structural interfaces (e.g., beam-to-column connections); (2) elastic pre-tensioning elements (e.g., high strength steel tendons); and (3) energy dissipation elements (EDs: friction-based, yielding or viscous) which are activated when separation in structural interfaces initiates. The most recent self-centering devices are realized by the application of shape memory alloys (SMA) materials, which exhibit stable flag-shaped hysteresis and have been proved useful for seismic hazard mitigation for building systems.

SMA-based devices have been studied by a large number of researchers for vibration control of building structures (Clark *et al*. 1995; Krumme *et al.* 1995; Higashino and Aizawa 1996; Aizawa *et al.* 1998; Salich *et al.* 2001; Xue and Li 2007; Zuo *et al.* 2008; Ma and Yam 2011). In 2005, Han *et al.* developed an SMA damper that can simultaneously work in tension, compression, and torsion. The damper utilizes super-elastic NiTi wires that are subjected to tensile strains for all loading cases. To the verify effectiveness of the damper for tensile, compressive, and torsional motion, analytical and experimental studies were carried out on three reduced-scale dampers.

The Basilica of San Francesco in Assisi, Italy is another case when SMA devices are implemented. The 1997 Umbria-Marche earthquake severely damage the building, which left the main challenge to restore the building to an adequate safety level, while maintaining the original concept of the structure. In order to reduce the seismic forces transferred to the tympanum, a connection between the tympanum and the roof was created using super-elastic SMAs (Fig. 4.18). The SMA devices have demonstrated different structural properties for different horizontal forces. Under low horizontal forces, they are stiff and they bear insignificant displacements; for cases when horizontal drifts are large, such as an earthquake, their stiffness reduces for controlled displacements of the masonry walls; in addition, under extreme intense horizontal loads, their stiffness increase to prevent collapse.

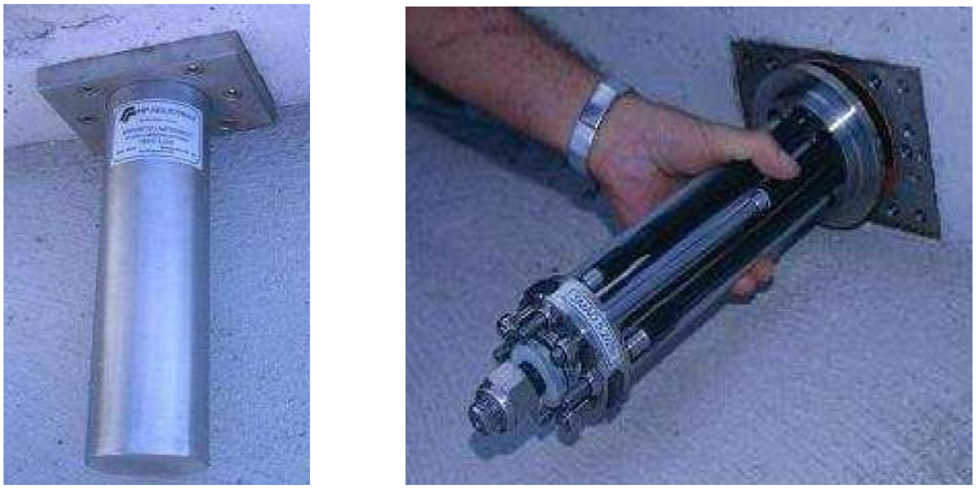

Fig. 4.18 Seismic retrofit of the Basilica of San Francesco in Assisi: particular of the SMA device

In 2011, Ozbulut *et al.* reviewed the SMA material, which introduces in detail about the shape memory alloys and their mechanical properties including strain rate effects, temperature effects, and corrosion and aging. The same article also listed some existing applications of SMA system against earthquakes.

Fugazza (2013) presented the uni-axial constitutive model for pseudo-elastic SMAs. In this study, a brief summarization of such model is provided. The model is a modification of the one proposed by Auricchio and Sacco (1997), which is capable of describing the material behavior under arbitrary loadings such as those involved in seismic excitations, where the response is mainly composed by sub-hysteresis loops internal to the main one associated with complete phase transformations. The model formulation, developed in the small deformation regime, relies on the assumption that the relationship between stresses and strains is represented by a series of straight lines whose form is determined by the extent of the transformation experienced. Further assumptions made are that no strength degradation occurs during cycling and that austenite and martensite branches have the same modulus of elasticity.

4.5.1 Time-continuous Model

The study assume to work with one scalar internal variable, ξ_S, representing the martensite fraction, and with two processes which may produce its variations: the conversion of austenite into martensite ("A to M"), and the conversion of martensite into austenite ("M to A"). (Fig. 4.19)

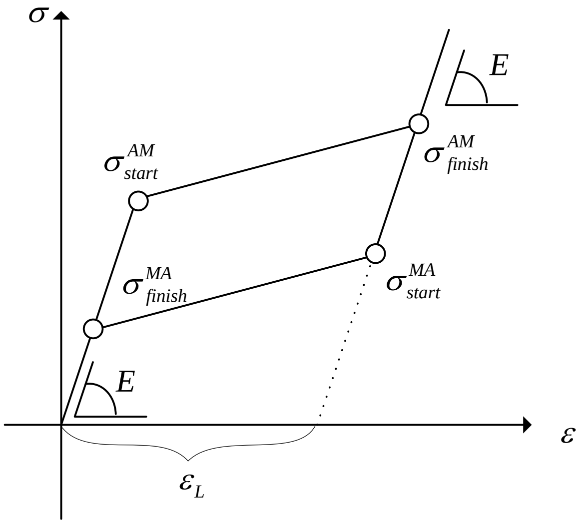

Fig. 4.19 Stress-strain relationship exhibited by the super-elastic shape-memory alloy constitutive model. Sketch of the material response under tensile loads

For both processes, linear kinetic rules to describe the evolution in time of the martensite fraction are chosen. In particular, the activation conditions for the conversion of austenite into martensite are:

$$\sigma_S^{AM} < |\sigma| < \sigma_F^{AM} \text{ and } \dot{\overline{|\sigma|}} > 0 \qquad (4.45)$$

where σ_S^{AM} and σ_F^{AM} are material parameters representing the stress levels at which the "A to M" transformation starts and finishes respectively. $| \bullet |$ is the absolute value and a superpose dot indicates a time derivative (i.e. $d|\sigma|/dt$). The corresponding evolutionary equation is set equal to:

$$\dot{\xi}_S = -(1-\xi_S)\frac{\dot{\overline{|\sigma|}}}{|\sigma| - \sigma_F^{AM}} \tag{4.46}$$

On the other hand, the activation conditions for the conversion of martensite into austenite are:

$$\sigma_F^{MA} < |\sigma| < \sigma_S^{MA} \text{ and } \dot{\overline{|\sigma|}} < 0 \tag{4.47}$$

where σ_F^{MA} and σ_S^{MA} are material parameters representing the stress levels at which the "M to A" transformation starts and finishes respectively. The corresponding evolutionary equation is set equal to:

$$\dot{\xi}_S = \xi_S \frac{\dot{\overline{|\sigma|}}}{|\sigma| - \sigma_F^{MA}} \tag{4.48}$$

4.5.2 Strain Decomposition and Elastic Relation

Limiting the discussion to a small deformation regime, the following additive decomposition of the total strain, ε, is assumed:

$$\varepsilon = \varepsilon_{el} + \varepsilon_L \times \xi_S \times \mathrm{sgn}(\sigma) \tag{4.49}$$

where ε_{el} is the elastic strain, ε_L is the maximum residual strain and $\mathrm{sgn}(\bullet)$ is the sign function. The maximum residual strain ε_L, regarded as a material constant, is a measure of the maximum deformation obtainable only by a multiple-variant martensite detwinning, hence, a measure of the maximum deformation obtainable aligning all the multiple-variant martensites in one direction. Moreover, the presence of sgn(σ) in Eq. (4.49), indicates that the direction of the effect relative to the martensite fraction is governed by the stress. The elastic stress is assumed to be linearly related to the stress:

$$\sigma = E \times \varepsilon_{el} \tag{4.50}$$

with *E* the elastic modulus of both the austenitic and martensitic branch.

4.5.3 *Time-discrete Model*

While during the development of the time-continuous model, the stress is assumed to be the control variable. On the other hand, the strain is assumed as the control variable during the development of the time-discrete model. The choice is consistent with the fact that, from the point of view of the integration scheme, the time-discrete problem is considered strain-driven. Accordingly, knowing the strain at time t_{n+1} and the solution at time t_n, one should compute the new solution at time t_{n+1}. To minimize the appearance of subscripts (and to make the equations more readable), the following convention is made:

$$a_n = a(t_n)\,,\ a = a(t_{n+1}) \tag{4.51}$$

where a is a generic quantity. Therefore, the subscript n indicates a quantity evaluated at time t_n, while no subscript indicates a quantity evaluated at time t_{n+1}.

The model uses a backward-Euler scheme to integrate the time-continuous evolutionary Equations (4.46) and (4.48). Written in residual form and after clearing the fractions, the time-discrete evolutionary equations specialized to:

$$\Re^{AM} = \lambda_M (|\sigma| - \sigma_F^{AM}) + (1 - \xi_S)(|\sigma| - |\sigma_n|) = 0 \tag{4.52}$$

$$\Re^{MA} = \lambda_M (|\sigma| - \sigma_F^{MA}) + \xi_S (|\sigma| - |\sigma_n|) = 0 \tag{4.53}$$

where the martensite fraction increment λ_M is defined as:

$$\xi_S = \xi_{S,n} + \lambda_M \text{ or } \lambda_M = \int_{t_n}^{t_{n+1}} \xi_S dt \tag{4.54}$$

The quantity λ_M can be computed expressing the stress as a function of λ_M and requiring the satisfaction of the evolutionary equation corresponding to the active phase transformation.

Introduction of Eq. (4.50) into Eq. (4.49) indicates that:

$$\operatorname{sgn}(\sigma) = \operatorname{sgn}(\varepsilon) \tag{4.55}$$

Hence, Eq. (4.49) can be rewritten as:

$$\varepsilon = \varepsilon_{el} + \varepsilon_L \times \xi_S \times \operatorname{sgn}(\varepsilon) \tag{4.56}$$

Making use of Eq. (4.56), substitution of Eq. (4.50) into Eq. (4.52) and (4.53) transforms the time-discrete evolutionary equations in two equations which can be solved in terms of λ_M .

4.5.4 Algorithmic Tangent Modulus

A discussion of the construction of the tangent modulus consistent with the time-discrete model is followed. The use of a consistent tangent modulus preserves the quadratic convergence of the Newton method.

From the linearization of the Eq. (4.49), one could get:

$$d\sigma = E[d\varepsilon - \varepsilon_L \times \mathrm{sgn}(\varepsilon) d\lambda_M] \tag{4.57}$$

Assuming that:

$$d\lambda_M = H d\varepsilon \tag{4.58}$$

One could solve Eq. (4.57) in terms of $d\sigma$, obtaining the relation:

$$d\sigma = E^T d\varepsilon \tag{4.59}$$

where the tangent elastic modulus E^T is given by:

$$E^T = E[1 - \varepsilon_L H \,\mathrm{sgn}(\varepsilon)] \tag{4.60}$$

The quantity H is computed from the linearization of the discrete evolutionary equations corresponding to the active phase transformation. Then, from Equations (4.52) and (4.53), one could get:

$$d\Re^{AM} = (1 - \xi_{S,n}) d|\sigma| + d\lambda_M (|\sigma_n| - \sigma_F^{AM}) = 0 \tag{4.61}$$

$$d\Re^{MA} = \xi_{S,n} d|\sigma| + d\lambda_M (|\sigma_n| - \sigma_F^{MA}) = 0 \tag{4.62}$$

Since $d|\sigma| = \mathrm{sgn}(\sigma) d\sigma = \mathrm{sgn}(\varepsilon) d\varepsilon$, relation (4.57) allows to solve Eqs. (4.61) and (4.62) in terms of $d\lambda_M$ obtaining respectively:

$$H = H^{AM} = \frac{-\mathrm{sgn}(\varepsilon)(1 - \xi_{S,n})E}{(1 - \xi_{S,n})[-\mathrm{sgn}(\varepsilon) E \varepsilon_L] + \sigma_n - \mathrm{sgn}(\varepsilon)\sigma_F^{AM}} \tag{4.63}$$

$$H = H^{MA} = \frac{\text{sgn}(\varepsilon)\xi_{S,n}E}{\xi_{S,n}[\text{sgn}(\varepsilon)E\varepsilon_L] + \sigma_n - \text{sgn}(\varepsilon)\sigma_F^{MA}} \tag{4.64}$$

Also, substituting Eq. (4.57) into Equations (4.52) and (4.53), it is possible to get the value of martensite fraction during the deformation history.

In particular, for the conversion of austenite into martensite, one has:

$$\xi = \xi^{AM} = \frac{\xi_{S,n}E\varepsilon - \text{sgn}(\varepsilon)\xi_{S,n}\sigma_F^{AM} - E\varepsilon + \sigma_n}{-\text{sgn}(\varepsilon)\sigma_F^{AM} + \text{sgn}(\varepsilon)\xi_{S,n}E\varepsilon_L - \text{sgn}(\varepsilon)E\varepsilon_L + \sigma_n} \tag{4.65}$$

while for the conversion of martensite into austenite, one has:

$$\xi = \xi^{MA} = \frac{\xi_{S,n}E\varepsilon - \text{sgn}(\varepsilon)\xi_{S,n}\sigma_F^{MA}}{-\text{sgn}(\varepsilon)\sigma_F^{MA} + \text{sgn}(\varepsilon)\xi_{S,n}E\varepsilon_L + \sigma_n} \tag{4.64}$$

4.5.5 Numerical Assessment

A SDOF bilinear system is created to study the model presented above. The system has a period of 0.8 sec and a 1% linear damping ratio. The numerical assessment is evaluated in Matlab and OpenSees platform using self-centering material model. Compared to the material model in section 4.5.4, which captures the material level stress-strain relations, the implemented model focuses more on the performance of the self-centering devices. The modeling procedure of the material in OpenSees is shown in Table 4.10. The code was written by Jeff Erochko from University of Toronto.

Table 4.10 Self-centering material model in OpenSees developed by Jeff Erochko

uniaxialMaterial SelfCentering $matTag $k1 $k2 $sigAct $beta <$epsSlip> <$epsBear> <rBear>	
$matTag	integer tag identifying material
$k1	Initial Stiffness
$k2	Post-Activation Stiffness (0<$k2<$k1)
$sigAct	Forward Activation Stress/Force
$beta	Ratio of Forward to Reverse Activation Stress/Force
$epsSlip	slip Strain/Deformation (if $epsSlip = 0, there will be no slippage)
$epsBear	Bearing Strain/Deformation (if $epsBear = 0, there will be no bearing)
$rBear	Ratio of Bearing Stiffness to Initial Stiffness $k1

Fig. 4.20 presents all the physical meaning of the variables from Table 4.10. The variable sigAct is same as σ_{start}^{AM} from section 4.5.4. The k1 and k2 variable corresponds to the elastic stiffness and transition stiffness from section 4.5.4. In addition, the model incorporates the slippage where three additional yet optional variables are defined. For beta value, this work assumes to be one as being compatible with the behaviors obtained from many material tests.

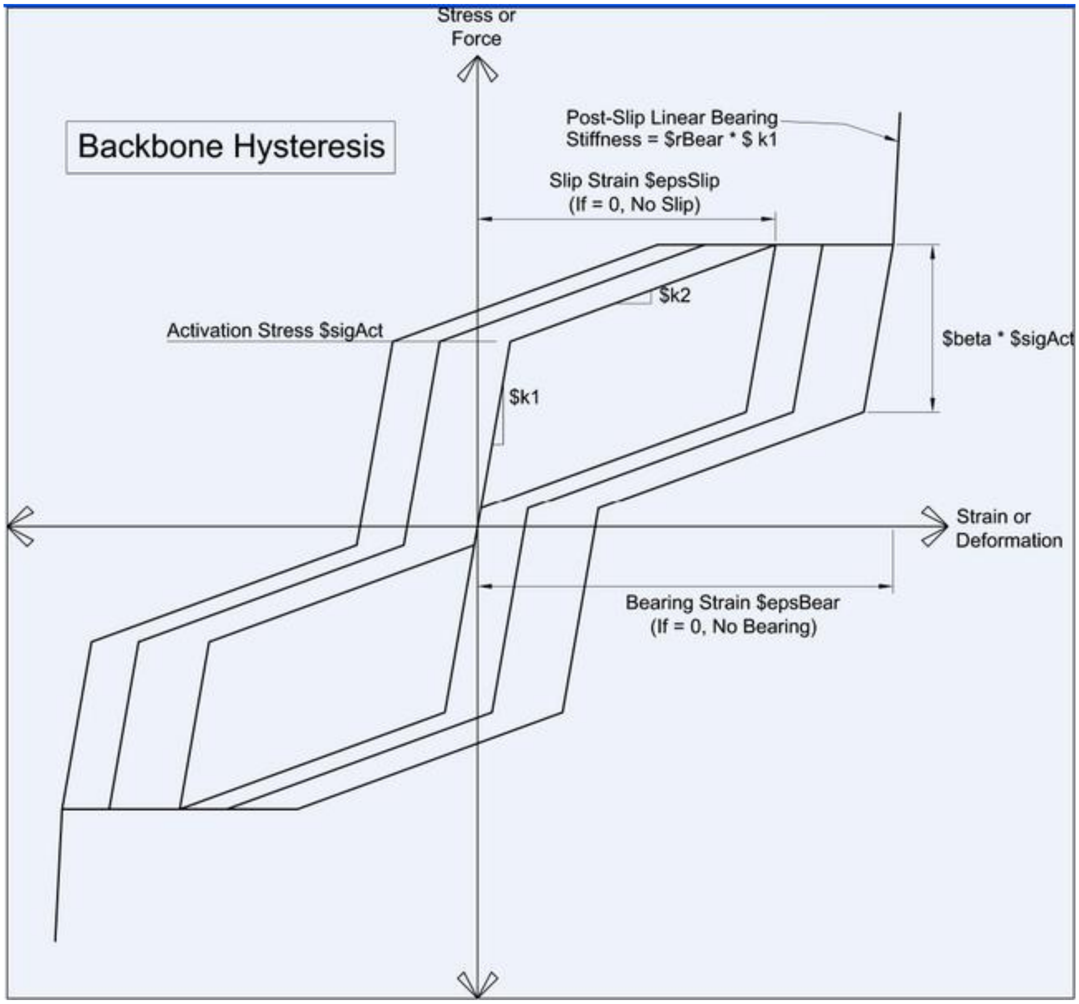

Fig. 4.20 OpenSees model of self-centering device (from online OpenSees document)

In order to show the effectiveness of the self-centering system, the numerical analysis is divided to three steps: first, the bilinear system is excited with a set of ground motions; second, the bilinear system is equipped with additional damper (10% of nonlinear damping ratio); last, the bilinear system is equipped with the self-centering devices. A typical displacement time history analysis is presented in Fig. 4.21.

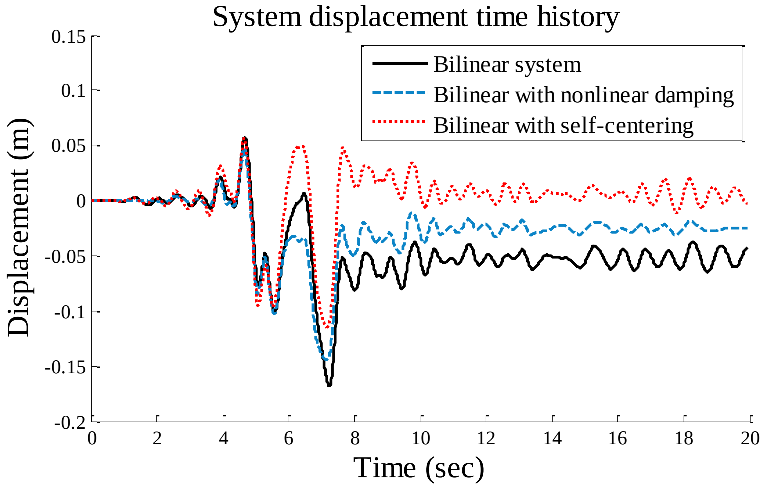

Fig. 4.21 Self-centering effect illustrated by time history analysis

From Fig. 4.21, one could easily notice some significant residual drift left inside the bilinear system after the ground motion is over. In addition, it is obvious that only adding the damper does not help eliminate the residual drift. On the other hand, the self-centering system can always drive the system back to its original position after the motion is over. The internal force of the self-centering model is presented below in Fig. 4.22.

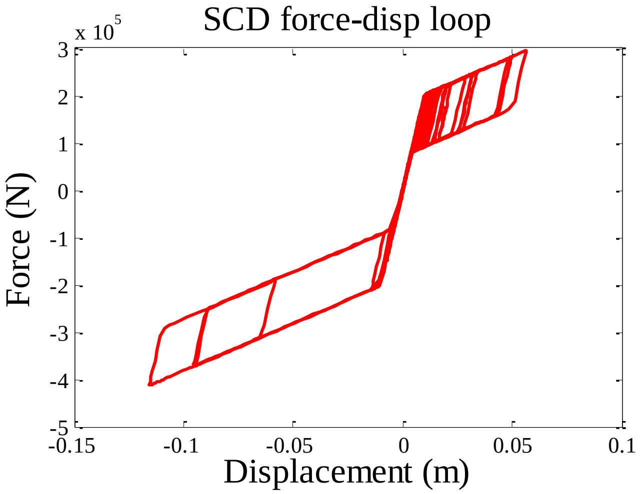

Fig. 4.22 Numerical behavior of SMA device

4.6 Concluding Remarks

This chapter covers the study target of this study - seismic protective devices for building systems. Various types of devices have been presented. One could refer to these technologies to design or retrofit a certain building to improve its performance against earthquakes. The emphasis is on base isolation, NSD and self-centering system. In addition, numerical modeling schemes for these devices have been proposed and implemented in OpenSees. This enables the numerical evaluation for such devices and future PBEE implementation of the optimum design for these protective devices.

5. OPTIMAL ISOLATION DESIGN FOR BUILDING SYSTEMS

Seismic isolation is a viable method to reduce seismic damages to buildings under moderate and severe earthquake events. In order to systematically evaluate and optimize the building responses, this chapter develops and applies the performance-based analysis and design methodology to assess the seismic vulnerability of buildings and to optimally design the isolation devices to reduce the direct losses due to earthquake damages. An isolated steel moment frame building tested in the 2011 E-Defense blind contest is selected and modeled in detail in OpenSees. Its modeling details and seismic responses are validated against the full scale shaking table test results. Subsequently, the fragility functions are derived for the test structure when subject to a suite of near-fault ground motions exhibiting distinctive acceleration or velocity pulses. In order to quantify the system level damage states of the building, a total loss ratio is proposed to account for the direct loss due to structural, nonstructural and isolation components in relation to the total repair cost of the original structure. With the consideration of uncertainties, the fragility functions are derived for conventionally designed and base-isolated steel moment frame structure. Finally, the total loss ratios are computed for various isolation designs. The optimal isolation is derived for cases with the minimum total loss ratio. It is shown that the optimal design of isolation devices can reduce the total loss ratio more than 50% of that of the un-isolated structure and it also outperforms the adopted design in the test program. The study demonstrates a systematic way of achieving the optimal isolation design with considerations of uncertainties in earthquake input and the combined structural and non-structural damages.

5.1 Introduction

Buildings may be susceptible to earthquake damages resulting both direct and indirect loss. In order to mitigate seismic hazards on buildings, seismic design codes can be improved and seismic protective devices in the form of passive or semi-active can be used (Lafontaine *et al.* 2009; Lee *et al.* 2006). Base isolation is an effective passive device, which can significantly reduce the seismic lateral force demands in the superstructure relative to a fixed-base building. It improves the seismic resistances of structures by dissipating and deflecting earthquake input energy (through lengthening the fundamental structural period to avoid the dominant frequency of ground motions) and consequently reduces the cost for repair and rehabilitation after earthquake events (Kelly 1986; Skinner *et al.* 1993).

Although the current design codes (e.g. ASCE 7-10 (2010)) provide descriptive method for designing the base isolation systems for buildings, they cannot incorporate uncertainties inherent with ground motion characteristics, building modeling parameters (such as material properties, member stiffness and strength, etc.), capacity estimation and variations in geometric properties of buildings etc. More importantly, the isolation design cannot be directly related to the expected performance of buildings. The recent development of performance-based earthquake engineering (PBEE) methodology provides a probabilistic framework to assess and improve the seismic performance of buildings to achieve the desired performance objectives. (Ghobarah 2001; SEAOC 1995; Porter *et al.* 2007). Through fragility functions, which define the conditional probability of engineering demand parameters (EDPs) exceeding the damage states (DS) at given earthquake intensity measure (IM), uncertainties and variabilities can be incorporated to evaluate the vulnerability of structural components and the system level performance (Hwang *et al.* 2000; Karim and Yamazaki 2001; Zhang and Huo 2009).

The PBEE framework is particularly attractive in the case of base isolation design if the device parameters can be directly related to a probabilistic performance index. This facilitates comparing different designs under a consistent performance index. Sayani and Ryan (2009) developed a response index to compare the relative performance of many systems or to predict the best system to achieve a given performance objective for both base-isolated and fixed-base buildings. Zhang and Huo (2009) developed a performance index that considers both column and isolator damage for isolated bridges. Besides performance index, PBEE can also provide the expected losses to stakeholders to provide direct economic comparisons for different systems. Recent study by Mander *et al.* (2012) determines losses without need for customary fragility curves and proposes a closed-form stochastic loss estimation model for seismically damaged structures. Graf and Lee (2009) presented a simple framework to evaluate the cost to repair building damage using engineering parameters related to seismic building codes. Most current loss approaches use probabilistic integrated methodologies such as fragility curves to estimate the losses due to structural damage (i.e. combines fragility curves with loss functions) (Dhakal *et al.* 2006; Solberg *et al.* 2008; Aslani and Miranda 2005, Bai *et al.* 2009).

This section adopts the performance-based methodology to evaluate the effectiveness and optimum design parameters of isolation devices such that the overall damaging potential of seismically isolated building system is minimized. A total loss ratio is defined to account for the direct loss due to both structural and nonstructural damage in relation to the total repair cost of the original structure. By relating fragility functions at different damage states to the total loss ratio, isolation devices with various mechanical properties can be evaluated under this probabilistic framework to derive the optimal design based on minimum damage probability in terms of the total loss ratio.

The section is organized as follows. Following the introduction of the PBEE framework is provided for deriving the fragility functions and defining the damage states of buildings in Chapter 3. A loss model that defines the total loss ratio is proposed. A numerical model of a five-story steel moment-resisting frame is developed and calibrated with test data. The fragility curves are derived for the model building for both un-isolated and isolated cases. A detailed parametric study of various isolation parameters is conducted and the total loss ratio is obtained to serve as the criteria for evaluating the merit of each design. The optimal design range for isolation devices is finally determined along with its 95% confidence interval.

5.2 Loss Model and Total Loss Ratio

Loss estimation is compatible with PBEE framework and the study about loss has been going on for years. The major stream of loss estimation study is to find the economic losses for large number of buildings within a geographical region such as a city and a county. This type of regional loss estimation studies is used mainly for insurance industry and sometimes for the federal government. On the other side, relatively less research has been done for individual structure loss estimation. To estimate the loss to a specific building, the damage is usually categorized into different components such as structural damage and non-structural damage. Damage to each of these components is evaluated in terms of percentage of the replacement cost of the component. Evolutions of the loss to a specific building include using a set of ground motions rather than only using one motion, and incorporating probabilistic approaches while evaluating the structural performance.

In this study, besides the investigation of building damage potential, a probabilistic loss estimation framework is presented, which directly relates earthquake hazard to building response and hence to total losses in the form of percentage. The loss estimation framework is closely tied with the fragility functions that define the damage that incurs the performance of a certain design. The loss model has been calibrated and validated with designed buildings documented empirically such as ATC-40 (1996), ATC-58 (2011) and RSmeans construction cost data (2009).

5.2.1 Damage Indicators

Many existing studies define the performance of a certain building by evaluating both inter-story drifts and floor accelerations (Lafontaine *et al.* 2009). To incorporate the comprehensive damage states for the isolated building system, this study uses peak transient inter-story drift ratio, absolute floor accelerations, and horizontal bearing drift ratio as the damage indicators for the isolated building. Correspondingly, the physical meanings related with these *EDP*s are structural damage, non-structural damage and bearing damage.

The structural components include all the elements needed for the superstructure such as columns and beams that provide support against lateral and gravity loads. Williams *et al.* (1997) demonstrate that plastic displacement and ductility are consistently reliable indicators of severe damage to the structural members. Mander *et al.* (2007) choose the maximum pier drift ratio as the parameter to study the damage to bridges. In additional to these studies, numerous studies have also proved that the damage to the structural components is usually indicated by the structural curvature or displacement/drift.

The non-structural elements usually refer to all the equipments and building facility, suspended ceiling, automatic sprinklers, elevators, etc. Current studies often consider the damage of non-structural components being highly relevant to absolute floor acceleration. Previous studies found that seismic damage to non-structural systems can be triggered at response intensities smaller than those required to produce structural damage. Consequently, a big part of building seismic losses were related to the damage of nonstructural components. For example, Reinhorn *et al*. (2010) show that after Miranda earthquake in 2003, 82%, 87% and 92% loss are due to the general nonstructural components to office buildings, hotels and hospitals respectively. Overall, the general non-structural systems represent 75% of the loss exposure of U.S. buildings to earthquakes, and account for over 78% of the total estimated national annualized earthquake loss. (Reinhorn *et al*. 2010). To reduce the damage to the non-structural building components, some previously studies suggest to reduce the floor acceleration of buildings where the concept of base-isolation are highly recommended. (Lafontaine *et al.* 2009) Other than these non-structural components, Haselton *et al*. (2007) also points out in a PEER report about some non-structural components that are sensitive to other intensity indicators. For example, the report adopts *EDP* of transient drift ratio to indicate damages to drywall partitions and finishing; adopts inter-story drift ratio to indicate damages to exterior glazing; and adopts damaged area to indicate damages to interior paint. This loss model in this study relates non-structural level damage to the maximum top floor acceleration.

With the purpose of shifting the superstructure's damage to the isolation system, repairing and/or replacing isolators are unpreventable from medium and large ground motions. One of the discussions address the issue that base-isolated buildings can be vulnerable to the large pulse-like ground motions generated at near-fault locations (Hall and Heaton 1995). The nonlinear shear strain of the isolation system is significantly large under near-fault motions. Such large response can cause undesired instability issue of the bearings, which leads to intensive damage to the bearings and the super-structural members. In fact, isolation devices possess various mechanical properties and their behaviors are often highly nonlinear and sometimes frequency- and rate-dependent (Naeim and Kelly 1999). Existing studies usually relate the damages of the bearings with their shear ratio, displacement or drift (Zhang and Huo 2009). The detailed components for these three above categories are summarized in Table 5.1 according to RSMeans building construction cost data (2009) given.

Table 5.1 Components of the base-isolated building system

Structural components	SUBSTRUCTURE	Foundation
		Basement Excavation
	SHELL	Superstructure
		Exterior Enclosure
		Roofing
	INTERIORS	Partitions
		Fittings
		Stair
		Floors and
Non-structural components	EQUIPMENT	Suspended
		Commercial
		Institutional
		Vehicular
	SERVICES	Conveying
		Plumbing
		HVAC
		Fire
		Electrical
Base isolators	BEARINGS	

5.2.2 Building Performance Index: Total Loss Ratio

The total loss ratio (*TLR*) serves as a factor to evaluate the performance of a given design and the ratio quantifies the cost of structural repairs as a percentage of the replacement value of the structural portion of a building. In order to compute *TLR*, this study maps the damage categories with the developed damage states. The expression for *TLR* for a base-isolated building is given as:

$$TLR = \frac{c_{str}\sum_{i=1}^{4} P_{(i)}^{st} r_{(i)}^{st} + c_{non-str}\sum_{i=1}^{4} P_{(i)}^{ns} r_{(i)}^{ns} + c_{iso}\sum_{i=1}^{4} P_{(i)}^{iso} r_{(i)}^{iso}}{c_{str} + c_{non-str} + c_{iso}} \tag{5.1}$$

where i = 1 to 4 stands for the four damage states. $r_{(i)}^{st}, r_{(i)}^{ns}$, and $r_{(i)}^{iso}$ are the percentage damaged for each of the damage state for structural components, non-structural components, and isolation system with detailed values presented in Table 5.2. c_{str}, $c_{non\text{-}str}$ and c_{iso} stands for the cost for the three aforementioned *EDP*s and $P_{(i)}^{st}$, $P_{(i)}^{ns}$, $P_{(i)}^{iso}$ are the probabilities that are bounded by the four fragility curves within each fragility curves of these three components.

To make calculation simpler, one could assume that structural components has a value of *A*, and the other two categories cost α *A* (non-structural components) and β *A* (isolation systems), respectively. The coefficients α and β, are obtained based on previous observations and value estimations of total non-structural components and isolation system. The value of α varies with different types of building according to their functions and placement of force sensitive components. For this study, α values of 0%, 50% and 100% are chosen and studied. β is set to 8% in this study as the total cost for a base isolation system is usually within 10% of the structural cost (the upper bound of β). Then Eq. (5.1) can be formed as:

$$TLR = \frac{\sum_{i=1}^{4} P_{(i)}^{st} r_{(i)}^{st} + \alpha\sum_{i=1}^{4} P_{(i)}^{ns} r_{(i)}^{ns} + \beta\sum_{i=1}^{4} P_{(i)}^{iso} r_{(i)}^{iso}}{1+\alpha+\beta} \tag{5.2}$$

The total loss of the isolated building system is the sum of loss in each state and the total value of the base isolated system is $(1+\alpha+\beta)A$ and this is the denominator by which the TLR is normalized. Since the loss ratio at different damage states are proportional to damaged percentage of the building, this study follows HAZUS definition, where four damage states are defined in Table 5.2:

Table 5.2 Damage states and damage ratio

Description		Percent Damage	Accel. (non-str.)	Disp. (str.)	Bearing Drift (iso.)
1	Slight	2%	0.25 g	0.40%	100%
2	Moderate	10%	0.50 g	0.69%	150%
3	Extensive	50%	1.0 g	1.57%	200%
4	Complete	100%	2.0 g	4.00%	250%

The presented loss model includes three fragility analyses for maximum inter-story drift, absolute maximum top floor acceleration, and bearing drift. For each of these cases, the damage states are bounded by the four fragility curves for each state, as shown in Fig. 5.1. The probability of being in each damage state can be computed as the difference between the conditional probabilities of the bounding fragility curves. For each of the three components (e.g. structural components), conditional probability values ($P_{(1)}$, $P_{(2)}$, $P_{(3)}$, and $P_{(4)}$) that correspond to each performance level can be obtained for a given intensity measure from the fragility curves and they satisfy $0 \le \sum_{i=1}^{4} P_{(i)} \le 1$.

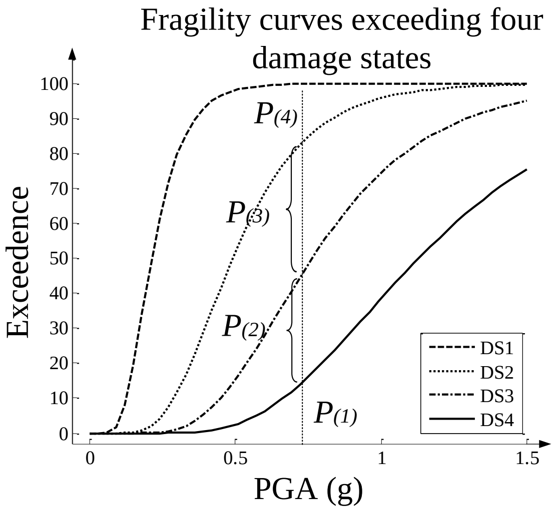

Fig. 5.1 Illustration of bounded probability in percentage for each state

In order to make the concept of *TLR* clearer, an example of how the *TLR* is calculated for a base-isolated building system is provided. Suppose our goal is to estimate the expected *TLR* of earthquakes with return frequency of 10% in 50 years (e.g. PGA = 0.55g). For the structural damage, the probability bounded by each damage state can be shown from the fragility curve for structural members that are dominated by inter-story drift. Similarly, for the non-structural damage probability and isolator damage probability, which can be shown from acceleration fragility curves and bearing drift fragility curves. Suppose one could get the following probabilities:

$$P_{(str)} = [10\%\ 25\%\ 35\%\ 15\%],\ P_{(non-str)} = [8\%\ 32\%\ 46\%\ 14\%],\ P_{(iso)} = [21\%\ 23\%\ 22\%\ 12\%].$$

The loss of structural elements would be:

$$(10\% \times 2\% + 25\% \times 10\% + 35\% \times 50\% + 15\% \times 100\%) \times A = 0.352A.$$

As the non-structural members cost αA, the loss of non-structural elements would be:

$$(8\% \times 2\% + 32\% \times 10\% + 46\% \times 50\% + 14\% \times 100\%) \times \alpha A = 0.4036\alpha A,$$

In addition, given the isolation system cost βA, the loss of the isolation system is computed as: $(21\% \times 2\% + 23\% \times 10\% + 22\% \times 50\% + 12\% \times 100\%) \times \beta A = 0.2572\beta A$.

Therefore, the *TLR* is computed as: $TLR = \dfrac{0.352A + 0.4036\alpha A + 0.2572\beta A}{(1+\alpha+\beta)A} \times 100\%$. For example, when $\alpha = 100\%$ and $\beta = 8\%$, *TLR* can be calculated as:

$$TLR = \frac{0.352 + 0.4036 \times 1 + 0.2572 \times 0.08}{(1+1+0.08)} \times 100\% = 37.32\%.$$

5.3 Fragility Analysis and Results

In this section, the methodology described in the previous section is applied to derive the fragility curves of a typical as-built and shake table tested steel building constructed in Japan and of the retrofitted building using seismic isolation devices.

5.3.1 Building layout

The selected building model for this study adopts the building specimen in contest 2011 tested by the E-Defense shaking table. The E-Defense shaking table facility, whose construction was completed in 2005, is the largest earthquake simulator capable of subjecting full-scale structures to the strongest earthquakes recorded in the world. The structural layout of the studied building is depicted in Fig. 5.2, which represents a two bay by two bay plane with 7-m and 5-m span in one direction and two 5-m spans in another. Fig. 5.2(a) shows the elevation view of the frame with a 3.85-m first story and four 3-m stories above. Fig. 5.2(b) shows the plan view also in the unit of mm. The entire building sample is seated on nine FPS bearings, which are fixed to the E-defense shaking table. The general force-displacement relationship for the isolation system is assumed to be smoothed bilinear as shown in Fig. 5.2(c). The first seven frequencies of the building is 1.52 Hz, 1.58 Hz, 1.87 Hz, 4.81 Hz, 4.98 Hz, 5.87 Hz, 9.35 Hz and the first mode period T_1 is 0.65 second. The mode for story torsion is the eighth mode and is insignificant for this case.

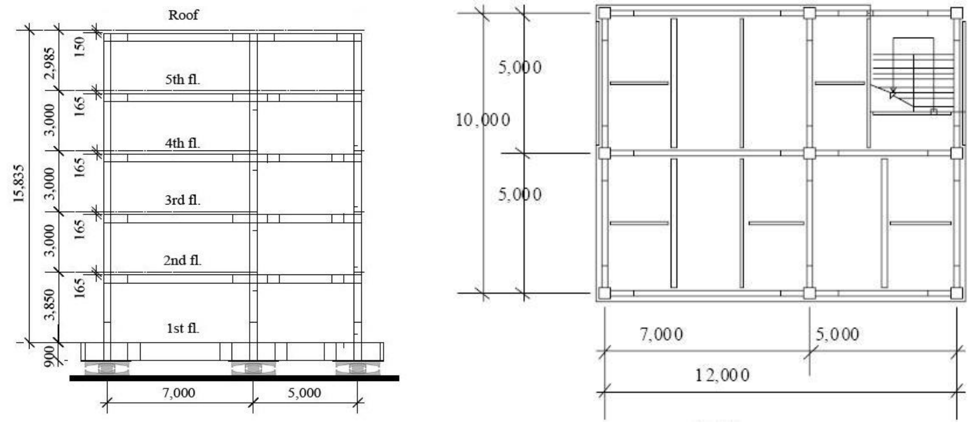

(a) Elevation Plan **(b)** Floor Plan

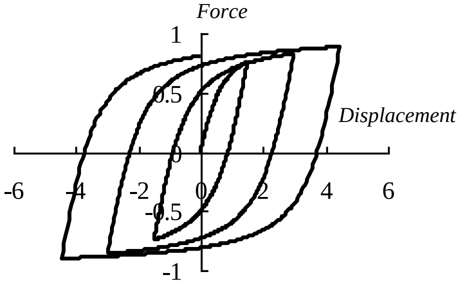

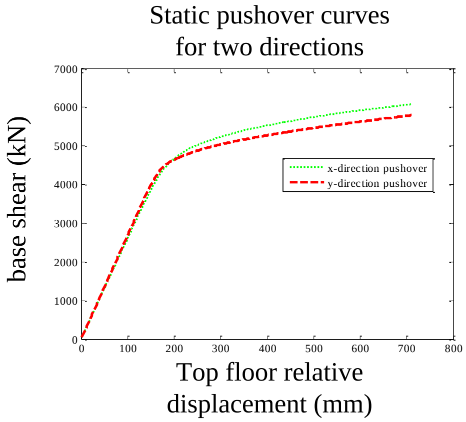

(c) Smoothed bilinear loop

(d) two directional pushover analysis

Fig. 5.2 Plan and elevation of full-scale 5-story steel MF building with triple pendulum isolation bearings

The nonlinear building model follows a bilinear hysteretic behavior, which include elastic stiffness K_1, post-yielding stiffness K_2, characteristic strength Q_d, yielding displacement D_y and yielding force F_y. Any three of these five properties can be used to completely describe the shape of the bilinear model. For this study, the bilinear behavior is characterized with K_1, K_2 and $Q_{d.}$

The static pushover analysis (Fig. 5.2(d)) reveals that the bilinear parameters of the designed building is Q_{d_B} = 4194 kN; K_{1_B} = 25 MN/m and K_{2_B} = 1700 kN/m. The story weights are 842 kN, 841 kN, 822 kN, 816 kN, 798 kN, 1153 kN for the ground level to the roof level respectively which adds up to 5309 kN above the isolation system. Nine FPS bearings are placed under the building and they were all tested before being installed into the building. The bearing geometry is given in Fig. 5.3(a), the design presented a triple pendulum isolation system with two sliding surfaces. Makris and Vassiliou (2011) discovered similar response between friction along the two sliding surfaces and a bilinear behavior with large initial stiffness. Solid line in Fig. 5.3(b) shows the real FPS response from the test and the dotted line completes the bilinear hysteretic loop that is being used for this study. Based on the conclusion from Makris and Vassiliou (2011), this study considers a bilinear behavior of the triple pendulum isolation system. This has also been proved from shaking table tests of the isolation system shown in Fig 5.3(c). These designed isolators add up to Q_{d_I} = 386 kN; K_{1_I} = 35 MN and K_{2_I} = 760 KN/m. This design corresponds to a Q_{d_I} / Q_{d_B} = 9.2% and K_{1_I} / K_{1_B} = 1.4 and a stiffness ratio of N = K_{1_I} / K_{2_I} = 46.

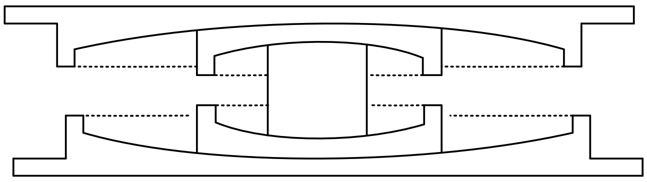

(a) Geometry of the tested TFP bearings

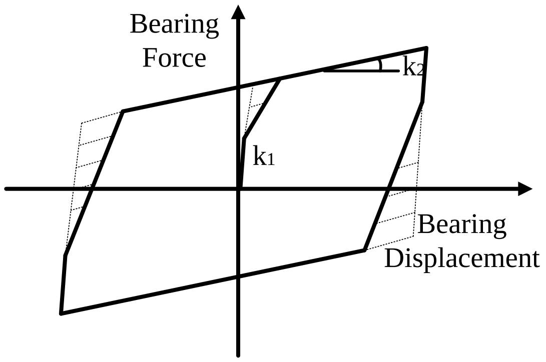

(b) Equivalent bilinear behavior

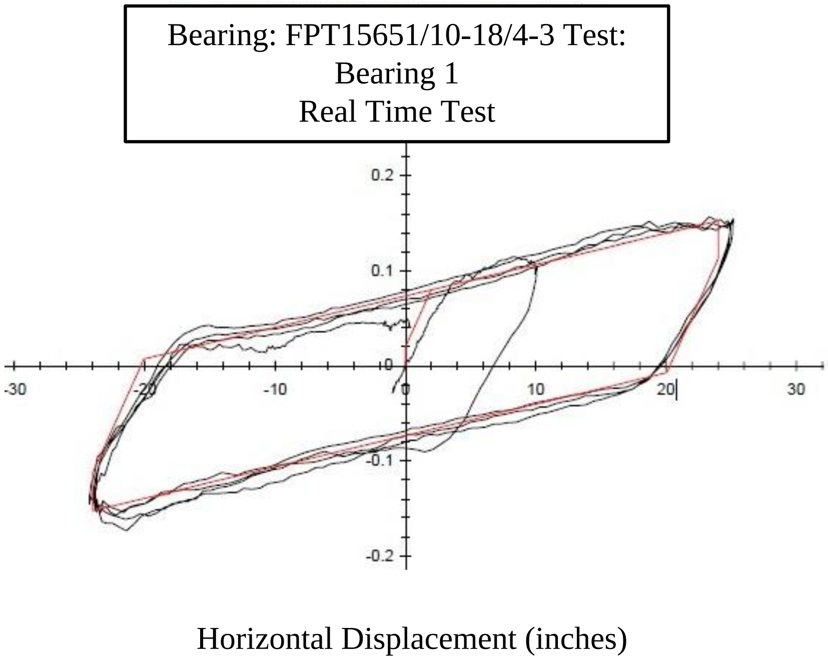

(c) Real time tested data of the bearings

Fig. 5.3 Triple pendulum isolation bearings and their bilinear behavior

To reduce the computation work and model parameters, one common engineering approach is to develop calibrated simplified models to replace the usually complicated 3D models. For example, Zhang and Huo (2009) simplified the 3D bridge model into 2D and they reasonably matched the simplified model with the original model. Mander *et al.* (2007) also simplified bridge pier into a one-DOF model before running IDA analysis. This study conducted 3D nonlinear dynamic response history analyses using the selected ground motions in the software platform OpenSees. The original 3D model assumes all diaphragms are rigid. The sophisticated model has thousands of nodes and elements, which simulate all the beams and columns with displacement-based elements considering nonlinear spreading plasticity along the elements. The simulation results from the 3D model closely matches well with the tested sample building. However, it is very time-consuming to analyze all one-hundred motions with this model. In fact, this work performs an extensive parametric study that requires much more computation running the original 3D model. Therefore, a simplified 3D model has been established guided by the performance of the original 3D model. Due to the rigid diaphragm and the in-significance torsional effect, a 3D lumped mass model with equivalent story stiffness is chosen for the simplified model (Fig. 5.4(a)). The story stiffness K_1-K_5 still follows the bilinear relationship and provides 2.5% of the elastic stiffness after they yield. Fig. 5.4(b) and 5.4(c) indicates that the simplified 3D model matches pretty well with the tested data of the real structure for both fixed-base and isolated building. For more ground motions, this study also performed PSDA analysis and created fragility curves for both the original model and the simplified model. Fig. 5.4(d) and 5.4(e) illustrate that the fragility curves for the simplified model is also very close to the original model.

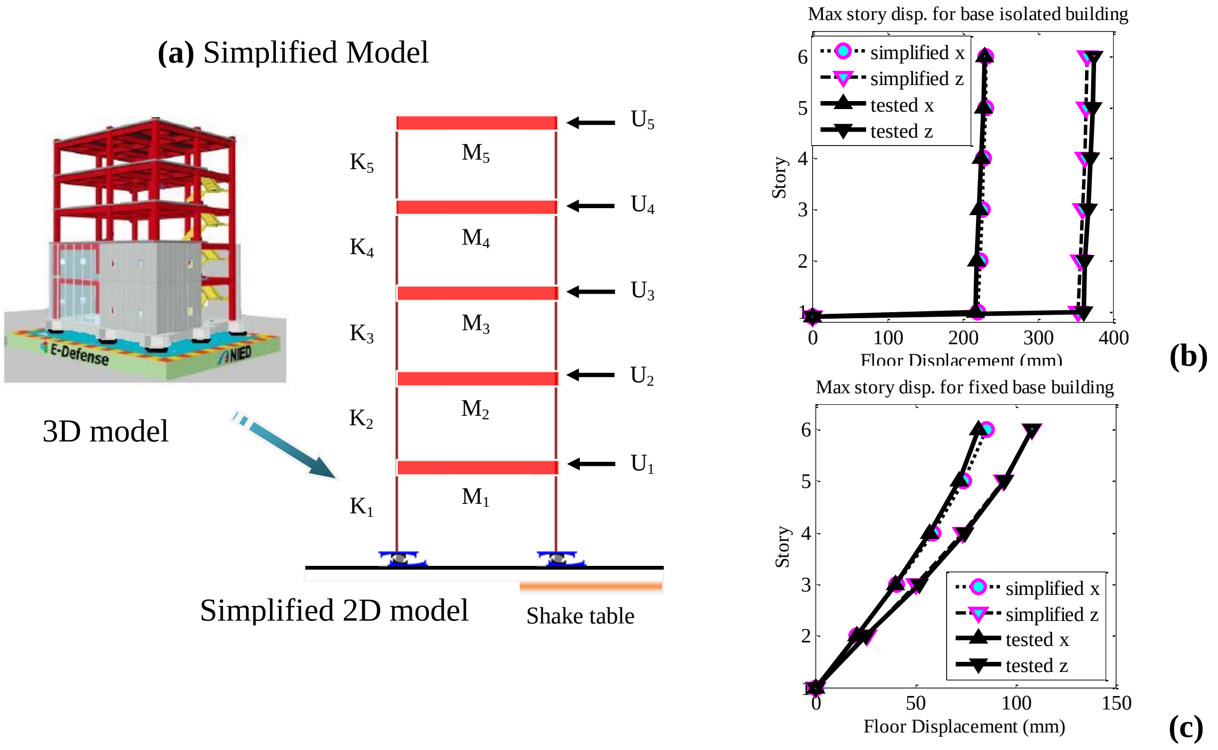

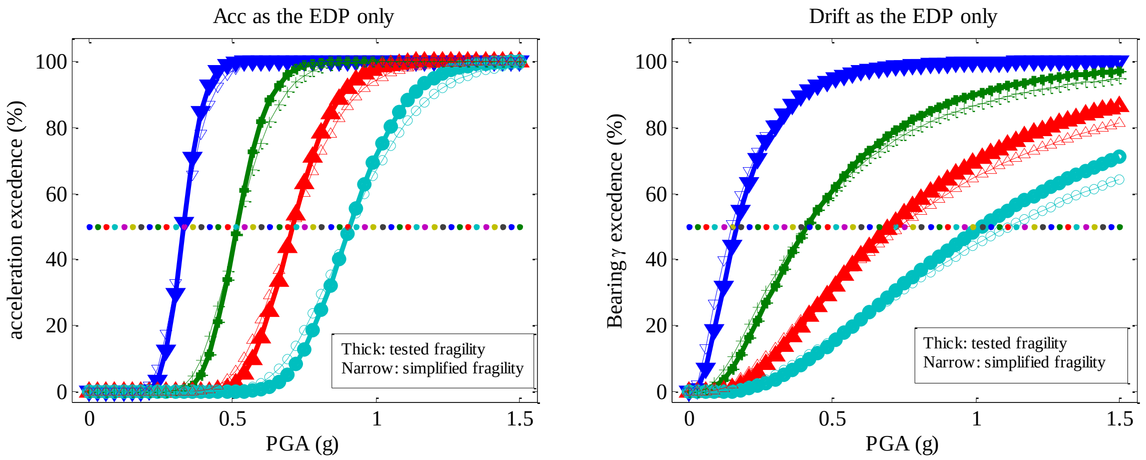

(d) Compare of acceleration fragility curve **(e)** Compare of inter-story drift fragility curve

Fig. 5.4 Simplified building model compared with 3D building model

5.3.2 Fragility Curves of the Fixed Base Building and the Isolated Building

Fig. 5.5 illustrates the relationship between computed *EDP* and the corresponding PGA(g) of un-scaled ground motions in logarithmic scale. The closer each point gets to the regressed linear line, the better *EDP* and *IM* are correlated, indicating better regression results.

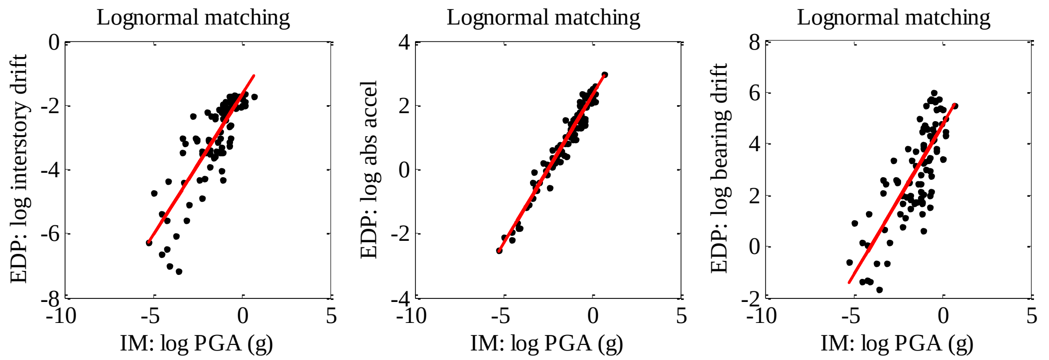

Fig. 5.5 Lognormal matching for the three EDPs: inter-story drifts; acceleration and bearing drift

Fig. 5.6 shows the fragility curves for base-fixed and base-isolated building. Fig. 5.6(a) shows the inter-story drift exceedance 1.0%. It is obvious that the building is well protected by the isolation device and the drift has zero chance to reach 1.0% at a 1.5 (g) ground motion PGA level; Fig. 5.6(b) shows that the roof absolute acceleration has also been reduced. The figure shows that for PGA near 0.5 (g), the un-isolated building roof acceleration has nearly 100% chance to reach 1.0 (g) whereas the chance for isolated building is close to zero.

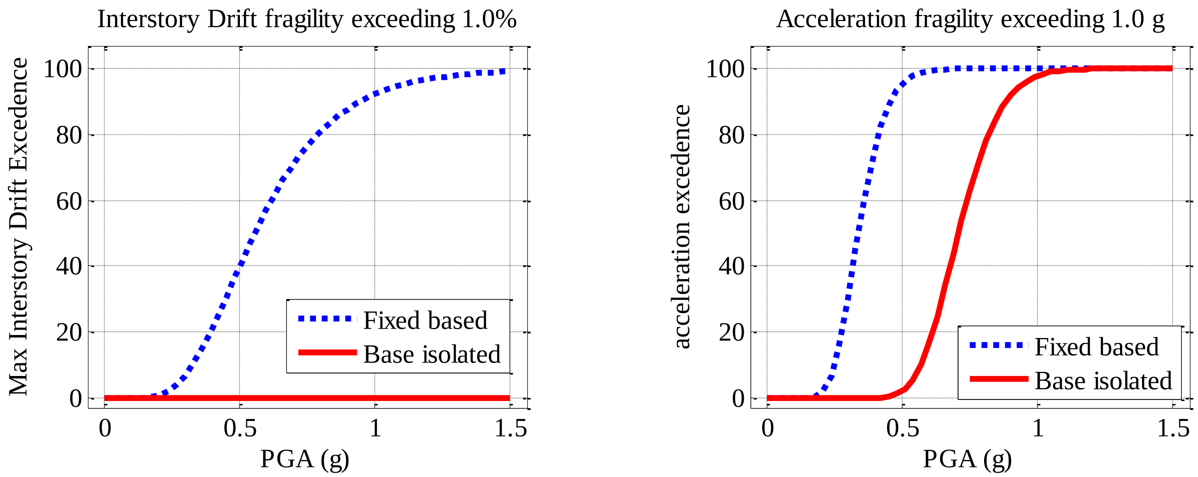

(a) Inter-story drift fragility **(b)** Acceleration fragility

Fig. 5.6 Isolation effect in terms of inter-story drift and absolute acceleration

5.4 Optimal Design for the Seismic Isolation System

Although the designed and tested isolators for the building are triple pendulum bearing, other types of isolators can also be used for base isolation design. Until now, three types of isolators are commonly used: elastomeric bearings (ERB), lead-rubber bearings (LRB), and friction pendulum systems (FPS). Details about isolation systems and their numerical modeling scheme has been explained in Chapter 4. This section systematically investigates the influence of mechanical properties of isolation devices to the dynamic response, potential damage, and *TLR* of an isolated building. In addition, a parametric study has been conducted to explore the optimum design for isolation system.

To launch the performance-based design of base-isolation system, all the possible design features of the isolation system should be considered. For each design, a performance index - *TLR* will be computed based on the presented loss model and compared with that of the other designs. In this study, the author systematically selects the isolation system features with various combinations of isolation parameters, which is summarized as follows: The ratio between the pre-yielding stiffness K_1 and post-yielding stiffness K_2 is measured by a parameter $N = K_{1\_I}/K_{2\_I}$. In this study, N is chosen to be 10, 20, and 50 respectively to represent these different isolation systems, where I stands for isolators. Then, for each of the three specified N, the post yielding stiffness K_{2_I} for the isolation system is varied from 0.01 to 0.08 times of the building elastic stiffness K_{1_B}, and the bearing yielding strength Q_{d_I} is varied from 0.03 to 0.45 times the building yielding strength Q_{d_B}.

To interrogate the performance over the expected range of earthquake ground motion intensities, nonlinear time-history analysis are conducted at different hazard levels. Haselton *et al*. (2007) selected seven hazard levels for LA Bulk Mail site, ranging from *IM* levels that have a 50%-in-5-years probability (7.2 years recurrence) to high-intensity motions that have a less than 2%-in-50-years probability (2475-years recurrence). Beyond the 2%-in-50-years hazard, ground motions intensity are incremented to the collapse level. In this study, four hazard levels are selected and they are given in Table 5.3. The *TLR* for each hazard level are computed, recorded and compared to show the efficiency of isolation. A lower mean value corresponds to a smaller total loss implying a better isolation design.

Table 5.3 Uniform mean hazard results

Spectral acceleration for each hazard level				
Hazard level	20% in 5 years	10% in 50 years	2% in 50 years	collapse
Equivalent mean return period	22	475	2475	-
	0.20 (g)	0.55 (g)	0.82 (g)	1.20 (g)

Fig. 5.7 illustrates to the *TLR* as a function of Q_{d_I} / Q_{d_B} and K_{2_I} / K_{1_B} to reach the different hazard levels for the given steel building with a stiffness ratio N = 20. The bottom point on the contour represents the smallest loss ratio leading to the repairing cost of a given hazard intensity, which also corresponds to a lowest fragile probability that incurs the best structural performance. The bearing parameters at these bottom (optimizing) points therefore represent the optimal design. Fig. 5.8 shows similar surfaces for *TLR* for pulse type motions with non-structural parameter α set to zero and N=50 (close to the tested FPS bearings). Four figures are presented for the four different hazard levels. It is very easily identified that the optimal range for this case is $Q_{d\_I} = 0.12\ Q_{d\_B}$ and $K_{2\_I} = 0.08\ K_{1\_B}$.

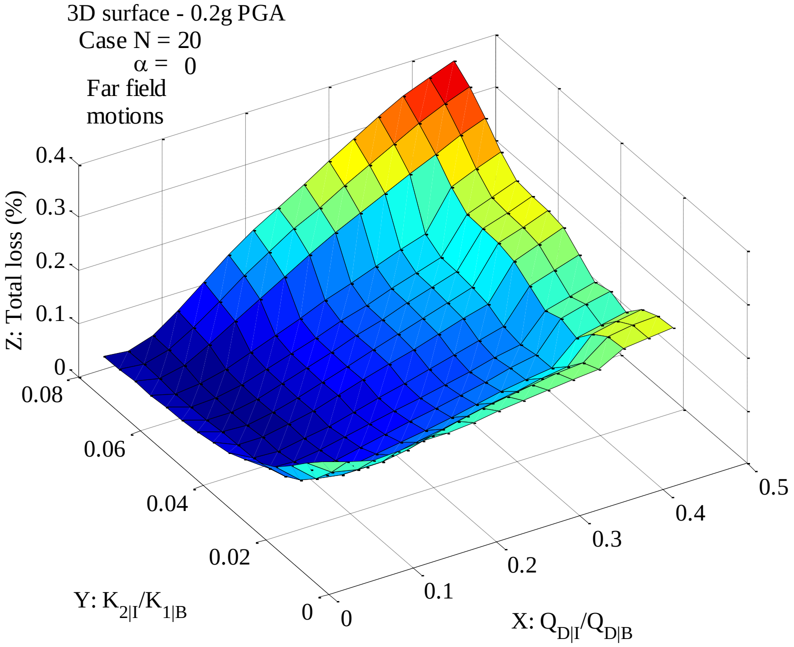

Fig. 5.7 Influence of Q_{d_I} and K_{2_I} of isolation devices (N = 20) on *TLR* with Far-field motions and α = 0.0 at 50%-in-5-years hazard level

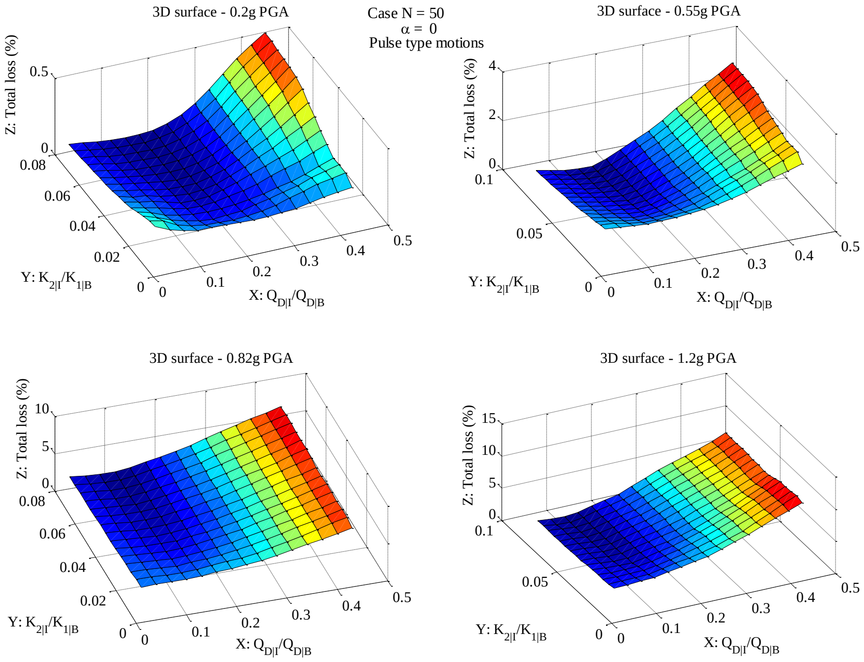

Fig. 5.8 Influence of Q_{d_I} and K_{2_I} of isolation devices (N = 50) on *TLR* with Pulse-type motions and α = 0.0 at different hazard levels

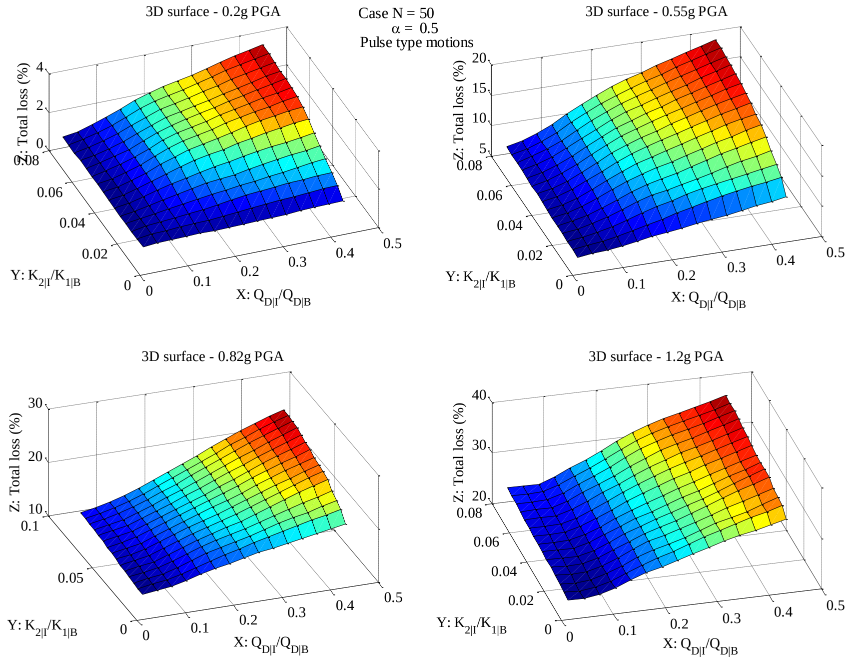

Fig. 5.9 Influence of Qd_I and K2_I of isolation devices (N = 50) on TLR with Pulse-type motions and α = 0.5 at different hazard levels

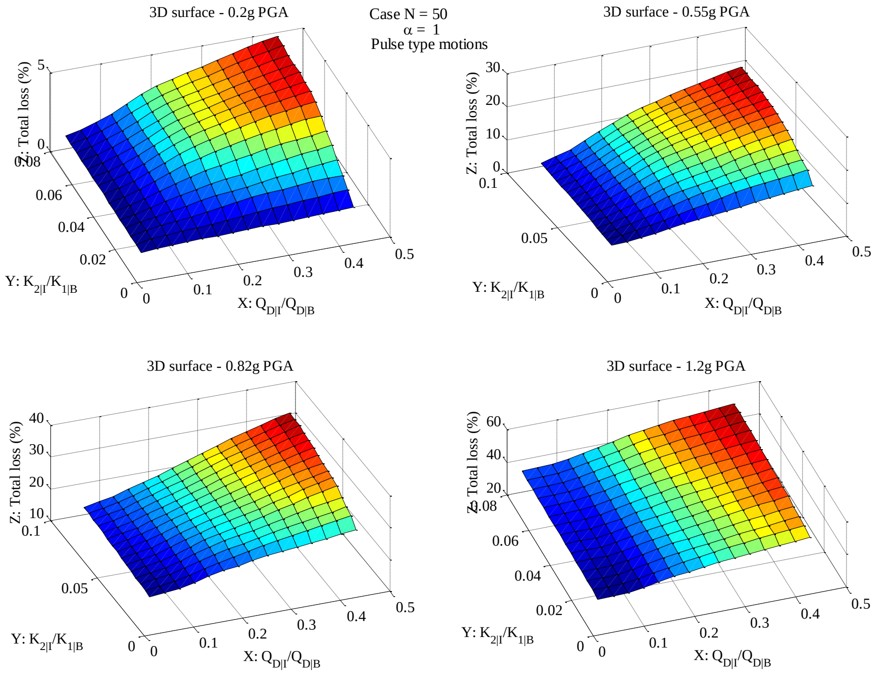

Fig. 5.10 Influence of Q_{d_I} and K_{2_I} of isolation devices (N = 50) on *TLR* with Pulse-type motions and α = 1.0 at different hazard levels

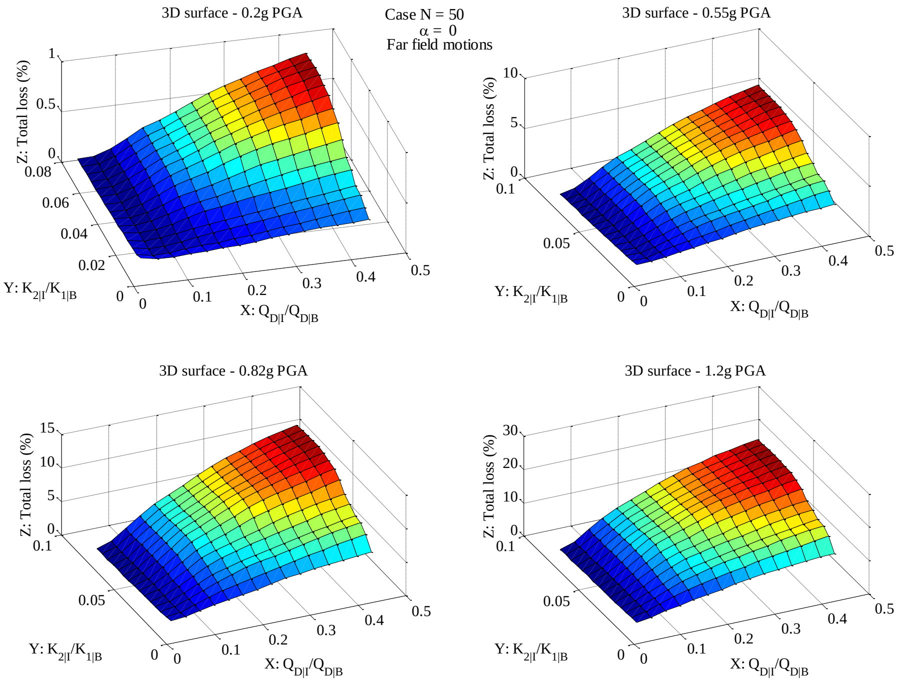

Fig. 5.11 Influence of Qd_I and K2_I of isolation devices (N = 50) on TLR with Far-field motions and α = 0.0 at different hazard levels

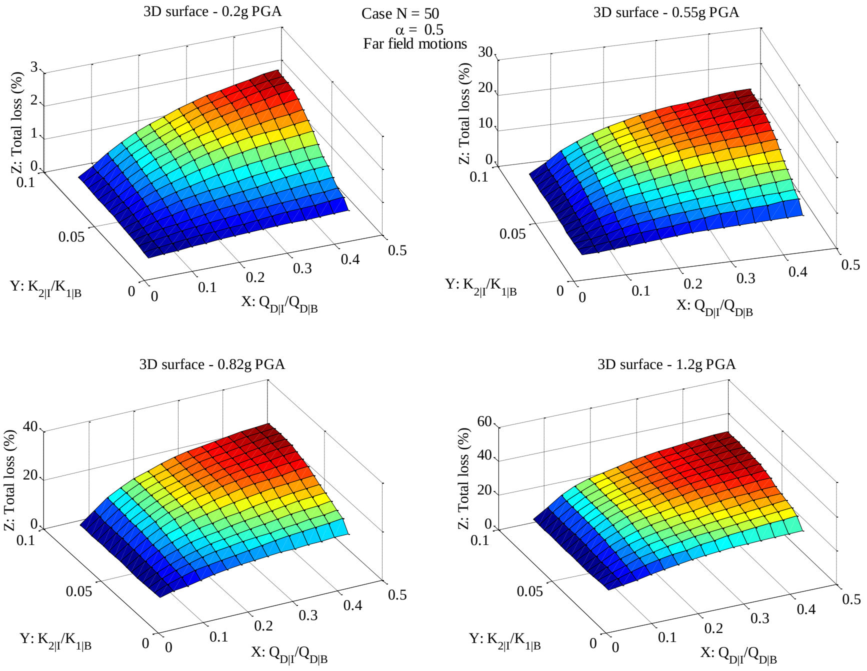

Fig. 5.12 Influence of Q_{d_I} and K_{2_I} of isolation devices (N = 50) on *TLR* with Far-field motions and α = 0.5 at different hazard levels

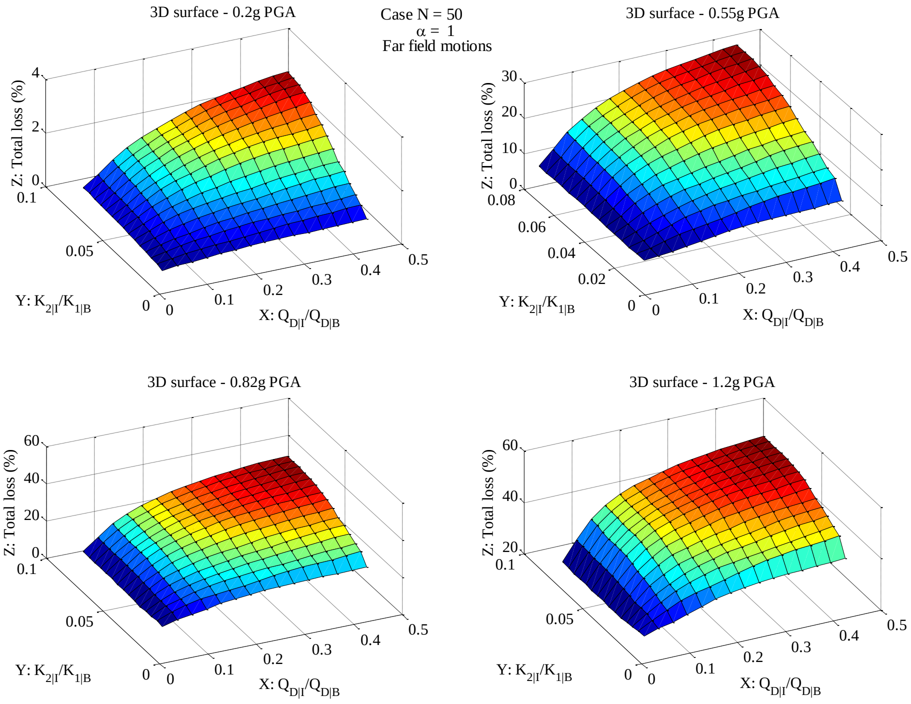

Fig. 5.13 Influence of Qd_I and K2_I of isolation devices (N = 50) on TLR with Far-field motions and α = 1.0 at different hazard levels

For a triple pendulum system with the stiffness ratios at around 50, Fig. 5.9 to Fig. 5.13 covers all the cases considering different α for non-structural component levels, different hazard intensity levels, and different types of ground motions. The approximated optimal parameter combinations for the isolation system as identified by the bottom points on these plots are summarized in Table 5.4. The presented data first indicate that the optimum range is not sensitive to stiffness ratio N. Then, tables show that the optimal bearing characteristic strength Q_{d_I} is averaged around 10% of Q_{d_B}. Pulse-type motions without non-structural components ($\alpha = 0$) may give larger Q_{d_I} up to 0.21 Q_{d_B}. However, since non-structural loss is usually unpreventable, Q_{d_I} optimal range is hence narrowed down to 0.03-0.12 of Q_{d_B}. One could also notice that small PGA (0.20g) hazard level may result some in different locations of the bottom points than other levels with a much larger return period. This is because the damage of isolation system becomes more crucial affecting the *TLR* for smaller hazard levels. Another important observation is that when considering non-structural components, K_{2_I} range is almost fixed at a small value 0.01. This means that in order to minimize the *TLR*, the study suggests to replace the isolation system rather than allowing earthquakes to damage the structural members.

Although the locations of the minimum points are slightly different for all the different situations, it can be generally concluded that the bearing with Q_{d_I} = (0.06-0.12) Q_{d_B} and K_{2_I} = 0.01 K_{1_B} would be a good choice for retrofitting the prototype building. The designed isolation system, which has Q_{d_I} / Q_{d_B} = 9.2% and K_{2_I} / K_{1_B} = 0.03, provides a reasonable design near to the optimized range from this study. Another observation is that K_{1_I} / K_{1_B} increases proportionally with stiffness ratio N. Since the elastic stiffness K_{1_I} is N times the post-yielding stiffness K_{2_I}, the results once more imply that K_{1_I} is insignificant whereas K_{2_I} plays a much more crucial role for optimal design of isolation devices. This matches the isolator design theory where the post yielding stiffness K_{2_I} dominates the bearing behavior for severe ground motions.

Table 5.4 Optimal range for design variables when structure experiences pulse-type motions

Stiffness ratio N = K_{1_I}/K_{2_I} = 10		0.20 (g)	0.55 (g)	0.81 (g)	1.20 (g)	Range
$\alpha = 0.0$	Q_{D_I}/Q_{D_B}	0.21	0.15	0.12	0.09	0.09 - 0.21
	K_{2_I}/K_{1_B}	0.08	0.08	0.08	0.08	0.08 - 0.08
	K_{1_I}/K_{1_B}	0.8	0.8	0.8	0.8	0.8 - 0.8
$\alpha = 0.5$	Q_{D_I}/Q_{D_B}	0.03	0.03	0.03	0.03	0.03 - 0.03
	K_{2_I}/K_{1_B}	0.01	0.01	0.01	0.01	0.01 - 0.01
	K_{1_I}/K_{1_B}	0.1	0.1	0.1	0.1	0.1 - 0.1
$\alpha = 1.0$	Q_{D_I}/Q_{D_B}	0.06	0.03	0.03	0.03	0.03 - 0.06
	K_{2_I}/K_{1_B}	0.01	0.01	0.01	0.015	0.01 - 0.015
	K_{1_I}/K_{1_B}	0.1	0.1	0.1	0.15	0.1 - 0.15
Stiffness ratio N = K_{1_I}/K_{2_I} = 20		0.20 (g)	0.55 (g)	0.81 (g)	1.20 (g)	Range
$\alpha = 0.0$	Q_{D_I}/Q_{D_B}	0.18	0.15	0.12	0.09	0.09 - 0.18
	K_{2_I}/K_{1_B}	0.08	0.08	0.08	0.08	0.08 - 0.08
	K_{1_I}/K_{1_B}	1.6	1.6	1.6	1.6	1.6 - 1.6
$\alpha = 0.5$	Q_{D_I}/Q_{D_B}	0.12	0.03	0.03	0.03	0.03 - 0.12
	K_{2_I}/K_{1_B}	0.01	0.01	0.01	0.01	0.01 - 0.01
	K_{1_I}/K_{1_B}	0.2	0.2	0.2	0.2	0.2 - 0.2
$\alpha = 1.0$	Q_{D_I}/Q_{D_B}	0.06	0.03	0.03	0.03	0.03 - 0.06
	K_{2_I}/K_{1_B}	0.01	0.01	0.01	0.01	0.01 - 0.01
	K_{1_I}/K_{1_B}	0.2	0.2	0.2	0.2	0.2 - 0.2
Stiffness ratio N = K_{1_I}/K_{2_I} = 50		0.20 (g)	0.55 (g)	0.81 (g)	1.20 (g)	Range
$\alpha = 0.0$	Q_{D_I}/Q_{D_B}	0.18	0.12	0.12	0.09	0.09 - 0.18
	K_{2_I}/K_{1_B}	0.08	0.08	0.08	0.08	0.08 - 0.08
	K_{1_I}/K_{1_B}	4	4	4	4	4 - 4
$\alpha = 0.5$	Q_{D_I}/Q_{D_B}	0.03	0.03	0.03	0.03	0.03 - 0.03
	K_{2_I}/K_{1_B}	0.03	0.01	0.01	0.01	0.01 - 0.03
	K_{1_I}/K_{1_B}	1.5	0.5	0.5	0.5	0.5 - 1.5
$\alpha = 1.0$	Q_{D_I}/Q_{D_B}	0.03	0.03	0.03	0.03	0.03 - 0.03
	K_{2_I}/K_{1_B}	0.01	0.01	0.01	0.01	0.01 - 0.01
	K_{1_I}/K_{1_B}	0.5	0.5	0.5	0.5	0.5 - 0.5

Table 5.5 Optimal range for design variables when structure experiences far-field motions

Stiffness ratio N = K_{1_I}/K_{2_I} = 10		0.20 (g)	0.55 (g)	0.81 (g)	1.20 (g)	Range
α = 0.0	Q_{D_I}/Q_{D_B}	0.06	0.03	0.03	0.03	0.03 - 0.06
	K_{2_I}/K_{1_B}	0.08	0.08	0.08	0.08	0.08 - 0.08
	K_{1_I}/K_{1_B}	0.8	0.8	0.8	0.8	0.8 - 0.8
α = 0.5	Q_{D_I}/Q_{D_B}	0.03	0.03	0.03	0.03	0.03 - 0.03
	K_{2_I}/K_{1_B}	***0.01****	***0.08***	***0.02***	***0.02***	0.01 - 0.08
	K_{1_I}/K_{1_B}	0.1	0.8	0.2	0.2	0.1 - 0.8
α = 1.0	Q_{D_I}/Q_{D_B}	0.03	0.03	0.03	0.03	0.03 - 0.03
	K_{2_I}/K_{1_B}	0.01	0.01	0.02	0.02	0.01 - 0.02
	K_{1_I}/K_{1_B}	0.1	0.1	0.2	0.2	0.1 - 0.2
Stiffness ratio N = K_{1_I}/K_{2_I} = 20		0.20 (g)	0.55 (g)	0.81 (g)	1.20 (g)	Range
α = 0.0	Q_{D_I}/Q_{D_B}	0.06	0.03	0.03	0.03	0.03 - 0.06
	K_{2_I}/K_{1_B}	0.065	0.08	0.08	0.08	0.065 - 0.08
	K_{1_I}/K_{1_B}	1.3	1.6	1.6	1.6	1.3 - 1.6
α = 0.5	Q_{D_I}/Q_{D_B}	0.03	0.03	0.03	0.03	0.03 - 0.03
	K_{2_I}/K_{1_B}	***0.02***	***0.045***	***0.01***	***0.08***	0.01 - 0.08
	K_{1_I}/K_{1_B}	0.4	0.9	0.2	1.6	0.2 - 1.6
α = 1.0	Q_{D_I}/Q_{D_B}	0.03	0.03	0.03	0.03	0.03 - 0.03
	K_{2_I}/K_{1_B}	***0.01***	***0.01***	***0.01***	***0.08***	0.01 - 0.08
	K_{1_I}/K_{1_B}	0.2	0.2	0.2	1.6	0.2 - 1.6
Stiffness ratio N = K_{1_I}/K_{2_I} = 50		0.20 (g)	0.55 (g)	0.81 (g)	1.20 (g)	Range
α = 0.0	Q_{D_I}/Q_{D_B}	0.03	0.03	0.03	0.03	0.03 - 0.03
	K_{2_I}/K_{1_B}	0.08	0.08	0.08	0.08	0.08 - 0.08
	K_{1_I}/K_{1_B}	4	4	4	4	4 - 4
α = 0.5	Q_{D_I}/Q_{D_B}	0.03	0.03	0.03	0.03	0.03 - 0.03
	K_{2_I}/K_{1_B}	0.01	0.02	0.03	0.03	0.01 - 0.03
	K_{1_I}/K_{1_B}	0.5	1	1.5	1.5	0.5 - 1.5
α = 1.0	Q_{D_I}/Q_{D_B}	0.03	0.03	0.03	0.03	0.03 - 0.03
	K_{2_I}/K_{1_B}	0.01	0.01	0.03	0.03	0.01 - 0.03
	K_{1_I}/K_{1_B}	0.5	0.5	1.5	1.5	0.5 - 1.5

* the tilted data implies that a wide range close to the values is also close to optimal

The *TLR* for pulse-type motions and for far-field motions are summarized in Table 5.6 and 5.7, respectively. By choosing *TLR* as the performance index for the isolated building, this study discovered that the major total loss of the isolated building system comes from non-structural components. This is true because the isolation design helps to significantly reduce the inter-story drifts, which protects the structural members. After optimization, it is obvious that the minimum total loss resulted from near fault pulse-type motions is larger than the total loss from far-field motions. Moreover, it has been proved again that with K_2 fixed at a specific range, N value has small impact in terms of *TLR*.

Table 5.6 Minimum loss from pulse-type motions

Stiffness ratio $N = K_{1\_I}/K_{2\_I} = 10$		0.20 (g)	0.55 (g)	0.81 (g)	1.20 (g)
$\alpha = 0.0$	Minimum Loss	0.0475	0.8665	1.8569	3.1654
$\alpha = 0.5$	Minimum Loss	0.4449	4.9161	12.1373	20.8383
$\alpha = 1.0$	Minimum Loss	0.5613	6.6987	17.1603	29.7979
Stiffness ratio $N = K_{1\_I}/K_{2\_I} = 20$		0.20 (g)	0.55 (g)	0.81 (g)	1.20 (g)
$\alpha = 0.0$	Minimum Loss	0.0289	0.6492	1.5038	2.6624
$\alpha = 0.5$	Minimum Loss	0.4613	4.9816	12.15	20.6912
$\alpha = 1.0$	Minimum Loss	0.6	6.8023	17.173	29.5618
Stiffness ratio $N = K_{1\_I}/K_{2\_I} = 50$		0.20 (g)	0.55 (g)	0.81 (g)	1.20 (g)
$\alpha = 0.0$	Minimum Loss	0.0082	0.4639	1.218	2.3568
$\alpha = 0.5$	Minimum Loss	0.4996	5.0801	12.331	20.6194
$\alpha = 1.0$	Minimum Loss	0.6785	6.9901	17.5198	29.5549

Table 5.7 Minimum loss from far-field motions

Stiffness ratio $N = K_{1\_I}/K_{2\_I} = 10$		0.20 (g)	0.55 (g)	0.81 (g)	1.20 (g)
$\alpha = 0.0$	Minimum Loss	0.0177	0.3944	0.9125	1.8339
$\alpha = 0.5$	Minimum Loss	0.2626	3.3991	8.0201	17.0322
$\alpha = 1.0$	Minimum Loss	0.301	4.7994	11.3366	24.5639
Stiffness ratio $N = K_{1\_I}/K_{2\_I} = 20$		0.20 (g)	0.55 (g)	0.81 (g)	1.20 (g)
$\alpha = 0.0$	Minimum Loss	0.0153	0.3674	0.8431	1.6636
$\alpha = 0.5$	Minimum Loss	0.2668	3.4168	7.9258	16.2316
$\alpha = 1.0$	Minimum Loss	0.3147	4.7844	11.2301	23.7958
Stiffness ratio $N = K_{1\_I}/K_{2\_I} = 50$		0.20 (g)	0.55 (g)	0.81 (g)	1.20 (g)
$\alpha = 0.0$	Minimum Loss	0.0118	0.2985	0.765	1.6056
$\alpha = 0.5$	Minimum Loss	0.2812	3.4866	8.3668	16.1135
$\alpha = 1.0$	Minimum Loss	0.3734	4.9724	12.1609	23.4974

Table 5.8 provides the *TLR* for from pulse-type motions with different non-structural values and isolation stiffness pre-post yielding stiffness ratios. For example, by assuming value of the non-structural components is same as structural components (i.e. $\alpha = 1.0$), the designed isolation system according to ASCE 7-05 reduced about 500% loss for small PGA motions (50%-in-5-

years) and reduced about 300% loss rare ground motions (2%-in-50-years). It is also noticed that the optimal designs gives even better protection of 770% loss for small PGA motions (50%-in-5-years) and reduced about 500% loss rare ground motions (2%-in-50-years). A noticeable 30-40% better performance can be improved from the optimal design over the designed isolation for this case with the presented PBEE framework.

Table 5.8 *TLR* (%) for different designs from pulse-type ground motions

Pulse-type Motions				
$\alpha = 0.0$				
Case	0.2 (g)	0.55 (g)	0.82 (g)	1.20 (g)
Fixed	1.56	12.04	23.56	38.72
Designed	0.07	1.26	2.58	4.21
Optimal when N=10	0.05	0.87	1.86	3.17
Optimal when N=20	0.03	0.65	1.50	2.66
Optimal when N=50	0.01	0.46	1.22	2.36
$\alpha = 0.5$				
Case	0.2 (g)	0.55 (g)	0.82 (g)	1.20 (g)
Fixed	4.50	31.10	47.84	59.13
Designed	0.68	7.13	17.87	27.65
Optimal when N=10	0.44	4.92	12.14	20.84
Optimal when N=20	0.46	4.98	12.15	20.69
Optimal when N=50	0.50	5.08	12.33	20.62
$\alpha = 1.0$				
Case	0.2 (g)	0.55 (g)	0.82 (g)	1.20 (g)
Fixed	5.97	40.63	59.98	69.34
Designed	0.99	10.06	25.51	39.37
Optimal when N=10	0.56	6.70	17.16	29.80
Optimal when N=20	0.60	6.80	17.17	29.56
Optimal when N=50	0.68	6.99	17.52	29.55

Table 5.9 provides the *TLR* for from far-field motions with different non-structural values and isolation stiffness pre-post yielding stiffness ratios. Compared with results from pulse-type motions, the *TLR* out of far-field motions is much smaller. However, the conclusion is the similar that the optimal isolation design is obviously desirable.

Table 5.9 *TLR* (%) for different designs from far-field ground motions

Far-field Motions				
α = 0.0				
Case	0.2 (g)	0.55 (g)	0.82 (g)	1.20 (g)
Fixed	0.92	9.22	15.45	33.94
Designed	0.04	0.92	1.99	3.20
Optimal when N=10	0.02	0.39	0.91	1.83
Optimal when N=20	0.02	0.37	0.84	1.66
Optimal when N=50	0.01	0.30	0.77	1.61
α = 0.5				
Case	0.2 (g)	0.55 (g)	0.82 (g)	1.20 (g)
Fixed	2.61	22.36	35.98	51.26
Designed	0.40	4.68	11.95	23.69
Optimal when N=10	0.26	3.40	8.02	17.03
Optimal when N=20	0.27	3.42	7.93	16.23
Optimal when N=50	0.28	3.49	8.37	16.11
α = 1.0				
Case	0.2 (g)	0.55 (g)	0.82 (g)	1.20 (g)
Fixed	3.19	28.20	42.95	55.95
Designed	0.59	6.84	17.22	29.97
Optimal when N=10	0.30	4.80	11.34	24.56
Optimal when N=20	0.31	4.78	11.23	23.80
Optimal when N=50	0.37	4.97	12.16	23.50

5.5 Concluding Remarks

This study applies the performance-based methodology to assess the seismic performance for the base isolated building system. First, a nonlinear numerical model was created that matches well with the shaking table tested steel moment frame building. Then, the seismic performance is evaluated with the established loss model that defines the total loss ratio of the building considering damage for structural, nonstructural and isolation system. Fragility curves are generated with PSDA method for base-fixed and base-isolated building using a large number of nonlinear time history analyses. A composite total loss ratio is developed to measure the global damage states of building systems. The proposed performance-based framework accounted for important sources of uncertainty in the ground motion hazard, the structural response, structural and nonstructural damage, repair costs, etc. Hence, this approach serves to build a link between the building performances with isolation parameters to design. The fragility function method with the established loss model builds up a good measurement to investigate the optimum isolation design for building systems. Therefore, this study not only shows the significant reduction of damage probability of building system from isolation system, but also identifies the optimal range of isolation parameters throughout an extensive parametric study. The optimal range covers various isolation devices of different post-yielding stiffness and characteristic strength. The study reveals distinguishable trends that lead to the following conclusions.

- This study presents the total loss ratio as the damage index for building seismic performance. Three *EDP*s used as the damage indicators are building inter-story drifts, floor accelerations and bearing drifts. The presented *TLR* equation is compatible with the general PBEE framework and provides an intuitive grasp of building damage.
- The three commonly used types of bearings are created with coupled Bouc-Wen model and their dynamic behaviors are illustrated in this study. The coupled Bouc-Wen model is implemented in OpenSees as a user element and can be used as an ideal material model for base-isolation systems.
- The optimal design parameters for isolation devices, which will result in the minimum damage probability for buildings for different hazard levels, are functions of structural properties and damage states. It is shown that the elastic stiffness of isolation devices, K_{1_I} is not sensitive in affecting the damage potential, which agrees with previous studies. In addition, the bearing yield strength remains in a reasonable range. The superstructure will experience minimum damage probability when the characteristic strength Q_{d_I} of isolation devices is about 0.06-0.12 Q_{d_B} and the post-yielding stiffness K_{2_I} is about 0.01 K_{1_B}. For a given isolation device, the

optimum design parameters can be determined based on the known value of pre- to post-yielding stiffness ratio N.

To conclude, the study offers an efficient way to select optimum isolation design parameters based on structural properties and performance objective while incorporating the uncertainties in ground motions and variability of structural properties under the fragility function framework.

6. DIMENSIONAL ANALYSIS OF INELASTIC STRUCTURES WITH NEGATIVE STIFFNESS DEVICES AND SUPPLEMENTAL DAMPING DEVICES

The NSF funded project group successfully designed and presented the NSD as a passive control device. Since 2009, three phases of lab experiments and numerical analysis have been performed to test the idea of negative stiffness as well as the presented design. However, since this is a brand new system, very little analysis in terms of studying the behavior of the proposed NSD system was made other than the lab tests and a limited number of numerical simulations. Chapter 4 of this study presented various seismic protective devices for building system, where the concept of the negative stiffness devices is new and innovative. This chapter systematically investigates the performance of the NSD system through a couple steps. First, the study proposes a numerical model incorporating the frictional damping effect for NSD that behaves closer to the tested NSD system. This study evaluates the performance of NSD under near-fault pulse type motions, whose effect on the dominant frequency and peak amplitude can be disarmed from the system itself. Then the dimensional analysis is performed based on a SDOF bilinear system to study the effectiveness of the NSD as well as the other parameters related with the system. Results show that, over certain range, the NSD can reduce acceleration without increasing the displacement of the system. Finally, a case study is performed to deepen the understanding of the NSD system.

6.1 Introduction

In the fifth section of Chapter 4, the numerical cubic model for NSD system has been proposed. The elastic behavior of such system can be fully captured from the model and four different stages according to horizontal drift of the NSD behavior have been introduced.

One more objective is to evaluate NSD's performance and to propose a design method for the NSD as well as the retrofitted system. Due to the NSD being a new concept that has not be standardized in the design code, this study introduces the performance-based design for the system. In terms of performance, previous studies found that several factors could influence the structural dynamic responses, among which the characteristics of the input motion are the critical ones. These input characteristics and the structure's mechanical properties (include NSD and damping system) together determine the final structural responses. To investigate only the NSD system without the disturbance of these ground input motion characteristics, a comprehensive study is conducted in this chapter under the framework of dimensional analysis.

NSD is implemented in single degree of freedom (SDOF) bilinear structures for the dimensional analysis. The SDOF system has four components (Fig. 6.1): the original bilinear system, the original damping, the supplemental damping to the system before implementing the NSD system, and the NSD system. The following sections of this study shows that the NSD should never be added to the original system unless sufficient amount of damping has been added first.

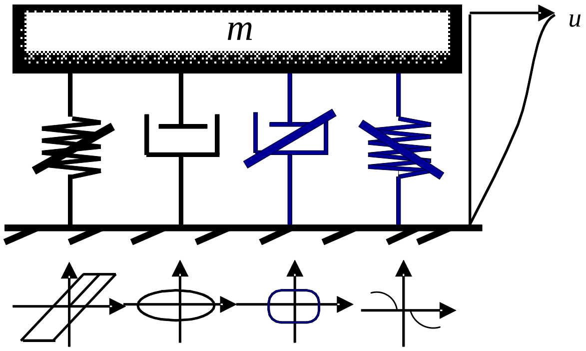

Fig. 6.1 Illustration of the single DOF system

The dimensional analysis has been proved effective and it has been introduced in Chapter 3. In order to evaluate the significance of NSD system, this study derives in section 6.5 a new set of dimensionless parameters based on existing ones to fully describe the normalized structural responses of the system equipped with NSD, which show remarkable order. As for ground motions, this study selected distinguishable pulses that represents the kinematic characteristics of devastating near-fault earthquakes. Individual case studies with some random and famous earthquakes are also presented to show the "NSD effect".

The structure of this part of work is summarized here: First, the study proposes the modified cubic model with slight friction damping and validated the model with the tested data. Then, the paper proposes the dimensional analysis framework for the NSD system. After that, the results from the dimensional analysis are presented, which reveals the effectiveness of the NSD system.

6.2 Modified Cubic Model with Friction Damping

A series of shaking table tests of the presented NSD mechanism were performed for the NSD project. Compared with the numerical elastic model presented in section 4.4, some frictional damping is observed from the shaking table tests. The presented model also allows one to add some damping into the system. It is obvious that the NSD model matches the tested data even better by incorporating the frictional damping behavior. However, considering the damping is usually small and sometimes can be neglected, the presented model sets this part as an option.

The damping is a nonlinear damping with the expression: $f_{d-}(\dot{u}) = c_{d-}\left|\dot{u}\right|^{\alpha-} sgn(\dot{u})$, where $sgn(\bullet)$ is the sign function. In this study, the authors fix the variable α^{-} at 0.2. The variable $c_{d}^{-} = 2m\omega_0\xi_{n}^{-}$ is the damping coefficient and the NSD damping ratio ξ_{n}^{-} is specified by the user. Testing data recommend ξ_{n}^{-} smaller than 5%. The NSD friction damping is different from the supplementary damping this study recommends for the NSD system in the later part of this study. It turns out that the NSD damping ratio ξ_{n}^{-} is 1/10 to 1/6 of the supplementary nonlinear damping ratio. Fig. 6.2 shows the NSD model incorporating the aforementioned friction damping.

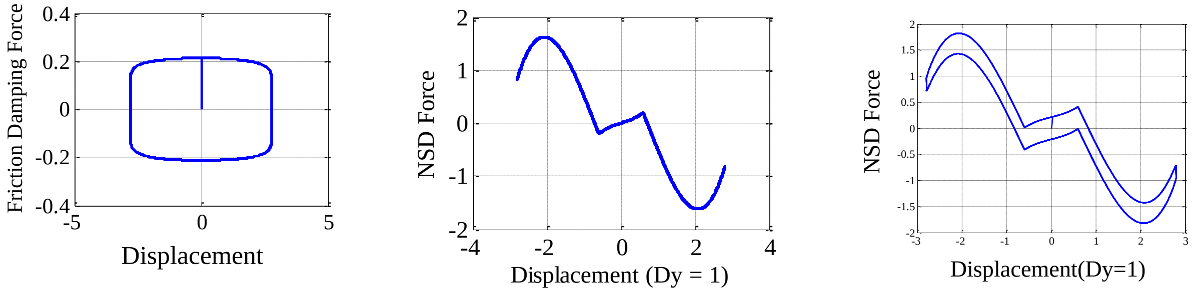

(a) the behavior of the NSD friction damping **(b)** the original NSD behavior **(c)** NSD with friction damping

Fig. 6.2 Refining the model by adding the option of small nonlinear damping

Fig. 6.3 demonstrates the comparison of the two models presented above. The dotted blue curve is the cubic model and it matches perfectly with the solid red line, which is defined by Eq. (4.39) to (4.42). The dotted grey curve corresponds to the NSD model considering the effect of friction damping.

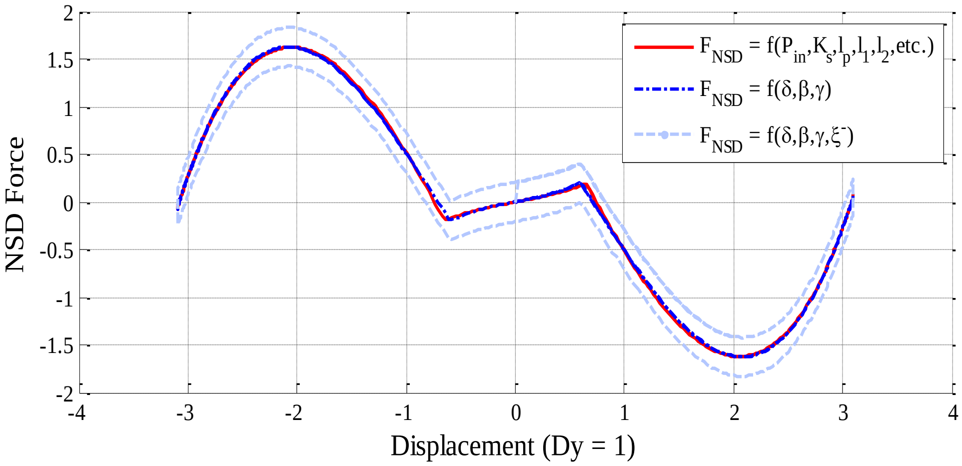

Fig. 6.3 Comparison of the two different numerical models

Fig. 6.3 shows a case when NSD behavior stops at the third stage. One could notice that the cubic model matches perfectly with the physical model from stage one to stage three. For the fourth stage that is not reached in this case, the cubic function produces a lower NSD magnitude than the physical model. However, the fourth stage is a rare case when an un-desirable extraordinary displacement occurs to the system. Later on in the study, it is shown that NSD should always work with sufficient supplemental damping as a combined system such that this stage 4 could be avoided.

6.3 Validation of the Presented Model

In this section, validations of the cubic numerical model are presented. First, the proposed numerical model is verified with two different numerical methods: the Runge-Kutta method and the Newmark method. Fig. 6.4 shows a designed NSD system excited by a pulse. Results show that these two solution methods lead to same numerical results. In this study, major analysis are performed using the Newmark integration approach, which is supposed to be computationally faster.

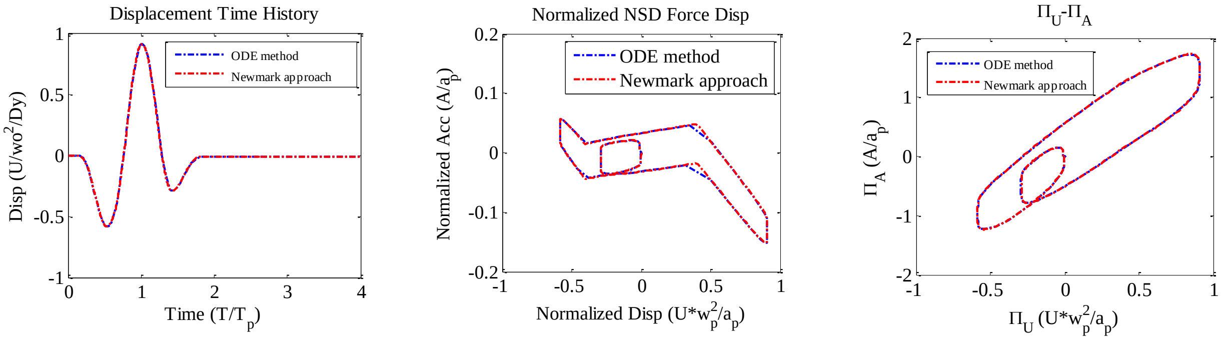

(a) comparison of the displacement time history **(b)** comparison of the hysteresis loop for NSD **(c)** comparison of the overall system force

Fig. 6.4 Results from different solution methods

Then, the cubic model is compared with the experimental data sampled from a shaking table test. The tested case is sampled from the second phase test of the project, which is a three-story building with the NSD system built at the base level shown in Fig. 6.5. The real time NSD force-displacement relationship is demonstrated in Fig. 6.6(a). It can be noticed that the system displacement reached the second stage. The cubic model simulates the system well as illustrated in Fig. 6.6(b). One could easily tell from the hysteresis loop that both the shape and magnitude of the presented model reasonably matches the tested data.

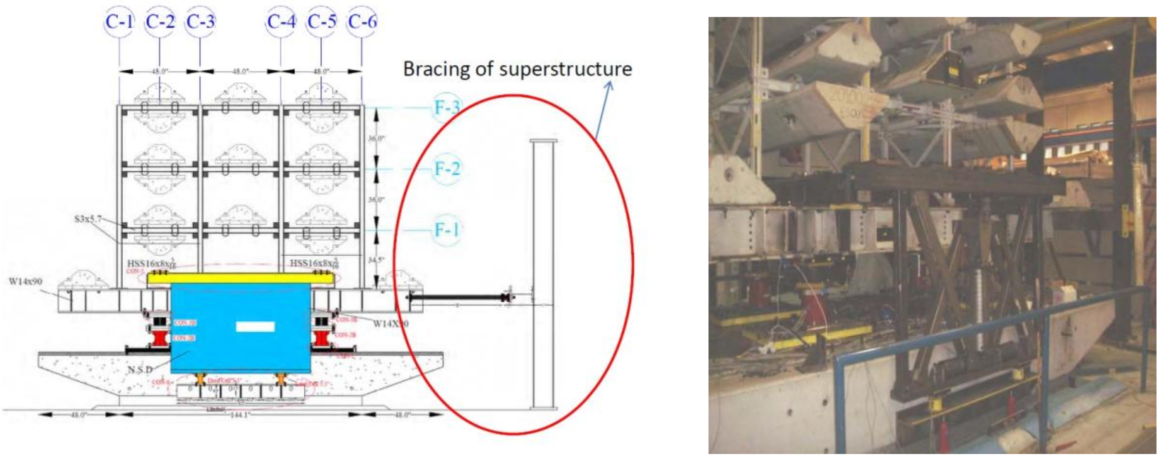

Fig. 6.5 Three-story test specimen to study NSD behavior (Development of Next Generation Adaptive Seismic Protection Systems Completion of first phase experiments for proof of concept, Aug 2010)

The comprehensive physical model given by Salis *et al*. (2012) and the cubic model are closely related: if one is given all the parameters for the physical model (P_{in}, K_s, l_p, l_1, l_2, k_{s1}, k_{s2}, etc.), there will be a corresponding and unique set of δ^-, β^-, and γ^- values for the cubic model. On the other hand, given a set of cubic parameters (i.e. δ^-, β^-, and γ^-), one could logically choose/design all the variables for the comprehensive model. As a brief summary, the cubic function model successfully reduced the NSD variables to three, which lays a foundation for the parametric study and dimensional analysis presented later in the chapter. With the help of the presented model, this work explores the effectiveness of negative stiffness system as well as the suggesting the optimal design criteria for its variables.

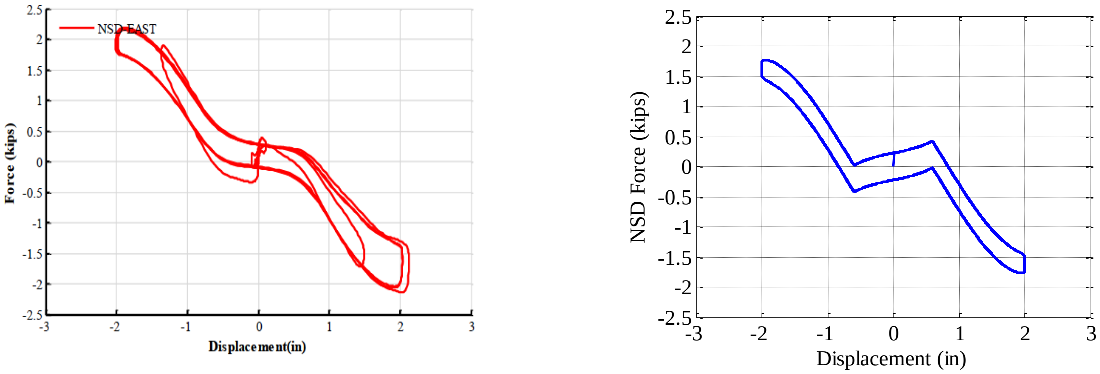

(a) Tested results **(b)** Simulated results

Fig. 6.6 Matching the cubic model with tested results

6.4 Case Studies for NSD Specimen

After the detailed introduction of the numerical models for NSD, this section provides individual cases that reflect the working algorithm of NSD system. The behavior of the device is demonstrated from time history analysis and force-to-displacement plots. In order to represent general civil structures, this study selects a SDOF bilinear system with the structure properties provided in Table 6.1:

Table 6.1 Sample SDOF structural properties for NSD study

variable	*Mass*	D_y	w_o	ε	ξ	$\Pi_{\xi n}$	α	δ	β	γ	$\xi^{-}/\Pi_{\xi n}$
units	(kg)	(m)	(rad/sec)	-	-	-	-	-	-	-	-
	5000	0.036	10.472	0.06	2.50%	20%	0.4	0.3	0.5	3	10%

Three case studies have been presented corresponding to three different ground excitations. The earthquake ground motions selected are the 2011 Tōhoku earthquake and the well known 1940 El Centro quake. In addition, a type-A pulse with a smaller frequency is selected. Fig 6.7 shows the time history of the selected ground motions. Since pulses are explained in detail in section 6.5, the time-history of the type-A pulse is not illurstrated here.

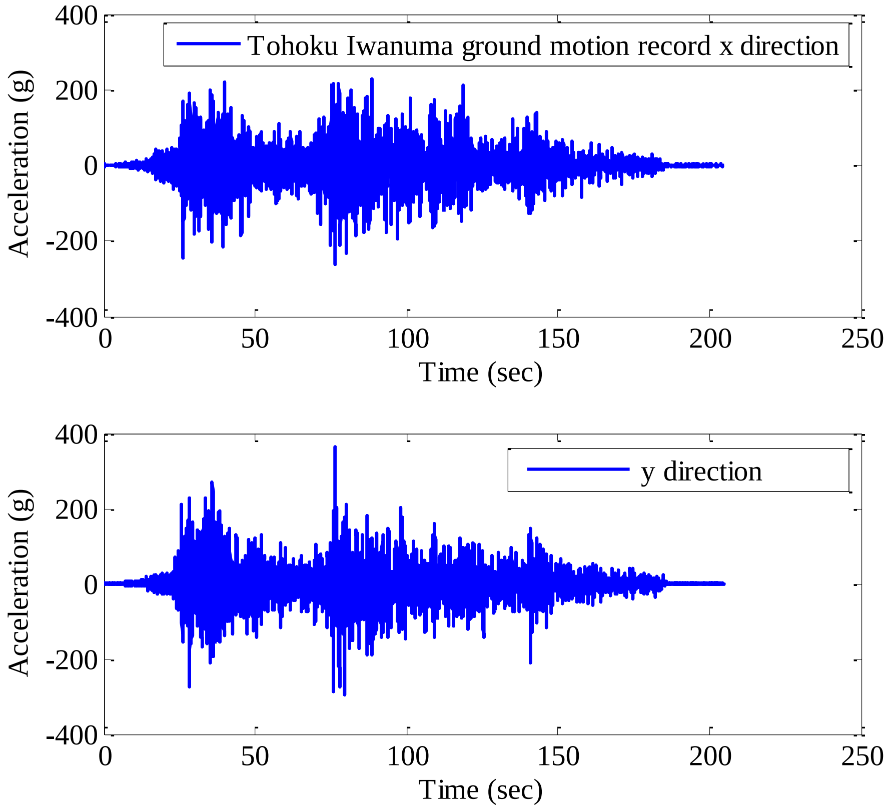

(a) Two direction time history of 2011 Tōhoku ground motion, Japan

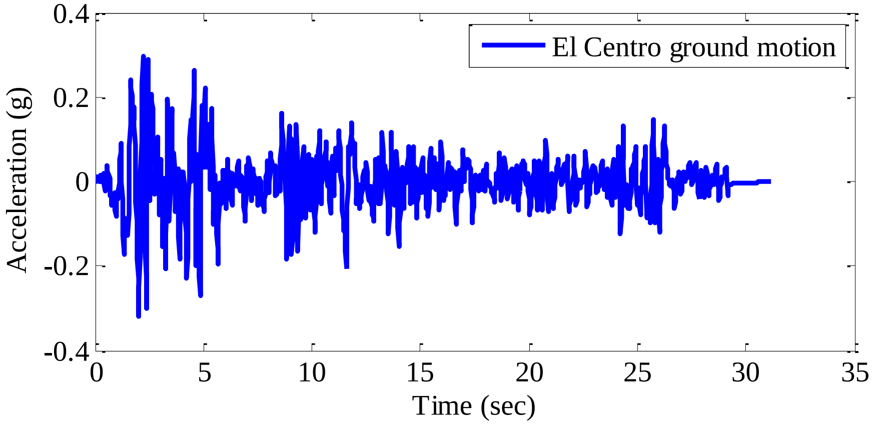

(b) Time history of 1940 El Centro ground motion, California, USA

Fig. 6.7 Time history of the studied ground motions

In addition, the detailed descriptions of these motions are summarized in Table 6.2:

Table 6.2 Ground motion Characteristics

Motions	ω_p	a_p	Δt	Θ_o
	(rad/s)	*(g)*	*(sec)*	-
Tōhoku Iwanuma	14.45	0.409	0.01	0
El Centro	10.68	0.3188	0.02	0
Pulse A	5	0.4	0.01	0

Fig. 6.8 shows the simulated results for the system excited with Tōhoku earthquake. In order to test the NSD effectiveness, analyses were performed in three different steps: The first step analyzes the nonlinear response of the original bilinear system; second, before adding NSD, this study adds sufficient damping into the system; at last, the NSD is attached into the system. Fig. 6.9 shows simulated results for the El Centro earthquake. The solid black narrow curve corresponds to the step where only the bilinear system is excited with the earthquake force. This gives the initial stage when no controls are introduced to the system. The thick dotted red curve shows the bilinear system behavior with the help of nonlinear damping system. The solid thick

blue curve correspond to the step when both nonlinear damping and the NSD system is added onto the original bilinear system.

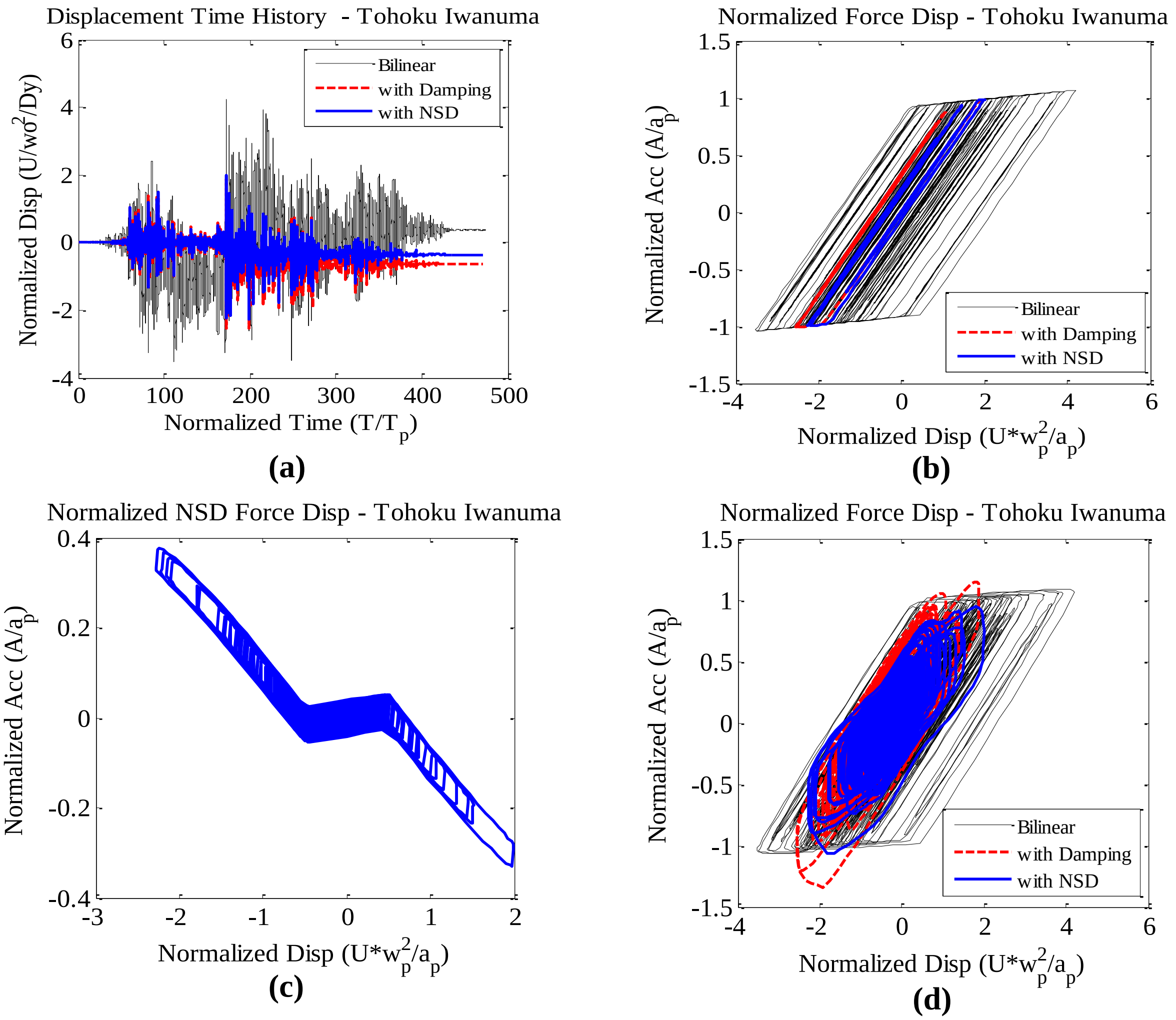

Fig. 6.8 Simulated results for the Tōhoku ground motion- (a) displacement time history; (b) the system hysteresis loop; (c) the NSD force-displacement relationship; (d) the internal force-displacement curve for the original system

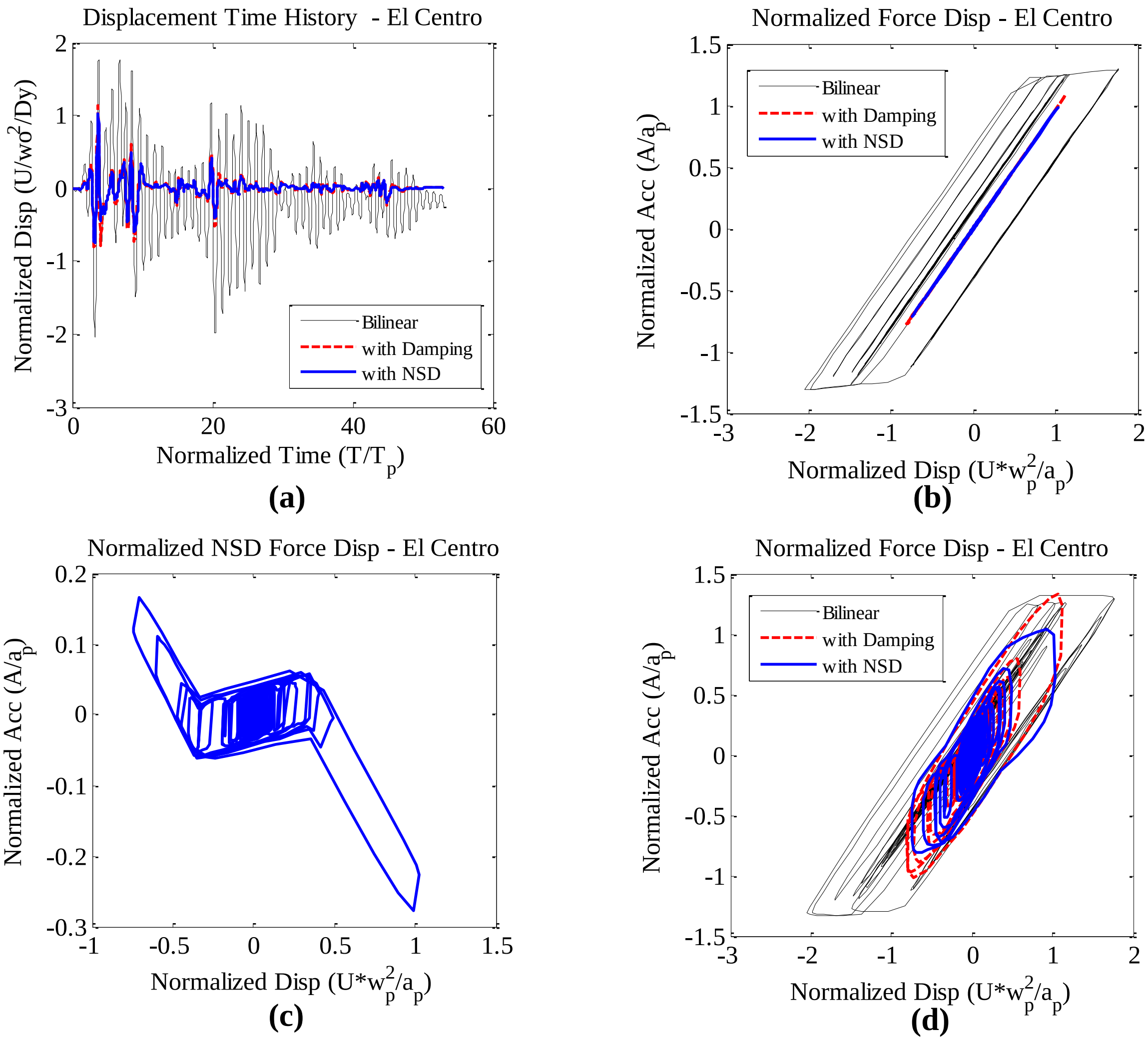

(a) **(b)**

(c) **(d)**

Fig. 6.9 Simulated results for the El Centro ground motion - (a) displacement time history; (b) the system hysteresis loop; (c) the NSD force-displacement relationship; (d) the internal force-displacement curve for the original system

These two cases demonstrate clearly the benefit of the NSD system. In the Tōhoku Iwanuma case, when the supplemental damping is added to the original system, the displacement is obviously reduced. However, the acceleration was increased to a larger level. This is because the effect of nonlinear damping will sometimes cause the increase of a bilinear system's acceleration. Zhang and Xi (2012) have further discussed this effect. This condition is resolved by adding the NSD: the combination of nonlinear damping and the NSD reduce not only the displacement, but also the absolute acceleration of the system. In addition to the displacement and acceleration, one could noticed that the NSD reduced the system's residual drift. This wasn't achieved by only adding the nonlinear damping to the system. For the El Centro case, the NSD system is also effective by reducing the around 50% of original displacement and 30% of original acceleration.

In fact, NSD does not always benefit for all different situations. There are still a few cases that NSD has very little benefit. In addition, if not properly designed, NSD might be harmful such as causing unstable issues to the original system. Fig. 6.10 corresponds a case that the proposed type-A pulse excites the system. One could notice from Fig. 6.10(d) that the system receives only a minor decrease of both peak displacement and peak acceleration, which means the NSD system renders little help despite the NSD had been triggered to the second stage for this specific case.

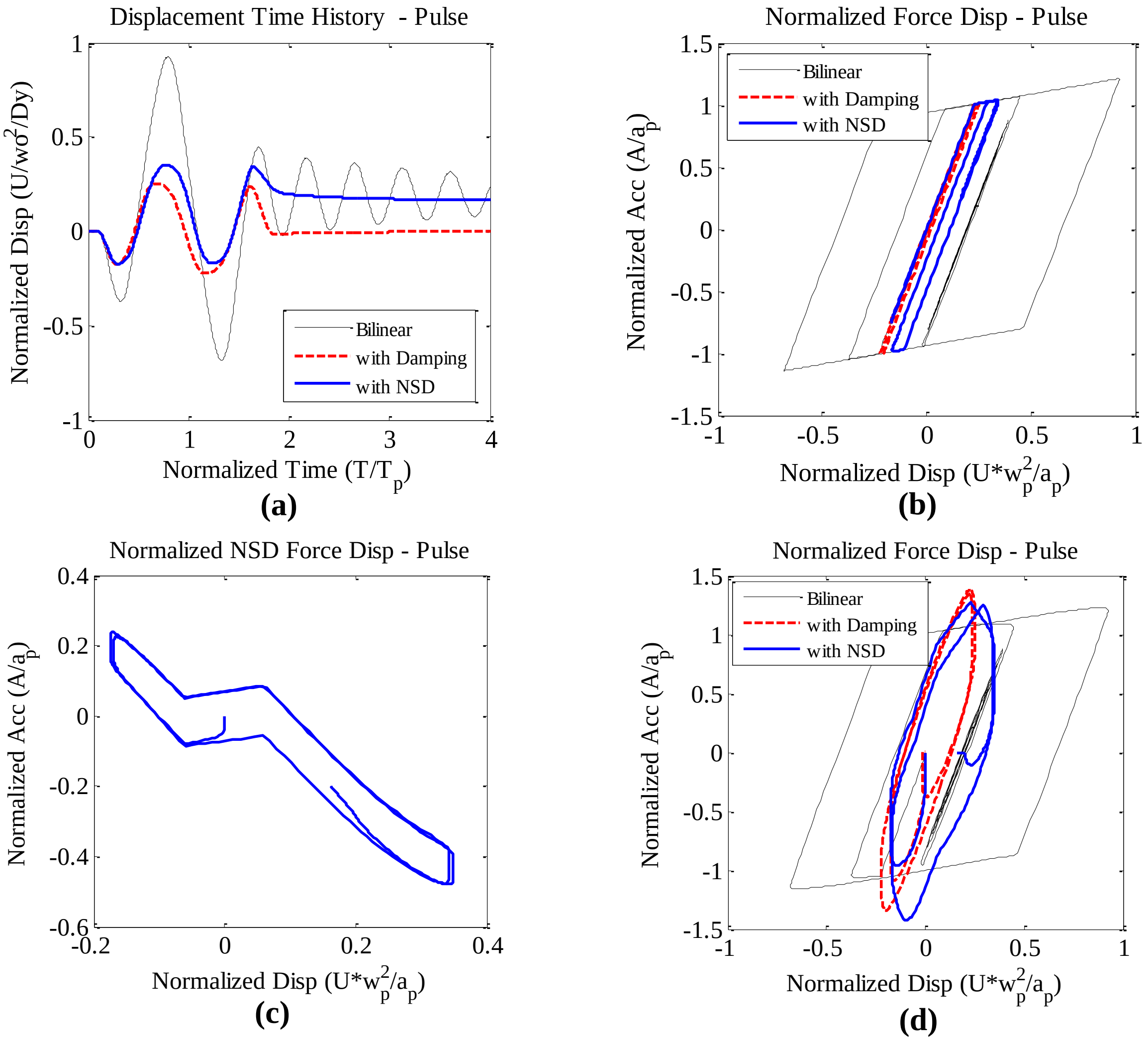

Fig. 6.10 Simulated pulse A results - a case when NSD provides little benefit - (a) displacement time history; (b) the system hysteresis loop; (c) the NSD force-displacement relationship; (d) the internal force-displacement curve for the original system

6.5 Simulation Framework for Parametric Studies

6.5.1 Characteristics of Near-fault Ground Motions and Distinguishable Pulses

Researchers have observed from the increasing database of ground motion records that near-fault ground motions of major earthquakes usually contain distinguishable velocity and displacement pulses (Bertero 1976, Bertero *et al.* 1978, Mavroeidis and Papageorgiou 2003). The near-fault ground motion are hard to avoid and would be destructive to most civil structures if the peak ground velocity is the integral of a distinguishable acceleration pulse (Bertero 1976, Makris and Black 2004b). Alavi and Krawinkler (2004) demonstrated that fixed-base structures with a period longer than the pulse period behave very differently from structures with a shorter period. Since NSD elongates the fundamental natural period of a civil structure, cautions need to be exercised when evaluating the NSD effects on the seismic demands imposed by near-fault shakings.

The theoretical justifications in seismology (Bolt 1971, Somerville *et al.*) have confirmed and highlighted the presence of severe energetic pulses in the near-fault region of an earthquake due to either rupture directivity or tectonic fling. After that, various researchers have developed closed-form approximation models to capture the leading kinematic characteristics of near-fault ground motions (Hall *et al*. 1995, Mavroeidis and Papageorgiou 2003, Makris and Chang 2000). Tang and Zhang (2011) proposed an approach to identify the pulse-like motions based on the congruence relationship between the response spectrum and the established dimensionless Π-response spectrum. On the other hand, for earthquake motions that do not exhibit distinguishable pulses, the potential hazard of these motions to the civil structures are much less compared with the pulse-type motions. At the same time, one could estimate the frequency content on the predominant period of the ground motion.

This study resembles near-fault ground motions with the cycloidal pulse models proposed by Makris and Chang (2000). The model is physically realizable for its zero final velocity and finite acceleration. The cycloidal pulse model classifies pulse excitations into three distinctive types, i.e. type A, type B and type C_n. A certain type of pulse contains only two input parameters, the acceleration amplitude, a_p (or velocity amplitude, v_p) and period T_p (or often used frequency, ω_p). Fig. 6.11 shows the four different types of pulses used in this study: Pulse type A, B, C_1 and C_2. Type A pulse (one-sine acceleration pulse) results in a forward ground displacement that is not recovered at the end of earthquake. Type B pulse (one-cosine acceleration pulse) is characterized by a forward-back velocity time history and a fully recovered ground displacement at the end of earthquake. Type C_n pulse exhibits n main cycles in its displacement history.

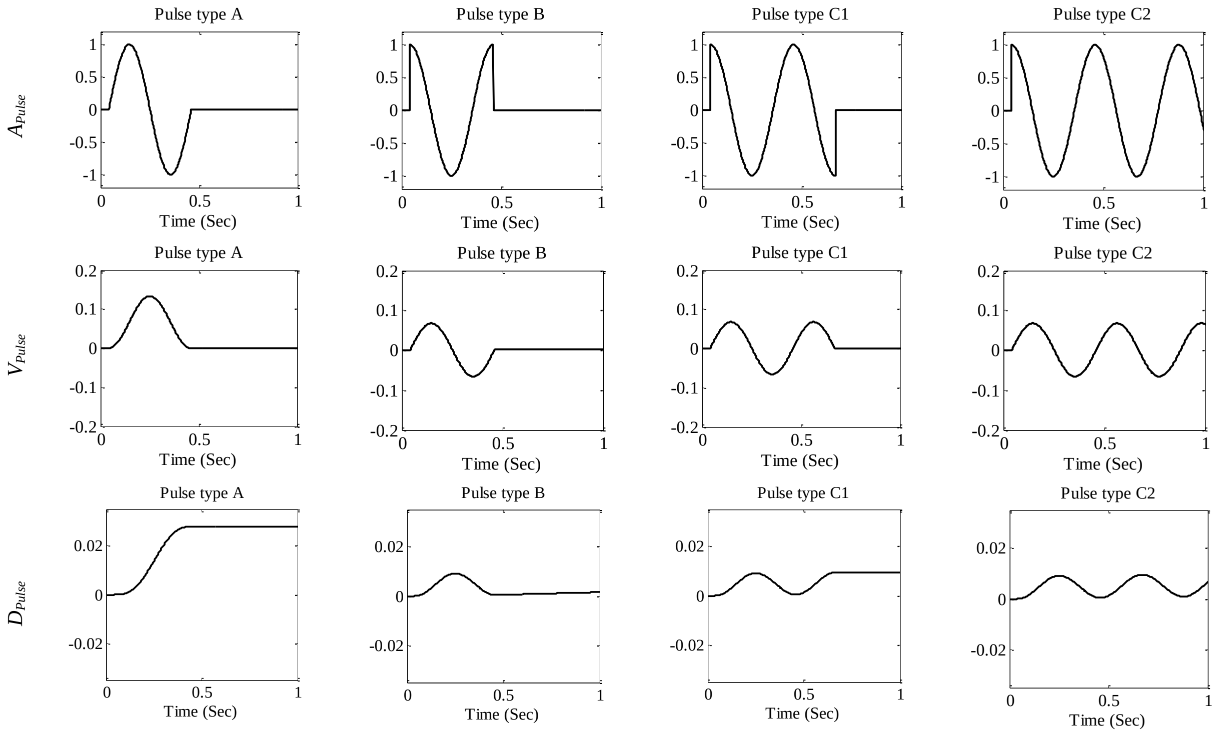

Fig. 6.11 Acceleration, velocity, and displacement for pulse type A,B,C_1, and C_2

6.5.2 Dimensional Analysis of Nonlinear Structure with NSD

Traditional nonlinear analysis for a fixed structure usually produces different or scattered inelastic structural responses from time history analysis using recorded ground motions. As shown from Chapter 3, the dimensional analysis is an effective method to interpret inelastic response especially for near fault pulse type motions. This study derives the dimensionless parameters for the proposed NSD system through rigorous dimensional analysis and examines the significance of these parameters in terms of affecting the structural responses.

By normalizing the inelastic displacement demand with respect to the energetic length scale of ground motions, the similar response (i.e. independent of the intensity of ground motions) can be obtained. The dimensional analysis of a bilinear SDOF system is briefly discussed to provide the logical and mathematic background behind the proposed numerical model for NSD system in this chapter.

For a SDOF bilinear system (Fig 6.1) subject to a general ground acceleration that can be characterized by characteristic amplitude a_p and characteristic frequency ω_p (or equivalently $T_p = 2\pi / \omega_p$), its equation of motion is expressed as:

$$m\ddot{u}(t) + c\dot{u}(t) + f_d(\dot{u}) + f_s(u) + f_{NSD}(u) = -m\ddot{u}_g(t) \tag{6.1}$$

where m is the system mass, c is the inherent structural damping (linear) and $\ddot{u}_g(t)$ is the ground acceleration input. The term $f_s(u)$ represents the inelastic structural force, whose stiffness drops to usually less than 10% after the structure yields. To fully characterize a bilinear system, one shall identify its yielding displacement D_y or characteristic strength Q_D, its pre-yielding stiffness K_1, and the post-yielding stiffness K_2. The nonlinear damping force $f_d(\dot{u})$ from

Eq. (6.1) is defined as $f_d(\dot{u}) = c_d |\dot{u}|^{\alpha} sign(\dot{u})$, where c_d is the damping factor of the nonlinear damper (in the units of $N/(ms^{-1})^{\alpha}$) and α is a constant controlling damper nonlinearity ranging from 0 to 1. The NSD force is defined in detail in section 4.4. By dividing Eq. (6.1) by the structural mass for both sides of the equation, it can also be written in another form:

$$\ddot{u}(t) + 2\xi\omega_0\dot{u}(t) + 2\xi_n\omega_0 |\dot{u}|^{\alpha} sign(\dot{u}) + \omega_0{}^2 D_y \tilde{f}_s(u,\dot{u}) + f_{NSD}(u)/m = -a_p g(\omega_p t) \tag{6.2}$$

where $\omega_0 = \sqrt{k_e/m}$ is the pre-yielding circular natural frequency of the structure, $\xi = c/(2m\omega_0)$ and $\xi_n = c_d/(2m\omega_0)$ are the damping ratio of linear and nonlinear viscous damping respectively. The function $\tilde{f}_s(u,\dot{u})$ describes the nonlinear resisting force–displacement relationship that depends on the yield displacement D_y and post-yield stiffness hardening ratio ε_s. The NSD term involves three terms, x_o^-, Q^-, and x_r^- (expressions of δ^-, β^-, and γ^-). The structural response *u(t)* from Eq. (6.2) is therefore a function of eleven independent parameters involved:

$$u(t), a(t) = f(\omega_0, \xi, \xi_n, D_y, \alpha, \varepsilon, a_p, \omega_p, x_o{}^-, Q^-, x_r{}^-) \tag{6.3}$$

According to the Buckingham's Π-theorem and choosing a_p and ω_p as the repeating variables, the number of independent dimensionless Π-parameters is determined as: (11 variables)-(2 reference dimensions) = 9 Π-parameters. Eq. (6.3) can be reformulated in terms of the dimensionless parameters as:

$$\Pi_u, \Pi_a = \varphi(\Pi_\omega, \Pi_\xi, \Pi_{\xi,n}, \Pi_{Dy}, \Pi_\alpha, \Pi_\varepsilon, \Pi_{D_o{}^-}, \Pi_{Q^-}, \Pi_{D_r{}^-}) \tag{6.4}$$

where $\Pi_u = u(t)\omega_p^2 / a_p$ is the structural displacement normalized by the characteristic length scale of ground motion, $\Pi_a = a(t)/a_p$ is the normalized acceleration, $\Pi_\omega = \omega_0/\omega_p$ is the dimensionless frequency ratio, $\Pi_\xi = \xi$ is the linear viscous damping ratio, $\Pi_{Dy} = D_y \omega_p^2 / a_p$ is normalized yielding displacement, $\Pi_\alpha = \alpha$ is the fractional exponent of nonlinear viscous damper and $\Pi_\varepsilon = \varepsilon$ is the post- to pre-yielding ratio. Zhang and Xi (2012) gives an accurate expression of the dimensionless nonlinear damping ratio as:

$$\Pi_{\xi,n} = \frac{\xi_n}{(a_p / \omega_p)^{1-\alpha}} = \frac{c_d}{2m\omega_0 (a_p / \omega_p)^{1-\alpha}} \tag{6.5}$$

Table 6.3 summarizes the identified dimensionless *Π*-parameters for bilinear structure, linear and nonlinear damping system, and the NSD system.

Table 6.3 *Π*-parameters for bilinear structure, linear and nonlinear damping system, and NSD system

	Target of the dimensionless analysis	formula	Range
Π_u	relative displacement	$u(t)\omega_p^2/a_p$	-
Π_a	absolute acceleration	$a(t)/a_p$	-
Π_ω	natural frequency	ω_o/ω_p	0.1 - 10.0
Π_{Dy}	yielding displacement	$D_y\ \omega_p^2/a_p$	0.01 - 5
Π_ε	post yielding stiffness ratio	ε	0.01 - 0.2
Π_ξ	linear damping ratio	ξ	0.02 - 0.1
Π_α	nonlinear damping coefficient	α	0.1 - 1.0
$\Pi_{\xi n}$	nonlinear damping ratio	$C_d/(2\ m\ \omega_o)/(a_p/\omega_p)^{1-\alpha}$	0.02 - 0.35
Π_Q	NSD internal force	$(F_{NSD})/m/a_p$	-
Π_{xo}-	NSD gap length	$\delta^-\ D_y\ \omega_p^2/a_p$	-
Π_Q-	NSD peak amplitude	$\beta^-\ Q_D/ma_p$	-
Π_{xr}-	NSD relaxation length	$\gamma^-\ D_y\ \omega_p^2/a_p$	-

The study in the following part of this work fixes four *Π*-parameters $\Pi_\omega, \Pi_\xi, \Pi_\alpha, \Pi_\varepsilon$ as they usually don't change significantly for different systems. For example, the linear damping ratio $\Pi_\xi = \xi$ is fixed at 1.5% and the coefficient Π_α is equal to 0.4 for the nonlinear damping. The remaining five terms, Π_{Dy}, $\Pi_{\xi n}$, Π_{xo}-, Π_Q-, Π_{xr}- are important variables that affects the NSD system.

Therefore, extraordinary focus is placed on these five terms as well as different pulse type motions, which as a whole controls the fundamental NSD performance.

6.6 Simulated Results

In this section, a sequence of nonlinear acceleration and displacement spectra are presented for the four different pulse types mentioned above. The performance of NSD system is evaluated using different approaches. All of these approaches in this section fix the normalized NSD terms, (i.e. Π_{xo}-, Π_{Q}-, and Π_{xr}-). First approach fixes the nonlinear damping ratio $\Pi_{\xi n}$, aiming at working out an optimal range for Π_{Dy} over which NSD produces its best effect. Second approach compares effectiveness of NSD with both linear and nonlinear damping. Third approach the damping ratio $\Pi_{\xi n}$ is modified to provide an optimal range for the supplementary damping.

6.6.1 NSD Effectiveness

The first approach explores type of system that NSD system receives the best effect. Similar to the case studies, this part of work compares the results from bilinear system, bilinear system with nonlinear damping, and bilinear system with NSD plus nonlinear damping. First, the authors fix the NSD parameters at $\delta^{-} = 0.3$, $\beta^{-} = 0.5$, and $\gamma^{-} = 3$, which corresponds to a fixed set of Π_{xo}-, Π_{Q}-, Π_{xr}- values in the dimensional analysis. With NSD parameters fixed, different Π_{Dy} values are selected to detect the features of bilinear systems that implementing the NSD system would be most effective. First, Π_{Dy} is chosen from 0.1 to 10.0 and the response spectra are plotted in Fig. 6.12. Smaller Π_{Dy} indicates the structural system is highly nonlinear while larger Π_{Dy} (e.g. Π_{Dy} =10) represents an essential linear system.

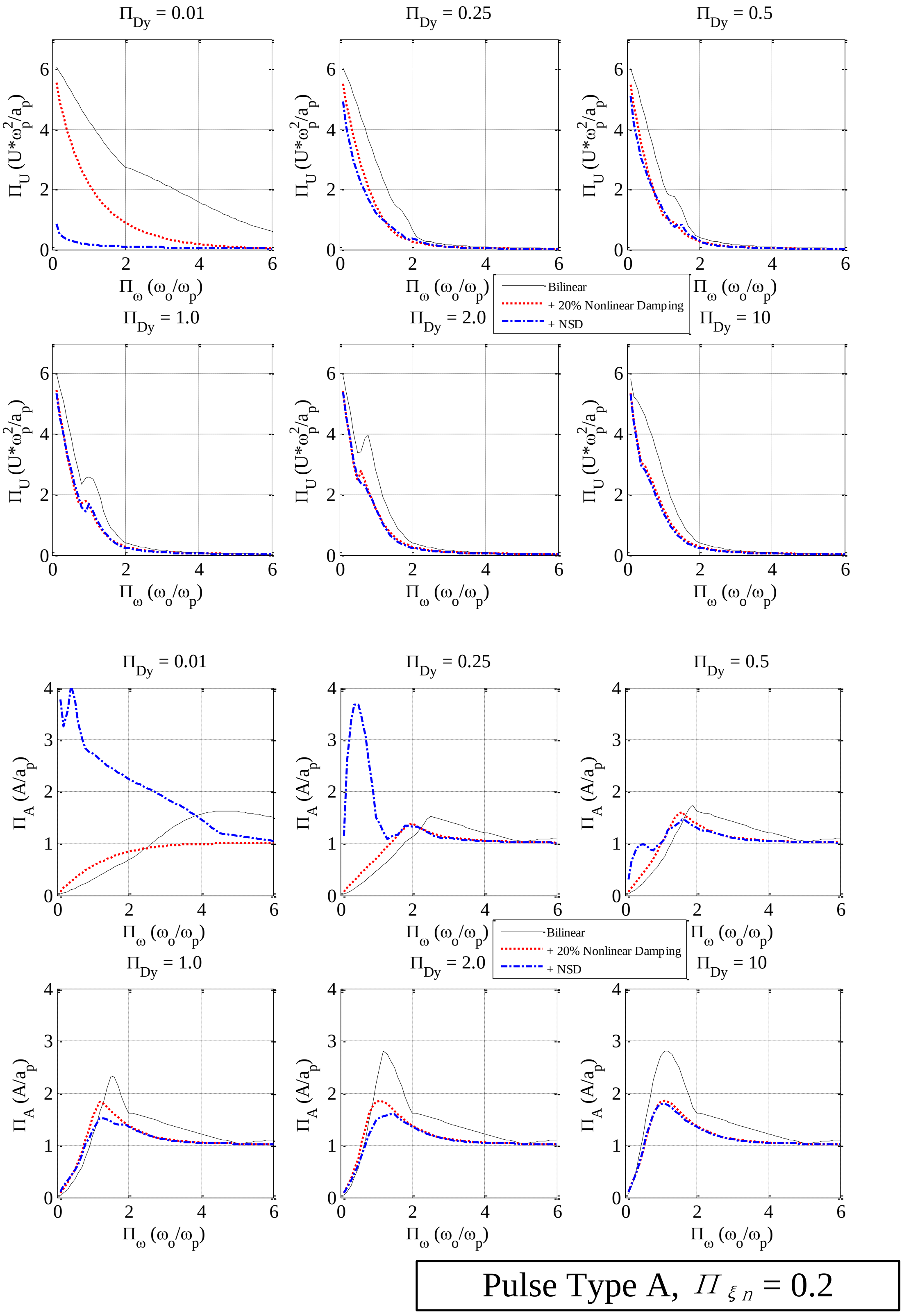
Π_{Dy} = 0.01
Π_{Dy} = 0.25
Π_{Dy} = 0.5
Π_{Dy} = 1.0
Π_{Dy} = 2.0
Π_{Dy} = 10
$\Pi_U\ (U^*\omega_p^2/a_p)$
$\Pi_A\ (A/a_p)$
$\Pi_\omega\ (\omega_o/\omega_p)$
0
1
2
3
4
6
Bilinear
+ 20% Nonlinear Damping
+ NSD
Pulse Type A, $\Pi_{\xi n} = 0.2$

(a)

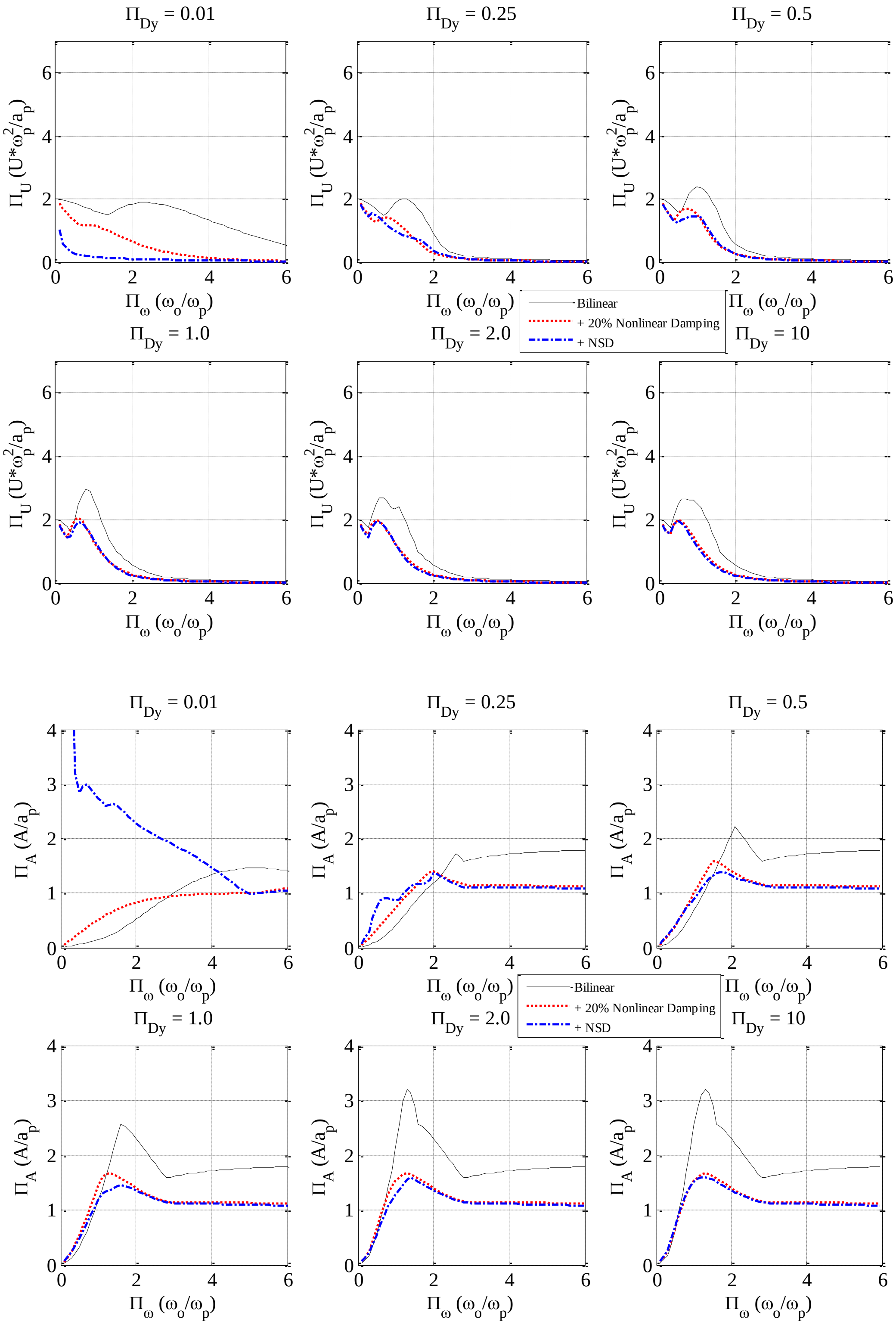

Pulse Type B, $\Pi_{\xi n} = 0.2$

(b)

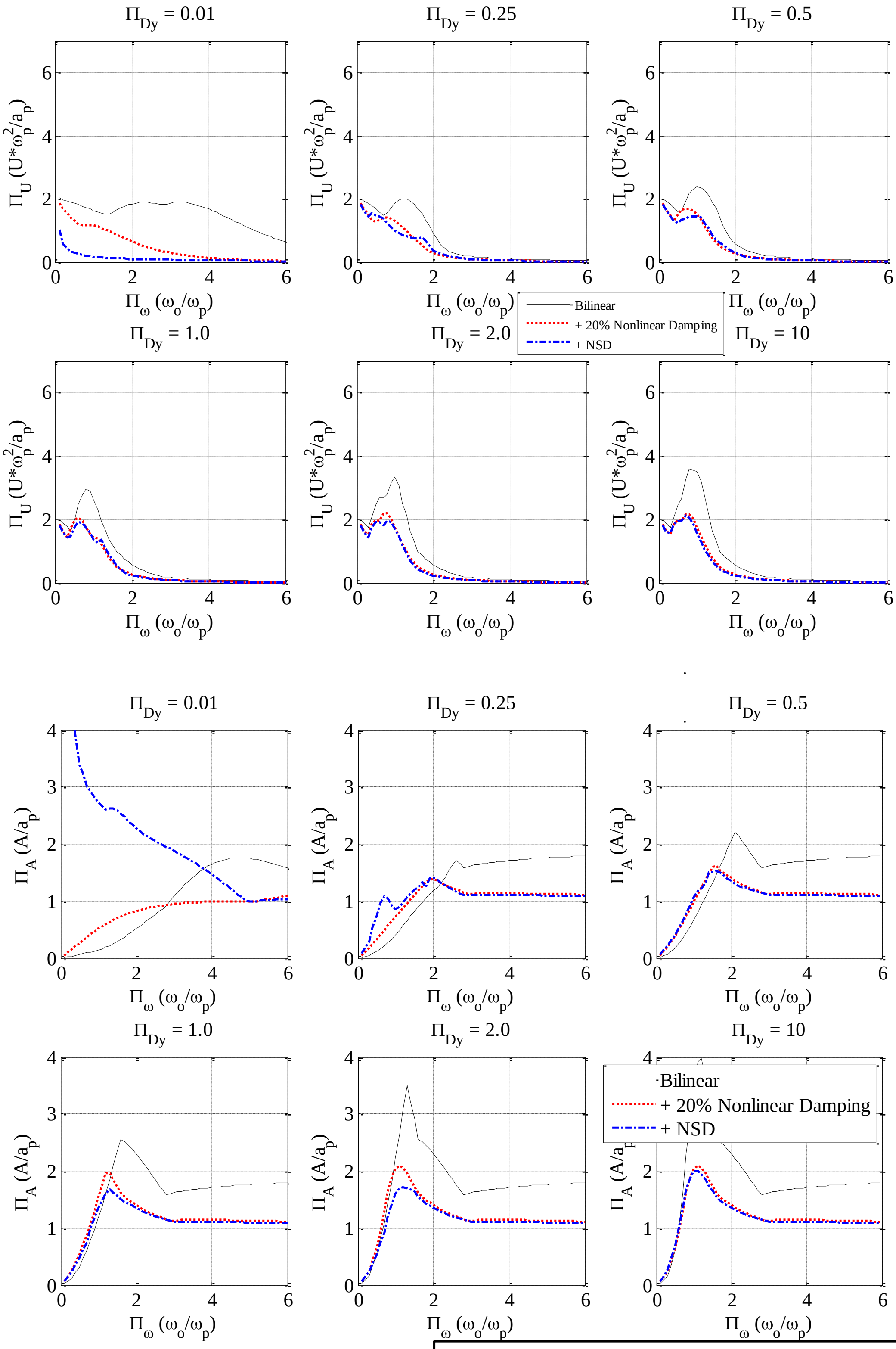

Pulse Type C1, $\Pi_{\xi n}$ = 0.2

(c)

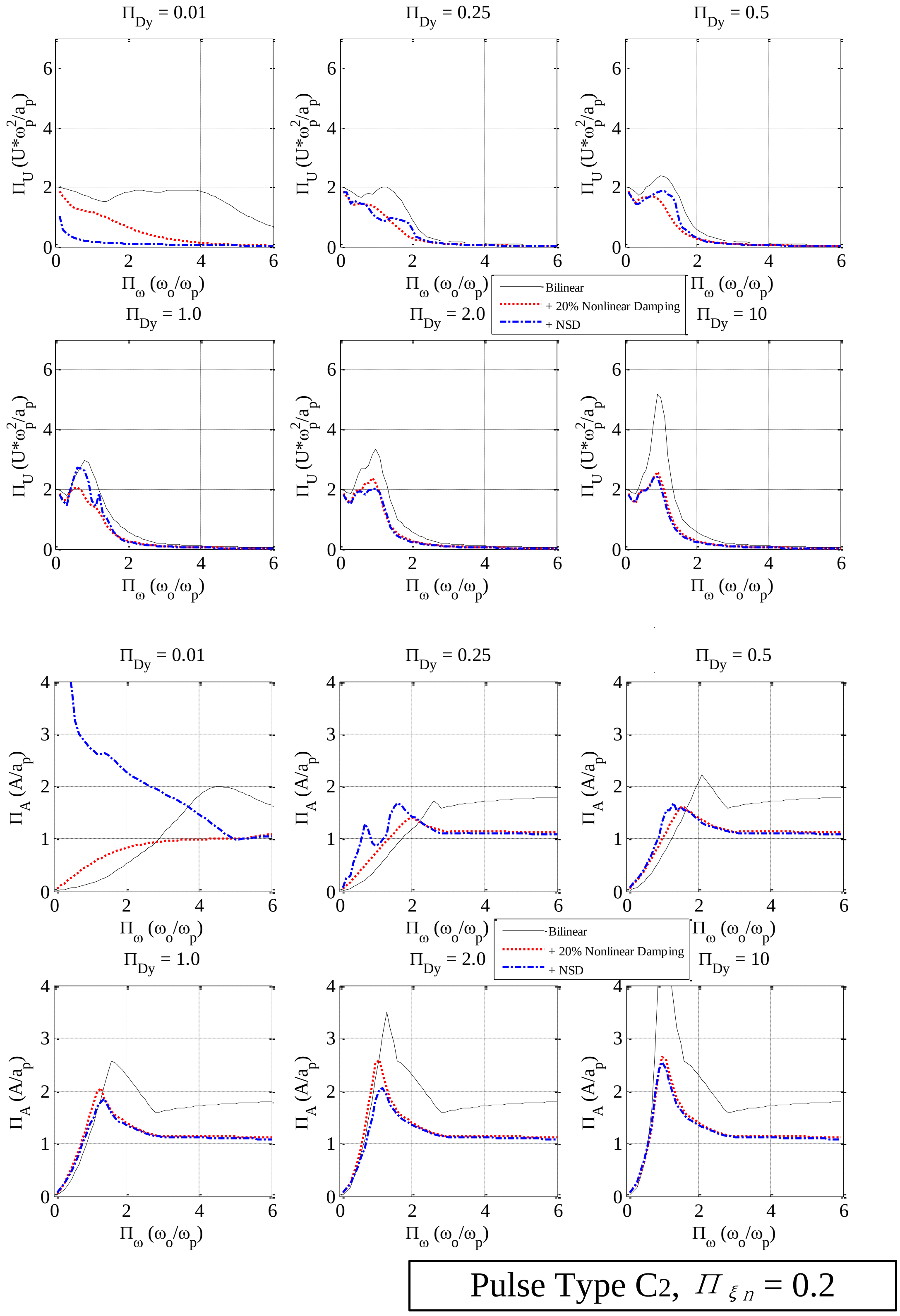

(d)

Fig. 6.12 Study of the effectiveness of NSD system over different ranges of Π_{Dy}. (a) pulse type A, (b) pulse type B, (c) pulse type C_1, (d) pulse type C_2

The above results indicate that the NSD provides benefit to the structural system over the Π_{Dy} range between 0.5 and 5.0, which covers a typical range for most civil structures. For a Π_{Dy} between 0.5 and 5.0, the NSD effect is remarkable over the frequency range of Π_{ω} from 0.6 to 2.0. For a Π_{Dy} smaller than 0.5, since the cubic model proportions the NSD engaging point according to the D_y of the bilinear system, stage four is easily reached such that huge positive force is generated by the NSD system. The positive force helps to constrain the displacement rapidly at the cost of significantly increasing the internal force of structural system. This situation has not been tested in the lab for two reasons: (1) extreme soft system can be constructed for this test, which will easily collapse even without NSD system; and (2) the design to choose the NSD engaging point smaller than D_y does not necessary work for such bilinear systems that yields at an extreme early stage of displacement. Therefore, for smaller D_y, it is recommended to increase the gap length and further extend the relaxation length to avoid the fourth stage. On the other hand, for a Π_{Dy} larger than 5.0, the NSD effect becomes small and negligible.

For different types of pulse, this study gets the following observations: Type A pulse inputs the largest energy to the system such that a large increase of absolute acceleration takes place over Π_{Dy} range from 0.01 to 0.25. All the other types of pulses do not have large acceleration increase for the case Π_{Dy} = 0.25. For pulse type B, the NSD is most effective near Π_{Dy} = 1. For pulse type C_1 and C_2, the NSD is most effective near Π_{Dy} = 2.

6.6.2 Difference of Linear or Nonlinear Damping Modeling for NSD

This section tests the difference between linear and nonlinear modeling scheme of the supplemental damping system for the NSD system. Fig. 6.12 shows the simulated results where five curves are plotted and compared for each spectrum: original bilinear system with 2.5% linear damping, original bilinear system with linear supplemental damping, original bilinear system with nonlinear damping, original bilinear system with linear supplemental damping and the NSD system, original bilinear system with nonlinear damping and the NSD system. First, it is obvious that NSD helps to reduce the absolute acceleration without increasing the relative displacement. In addition, the solid red line in the spectra has a lower peak value than the solid blue line, which indicates that the NSD is most effective considering the supplemental damping system being a nonlinear damping system. In fact, the original nature of the damping system would never be linear. Therefore, the conclusion here would also be preferable.

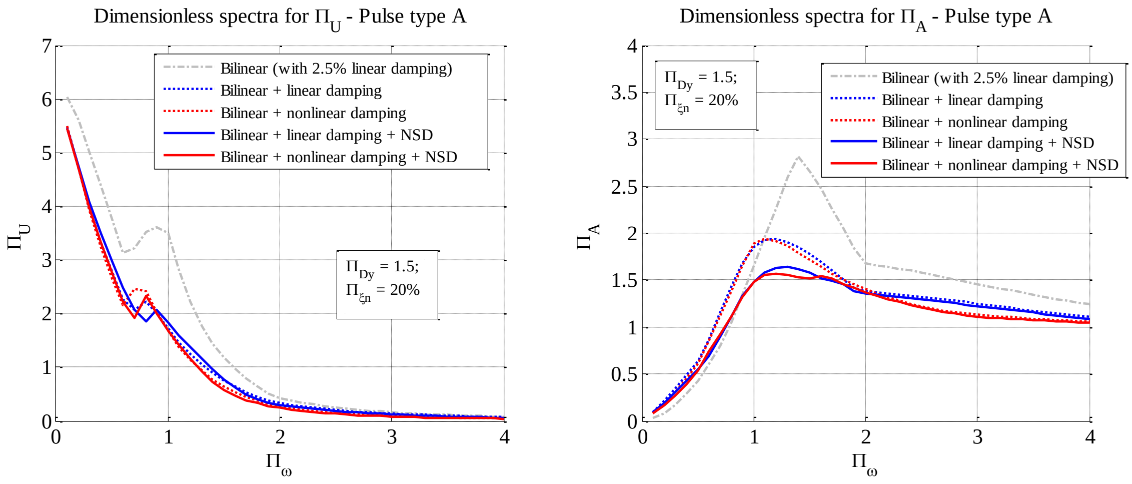

(a)

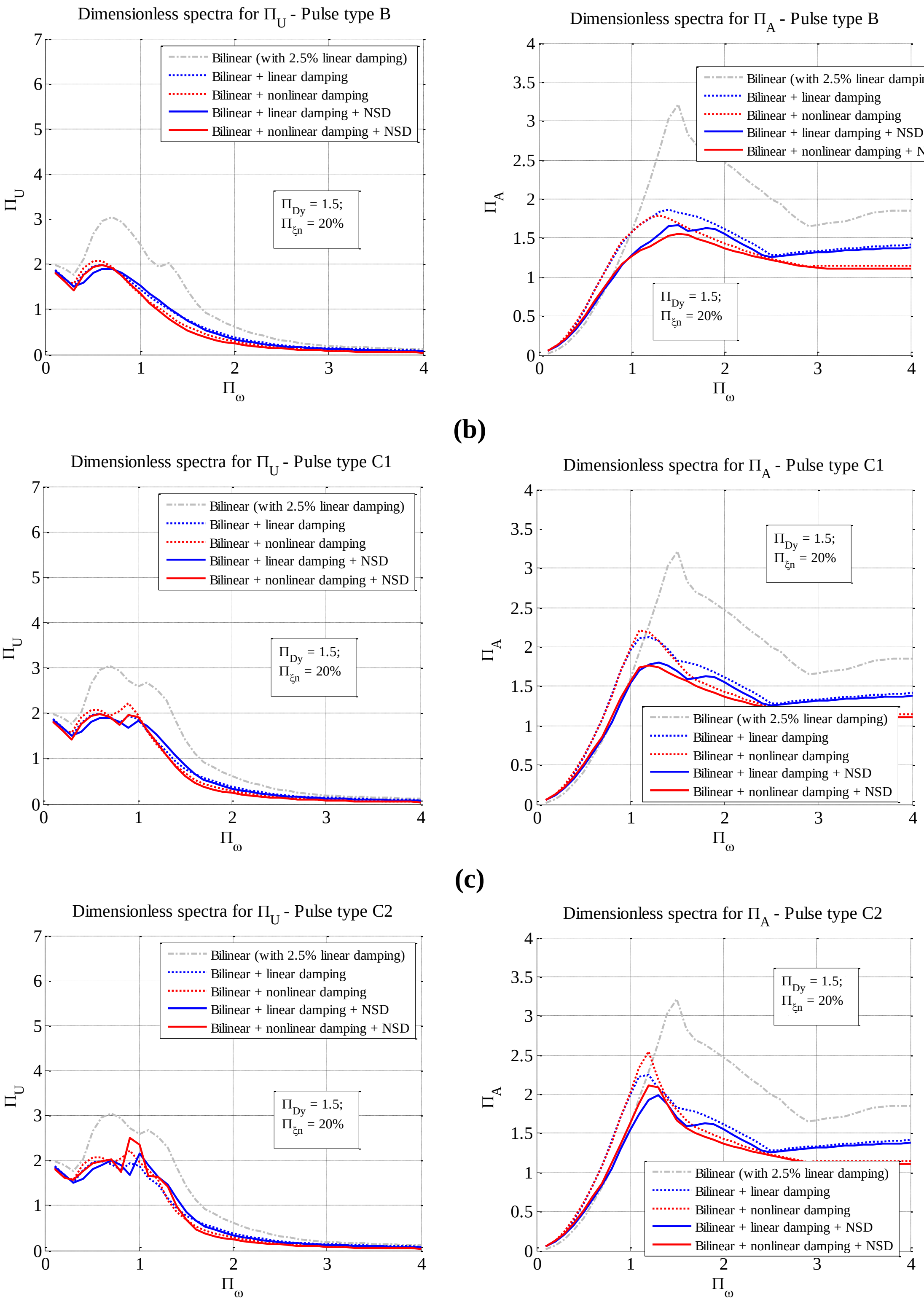

(b)

(c)

(d)

Fig. 6.13 Comparison of linear and nonlinear damping. (a) pulse type A, (b) pulse type B, (c) pulse type C_1, (d) pulse type C_2

6.6.3 *Optimal Nonlinear Damping Ratio for NSD*

The previous section suggests modeling a nonlinear damping behavior for the supplemental damping system; this section evaluates the effectiveness of the nonlinear damping ratio. This study evaluated NSD system with different nonlinear damping ratios when Π_{Dy} is fixed at 1.5. Three different $\Pi_{\xi n}$ values are selected to represent different levels of supplement damping. From Fig. 6.14, this study observed that NSD effect is more obvious for $\Pi_{\xi n}$ between 15% to 25%. For an even larger damping after 25%, it seems harder to implement such large damping in real practice. In addition, the marginal effect brought by the damping to the system decreases, which is shown from the case with 35% damping ratio. In fact, the damping is really a choice made by the designer of the NSD system. This study recommends a supplement nonlinear damping ratio at around 20%-25% such that NSD benefits the system while the damping is sufficient but not costing too much. Notice that less than 15% nonlinear damping ratio might not be sufficient. This is shown in Fig. 6.14(d) when pulse type C_2 is exciting the system. One could observe that when $\Pi_{\xi n}$ is less than 15%, the displacement for NSD system over the spectrum occasionally (when Π_ω is near one) exceeds that of the original bilinear system. This effect is defined as instability effect of the NSD system, which should be avoided by adding sufficient damping.

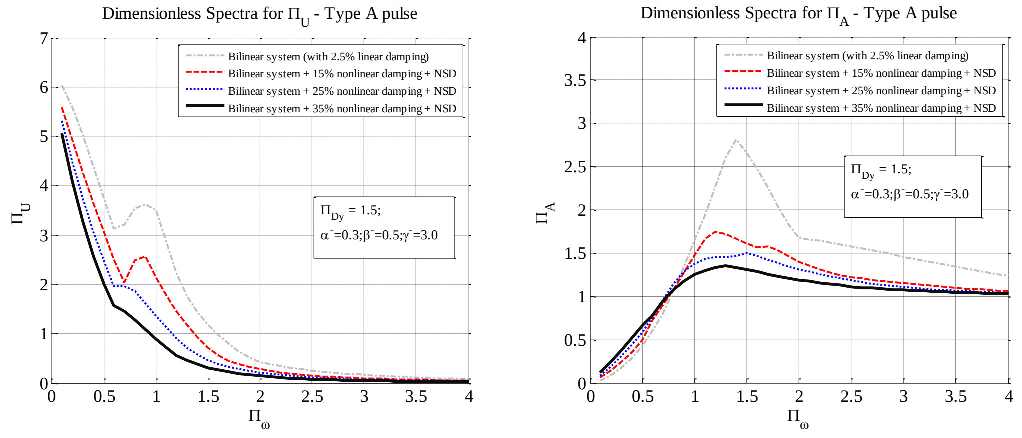

(a)

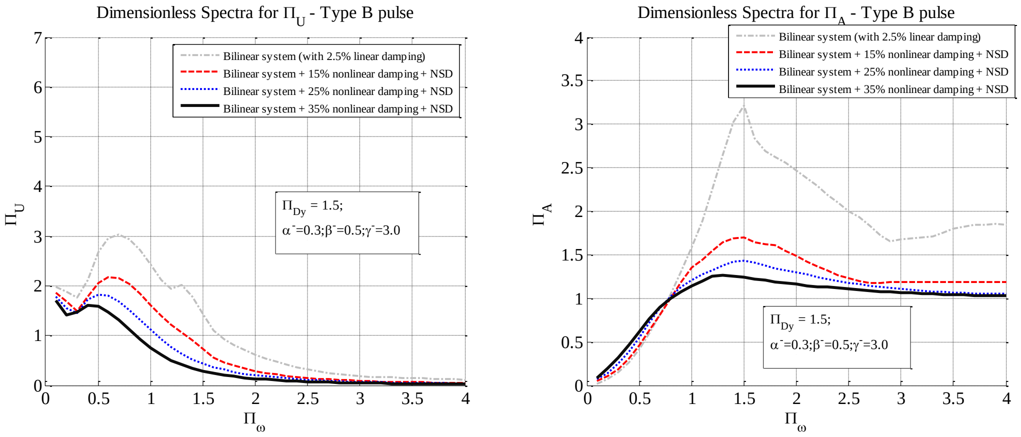

(b)

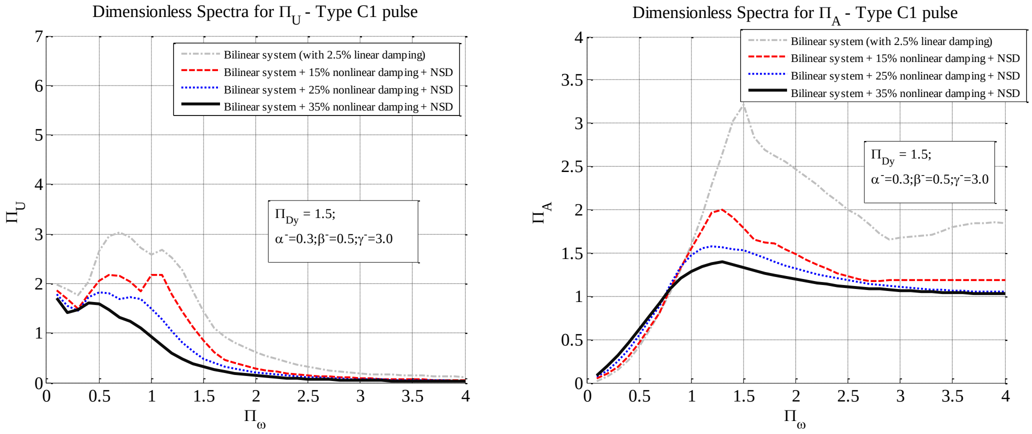

(c)

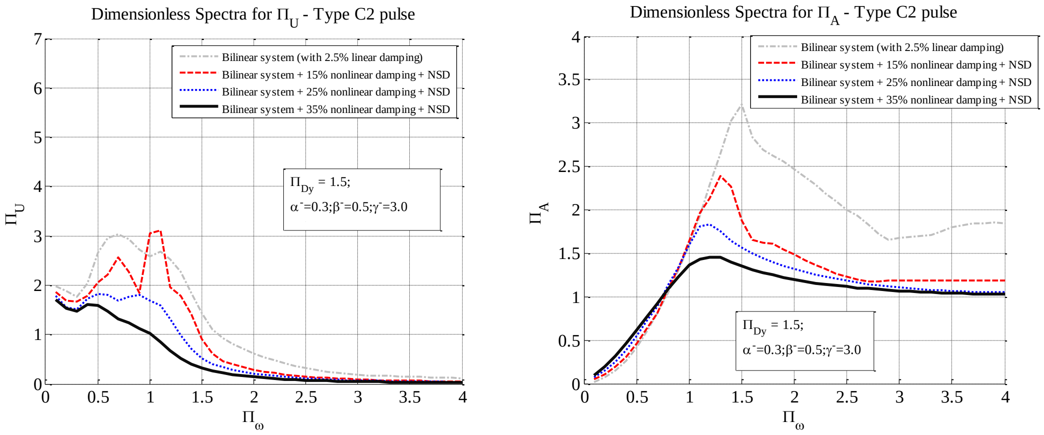

(d)

Fig. 6.14 Illustration of the effect from different levels of nonlinear damping for the system. (a) pulse type A, (b) pulse type B, (c) pulse type C_1, (d) pulse type C_2

At last, Fig. 6.15 shows a comprehensive set of dimensional spectra. In additional to the curves from Fig. 6.14, Fig. 6.15 investigated the cases without NSD (represented by dotted lines). One could easily notice from this approach that the solid lines (with the help of NSD) correspond to lower spectral displacement and acceleration, which again proves that NSD is incredibly potent.

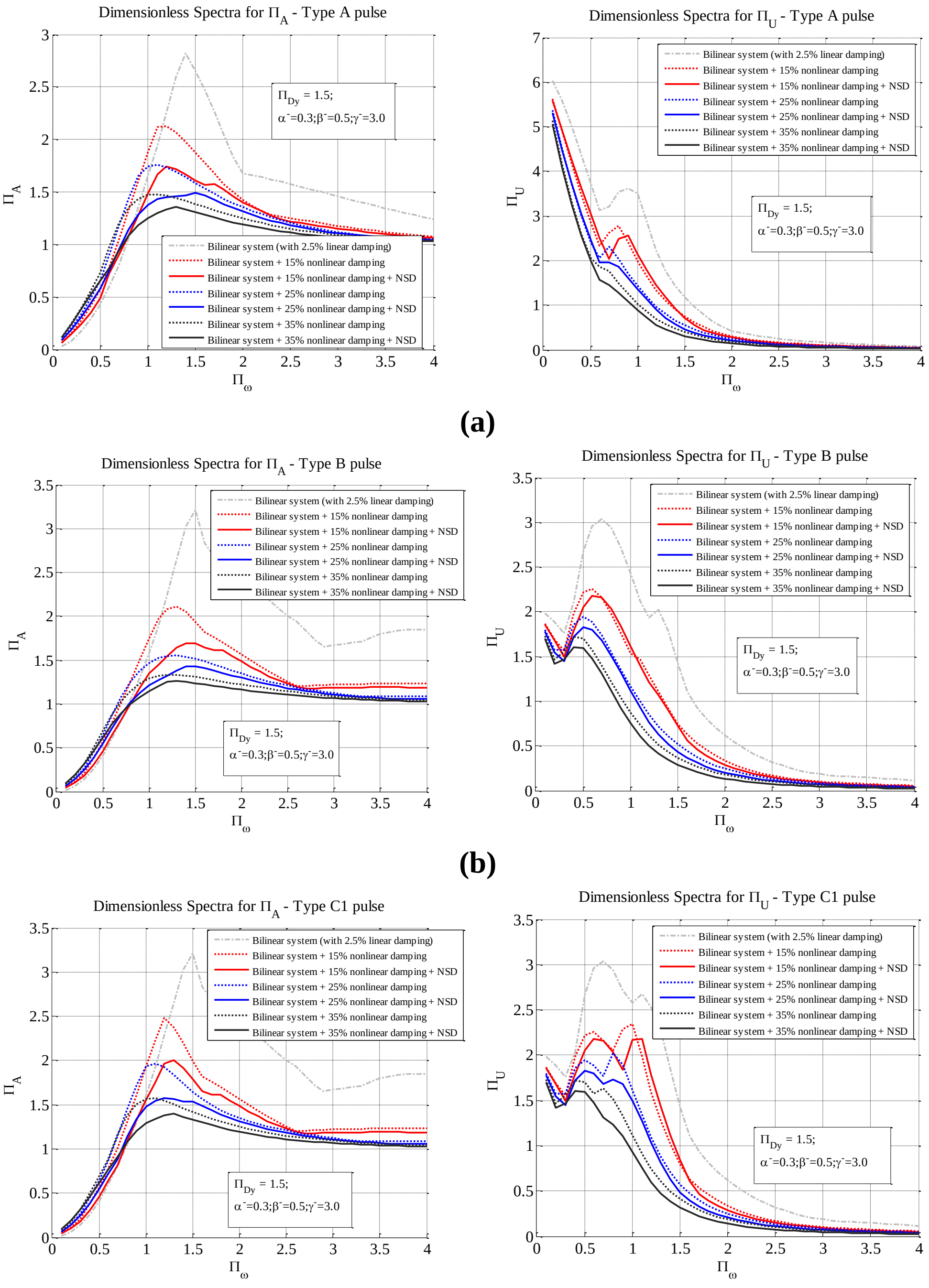

(a)

(b)

(c)

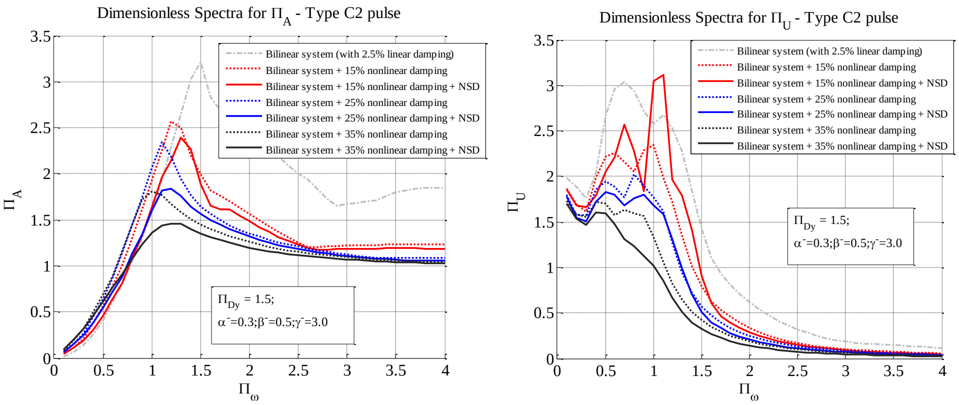

(d)

Fig. 6.15 Comparison of different levels of nonlinear damping with and without NSD system. (a) pulse type A, (b) pulse type B, (c) pulse type C_1, (d) pulse type C_2

6.7 Optimal Design of the NSD System

Analyses from previous sections lead to the following discussion to study and determine the optimal range that NSD can best benefit the bilinear structural system. The purpose of this section is to examine and to suggest the best parametric range for designing a NSD system. The study anchors the Π_{Dy} and $\Pi_{\xi n}$ at a recommended value from the above studies, trying to find an optimal design of NSD parameters (i.e. Π_{xo}-, Π_{Q}-, Π_{xr}-).

The purpose of this approach is to understand completely the best system performance based on different NSD designs. Since the proposed NSD system is new, a performance-based evaluation with a Monte-Carlo method is launched here based on the results from the presented dimensionless spectra. The three different coupled dimensions: Π_{xo}-, Π_{Q}-, Π_{xr}- are repeated over the range of Π_{xo}-=[0.1~0.9]Π_{Dy}, Π_{Q}-=[0.1~0.7] Π_{QD}, and Π_{xr}-=[2.0~6.0]Π_{Dy}. In addition, considering the capacity of the NSD pre-compressed spring, this study categories a bilinear system by the size of an engineering structure. For smaller structures such as wood frame buildings, the NSD system capacity can be as large as 70% of the characteristic strength Π_{QD}; however, for larger and heavier structures, this work assumes the capacity of NSD to be less than 50% of the structural strength. Similar to the previous sections, the NSD system is tested with four different types of pulses. In addition, three different levels of Π_{Dy} values (0.5, 1.0, and 1.5) were chosen to represent different structures.

For a performance-based approach, one should define the performance index from the measured damage. In this case, this study defines the "better" or "worse" performance of a NSD system based on the displacement and acceleration spectra. The performance index for acceleration is based on the optimal acceleration at Π_{ω}=1. This is because an acceleration spectrum usually has only one peak value near Π_{ω}=1, which is shown from Fig. 6.12 to 6.15. In addition, due to the observation that an acceleration spectrum with smaller peak magnitude usually corresponds to smaller overall acceleration, a spectrum with less peak magnitude is considered to have a better acceleration response. For displacement spectra, the situation is a bit more complicated since there might be multiple local maximum values within a single displacement curve. Therefore, the performance index for displacement spectra is based on the average weighted value at Π_{ω} = 0.5, 1.0, and 1.5. In addition, similar to the acceleration spectra, the displacement curve with a less performance is considered a better performance.

Tables 6.4 and 6.5 summarize the best performance of acceleration and displacement by optimizing the NSD parameters. These tables reflect the behaviors of smaller systems where NSD capacity can reach 70% of the system characteristic strength. For Table 6.4, the first column is the range for Π_{Dy}. The second to fourth column provides the optimal range of NSD system in order to optimize the acceleration. Fifth column is the optimized performance index for acceleration from the adaptive system (i.e. bilinear system plus damping plus NSD). The sixth column is the performance index of acceleration from bilinear system plus damping but no NSD. The seventh column is the index for only the bilinear system. The eighth column is the displacement index for the adaptive system with NSD parameters optimized for acceleration. The ninth column is the displacement index for bilinear system plus damping with NSD parameters optimized for acceleration. And the last column is the displacement index for bilinear system only without NSD system. The contents in the columns of Table 6.5 are similar to Table 6.4 but with the focus to optimize the stuctural displacement. The last three columns in Table 6.5 correspond to the acceleration indices with NSD parameters optimized for displacement. From such performance-based approach, the best ranges of NSD parameters for such system undergoing different types of pulse are presented.

Table 6.4 Optimized NSD parameters to reduce absolute acceleration

δ^- from 0.1 to 0.9 increased by 0.2; β^- from 0.1 to 0.7 increased by 0.2; γ^- from 2 to 6 increased by 1									
Pulse A	Optimizing Acceleration								
Π_{Dy}	δ^-	β^-	γ^-	Π_A^{NSD} *Optm* *	Π_A^{NLDp}	Π_A^{BL}	Π_U^{NSD}	Π_U^{NLDp}	Π_U^{BL}
0.5	0.5	0.7	4	1.451	1.639	1.816	1.469	1.667	2.854
1	0.1	0.7	2	1.334	1.860	1.760	1.677	2.466	2.711
1.5	0.1	0.7	2	1.263	1.936	2.816	1.575	1.645	2.811
Pulse B	Optimizing Acceleration								
Π_{Dy}	δ^-	β^-	γ^-	Π_A^{NSD} *Optm* *	Π_A^{NLDp}	Π_A^{BL}	Π_U^{NSD}	Π_U^{NLDp}	Π_U^{BL}
0.5	0.1	0.7	3	1.359	1.630	2.286	1.144	1.261	2.019
1	0.1	0.7	2	1.290	1.794	2.690	1.253	1.352	2.070
1.5	0.1	0.7	2	1.324	1.794	3.216	1.284	1.348	2.182
Pulse C1	Optimizing Acceleration								
Π_{Dy}	δ^-	β^-	γ^-	Π_A^{NSD} *Optm* *	Π_A^{NLDp}	Π_A^{BL}	Π_U^{NSD}	Π_U^{NLDp}	Π_U^{BL}
0.5	0.3	0.5	3	1.552	1.649	2.286	1.176	1.261	2.019
1	0.1	0.7	2	1.440	2.073	2.690	1.334	1.398	2.068
1.5	0.1	0.7	2	1.414	2.211	3.216	1.396	1.573	2.212
Pulse C2	Optimizing Acceleration								
Π_{Dy}	δ^-	β^-	γ^-	Π_A^{NSD} *Optm* *	Π_A^{NLDp}	Π_A^{BL}	Π_U^{NSD}	Π_U^{NLDp}	Π_U^{BL}
0.5	0.3	0.3	2	1.586	1.649	2.286	1.192	1.325	2.103
1	0.3	0.7	3	1.833	2.102	2.690	1.392	1.415	2.207
1.5	0.1	0.7	2	1.492	2.545	3.216	1.421	1.573	2.212

* All the optimal accelerations are the smallest peak value of acceleration among all the different design

Table 6.5 Optimized NSD parameters to reduce relative displacement

δ^- from 0.1 to 0.9 increased by 0.2; β^- from 0.1 to 0.7 increased by 0.2; γ^- from 2 to 6 increased by 1

Pulse A	Optimizing Displacement								
Π_{Dy}	δ^-	β^-	γ^-	Π_U^{NSD} *Optm* **	Π_U^{NLDp}	Π_U^{BL}	Π_A^{NSD}	Π_A^{NLDp}	Π_A^{BL}
0.5	0.9	0.7	2	1.219	1.667	2.854	6.001	1.639	1.816
1	0.9	0.7	2	1.579	2.466	2.711	1.905	1.860	1.760
1.5	0.9	0.7	2	1.404	1.645	2.811	2.064	1.936	2.816
Pulse B	Optimizing Displacement								
Π_{Dy}	δ^-	β^-	γ^-	Π_U^{NSD} *Optm* **	Π_U^{NLDp}	Π_U^{BL}	Π_A^{NSD}	Π_A^{NLDp}	Π_A^{BL}
0.5	0.9	0.7	2	1.065	1.261	2.019	2.553	1.630	2.286
1	0.1	0.7	2	1.253	1.352	2.070	1.440	1.794	2.690
1.5	0.9	0.1	6	1.280	1.348	2.182	1.666	1.794	3.216
Pulse C1	Optimizing Displacement								
Π_{Dy}	δ^-	β^-	γ^-	Π_U^{NSD} *Optm* **	Π_U^{NLDp}	Π_U^{BL}	Π_A^{NSD}	Π_A^{NLDp}	Π_A^{BL}
0.5	0.9	0.7	2	1.121	1.261	2.019	2.734	1.649	2.286
1	0.7	0.3	2	1.296	1.398	2.068	1.759	2.073	2.690
1.5	0.3	0.7	2	1.346	1.573	2.212	2.092	2.211	3.216
Pulse C2	Optimizing Displacement								
Π_{Dy}	δ^-	β^-	γ^-	Π_U^{NSD} *Optm* **	Π_U^{NLDp}	Π_U^{BL}	Π_A^{NSD}	Π_A^{NLDp}	Π_A^{BL}
0.5	0.9	0.3	2	1.171	1.325	2.103	2.423	1.649	2.286
1	0.5	0.1	2	1.383	1.415	2.207	2.035	2.102	2.690
1.5	0.1	0.7	2	1.421	1.573	2.212	2.365	2.545	3.216

** All the optimal displacements are the smallest average weighted value at Π_ω = 0.5, 1.0, and 1.5 among all the different design

The systematic study presented above shows clearly that NSD is desirable with its advantage of reducing both the structural acceleration and displacement. One could confidently conclude that the NSD is especially helpful to reduce the floor acceleration of the system. By looking at multiple individual cases (such as the ones shown in section 6.4), one would notice that for a fixed type of pulse and Π_{Dy}, the NSD contributes the most to the system when its performance falls into the second stage and close to the third stage. Result from Table 6.4 and 6.5 also matches this conclusion, which provides the optimal NSD design, when maximum NSD drift falls into the second stage for most cases.

The above study shows that if one could offer the NSD capacity (β^-) up to 70% of the structural strength (Q_D), the system may benefit from a reduction of acceleration up to 70% (33% on average for all the scenarios with different Pulse types and Π_{Dy} value) with the help of the NSD system. In addition, NSD can also reduce the maximum displacement up to half of the damped system with an average reduction of 11.3%. Similar work has been done for lager size systems whose β^{-} value can only be 50%, 30%, and 10%. The study shows that these systems receive average acceleration reduction of 22%, 14%, and 5%, respectively. For displacement, when β^{-} value is set to 50%, 30%, and 10%, the average reduction will be 10.0 %, 9.11% and 8.47%. Fig. 6.16 shows the NSD effect influenced by the provided capacity.

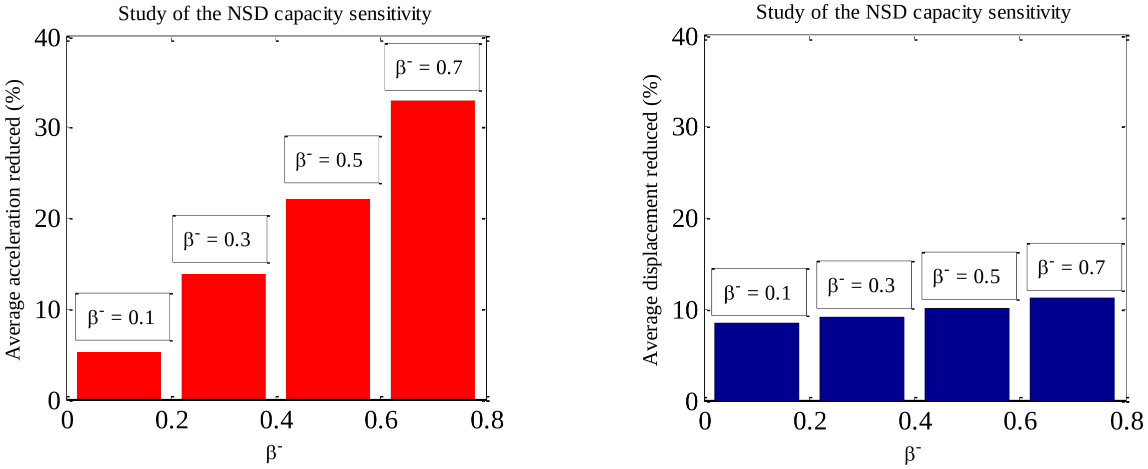

(a) Average acceleration reduction **(b)** Average displacement reduction

Fig. 6.16 NSD benefit provided its capacity

In order to reduce and to get the optimal acceleration, Table 6.4 and 6.5 suggests the applications of NSD system at maximum capacity ($\beta^{-}=0.7$). Table 6.4 shows that the performance indices for displacement corresponding to the optimal acceleration are small and not harmful to the system. Comparing the eighth column from Table 6.4 with the fifth column from Table 6.5, one could find that the system responses while optimizing NSD parameters for acceleration have small difference from that while optimizing NSD parameters for displacement. On the other hand, the eighth column from Table 6.5 generates huge difference from the fifth column in Table 6.4, which suggests not optimizing displacement without considering the significant increase of the system acceleration. To conclude, this indicates that NSD is powerful to reduce the structural acceleration and displacement. By optimizing the system acceleration, the system displacement is also close to the optimized values but not vise versa. Hence, this study recommends optimizing the NSD variables by optimizing the system acceleration.

The above analysis reveals how each NSD parameter affects the SDOF system. A couple observations are concluded below:

1) Sufficient damping is required for NSD system such that one could design a NSD system with larger capacity. Especially for the NSD system with smaller Π_{Dr}- or γ^{-} valus, at least 20% of damping should be provided. Without enough damping, NSD might be unstable over certain Π_{ω} range.

2) For the four different pulse types, pulse A has the largest response. At the same time, the NSD becomes more effective for pulse type A. For the other three types of pulse, NSD effect reduces.

3) When fixing Π_{Dy} and providing sufficient damping, a stronger NSD force capacity will bring better results. The definition of stronger NSD force corresponds to a smaller Π_{Do}- or δ^{-} so that the NSD force comes to effect earlier, a bigger Π_{Q}- or β^{-} so that NSD peak magnitude is higher; and a smaller Π_{Dr}- or γ^{-} such that the peak of the NSD reaches earlier. Fig. 6.17 are the spectra using some of the δ^{-}, β^{-}, and γ^{-} values selected from Table 6.4 and 6.5. It is remarkable that the case with NSD parameters $\delta^{-} = 0.1$, $\beta^{-} = 0.7$, and $\gamma^{-} = 2.0$ (red dotted line) helps to reduce the structure's absolute acceleration up by 50%.

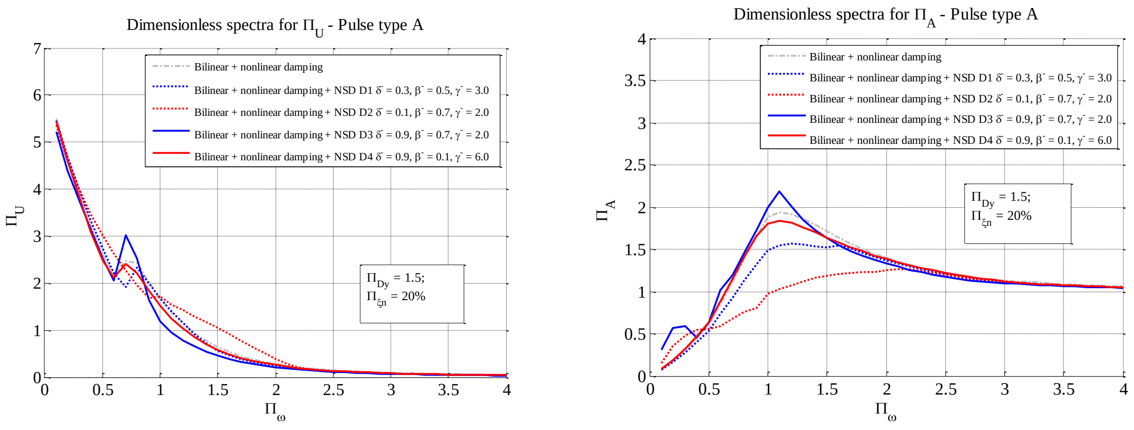
Dimensionless spectra for Π_U - Pulse type A
Dimensionless spectra for Π_A - Pulse type A
Bilinear + nonlinear damping
Bilinear + nonlinear damping + NSD D1 $\delta^- = 0.3, \beta^- = 0.5, \gamma^- = 3.0$
Bilinear + nonlinear damping + NSD D2 $\delta^- = 0.1, \beta^- = 0.7, \gamma^- = 2.0$
Bilinear + nonlinear damping + NSD D3 $\delta^- = 0.9, \beta^- = 0.7, \gamma^- = 2.0$
Bilinear + nonlinear damping + NSD D4 $\delta^- = 0.9, \beta^- = 0.1, \gamma^- = 6.0$
Π_{Dy} = 1.5;
$\Pi_{\xi n}$ = 20%
Π_U
Π_A
Π_ω

(a)

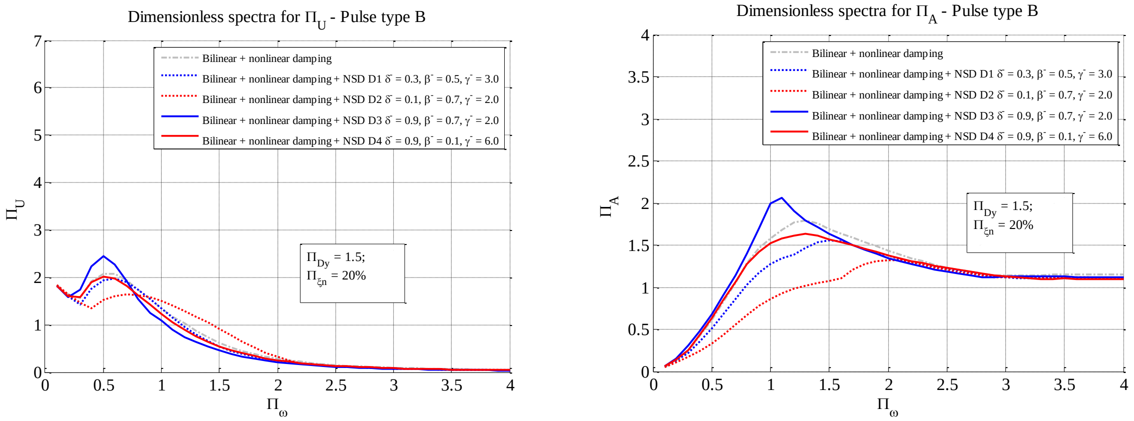
Dimensionless spectra for Π_U - Pulse type B
Dimensionless spectra for Π_A - Pulse type B
Bilinear + nonlinear damping
Bilinear + nonlinear damping + NSD D1 $\delta^- = 0.3, \beta^- = 0.5, \gamma^- = 3.0$
Bilinear + nonlinear damping + NSD D2 $\delta^- = 0.1, \beta^- = 0.7, \gamma^- = 2.0$
Bilinear + nonlinear damping + NSD D3 $\delta^- = 0.9, \beta^- = 0.7, \gamma^- = 2.0$
Bilinear + nonlinear damping + NSD D4 $\delta^- = 0.9, \beta^- = 0.1, \gamma^- = 6.0$
Π_{Dy} = 1.5;
$\Pi_{\xi n}$ = 20%
Π_U
Π_A
Π_ω

(b)

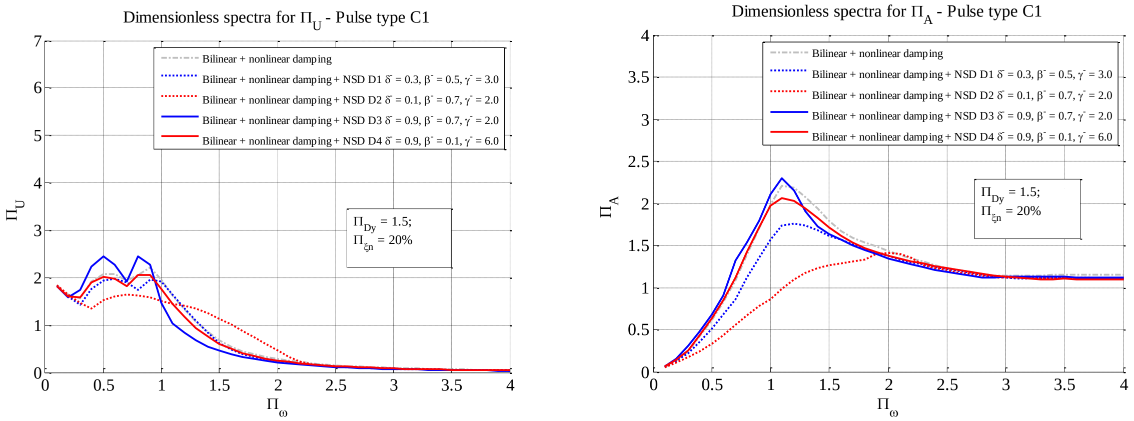
Dimensionless spectra for Π_U - Pulse type C1
Dimensionless spectra for Π_A - Pulse type C1
Bilinear + nonlinear damping
Bilinear + nonlinear damping + NSD D1 $\delta^- = 0.3, \beta^- = 0.5, \gamma^- = 3.0$
Bilinear + nonlinear damping + NSD D2 $\delta^- = 0.1, \beta^- = 0.7, \gamma^- = 2.0$
Bilinear + nonlinear damping + NSD D3 $\delta^- = 0.9, \beta^- = 0.7, \gamma^- = 2.0$
Bilinear + nonlinear damping + NSD D4 $\delta^- = 0.9, \beta^- = 0.1, \gamma^- = 6.0$
Π_{Dy} = 1.5;
$\Pi_{\xi n}$ = 20%
Π_U
Π_A
Π_ω

(c)

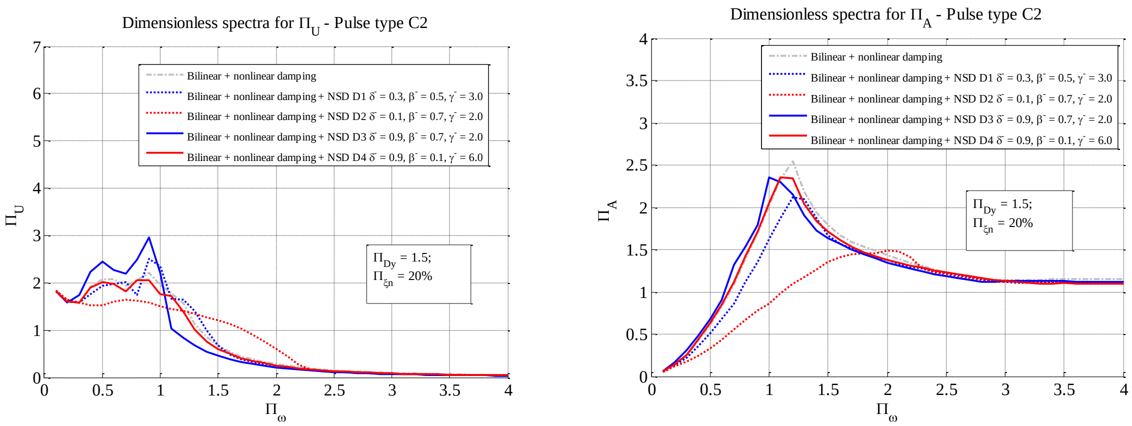

(d)

Fig. 6.17 Four cases of different NSD design. (a) pulse type A, (b) pulse type B, (c) pulse type C_1, (d) pulse type C_2

6.8 Discussions of the Fourth Stage

One might observe from Table 6.5 that the optimal displacement occasionally happens when no NSD is used such as the case Π_{Dy}=1.5 with pulse type B. For these cases, the best displacement happens when NSD kicks in late ($\bar{\delta}=0.9$), magnitude is small ($\bar{\beta}=0.1$), and relaxes at a larger displacement ($\bar{\gamma}=6.0$). This kind of scenario happens when the system equipped with NSD stretches into the fourth stage. An example is shown from Fig. 6.18 (Pulse type A, Π_{Dy} =0.5, $\bar{\delta}$=0.1, $\bar{\beta}$=0.9, and $\bar{\gamma}$=2.5).

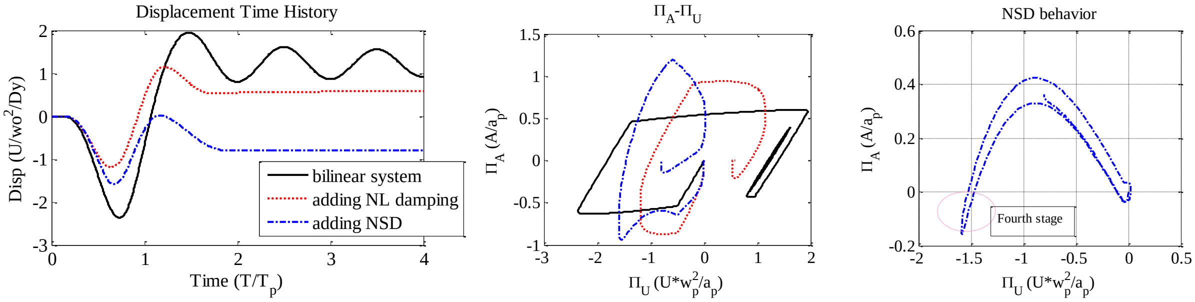

Fig. 6.18 A case that the NSD reaches its fourth stage

It is concluded that keeping NSD within the first three stages is desirable in real application. For the last stage when extreme displacement happens, the system becomes unstable and NSD usually brings little help, if not being harmful. In fact, the fourth stage is quite rare. In real practice, severe ground motions such as the 2011 Tōhoku motion in the first case study usually triggers a well-designed NSD system to the second stage. However, there are still scenarios when the fourth stage is reached. Researches on how to avoid the fourth stage would be a great topic for future studies.

6.9 Concluding Remarks

As an innovative generation of adaptive stiffness and damping devices, the negative stiffness device might inherently benefits civil structures by weakening it in a smart way. The NSD project team proposed a new design for NSD system and tested the system in three phases in recent years. However, there are no further tests or simulations to show the effectiveness of the device or to prove whether it can be used in real world civil structures. Therefore, the goal of this study is to better explore the NSD behavior. First, the study proposed a cubic elastic model that numerically simulates the NSD system, which gives a detailed explanation of three parameters to fully characterize (1) the horizontal displacement when NSD effect starts; (2) the peak NSD amplitude; (3) the horizontal displacement where NSD force becomes to zero (pre-compressed spring relaxes to its natural length). In the second part of the study, the dimensional analyses framework was presented for NSD system. Three dimensionless Π-terms for the three proposed NSD parameters were developed. Then, the third part of this work provides the simulated results and shows the optimal range Π_{Dy} range that NSD can help better the system response. This part also gives the recommendation of the minimum supplemental nonlinear damping ratio needed for the NSD system. Finally, the last part of this work provided the optimal design range for the proposed NSD parameters.

A couple conclusions can be reached from this work:

(i) A large number of simulations have been made in the work from which prove the NSD being effective in a systematic way. The NSD helps to reduce both the structural acceleration and displacement. NSD effect is extremely remarkable to reduce the acceleration.

(ii) NSD is most effective over the Π_{Dy} range between 0.5 and 5.0, which covers most of the civil structures.

(iii) As an adaptive stiffness and damping system, supplemental damping is needed for the NSD system. This study recommends a nonlinear damping ratio $\Pi_{\xi n}$ of 20% to 25%.

(iv) Optimal design variables for NSD system (i.e. δ^-, β^-, and γ^-) was given from a performance-based approach. Due to the nature of NSD system helps to reduce the structural acceleration, this study suggests optimizing the NSD parameters according to reducing the structural acceleration. The conclusion is that: (a) the force magnitude β^- is constrained by the size and type of the civil structure. The larger β^- one could provide to the system, the better response a system can benefit from NSD. (b) The adaptive system receives the best performance over the range $\delta^- \in [0.1, 0.3]$ and $\gamma^- \in [2, 3]$.

(v) Forth stage that significantly increases the system internal force to constrain displacement is proved undesirable. Option to avoid NSD falling into this stage shall be discussed in the future study.

7. CONCLUSIONS AND FUTURE WORK

7.1 Conclusions

Historical earthquake events damaged or destroyed countless numbers of buildings. The goal of modern seismic design is to achieve a controlled response that does not jeopardize the integrity of structures and safety of their occupants during and immediately after major earthquakes. This is usually achieved through numerous structural lateral load-resisting systems such as ductile moment-resisting frames, braced frames, and shear walls that are designed to provide displacement capacity through inelastic ductile action at carefully detailed locations while limiting the seismic forces induced in the structure. However, because of their hysteretic characteristics, yielding systems are expected to sustain damage through repeated inelastic actions as well as residual deformations, which can greatly impair the structure and increase repair costs.

To overcome this deficiency, there have been intensive research efforts in the field of structural engineering over the past decades to employ smart structure technologies in seismic response control of structures. A large number of innovative systems and devices have been developed either to reduce the earthquake forces acting on a structure or to absorb a part of the seismic energy. These proposed seismic protective devices, in either passive or adaptive passive forms, could be used to significantly improve the seismic performances of buildings in high seismicity regions. In the meanwhile, optimal design of the stiffness and damping properties of these devices is important to fulfill their advantages and achieve multi-performance objectives when the devices are subjected to earthquakes with various mechanisms, frequency contents and intensities.

The ultimate goal of this research is to explore new seismic protective devices and/or optimally design existing devices to better protect buildings such that the total cost (both direct and indirect) due to earthquake damages can be reduced to a minimum level. In order to minimize seismic loss of buildings, understanding their seismic performances would be necessary for future seismic designs. Therefore, a comprehensive study to estimate the peak inelastic drift ratio as well as the residual drift ratio for generalized bilinear systems has been presented. The proposed formula is guided by the rigorous dimensional analysis such that both the peak transient drift responses and the residual drift of bilinear SDOF systems are presented in dimensionless form showing remarkable order. The proposed formula also incorporates a dimensionless nonlinearity index that takes into account of the pre-yielding strength, ground motion amplitude, and softening or hardening post-yield behavior. Strong correlation is revealed between the normalized nonlinear drift demands, the dimensionless structure-to-pulse frequency, and the dimensionless nonlinearity. Regressive equations for peak transient drift and residual drift demands are proposed. The proposed equations estimating the structural response have been validated with the simulation results. The study have shown that the proposed model is able to give dependable predictions with a normalized error range from 40%-65%, which is a huge improvement compared with existing approaches.

This study also tries to improve the accuracy of numerical modeling and simulations. In particular, this study adopts the open source software OpenSees to model and analyze the performance of buildings equipped with various protective devices. Numerical models for protective devices are first developed and calibrated in Matlab. Dynamic behaviors for SDOF bilinear system equipped with protective devices have also been tested. For the next step, the authors developed user specified materials and sections in OpenSees such as the 1D and 2D coupled Bouc-Wen model to capture the behavior of isolation systems, the cubic material model for negative stiffness device, and hysteretic material model for the self-centering devices.

In addition, the development of performance-based earthquake engineering, more specifically the aim to achieve multiple performance levels under multiple earthquake hazard levels, has highlighted the importance of minimizing the damage that is sustained during moderate earthquakes. As a pioneering application of the performance-based framework, the study investigates the performance of seismic isolation system and proposed an innovative method of designing such system for buildings in an optimized way such that the potential loss from earthquakes can be minimized. The method develops a practical and intuitive performance index named the total loss ratio for a certain building based on the results produced from fragility analyses. For a given isolation device, the optimum design parameters can be determined based on the known value of pre- to post-yielding stiffness ratio N. The optimal design parameters for isolation devices, which will result in the minimum damage probability for buildings for different hazard levels, are functions of structural properties and damage states. It is shown that the elastic stiffness of isolation devices, K_{1_I} is not sensitive in affecting the damage potential. In addition, the bearing yield strength remains in a reasonable range. The superstructure will experience minimum damage probability when the characteristic strength Q_{d_I} of isolation devices is about 0.06-0.12 Q_{d_B}, which is the characteristic strength of the superstructure. In addition, the post-yielding stiffness K_{2_I} is about 1% of the post-yielding stiffness of the superstructure (K_{1_B}). This approach can be also applied to other seismic protective devices to study and explore the optimal ranges for their design variables.

As an innovative generation of adaptive stiffness and damping devices, the negative stiffness device might inherently benefit civil structures by weakening it in a smart way. Therefore, another study of this work evaluates the effectiveness of the NSD system under the dimensional analysis framework. It has been shown from a large number of simulations that NSD is only effective while sufficient damping is added to the system. In addition, the adaptive stiffness and damping system helps to reduce both the structural acceleration and displacement. NSD effect is extremely remarkable in terms of reducing the absolute acceleration. The study also provided suggestions for the NSD design.

7.2 Recommendations for Future Work

Through the findings of this research, a number of important areas related to the optimal design of seismic control devices and risk evaluation of buildings can be further studied. Recommendations for future research directions are as follows.

(i) The completed study is based on the 2011 E-defense tested 5-story steel moment frame building. However, various types of buildings were not evaluated in this study, such as high rises, wood frame buildings, and special functional buildings (hospital buildings and nuclear power plants, etc.) One of the future goals is to apply the PBEE framework to more building structures and apply the result from performance-based design to real structures.

(ii) The author would also like to provide an extensive study of self-centering device, taking advantage of the developed numerical model of such devices. The goal is to minimize if not to eliminate the permanent residual drift of buildings using such devices. The close-to-optimal design variables could be chosen under the proposed PBEE framework in this study. In addition, the performance of the protected system can be evaluated under the dimensional analysis framework to see the effectiveness of the device.

(iii) The fourth stage of negative stiffness device will sharply increases the system internal force to constrain displacement, which has been proved unrealistic and undesirable. Therefore, another goal of the author in the future is to propose some adjustment of NSD to avoid the fourth stage of performance.

(iv) At last, the author would put more effort to develop other innovative design schemes and strategies for passive control devices under PBEE framework. Given certain performance objective of buildings, the design scheme will lead to the determination of optimal mechanical properties and locations of the seismic protective devices such that general engineering or social objectives could be achieved.

References

Aizawa, S., Kakizawa, T. and Higasino, M. (1998). "Case Studies of Smart Materials For Civil Structures", *Smart Materials and Structures*, 7, 617-626.

Applied Technology Council. "Earthquake Damage Evaluation Data for California", *ATC-13*, Redwood City, CA, 1985.

Applied Technology Council. "Seismic Evaluation and Retrofit of Concrete Building", *ATC-40*, Redwood City, CA, 1996.

Applied Technology Council. "Seismic Performance Assessment of Buildings", *ATC-58*, Redwood City, CA, 2011.

Akkar S., Yazgan U., Gulkan P.. (2004). "Deformation Limits for Simple Non-degrading Systems Subjected to Near-fault Ground Motions", *Proceedings of the 13th World Conference on Earthquake Engineering*, Vancouver, BC, Canada, 2004.

Alavi B., Krawinkler H.. (2001). "Effects of Near-field Ground Motion on Frame Structures", *Report No. 138*, The John A. Blume Earthquake Engineering Center, Stanford University, Stanford, CA, 2001.

Alavi B., Krawinkler H.. (2004). "Behavior of Moment-resisting Frame Structures Subjected to Near-fault Ground Motions", *Earthquake Engineering and Structural Dynamics*, 33(6), 687-706.

American Society of Civil Engineers (ASCE) (2000). *ASCE 30-00* "Guideline for condition assessment of the building envelope", Reston, VA.

American Society of Civil Engineers (ASCE) (2008). *ASCE 7-08* "Minimum Design Loads for Buildings and Other Structures", Reston, VA.

Aslani, H. and Miranda, E. (2005). "Probabilistic Earthquake Loss Estimation and Loss Disaggregation in Buildings", *Report No. 157*. John A. Blume Earthquake Engineering Center, Stanford University, Stanford, CA, 383 pages.

Astrom K.J. (1970). "Introduction to Stochastic Control Theory", Academic Press, New York, N.Y.

Auricchio, F. and Sacco, E. (1997). "A One-Dimensional Model for Superelastic Shape-Memory Alloys with Different Elastic Properties Between Austenite and Martensite", *International Journal of Non-Linear Mechanics*, 32, 1101-1114.

Baber T.T. and Noori M.N. (1985). "Random Vibration of Degrading Pinching Systems", *Journal of Engineering Mechanics*, ASCE, 111(8), 1010-1026.

Bai, J.W., Gardoni, P, Hueste, M.B. (2011). "Story-specific Demand Models and Seismic Fragility Estimates for Multi-story Buildings", *Structural Safety*, 33(1), 96-107.

Bai, J.W., Hueste, M.B., Gardoni, P, (2009). "Probabilistic Assessment of Structural Damage due to Earthquakes for Buildings in Mid-America", *Journal of Structural Engineering*, ASCE, 135(10), 1155-1163.

Barenblatt G.I. (1996). *Scaling, Self-Similarity, and Intermediate Asymptotics*. Cambridge University Press: Cambridge, U.K., 1996.

Basöz N, K.A., King S.A, Law K.H. (1999). "Statistical Analysis of Bridge Damage Data from the 1994 Northridge, CA, Earthquake", *Earthquake Spectra*, EERI, 15(1), 25-53.

Bertero V.V., (1976). "Establishment of Design Earthquakes - Evaluation of Present Methods", *Proceedings of International Symposium on Earthquake Structural Engineering*, Vol.1, St. Louis, Missouri, 1976.

Bertero V.V., Mahin S.A., Herrera R.A. (1978). "Aseismic Design Implications of Near-fault San Fernando Earthquake Records", *Earthquake Engineering and Structural Dynamics*, 6(1), 31-42.

Blind Analysis contest, (2011). "Numerical Prediction of Shaking Table Test of 5-story Steel Frame with and without Base Isolation", Website accessed on June 2012: http://www.cuee.titech.ac.jp/contest/.

Bolt B.A. (1971). "San Fernando Earthquake", *Magnitude, Aftershocks, and Fault Dynamics, Bulletin 196, Chapter 21. California Division of Mines and Geology*, California, 1975.

Bouc, R. (1971). "Mathematical Model for Hysteresis", Report to the Centre de Recherches Physiques, Marseille, France, 6-25.

Carlson, J. D., and Spencer Jr. B. F. (1996a). "Magneto-Rheological Fluid Dampers for Semi-Active Seismic Control", *Proceedings of the 3rd International Conference on Motion and Vibration Control*, Chiba, Japan 3, 35-40.

Carlson, J. D., and Spencer Jr. B. F. (1996b). "Magneto-Rheological Fluid Dampers: Scalability and Design Issues for Application to Dynamic Hazard Mitigation", *Proceedings of 2nd International Workshop on Structural Control*, Hong Kong, 99-109.

Casciati, F. (1989). "Stochastic dynamics of hysteretic media", *Structural Safety*, 6(2-4), 259-269.

Chen, R., Wills C. J., (2011). "HAZUS Annualized Earthquake Loss Estimation for California", California Geological Survey.

Choi E, D.R. and Nielson B. (2004). "Seismic Fragility of Typical Bridges in Moderate Seismic Zones", *Engineering Structures*, 26, 187-199.

Chopra A.K. and Goel R.K.. (2000). "Evaluation of NSP to Estimate Seismic Deformation: SDF Systems", *Journal of Structural Engineering*, ASCE, 126(4), 482-490.

Christopoulos, C., Pampanin, S., Priestley, M.J.N. (2003). "Performance-Based Seismic Response of Frame Structures Including Residual Deformations. Part I: Single-Degree of Freedom Systems", *Journal of Earthquake Engineering*, 7(1), 97-118.

Clark, P.W., Aiken, I.D., Kelly, J.M., Higashino, M. and Krumme, R.C. (1995). "Experimental and Analytical Studies of Shape Memory Alloy Damper for Structural Control", *Proceedings of SPIE*, 2445, 241-251.

Constantinou, M.C. and Symans, M.D. (1993). "Experimental Study of Seismic Response of Buildings with Supplemental Fluid Dampers", *The Structural Design of Tall Buildings*, 2(2), 93-132.

Cuesta I. and Aschheim M.A. (2001). "Inelastic Response Spectra using Conventional and Pulse R-factors", *Journal of Structural Engineering*, ASCE, 127(9):1013-1020.

Dhakal, R.P., Mander, J.B. (2006). "Financial Risk Assessment Methodology for Natural Hazards", *Bulletin of the New Zealand Society for Earthquake Engineering*, 39(2), 91-105.

Dupuis M.R., Best Tyler D.D., Elwood K.J., Anderson D.L., (2013). "Seismic Performance of Shear Wall Buildings with Gravity-Induced Lateral Demands", submitted for publication in *Canadian Journal of Civil Engineering*.

Dyke, S.J., Spencer Jr., B.F., Sain, M.K., and Carlson, J.D. (1996). "Modeling and Control of Magnetorheological Dampers for Seismic Response Reduction", *Smart Materials and Structures*, 5, 565-575.

Eberhard, M.O., Mookerjee, A., and Parrish, M. (2001). "Uncertainties in Performance Estimates for RC Columns", Richmond, CA: Pacific Earthquake Engineering Research Center. http://ce.washington.edu/~peera1.

Faraway J.J., (2004). "Linear Models with R", *Taylor and Francis.*

FEMA-177, F. E. M. A. (1989). "Estimating Losses from Future Earthquake (Panel Report and Technical Background)", Prepared by the Panel on Earthquake Loss Estimation methodology, Committee on Earthquake Engineering, Commission on Engineering and Technical System, and National Research Council for Federal Emergency Management Agency, Washington D.C., 231 pages.

FEMA-249, F. E. M. A. (1994). "Assessment of the State-of-the-art Earthquake Loss Estimation

Methodologies", Prepared by Risk Management Software, Inc, (RMS), and California Universities for Research in Earthquake Engineering (CUREe) for the National Institute of Building Sciences and Federal Emergency Management Agency, Washington, D.C. 300 pages.

FEMA-273, F. E. M. A. (1997). "NEHRP Guidelines for the Seismic Rehabilitation of Buildings", Washington, D.C.

FEMA-274, F. E. M. A. (1997). "NEHRP Commentary on the Guidelines for the Seismic Rehabilitation of Buildings", Washington, D.C.

FEMA-356, F. E. M. A. (1997). " Pre-standard and Commentary for the Seismic Rehabilitation ff Buildings", Washington, D.C.

FEMA manual, F. E. M. A. (1999). "Multi-hazard Loss Estimation Methodology, Earthquake model", HAZUS99 User's Manual. FEMA Mitigation Division Washington, D.C.

FEMA manual, F. E. M. A. (2003). " Multi-hazard Loss Estimation Methodology, Earthquake model", HAZUS®MH MR4 - Technical Manual." FEMA Mitigation Division Washington, D.C.

Florentin J.J. (1961). "Optimal Control of Continuous-Time Markov Stochastic Systems". *Journal of Electro. ontr., Institute of Electrical and Electronics Engineers*, 10, 473-488.

Freeman, J.R. (1932). "Earthquake Damage and Earthquake Insurance: Studies of a Rational Basis for Earthquake Insurance, Also Studies of Engineering Data for Earthquake-resisting Construction", McGraw-Hill, New York, 1st edition, 904 pages.

Fugazza, D. (2003). "Shape-memory Alloy Devices in Earthquake Engineering: Mechanical Properties, Constitutive Modeling and Numerical Simulations", *Dissertation*, supervised by Prof. Ferdinando Auricchio.

Gavin, H.P., Ortiz, D.S., and Hanson, R.D. (1994). "Testing and Modeling of a Prototype ER Damper for Seismic Structural Response Control", *Proceedings of the International Workshop on Structural Control*, USC Publication No. CE-9311, 166-180.

Goulet, C., Haselton C.B., Mitrani-Reiser J., Beck J., Deierlein G.G., Porter K.A., and Stewart J., (2007). "Evaluation of the Seismic Performance of a Code-Conforming Reinforced-Concrete Frame Building - from seismic hazard to collapse Safety and Economic Losses", *Earthquake Engineering and Structural Dynamics*. 36(13), 1973-1997.

Ghobarah A. (2001). "Performance-based Design in Earthquake Engineering: State of Development", *Engineering Structures*, ASCE, 23(8), 878-884.

Gillie J.L., Rodriguez-Marek A., McDaniel C. (2010). "Strength Reduction Factors for Near-fault Forward Directivity Ground Motions", *Engineering Structures*, ASCE, 32(1), 273-

285.

Graf, W.P. and Lee Y. (2009). "Code-oriented Damage Assessment for Buildings", *Earthquake Spectra*, EERI, 25(1), 17-37.

Gunturi S. (1993). "Building-specific Earthquake Damage Estimation", *Ph.D. Dissertation*, John A. Blume Earthquake Engineering Center, Dept. of Civil Engineering, Stanford University, Stanford, CA. 370 pages.

Hall J.F., Heaton T.H., Halling M.W., Wald D.J.. (1995). "Near-source Ground Motion and its Effects on Flexible buildings", *Earthquake Spectra*, EERI, 11(4), 569-605.

Han, Y.L., Xing, D.J., Xiao, E.T. and Li, A.Q. (2005). "NiTi-Wire Shape Memory Alloy Dampers to Simultaneously Damp Tension, Compression, and Torsion," *Journal of Vibration and Control*, 11, 1067-1084.

Haselton, C.B., Goulet, C.A., Mitrani-Reiser, J., Beck, J.L., Deierlein, G.G., Porter, K.A., Stewart, J.P., Taciroglu, E. (2007). "An Assessment to Benchmark the Seismic Performance of a Code-conforming Reinforced Concrete Moment-frame Building", *PEER Report 2007/12,* Pacific Earthquake Engineering Research Center.

Heaton, T.H., Hall, J.F., Wald, D.J., Halling, M.W. (1995). "Response of High-rise and Base-Isolated Buildings to a Hypothetical MW 7.0 Blind Thrust Earthquake", *Science*, 267, 206-211.

Higashino, M. and Aizawa, S. (1996). ‘‘Experimental and Analytical Studies of Structural Control System using Shape Memory Alloy,’’ *Proceedings of 2nd International Workshop on Structural Control*, 18-20 December, Hong Kong, 221-232.

Hwang, H., Jernigan, J.B., Lin, Y-W. (2000). "Evaluation of Seismic Damage to Memphis Bridges and Highway Systems", *Journal of Bridge Engineering*, ASCE, 5(4), 322-330.

IBC (2003). "ICC. 2003 International Building Code", International Code Council: Falls Church, VA.

IBC (2006). "ICC. 2006 International Building Code", International Code Council: Falls Church, VA.

Jaiswal, K., Wald, D., D'Ayala, D. (2011). "Developing Empirical Collapse Fragility Functions for Global Building Types", *Earthquake Spectra*, EERI, 27, 775-795.

Jangid, R.S. (2005). "Optimal Friction Pendulum System for Near-fault Motions", *Engineering Structures*, 27, 349-359.

Jangid, R.S. (2007). "Optimal Lead-rubber Isolation Bearings for Near-fault Motions", *Engineering Structures*, 29, 2503-2513.

Japan Society of Civil Engineers (JSCE). (2000). Earthquake Resistant Design Codes in Japan, Earthquake Engineering Committee, Tokyo.

Karim, K.R., Yamazaki, F. (2001). "Effect of Earthquake Ground Motions on Fragility Curves of Highway Bridge Piers Based on Numerical Simulation", *Earthquake Engineering and Structural Dynamics*, 30, 1839-1856.

Kawashima K., MacRae G.A., Hasegawa K., Ikeuchi T. and Oshima K.. (1992). "Ductility of Steel Bridge Piers from Dynamic Loading Tests", Y. Fukumoto and G. Lee (eds), *Stability and Ductility of Steel Structures under Cyclic Loading*, CRC Press, Boca Raton, 1992.

Kawashima K., Hasegawa K. and Nagashima H., (1991). "Experiment and Analysis on Seismic Response of Menshin bridges", *Proceedings of 1st US-Japan workshop on Earthquake Protective Systems of Highway Bridges*, National Centre for Earthquake Engineering Research, Buffalo, New York, U.S.A., 1991.

Keith Porter, R. K. a. R. B. (2007). "Creating Fragility Functions for Performance-Based Earthquake Engineering", *Earthquake Spectra*, EERI, 23(2), 471-489.

Kelly, J.M. (1986). "Aseismic base isolation: review and bibliography", *Soil Dynamics and Earthquake Engineering*, 5(3), 16, 202-216.

King, S., Kiremidjian, A., Pachakis, D., and Sarabandi, P. (2004). "Application of Empirical Fragility Functions from Recent Earthquakes", *Proceeding of the 13th World Conference on Earthquake Engineering*, Paper No. 2829, Canadian Association for Earthquake Engineering under auspices of International Association of Earthquake Engineering, Vancouver, BC, Canada.

Kircher, C.A., Reitherman, R.K., Whitman, R.V., and Arnold, C. (1997). "Estimation of Earthquake Losses to Buildings", *Earthquake Spectra*, 13(4): 703-720.

Krumme, R., Hayes, J. and Sweeney, S. (1995). "Structural Damping with Shape-Memory Alloys: One Class of Devices", *Proceedings of SPIE*, 2445, 225-240.

Kumar, A., Poonam, Saini, B. and Sehgal, V.K. (2007). "Active Vibration Control of Structures Against Earthquake using Modern Control Theory", *Asian Journal of Civil Engineering (Building and Housing)*, 8(3), 283-299.

Kunde, M.C., Jangid, R.S. (2006). "Effects of Pier and Deck Flexibility on the Seismic Response of the Isolated Bridges", *Journal of Bridge Engineering*, ASCE, 11, 109-121.

Lafontaine, M., Moroni, O., Sarrazin, M., Roschke, P. (2009). "Optimal Control of Accelerations in a Base-isolated Building Using Magneto-rheological Dampers and Genetic Algorithms", *Journal of Earthquake Engineering*, 13, 1153-1171.

Lee, C.L., Leung Su, R.K. (2012). "Fragility Analysis of Low-rise Masonry In-filled Reinforced Concrete Buildings by a Coefficient-based Spectral Acceleration Method", *Earthquake Engineering and Structural Dynamics*, 41, 697-713.

Lee C.M., Goverdovskiy V. and Temnikov A. (2007). "Design of Springs with 'Negative' Stiffness to Improve Vehicle Driver Vibration Isolation" *Journal of Sound and Vibration 302*, (4-5), 865-874.

Lee, H.J., Yang, G.Q., Jung H.J., Spenser, B.F., Lee, I.W. (2006). "Semi-active Neurocontrol of a Base-isolated Benchmark Structure". *Structure Control and Health Monitoring*, 13, 682-692.

Li, C. (2002). "Optimum Multiple Tuned Mass Dampers for Structures under the Ground Acceleration Based on DDMF and ADMF", *Earthquake Engineering and Structural Dynamics*, 31, 897-919.

Ma, H. and Yam, M.C.H. (2011). "Modeling of Self-Centering Damper and its Application in Structural Control", *Journal of Constructional Steel Research*, 67, 656-666.

Mackie, K. R., & Stojadinovic, B. (2003). "Seismic Demands for Performance-based Design of Bridges", Berkeley, CA: Pacific Earthquake Engineering Research Center, University of California Berkeley.

Mackie K.R., Stojadinovic, B. (2004). "Fragility Curves for Reinforced Concrete Highway Overpass Bridges", *Proceedings of 13th World Conference on Earthquake Engineering*, 1553.

Mackie, K.R., & Stojadinovic, B. (2005). "Fragility basis for California highway overpass bridge seismic decision making", Berkeley, CA: Pacific Earthquake Engineering Research Center, University of California Berkeley.

Mackie, K. R., & Stojadinovic, B. (2007a). "Performance-based Seismic Bridge Design for Damage and Loss Limit States", *Earthquake Engineering and Structural Dynamics*, 36(13), 1953-1971.

Mackie, K.R. and Stojadinovic, B. (2007b). "R-Factor Parameterized Bridge Damage Fragility Curves", *Journal of Bridge Engineering*, 12(4), 500-510.

Mackie, K.R., Wong, J., and Stojadinovic, B. (2011). "Bridge Damage and Loss Scenarios Calibrated by Schematic Design and Cost Estimation of Repairs", *Earthquake Spectra*, EERI, 27(4), 1127-1145.

MacRae G.A., Hodge C., Priestley M. J. N. and Seible F. (1994). "Route 5/405 Separation. Shake Table Tests of As-built and Retrofitted Configuration", *SSRP Report No. 94/16, Structural Systems Research Project, Department of Applied Mechanics and Engineering Sciences*, University of California, San Diego, 246 pages, 1994.

MacRae, G.A., Kawashima, K. (1997). "Post-Earthquake Residual Displacements of Bilinear Oscillators," *Earthquake Engineering and Structural Dynamics*, 26, 701-719.

Madden, G. J., Symans, M.D., and Wongprasert, N. (2002). "Experimental Verification of Seismic Response of Building Frame with Adaptive Sliding Base-isolation System", *Journal of Structural Engineering*, 128(8), 1037-1045.

Mahin, S. A. B., Vitelmo V. (1975). "An Evaluation of Some Methods for Predicting Seismic Behavior of Reinforced Concrete Buildings", Earthquake Engineering Research Center, *Report No. EERC 75-5*: 360 pages.

Mahin, S.A., Bertero, V.V. (1981). "Evaluation of Inelastic Seismic Design Spectra," *Journal of the Structure Division*, ASCE, 107(9), 1777-1795.

Makris N., Chang S. (2000). "Effect of Viscous, Visco-plastic and Friction Damping on the Response of Seismic Isolated Structures". *Earthquake Engineering and Structural Dynamics*. 2000; 29(1), 85-107.

Makris N and Zhang J, (2002). "Structural Characterization and Seismic Response Analysis of a Highway Overcrossing Equipped With Elastomeric Bearings and Fluid Dampers: A Case Study", *Report No. PEER-2002/17*, Pacific Earthquake Engineering Research Center, University of California, Berkeley, CA, November 2002.

Makris N. and Black C.J. (2004a). "Dimensional Analysis of Rigid-plastic and Elastoplastic Structures under Pulse-type Excitations", *Journal of Engineering Mechanics*, ASCE, 130(9), 1006-1018.

Makris N. and Black C.J. (2004b). "Dimensional Analysis of bilinear oscillators under Pulse-Type Excitations", *Journal of Engineering Mechanics*, ASCE, 130(9), 1019-1031.

Makris N. and Black C.J.. (2004c). "Evaluation of Peak Ground Velocity as a 'Good' Intensity Measure for Near-source Ground Motions", *Journal of Engineering Mechanics*, ASCE, 130(9), 1032-1044.

Makris N. and Psychogios T., (2006). "Dimensional Response Analysis of Yielding Structures with First-mode Dominated Response", *Earthquake Engineering and Structural Dynamics*, 35(10), 1203-1224.

Makris N. and Vassiliou M.F. (2011). "The Existence of 'Complete Similarities' in the Response of Seismic Isolated Structures Subjected to Pulse-like Ground motions and Their Implications in Analysis", *Earthquake Engineering and Structural Dynamics*, 40, 1103-1121.

Malhotra P.K. (1999). "Response of Buildings to Near-field Pulse-like Ground Motions", *Earthquake Engineering and Structural Dynamics*, 28(11), 1309-1326.

Mander J.B., Basöz N., (1999). "Seismic Fragility Curves Theory for Highway Bridges", *Proceedings of 5th US Conference on Lifeline Earthquake Engineering*, 31-40.

Mander, J.B., Dhakal, R.P., Mashiko, N., Solberg, K.M. (2007). "Incremental Dynamic Analysis Applied to Seismic Financial Risk Assessment of Bridges", *Engineering Structures*, 29(10), 2662-2672

Mander, J.B., Sircar, J., Damnjanovic, I. (2012). "Direct Loss Model for Seismically Damaged Structures", *Earthquake Engineering and Structural Dynamics*, 41, 571-586.

Mavroeidis GP, Papageorgiou AS. (2003). "A Mathematical Representation of Near-fault Ground Motions". *Bulletin of the Seismological Society of America*. 2003, 93(3), 1099-1131.

Mavroeidis G.P., Dong G., and Papageorgiou A.S. (2004). "Near-fault Ground Motions, and the Response of Elastic and Inelastic Single-degree-of-freedom (SDOF) Systems", *Earthquake Engineering and Structural Dynamics*, 33(9), 1023-1049.

Molyneux, W.G., (1957), "Supports for Vibration Isolation", *Aeronautical research Council*, Research Report CP322, UK.

Nagarajaiah S., Reinhorn A. M., Constantinou M. C., Taylor D., Pasala, D. T. R. and Sarlis, A. A. (2010). "True Adaptive Negative Stiffness: A New Structural Modification Approach for Seismic Protection". *5th World Conference on Structural Control and Monitoring*, Tokyo, Japan, July 12-14.

Network for Earthquake Engineering Simulation, (NEES). (2012). nees@berkeley project highlight: "NEES TIPS Seismic Isolation Hybrid Simulation", link accessed Jan 2014: http://www.youtube.com/watch?v=Uh6l5Jqtp0c

Naeim, F., Kelly, J.M. (1999). "Design of Seismic Isolated Structures: From Theory to Practice", NY: John Wiley & Sons.

Nielson, B.G., Desroches, R. (2007). "Seismic Fragility Methodology for Highway Bridges using a Component Level Approach", *Earthquake Engineering and Structural Dynamics*, 36, 823-829.

Noh, H.Y., Lignos, D.G., Nair, K.K., Kiremidjian, A.S. (2012). "Development of Fragility Functions as a Damage Classification/prediction Method for Steel Moment-resisting Frames using a Wavelet-based Damage Sensitive Feature", *Earthquake Engineering and Structural Dynamics*, 41, 681-669.

OpenSees (2007). "Open System for Earthquake Engineering Simulation. Pacific Earthquake Engineering Research Center, University of California: Berkeley, CA", http://opensees.berkeley.edu/.

Ozbulut, O.E. and Hurlebaus, S. (2011). "Seismic Assessment of Bridge Structures Isolated by a Shape Memory Alloy/Rubber-Based Isolation System", *Smart Materials and Structures*, 20(1), 015003.

Padgett, J. E., Nielson, B. G., & DesRoches, R. (2008). "Selection of Optimal Intensity Measures in Probabilistic Seismic Demand Models of Highway Bridge Portfolios", *Earthquake Engineering and Structural Dynamics*, 37(5), 711-725.

Pampanin, S., Christopoulos, C., Priestley, M.J.N. (2003). "Performance-Based Seismic Response of Frame Structures Including Residual Deformations. Part II: Multi-Degree of Freedom Systems", *Journal of Earthquake Engineering*, 7(1), 119-147.

Park, K.S., Jung, H.J., Lee, I.W. (2002). "A Comparative Study on Aseismic Performance of Base Isolation Systems for Multi-span Continuous Bridge", *Engineering Structures*, 24, 1001-1013.

Pasala, D.T.R, Sarlis, A.A., Nagarajaiah, S. Reinhorn, A.M, Constantinou, M.C, and Taylor, D., (2013). "Adaptive Negative Stiffness: A New Structural Modification Approach for Seismic Protection", *Journal of Structural Engineering*, ASCE, 139, NEES 1: Advances in Earthquake Engineering, 1112-1123.

Porter, K.A., and Kiremidjian, A.S. (2001). "Assembly-based Vulnerability of Buildings and Its uses in Seismic Performance Evaluation and Risk Management Decision-making", *Report No. 309*, John A. Blume Earthquake Engineering Center, Stanford University, Stanford, CA, 196 pages.

Porter, K.A. (2003). "An Overview of PEER's Performance-Based Earthquake Engineering Methodology", *Proceedings of Ninth International Conference on Applications of Statistics and Probability in Civil Engineering*, San Francisco, California.

Porter, K.A., Kennedy, R., Bachman, R. (2007). "Creating Fragility Functions for Performance-based Earthquake Engineering", *Earthquake Spectra,* EERI, 23(2), 471-489.

Reese, S., Bradley, B.A., Bind, J., Smart, G., Power, W., Sturman, J. (2011). "Empirical Building Fragilities from Observed Damage in the 2009 South Pacific Tsunami", *Earth-Science Reviews*, 107(1-2), 156-173.

Reinhorn A.M., Viti S., and Cimellaro G.P. (2005). "Retrofit of Structures: Strength Reduction with Damping Enhancement", *Proceeding of the 37th UJNR Panel Meeting on Wind and Seismic Effects*, Tsukuba, Japan.

Reinhorn A.M., Ryu K., and Maddaloni G., (2010). "Modeling and Seismic Evaluation of Nonstructural Components", NEES 10-0004.

Reitherman, Robert, (2012). "Earthquakes and Engineers: An International History", Reston, VA: ASCE Press. ISBN 9780784410622..

Riddell, R., Newmark, N. M. (1979). "Statistic Analysis of the Response of Nonlinear Systems Subjected to Earthquakes", *Structural Report Series 468*, Civil Engineering, University of Illinois.

RSMeans Engineering Department (2009). "RSMeans Building Construction Cost Data 2012", *John Wiley & Sons, Inc*., Hoboken, New Jersey.

Ruiz-Garcia, J., Miranda, E. (2005). "Performance-Based Assessment of Existing Structures Accounting for Residual Displacements", *Technical Report No. 153*, John A. Blume Earthquake Engineering Center, http://blume.stanford.edu, Stanford University, 444 pages.

Ruiz-Garcia, J., Miranda, E. (2006a). "Direct Estimation of Residual Displacement From Displacement Spectral Ordinates", *Paper No. 1101*, *Proceedings of 8NCEE*, 10 pages.

Ruiz-Garcia J., Miranda E. (2006b). "Residual Displacement Ratios for Assessment of Existing Structures", EESD, 35(3), 315-336.

Ruiz-Garcia J., Miranda E. (2006c), "Evaluation of Residual Drift Demands in Regular Multi-story Frames for Performance-based Seismic Assessment", *Earthquake Engineering and Structural Dynamics*, 35(13), 1609-1629.

Ruiz-Garcia J., Miranda E.. (2010), "Probabilistic Estimation of Residual Drift Demands for Seismic Assessment of Multi-story Framed Buildings", *Engineering Structures*, 32, 11-20.

Ryan K.L., Chopra, A.K., (2004). "Estimation of Seismic Demands on Isolators in Asymmetric Buildings using Non-linear Analysis", *Earthquake Engineering and Structural Dynamics*, 33(3), 395-418.

Salich, J., Hou, Z. and Noori, M. (2001). "Vibration Suppression of Structures using Passive Shape Memory Alloy Energy Dissipation Devices," *Journal of Intelligent Material Systems and Structures*, 12, 671-680.

Sarabandi, P., Pachakis, D., King, S., and Kiremidjian, A. (2004). "Empirical Fragility Functions from Recent Earthquakes", *Proceedings of the 13th World Conference on Earthquake Engineering, Paper No. 1211*, Canadian Association for Earthquake Engineering under auspices of International Association of Earthquake Engineering Vancouver, BC, Canada.

Sarlis A.A., Pasala D.T.R., Constantinou M.C., Reinhorn, Nagarajaiah S., and Taylor D.P. (2013). "Negative Stiffness Device for Seismic Protection of Structures". *Journal of Structural Engineering*, ASCE, 139, 1124-1133.

Sayani, P.J. and Ryan, K.L. (2009). "Comparative Evaluation of Base-isolated and Fixed-base Buildings using a Comprehensive Response Index", *Journal of Structure Engineering*, ASCE, 135(6), 698-707.

Scholl, R.E. (1979). ""Seismic Damage Assessment for High-rise Buildings: Annual Technical Report", URS/John A. Blume & Associates, Inc., San Francisco, CA. 131 pages.

Seigenthaler, R., (1970). "Earthquake-Proof Building Supporting Structure with Shock Absorbing Damping Elements", *Schweizerische Bauzeitung*, 20, 211 pages.

Shinozuka, M, Feng, M.Q., Lee J, Naganuma T. (2000). "Statistical Analysis of Fragility Curves", *Journal of Engineering Mechanics*, ASCE, 126(12), 1224-1231.

Simo, J.C., Hughes, T.J.R., (1998). "Computational Inelasticity", Interdisciplinary Applied Mathematics, Vol. 7, ISBN 978-0-387-97520-7.

Skinner, R.I., Robinson, W.H. McVerry, G.H. (1993). "An Introduction to Seismic isolation", Chichester: Wiley J. & Sons.

Solberg, K.M., Dhakal, R.P., Mander, J.B., and Bradley, B.A. (2008). "Computational and Rapid Expected Annual Loss Estimation Methodologies for Structures", *Earthquake Engineering and Structural Dynamics*, 37(1), 81-101.

Somerville PG, Smith NF, Graves RW, Abrahamson NA. (1997), "Modification of Empirical Strong Ground Motion Attenuation Relations to Include the Amplitude and Duration Effects of Rupture Directivity". *Seismological Research Letters*, 68(1), 199-222.

Somerville P.G. (2003). "Magnitude Scaling of the Near Fault Rupture Directivity Pulse", *Physics of the Earth and Planetary Interiors*, 137(1), 201-212.

Soong, T.T., and Reinhorn, A.M. (1993). "An Overview of Active and Hybrid Structural Vontrol Research in the U.S", *Structure Design of Tall Buildings*, 2, 192-209.

Spencer Jr. B. F., D., S. J., Sain, M. K., and Carlson, J. D. (1997). "Phenomenological Model for Magnetorheological Dampers", *Journal of Engineering Mechanics*, ASCE, 123(3), 230-238.

Spencer, Jr., B. F., Yang, G., Carlson, J. D., and Sain, M. K. (1998). "Smart Dampers for Seismic Protection of Structures: A Full-scale Study", *Proceedings of the 2nd World Conference on Structural Control*, Kyoto, Japan, 417-426.

Steinbrugge K.V., McClure, F., and Snow, A.J. (1969). "Studies in Seismicity and Earthquake Damage Statistics", Prepared for the U.S. Coast and Geodetic Survey, Department of housing and urban development, Washington D.C., part 1, 399 pages, part 2, 194 pages.

Structural Engineers Association of California (SEAOC). (1995). "Vision 2000 A Framework for Performance-Based Seismic Engineering", Structural Engineers association of California: Sacramento, CA.

Suduo, X. and Xiongyan, L. (2007). "Control Devices Incorporated with Shape Memory Alloy", *Earthquake Engineering and Engineering Vibration*, 6, 159-169.

Symans, M.D., and Constantinou, M.C. (1997a). "Experimental Testing and Analytical Modeling of Semi-active Fluid Dampers for Seismic Protection", *Journal of Intelligent Material Systems and Structures*, 8(8), 644-657.

Symans, M. D., and Constantinou, M.C. (1997b). "Seismic Testing of a Building Structure with a Semi-active Fluid Damper Control System", *Earthquake Engineering and Structural Dynamics*, 26(7), 759-777.

Symans, M.D. and Constantinou, M.C. (1998). "Passive Fluid Viscous Damping Systems for Seismic Energy Dissipation", *ISET Journal of Earthquake Technology*, 35(4), 185-206.

Symans, M.D., (2008a). "Special Issue on Design and Analysis of Structures with Seismic Damping Systems", *Journal of Structural Engineering*, ASCE, 134(1), 1-2.

Symans, M.D., Charney, F.A., Whittaker, A.S. (2008b). "Energy Dissipation Systems for Seismic Applications: Current Practice and Recent Developments", *Journal of Structural Engineering,* ASCE, 134(1), 3-21.

Symans, M.D. and Reigles, D.G. (2004). "Supervisory Fuzzy Logic Control of Smart Seismic Isolation Systems," *Proceedings of ASCE Structures Congress 2004*, Nashville, TN, May.

Tagami, J., Matsunaga, Y., Kurino, H., and Yamada, T. (2004). "High-Performance Passive Hydraulic Damper HiDAXe with Semi-Active Characteristics", *Kajima Technical Research Institute Annual Report 52(1)*, 85-90.

Tang, Y. and Zhang, J., (2011a). "Probabilistic Seismic Demand Analysis of RC Shear Walls Considering Soil-Structure Interaction Effects", *Engineering Structures*, 33(1), 218-229.

Tang, Y., and Zhang, J., (2011b). "Response Spectrum-oriented Pulse Identification and Magnitude Scaling of Forward Directivity Pulses in Near-fault Ground Motions", *Soil Dynamics and Earthquake Engineering,* DOI: 10.1016/j.soildyn.2010.08.006, 31, 59-76.

Tothong P & Luco N (2007). "Probabilistic Seismic Demand Analysis using Advanced Ground Motion Intensity Measures," *Earthquake Engineering and Structural Dynamics*, 36(13), 1837-1860.

Vibration data. "Kobe earthquake www.vibrationdata.com/earthquakes/kobe.htm",

Wen, Y.-K. (1976). "Method for Random Vibration of Hysteretic Systems", *Journal of Engineering Mechanics Division,* 102, 249-263.

Williams, M.S., Villemure, I., Sexsmith, R.G. (1997). "Evaluation of Seismic Damage Indices for Concrete Elements Loaded in Combined Shear and Flexure", *ACI Structural Journal*, 94(3), 315-322.

Whitman, R.V., Anagnos, T., Kircher, C.A., Lagorio, H.J. Lawson, R.S., and Schneider, P. (1997). "Development of a National Earthquake Loss Estimation Methodology", *Earthquake Spectra,* EERI, 13(4), 643-662.

Xue, S., Li, X. (2007). "Control Devices Incorporated with Shape Memory Alloy", Earthquake *Engineering and Engineering Vibration*, 6 (2), 159-169.

Yang, G, S.B., Carlson J.D., Sain M.K. (2002). "Large-scale MR Fluid Dampers: Modeling and Dynamic Performance Considerations", *Engineering Structures*, 24(3), 309-323.

Yang, J.N. (1975). "Application of Optimal Control Theory to Civil Engineering Structures", *Journal of the Engineering Mechanics Division*, 101(6), 819-838.

Yamazaki F, M.H., Hamada T. (2000). "Damage Assessment of Expressway Networks in Japan Based on Seismic Monitoring", *Proceedings of 12th World Conference on Earthquake Engineering*. 1551.

Zhang, J. and Huo, Y. (2009). "Evaluating Effectiveness and Optimum Design of Isolation Devices for Highway Bridges using the Fragility Function Method", *Engineering Structures*, 31(8), 1648-1660.

Zhang J., Tang Y. (2009). "Dimensional Analysis of Structures with Translating and Rocking Foundations under Near-fault Ground Motions", *Soil Dynamics and Earthquake Engineering*, 29(10), 1330-1346.

Zhang J and Xi W. (2012). "Optimal Nonlinear Damping for Inelastic Structures Using Dimensional Analysis", *Structures Congress* 2012, Chicago, IL, March 2012.

Zhang J., Xu S.Y., and Tang Y. (2011). "Inelastic Displacement Demand of Bridge Columns Considering Shear-flexure Interaction". *Earthquake Engineering and Structural Dynamics*, 40, 731-748.

Zuo, X.B., Li, A.Q. and Chen, Q.F. (2008). "Design and Analysis of a Superelastic SMA Damper," *Journal of Intelligent Material Systems and Structures*, 19, 631-663.